Development of a Label-free Graphene Hall Effect Biosensor

By

Davut Izci

School of Engineering

A Thesis Submitted to the Faculty of Science, Agriculture and Engineering for the Degree of Doctor of Philosophy

February 2019

Acknowledgements

I would like to acknowledge my supervisors John Hedley, Neil Keegan, Harriet Grigg and Konstantin Vasilevskiy for their guidance and support throughout my project and group members of Institute of Cellular Medicine; Carl Dale, Julia Spoors and Chen Fu for their help. Particularly Carl for his help in guiding me to graphene fabrication, characterisation and planning appropriate biochemical procedures for detection of biomolecules and observation of the system response. I would also like to thank the Nexus team at Newcastle; Anders Barlow, Jose Portoles and Billy Murdoch for their help and guidance in performing XPS, HIM imaging and providing training for performing SEM and EDX. In addition, I would like to thank to group members of Microsystems, Michelle Pozzi for his support in providing me equipment and Richie Burnett for valuable discussions on design and fabrication of PCB based Hall sensors and signal processing board. Also, a big thanks to technicians in electronics workshop Paul Watson and Paul Harrison for helping me with tools and equipment I needed throughout this time. Isabel Arce-Garcia in Advanced Chemical and Materials Analysis Department also deserves credit. I am grateful for her help in Raman analysis of my samples and surface coating works. I am grateful to my colleagues Tom Bamford for his help in printing graphene oxide devices, and Sinziana Popescu for her help on photoelectrochemical etching process on silicon carbide. Lastly, I would like to acknowledge the contribution of Nikhil Ponon and Rachel Savidis for their invaluable help in device fabrication and operating clean room equipment, and Aydin Sabouri, from Birmingham University, for his help to provide samples prepared by FIB for graphene suspension work. Last but not least, a heartfelt thanks to my wife, Tuba, for her consistent support and enduring love throughout this project. This project would have not been successful without her and our lovely daughter Helin Arya.

Collaborative Work

I would like to acknowledge the people listed below for their collaboration on related parts of the work.

- **Photoelectrochemical etch of SiC;**

My colleague, Sinziana Popescu, has provided the silicon carbide samples and platinum wire along with UV light source and Fresnel lens for use in this work. She also designed a Teflon plate for handling aqueous solution. The experiments and the characterisation works were carried out together.

- **FIB prepared substrates;**

Aydin Sabouri, from Birmingham University, has prepared silicon substrates having holes and trenches by performing focused ion beam milling techniques. The provided substrates were used for suspending CVD grown graphene.

- **Inkjet printing of GO Hall devices;**

My colleague, Tom Bamford, has printed the graphene oxide Hall devices on glass substrates for this work. He has also performed chemical reduction work and printed silver contacts after obtaining reduced graphene oxide samples.

Abstract

Graphene has recently motivated various research groups due to its peculiar properties and the research on this novel nanomaterial is growing rapidly. Electric transport properties of graphene make it a promising candidate for future nanoelectronics applications. Moreover, thermal, mechanical and optical properties are other powerful indications of its capability to open a new era in nanoscale developments in a variety of fields. Carbon materials have already been demonstrated to be promising in biomedical applications and graphene, as a building block for graphitic materials, holds a unique place in terms of biocompatibility; offering great opportunities due to its high surface to volume ratio and charge transport capability. Being electrically conductive and having ultrahigh mobility offers a great deal in electronic application developments. Therefore, in this study, the promise of graphene to build a biosensing platform has been investigated through developing a biosensor that exploits incredible electric transport properties of graphene along with its high sensitive and selective biocompatible structure. In order to achieve such a purpose, a label-free biosensing platform has been developed by employing Hall effect principle. This thesis presents all the details to form a biosensing platform along with the promising results that have been obtained.

List of Publications

Davut Izci, Carl Dale, Neil Keegan, and John Hedley, 2017. “Design and Construction of a High Sensitive Graphene Magnetosensing System”. DOI: 10.1109/ICSENS.2017.8233962. 2017 IEEE SENSORS.

Davut Izci, Carl Dale, Neil Keegan, and John Hedley, 2018. “The Construction of a Graphene Hall Effect Magnetometer”. DOI: 10.1109/JSEN.2018.2872604. IEEE Sensors Journal.

Davut Izci, Carl Dale, Neil Keegan, Julia Spoors, and John Hedley. “Development of a Label-free Graphene Hall Effect Biosensor”. (To be submitted soon to Biosensors & Bioelectronics Journal)

Contents

List of Figures

List of Tables

Glossary

2DEG	Two-dimensional electron gas
Al	Aluminium
AlGaAs	Aluminium Gallium Arsenide
Ar	Argon
Au	Gold
BHF	Buffered hydrogen peroxide
Bi	Bismuth
BSA	Bovine serum albumin
C	Carbon
$\mathbf{C_{17}H_{10}O_2}$	1-Pyrenecarboxylic acid
$\mathbf{C_6H_{13}NO_4S.xH_2O}$	MES Hydrate
$\mathbf{CH_3OH}$	Methanol
$\mathbf{CO_2}$	Carbon dioxide
Cr	Chromium
Cu	Copper
CVD	Chemical vapour deposition
DAQ	Data acquisition
DNA	Deoxyribonucleic acid
EDC	1-Ethyl-3-(3-dimethylaminopropyl) carbodiimide
EDX	Energy-dispersive X-ray spectroscopy
FIB	Focused ion beam
Ga	Gallium
GaAs	Gallium Arsenide
$\mathbf{H_2O}$	Water
$\mathbf{H_2O_2}$	Hydrogen peroxide
$\mathbf{H_2SO_4}$	Sulphuric acid
He	Helium
HF	Hydrofluoric acid
HIM	Helium Ion Microscopy
IC	Integrated circuit
IgG	Immunoglobulin G

InAs	Indium arsenide
InSb	Indium antimonite
IPS	Isopropanol
KCl	Potassium Chloride
KH_2PO_4	Sodium phosphate monobasic
KI	Potassium iodide
KOH	Potassium hydroxide
MES	2-(N-morpholino) ethanesulfonic acid
Na_2HPO_4	Sodium phosphate dibasic
NaCl	Sodium chloride
NH_4OH	Ammonium solution
NHS	N-hydroxysuccinimide
Ni	Nickel
nm	Nano meter
nM	Nano molar
NMP	N-Methyl-2-pyrrolidone
O	Oxygen
PBS	Phosphate buffered saline
POC	Point-of-care
SEM	Scanning electron microscopy
Si	Silicon
SiC	Silicon carbide
SQUID	Superconducting quantum interference device
XPS	X-ray photoelectron spectrometry
µm	Micro meter
µM	Micro molar

Chapter 1. Introduction

The invention of first biosensors [1] opened a new door to multidisciplinary research and it led to astonishing progress in applications of biosensors [2]. The use of biosensors has gained an outstanding importance in a variety of fields such as biomedicine, diagnosis, drug discovery, food safety, security and defence applications and environmental monitoring [3]. Implementation of novel biological techniques and improved instrumentation have enhanced the sensitivity limits and, with the accommodation of nanomaterials [4], an incredible progress towards forming innovative biosensors has been initiated. The biosensing field paves the way towards integration of novel biological techniques with nanomaterials, which will help develop specific biosensors having potentially ultrahigh sensitivities. Moreover, the developments are expected to allow facilitating biosensors as point-of-care systems which will improve diagnostics of diseases, make health care easier and allow real-time monitoring without any need for physical examination by experts.

Biosensor research is a dynamic field and the efforts are towards improving the systems by developing biosensing platforms that can achieve detection ranges of small concentrations. This is important for early diagnostics of any harmful biomolecule and, consequently, preventing potential undesired outcomes. To do so, utilization of novel materials along with new design and fabrication techniques are required. Devices used in detection process should be reduced in size as much as possible with reasonable design structures along with effective methods to detect lower concentrations. Size reduction is not only important for better sensitivity but also for achieving practical devices for end user. Meanwhile, operational conditions are also an important point that must be considered although having a highly sensitive sensing system is desired. Therefore, there should be a balance between sensitivity and applicability since fabrication, cost and practical implementation are of importance for the end user.

In conjunction with these requirements, the tendency in biosensing field is towards the development of point-of-care applications with fast response times since this is desirable in terms of users’ point of view. However, it requires too much effort as further development is needed to miniaturize the system and develop related instrumentation. Micro fabrication techniques have been established well enough to solve the issue to an extent. And yet, it is not sufficient to address the high sensitivity demand as low dimensions lead to instability [5] issue in materials. Thus, the devices must be prevented from being unstable as marching towards smaller sizes may cause the system to become unstable.

Graphene, as a nanomaterial, has been proved to be stable along with its one-atom thickness and two-dimensional structure [5, 6]. It holds unique electrical, mechanical, thermal and optical properties such as ultra-high mechanical stiffness, excellent electric transport properties and high thermal conductivity with optical transparency [7, 8]. Due to incredible properties, it allows development of various applications, from transistors to sensors and energy storage equipment to biomedical devices, with very high sensitive and effective performances [8-24]. Having high carrier mobility and gate controllable carrier concentration places graphene particularly as an outstanding nanomaterial for potential high sensitive future applications such as transparent conductors, flexible electronics, displays, transistors and high frequency electronic devices [25-27]. The advantages of graphene can be evolved in such a way to have very high sensitive biosensors along with excellent performances as a result of peculiar material properties it encompasses. Graphene could be utilized for biosensing purposes by employing its mechanical, electrical, optical or thermal properties [16, 28-39]. Therefore, a reasonable method should also be implemented to achieve bio-detection in a practical and cost-effective manner since biosensors can be in various forms in terms of their principal of operation such as electrochemical, mechanical or optical detecting mechanisms [2, 3, 40, 41].

This study was devoted to employ electronic properties of graphene since it possesses very high mobility. To do so, Hall effect mechanism was decided to be employed. The Hall effect phenomena is known for decades [42] and has been used for material characterization heavily [43]. However, it has found places in several industrial applications from cars, planes and sensitive positioning applications in factories to biosensing applications [44-60]. It is one of the best method that could be implemented for such a purpose since graphene has the highest carrier mobility ever known and has one-atom thickness [61]. Therefore, electrical properties of graphene make it an excellent candidate for such applications since the obtained transverse voltage depends on carrier mobility and thickness of the material.

Hall effect devices are currently dominating the market of the magnetic sensors [62-64] due to several advantages such as allowing miniaturization, being compatible with electronics integration, cheaper fabrication and room temperature operation with high linearity [65]. There has already been a considerable amount of reports to realize the potential of graphene as Hall effect sensors [63, 66-72]. The results reveal the great promise of graphene in this field since it beats all counterpart materials such as indium antimonite (InSb), and two-dimensional electron gas (2DEG) thin structures [71] which are the two types that are mostly employed in Hall effect applications requiring higher sensitivities.

The choice of employing Hall effect is not only due to exploiting the unique properties of graphene but also because of the magnetic field being adopted to operate devices. Apart from its key role in daily life from electric production to data storage and from quantitative explanation of physical properties of materials to particle acceleration [43, 44], magnetic field has a huge potential of providing non-destructive and highly efficient detection platforms in biosensing field [73]. It provides a low intrinsic background in biological systems since those systems have no comparable biological signal [74]. Therefore, the advantages of the magnetic field in biological systems is also exploited by combining it with the unique electric properties of graphene nanomaterial to form a highly sensitive and cost-effective biosensing platform.

1.1 Research Gap

Biosensors field is one of the fields that requires more improvements and currently an enormous amount of work is undertaken [3, 4, 75-79]. Using magnetism is one of the techniques that was widely used to form detection platforms for biosensing purposes since it has a huge promise [73, 80-82]. Several mechanisms were reported based on different applications of magnetism such as magnetoresistance [83-86], planar Hall effect [87-93], spin valve [94-98], superconducting quantum interference devices (SQUID) [99], and Hall effect [65, 100-108]. Amongst them, the Hall effect principle is the easiest way of achieving a magnetic sensor although it may not reach the sensitivity limits offered by some of those structures, e.g. SQUID sensors [48]. Although each application has some certain advantages in terms of sensitivity, the specific requirements for operation such as low temperature demand in SQUID sensors, or fabrication complexity could make them not practical. Thus, a considerable effort can be observed in biosensing applications that employ the Hall effect principle [109-115].

The Hall effect principle is discussed in detail in section 2.2. Briefly, it can be explained as the transverse voltage that occurs due to Lorentz force. This force is appeared due to deviation in electron flow which can be observed under the presence of perpendicularly applied magnetic field (See equation (2-1)). The obtained voltage depends on several parameters such as applied current and field, thickness and geometrical structure along with carrier mobility and density of a particular material (See equation (2-2)). Unlike the classical Hall effect, planar Hall effect is used to describe the change in magnetoresistance in ferromagnetic materials under an applied magnetic field [116]. Basically, the relationship is only geometrical meaning that in classical Hall effect the field is applied perpendicularly whereas in planar Hall effect it is applied in parallel to sensing plane.

In terms of materials, several structures have been reported such as silicon, bismuth, indium antimonite thin films and two-dimensional electron gas heterostructures for fabrication of Hall devices [117]. Commercially available Hall sensors are dominated by silicon, due to well-developed CMOS manufacturing process [63, 70, 118, 119]. However, in applications requiring higher sensitivity, heterostructures from III-V compounds are required because of superior electron transport properties they have [120-125]. However, manufacturing cost can be high and integration with signal processing circuitry may be difficult [63]. Indium antimonite [126] and bismuth [127] thin films are also used in Hall applications due to the high electron mobility properties they retain and the linear response they demonstrate for a wide range of field strengths. Recently, graphene has become a material of interest for many applications, it is a particularly promising candidate for Hall effect applications [61, 68, 71, 128] since it is one-atom thick and retains ultrahigh carrier mobility [27, 129], thus, causing charge carriers to be constrained in a two-dimensional plane, consequently, leading to a higher sensitivity and an outstanding resolution. Being intrinsically low noise material [71, 128, 130] is another advantage it has. Therefore, it encompasses the best material properties for such applications.

Various sensors based on graphene have been constructed hitherto for detection of hazardous gases [131-133], physiological signals [134], heavy metal ions [135, 136] and mechanical force [137, 138]. It was also used to detect nucleic acid [139], proteins [140], dopamine [141, 142], glucose [143, 144] and hydrogen peroxide [134]. Despite being the best material candidate for Hall effect sensors [145] and having attracted researchers for various engineering applications [10, 11, 13, 15, 137, 146-148], there has not been any considerable effort to utilise graphene as a Hall effect biosensor. However, a considerable amount of work has been devoted to development of graphene Hall effect sensors for different applications [66, 68, 145, 149-152].

Apart from the reasons given above, most of the reported Hall effect biosensors employ magnetic beads as a label for detection [153]. General implementation has been about functionalizing paramagnetic beads and making use of the ac susceptibility measurements [154] to detect signal change that occurs due to the existence of magnetic beads in case of binding events. Meanwhile, few works have employed a label-free approach; however, they have not been operated in real-time and, instead of using Hall devices, the Hall measurements were used as a supporting tool, for characterising the system [155-157]. In the light of the issues stated above, the aim of this research was to explore potential biosensor applications by exploiting the unique electric transport properties of graphene and adopting Hall effect sensing principle. To eliminate the disadvantages of labelled detection, this work has also focused on practical designs to develop a label-free Hall effect biosensor that can operate in liquid medium for real-time observation.

1.2 Motivation and Objectives

Hall effect sensing mechanism is one of the most promising methods as a sensing method amongst other magnetic sensors because of the practicality of implementation. In addition, sensitivity could be increased with arrangements on the material structure. The sensitivity limit for a Hall effect type sensor can be improved incredibly by employing the best suitable material choice. Because, materials with high carrier mobility, low carrier concentration and narrow band gaps provide the exact characteristics for high sensitivity Hall devices [43, 44, 158]. In addition, thickness reduction delivers an exceptional advantage since the charge carriers are confined, thus, causing a stronger force [61, 71, 72, 159].

Since the successful isolation of graphene [6], academia and industry has intensely been attracted by its unique properties such as ultrahigh electron mobility, lowest resistivity, optical transparency, incredible mechanical strength, flexibility, high surface area and compatibility to biomolecules [9, 10, 146, 156, 160-163]. All these properties make it a promising material for several applications, particularly, a candidate for sensing applications [164]. In terms of Hall effect sensing principle, graphene can be considered the best choice for such applications due to its incredibly high carrier mobility and atomically thin body. In addition, graphene does not require specific temperature to operate [165], hence, it can be used in room temperature with high sensitivity which will make the implementation of point-of-care applications possible. In addition, small variations in sensitivity due to thermal effects can be compensated via varying the gate voltage [63]. Moreover, it exhibits intrinsically low noise [130, 145], consequently, contributes the sensitivity improvement whilst being operated as a Hall sensor. Being compatible with biomolecules, having large surface to volume ratio and possessing great electrical properties of graphene motivates this research.

The objective was to design suitable geometrical structures from single layer graphene sheets with optimized length to width ratio and then to explore the promise of those structures as Hall effect sensors. After that the ultimate goal was to functionalize the sensor surface to form a biosensor which can be used in wet environment and provide real-time observation. This will result in creating Hall effect biosensors that do not need labels such as magnetic beads, thus, preventing any drawback; e.g. signal reduction due to separation distance between sensor to bead and time for a bead to reach the active surface area. Instead of developing an application specific biosensor, mouse IgG was used to show proof of principle.

1.3 Thesis Outline

This thesis presents development of a graphene biosensor by employing Hall effect sensing principle. The system was built to perform label-free detection in real-time. To do so, Immunoglobulin G (IgG) protein was used as a target analyte and the sensor surface was functionalized accordingly to characterise the system response. The thesis covers all the effort from design and fabrication to functionalization and characterization of the system to achieve the biosensing platform including driving and signal processing circuitry. Therefore, it is structured into 8 chapters and the whole steps that were undertaken to achieve the desired biosensing system are presented in related sections.

The first chapter is a brief introduction to the main concept of the work and outlines the field of study in general including the structure of the thesis. It also introduces the motivation that prompted to undertake this study along with the research gap in this field.

A literature review on graphene nanomaterial and Hall effect principle is presented in Chapter 2 along with their typical and unique properties and implementation to applications. Some of the magnetic field sensors are also presented briefly in this chapter since this work is, basically, related to magnetic field sensing and employs it to build a biosensing system. A brief introduction of biosensing concept is given with related literature regarding graphene and Hall effect biosensors.

Chapter 3 is devoted to the construction of required electronic circuitry for actuating sensors and obtaining the output since there are undesired effects which are causing less sensitive or less accurate results. This chapter takes a closer look at those effects and presents the solution to the problem by introducing the developed circuitry along with the promising results it provided.

Gold-based Hall effect sensors were designed and fabricated initially using different approaches as a cost-effective solution for Hall effect biosensors. The response of those devices was observed for potential biosensing outcomes. Chapter 4 gives the steps that were undertaken from design to fabrication and characterisation of gold Hall effect devices on different substrates having different structures.

The aim was initially to prepare graphene so that it can be used to fabricate Hall sensors on substrate. In addition, it was also aimed to prepare graphene in such a way that it can be adopted to form suspended Hall sensors. Then, the plan was to fabricate Hall devices from both suspended and supported graphene sheets and explore their behaviour in terms of sensitivity and repeatability. Therefore, different techniques such as epitaxial graphene growth on silicon carbide and CVD grown graphene were employed to prepare graphene so that it can be used to form supported and suspended structures. Chapter 5 presents various options that were adopted for this purpose with the feasibility along with the strength and weakness of each method.

In terms of fabricating devices, the main focus was to use CVD grown graphene, on a Si/SiO_2 substrate, as it is a promising method for obtaining large area graphene sheets. Therefore, commercially available graphene samples were purchased and used for microfabrication. In addition, direct printing of graphene oxide devices was also explored as an alternative method. The detailed overview on fabrication and obtained results are discussed in Chapter 6.

Chapter 7 demonstrates the performance of graphene Hall effect biosensors quantitatively as well as the further steps required to prepare and isolate the sensors for liquid medium. The obtained results are discussed in detail. Finally, the conclusion and final remarks on the work are given in Chapter 8 with potential further improvements that may be performed.

Chapter 2. Graphene, Hall Effect and Biosensors

In this chapter, a literature review on graphene nanomaterial, Hall effect principle and biosensors is presented. Unique properties of graphene and the production methods are discussed including the promise of it for future applications in various fields. Meanwhile, necessary quantitative expressions and qualitative explanation of the Hall effect sensing mechanism is described together with its implementation to applications. Moreover, a brief overview on magnetic types of sensors is given including applications. Finally, biosensing concept is explained and the literature related to Hall effect and graphene in biosensing is presented.

2.1 Graphene

Graphene is a two dimensional nanomaterial consisting of hexagonal honeycomb structure of carbon atoms [26]. It can be seen in single, double or multilayer forms. Researchers have started to study different aspects of it after it has been successfully isolated by a research group in Manchester University, UK, in 2004 [166]. The atomic structure of graphene is represented in Figure 2-1.

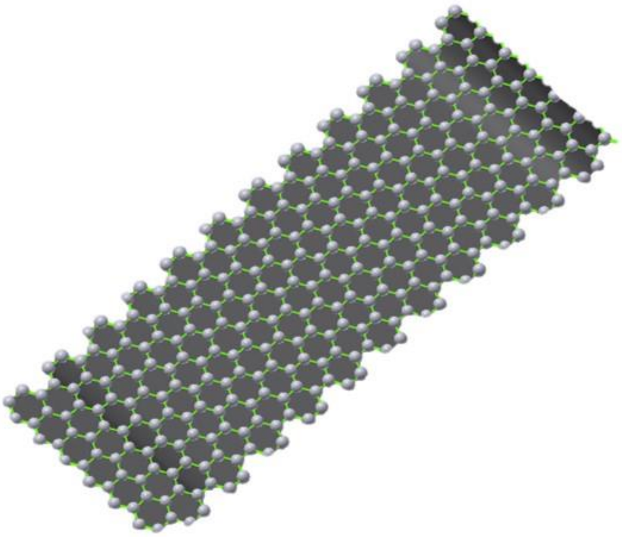

Figure 2-1: Representation of graphene's atomic structure. It is comprised of single layer carbon atoms in a hexagonal structure.

Unique electrical, mechanical and optical properties have been observed in graphene [11, 25, 129, 167-177]. Therefore, it is now an of interest nanomaterial for a wide range of research groups and industry because of its promising properties. It provides a multidisciplinary research area for researchers having different backgrounds. And it is estimated that graphene will revolutionize many applications in near feature [178]. The following sections provide more detailed outlook of graphene's properties, manufacturing, characterisation and potential future applications.

2.1.1 History

Carbon is an important material for life and sources of organic chemistry. Various structures having different physical properties are presented in carbon based systems [23]. Graphene is considered as the initial point to identify the electronic properties in all allotropes of carbon [179]. The theoretical studies of two-dimensional graphite were conducted many decades ago [180] and used for describing properties of different carbon-based materials. Figure 2-2 presents a brief historical outlook to discovery of graphene.

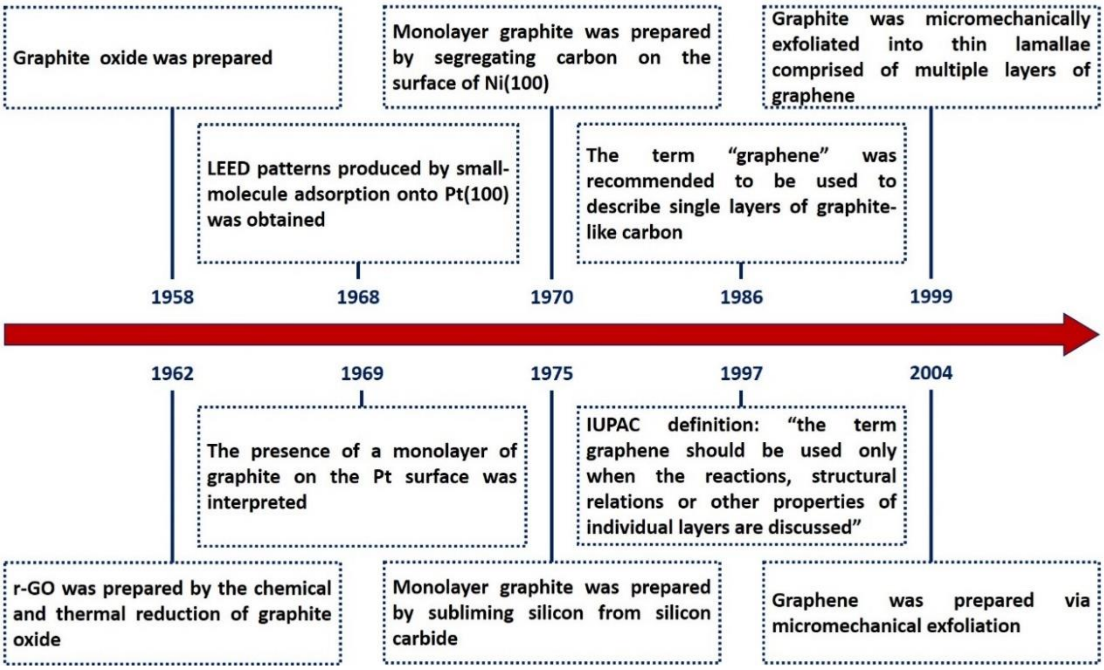

Figure 2-2: Timeline for history of isolation and characterisation of graphene. Adapted from [181].

Two decades ago, it was understood that graphene offers incredible condensed matter analogue of 3D quantum electrodynamics, however, it was assumed not to be in free state [23, 182] because two dimensional crystals were believed to be unstable thermodynamically and could not exist [166]. This idea has changed after discovery of graphene [6] and other two dimensional atomic crystals, such as single-layer boron nitride [183]. These discoveries showed that two dimensional crystals are continuous and more importantly exhibit high crystal quality [6, 175, 184]. Discovery of graphene brought Nobel prize to Andre Geim and Konstantin Novoselov in 2010 [185]. There has been a tremendously increasing number of researches so far. It is believed that graphene will revolutionize many applications due to its unique physical properties and has a potential of replacing silicon in electronics industry [23]. Since the famous prediction of Gordon Moore (known as Moore's Law) the number of transistors on a chip has increased significantly, and today that number is close to two billion. However, shrinking silicon more is not viable as there would be fabrication limitations and the quantum effects would take place. At that point a material which has the potential to replace silicon will be of interest. And graphene seems to have this potential if the bandgap issue can be overcome. Figure 2-3 shows the increasing trend in graphene related research.

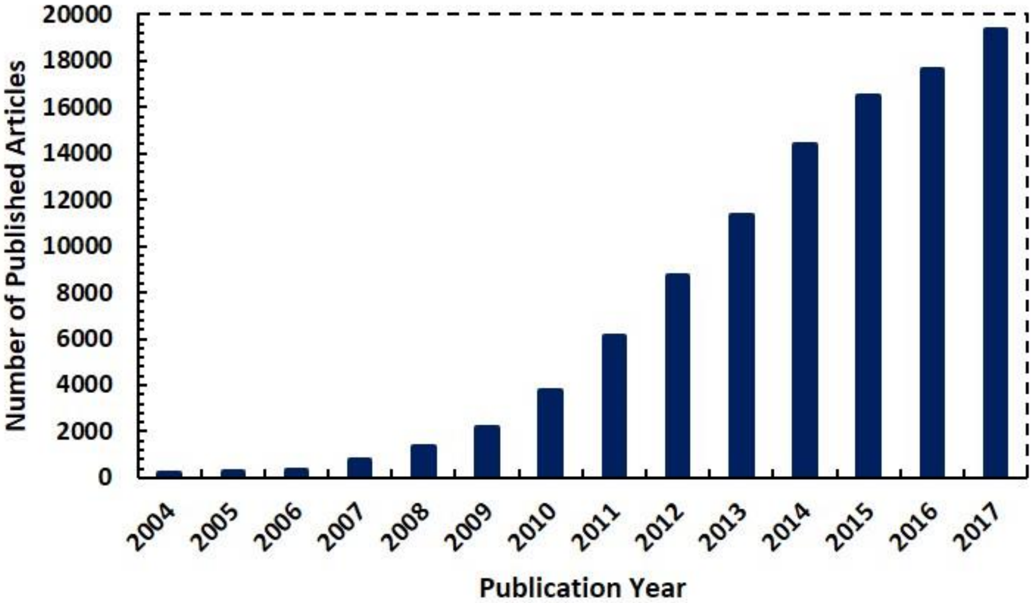

Figure 2-3: Trends in graphene research publications between 2004 and 2017. Performing a search in Scopus for articles published with "graphene" shows an expanding research from 156 in 2004 and reached to 19,348 by the end of 2017 (Accessed February 2018).

2.1.2 Properties

There has been an enormous number of studies for uncovering the properties of graphene since its discovery. The description of graphene is given as "the thinnest, most flexible and strongest material known" [186]. The C-C bond length of graphene is around 1.42 Å [173] and has a thickness of about 0.35 nm [187]. Graphene, with its two-dimensional structure, is the building block for all graphitic forms such as fullerene and carbon nanotube [23, 24, 166] as shown in Figure 2-4. The figure is a representation of how a monolayer of graphene is obtained from graphite and adopted to form other graphitic materials such as carbon nanotube and fullerene.

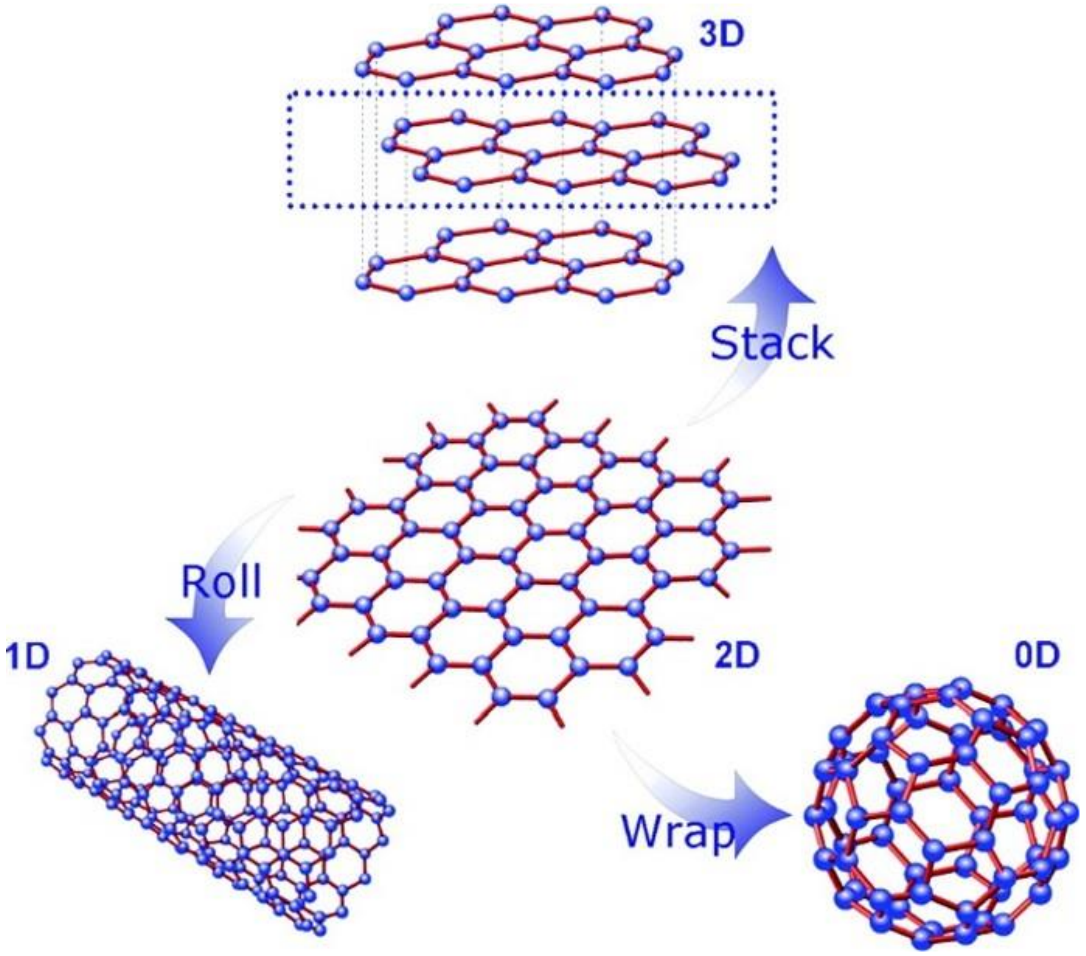

Figure 2-4: Single layer of Graphene as a 2D building block for all graphitic forms. It can be wrapped up to form zero-dimensional (0-D) fullerene or rolled into one dimensional (1-D) carbon nanotubes [24].

In terms of electronic point of view, graphene can be referred to as either a zero overlap semimetal or a zero band gap semiconductor [188] although graphite presents metallic behaviour and diamond behaves as insulator as two other formation of carbon atoms. A bandgap means the difference between the energies of the valence and the conduction bands of semiconductors. The movement of electrons from valence band to conduction band is observed with the existence of the bandgap. However, in a zero-bandgap semiconductor, the valence and the conduction bands meet as can be observed from Figure 2-5.

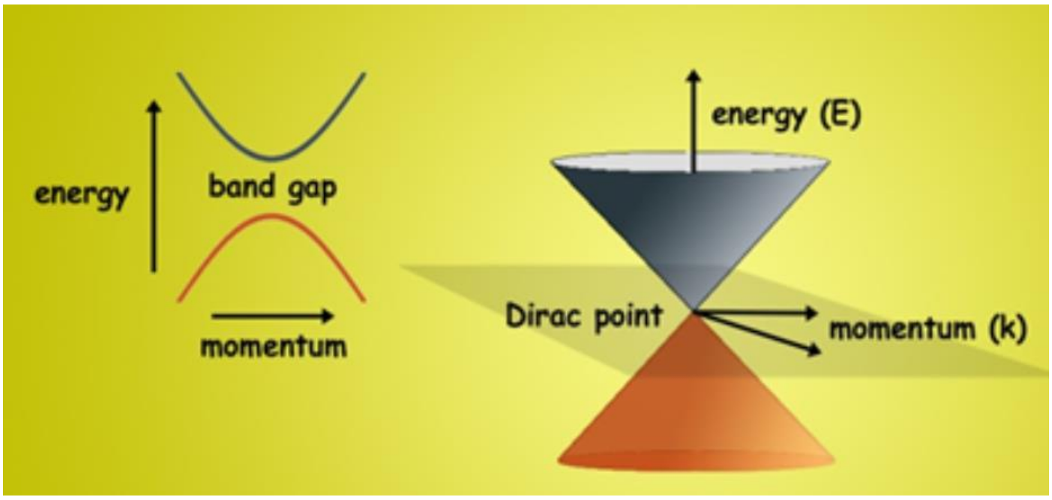

Figure 2-5: A representation of structures with bandgap (left) and zero bandgap (right). Adapted from Lawrence Berkeley National Laboratory.

Graphene has excellent electronic properties with a high carrier mobility of around 200,000 cm^{2}Vs^{-1} [23, 189]. The carrier concentration of graphene can be controlled by applying a gate voltage [5], thus, the conductivity can be tuned. The electrical conductivity of graphene is similar to copper, yet, it has a lower density and higher thermal conductivity than copper [23]. Experiments on graphene showed that it is the strongest material ever known with a Young's modulus of 1.1 TPa and a tensile strength of 130 GPa [23, 190]. Its density is lower than steel but it is stronger than steel up to 50 times [23]. It has a complete impenetrability to gases [148], and shows high thermal conductivity around 5000 Wm^{-1}K^{-1} [23, 178, 189]. Moreover, it has extraordinary optical properties with around 97.7 % transmittance [23, 168, 172]. Also, its intrinsic noise is lower than the other nano-sized materials which makes it a perfect candidate for electronics applications [63, 71, 128, 130]. Table 2-1 shows a comparison of electron mobility of graphene with other materials.

Graphene Ref [27]	200,000 cm^{2}V^{-1}s^{-1}
Carbon nanotube Ref [191]	100,000 cm^{2}V^{-1}s^{-1}
InSb Ref [192]	77,000 cm^{2}V^{-1}s^{-1}
Bi Ref [193]	12,000 cm^{2}V^{-1}s^{-1}
Silicon Ref [194]	1,400 cm^{2}V^{-1}s^{-1}

Table 2-1: Comparison of mobilities for different materials.

2.1.3 Manufacturing

It is vital to develop new techniques and improve the existing ones in order for a good understanding of graphene properties and developing effective applications for a wide range of fields. Thanks to rapid development in graphene research, several methods have been developed hitherto for synthesising graphene [195-200]. Currently, several options of obtaining graphene is available. These options provide more flexibility on controlling both graphene production and graphene-based device manufacturing. Yet, they have relatively high costs of fabrication which must be dealt with. A detailed classification of existing production methods is given in Figure 2-6.

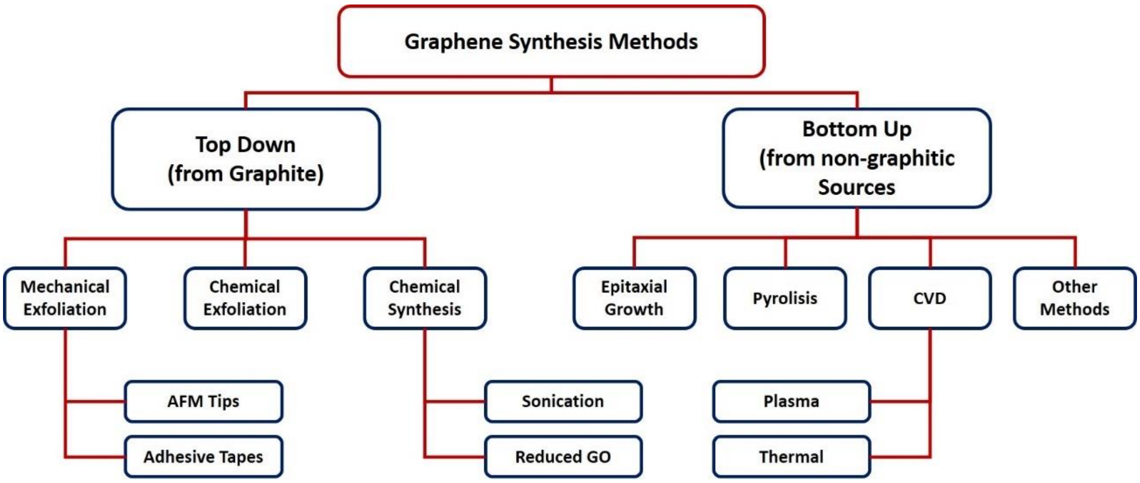

Figure 2-6: Classification of graphene production methods. Adapted from [196-198, 200, 201].

The developed methods can basically be classified under two main approaches as top-down and bottom up fabrications [23]. The first method is related to graphene production from graphite and the second one is graphene production from non-graphitic resources [200]. Each production method has its own specific way of implementation with its own superior advantages in terms of application point of view [195].

2.1.3.1 Exfoliation

Graphene was discovered by a simple production technique which is basically called as scotch tape method [5]. This method is based on mechanical cleavage of graphite crystals by peeling off with a tape repeatedly for several times. This technique requires time and patient to acquire single layer graphene sheets.

Natural and synthetic, highly ordered pyrolytic graphite (HOPG), graphite sources are currently available resources to produce graphene by mechanical cleavage. Graphene from natural graphite has better quality than the synthetic one [200]. However, this method brings an issue of large area production. Although this process is sufficient for research purposes, it is not convenient for mass production as it requires too much time to obtain single layer of graphene. In addition, formation of graphene layers is arbitrary and cannot be controlled with implementation of this technique.

Performing chemical exfoliation is also possible and several methods can be found in literature regarding this [202-206]. Although the latter approach seems to be more scalable method, it introduces problems, e.g. it is difficult to remove the hazardous solvents being used.

2.1.3.2 Chemical Vapour Deposition

Transitional metal substrates, e.g. copper or nickel, can be used to produce large area of graphene by performing thermal decomposition of hydrocarbons [207]. In order to be able to use graphene produced with this method, it must be transferred on to SiO_2 and SiC or flexible substrates. The transfer can be achieved via wet chemical etching of metal [208]. The reason of using a substrate is because of the need to support graphene since its atomically thin structure makes it difficult to handle. The use of substrates such as SiO_2 is due to their insulating properties which does not intervene the conductivity of graphene. Therefore, a silicon substrate would not be feasible to use since it is also conductive.

2.1.3.3 Graphene Oxide Reduction

Graphite oxide can be exfoliated for forming graphene oxide which can be further reduced thermally or chemically [187]. To do so, modified Hummers method [209] is used to treat the graphite with sulphuric acid and potassium permanganate. The layers are then separated by sonication to form graphene oxide. Further reduction is possible after this step either chemically or thermally [210]. The obtained graphene with this way has the potential in many applications such as sensors or electrochemical growth of nanoparticles.

2.1.3.4 Epitaxial Growth

Epitaxial graphene growth on silicon carbide is one of the promising methods for high quality and large area graphene growth. This mechanism can be classified as bottom-up production process and is performed by heating up silicon carbide samples to high temperatures under a vacuum environment or an inert gas flow. The idea is to sublimate silicon atoms and let the remaining carbon atoms to form graphene [211-213] since silicon sublimates in lower temperatures than carbon. It also requires a good control mechanism [213, 214] on growth conditions to prevent arbitrary formation of graphite flakes. This technique is implemented by using high temperature furnaces as it requires high temperatures of up to 2000 °C. The structure of silicon carbide is important for graphene formation. Generally, 4H-SiC or 6H-SiC structures have been reported for formation of graphene [211, 213, 215-219].

2.1.3.5 Other Methods

Apart from the methods explained above, there are many other methods available for manufacturing of graphene and detailed examination of these methods can be found in literature [195, 197, 199, 200, 206, 213, 220-234].

2.1.4 Characterisation

There are several ways of characterisation to analyse graphene structure. The important and common methods can be listed as light microscopy and Raman spectroscopy. Despite transparent property of graphene, it can be visualised when it is transferred on a silicon oxide substrate and the number of single or few layers can be identified [6, 235]. The simple methods of exfoliation [5, 6, 166] isolation and visualisation [235] of graphene flakes was the starting point of graphene research and still provides the opportunity of research in graphene with limited resources. Figure 2-7 demonstrates visualisation of graphene flakes on an oxide layer using optical microscopy [235].

Further characterisation can be made by performing Raman spectroscopy [235-240]. It is a popular characterisation technique that is used in graphene research. The presence of graphene can be confirmed if it is hard to identify via optical microscopy. It has specific features such as G band at about 1580 cm^{-1} and 2D band at about 2700 cm^{-1}. The G and 2D bands are corresponding to in-plane vibration of carbon atoms and two phonon resonance, respectively [241]. These peaks are notable in pristine graphene. However, other forms of graphene, such as graphene oxide or few-layer graphene, present additional disorder which is defined by D band. The latter band is observed at 1350 cm^{-1} and occurs due to defects in the sample [242]. Meanwhile, the substrate used to support graphene can also affect the spectra since graphene bonds are influenced by the substrate [243].

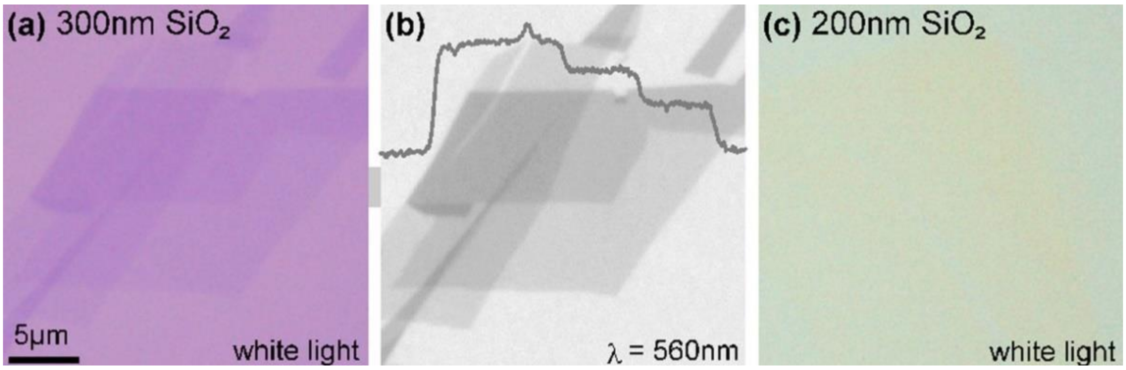

Figure 2-7: Visualisation of graphene under optical microscopy. Graphene crystallites on a SiO_2 substrate of 300 nm thickness under white (a) and green light (b). Monolayer graphene can be seen clearly, however, it is not possible to distinguish graphene with white light on a 200 nm thick substrate (c). Adapted from [235].

Raman measurement was reported to be very sensitive to variety of parameters [244] such as laser excitation energy, thickness, strain, density, quality and number of layers. The shapes, locations, intensities and ratios of the peaks can identify single, few and multilayer graphene as shown in Figure 2-8. Therefore, it is a useful tool for determining many properties of graphene as a non-destructive method. The 2D peak has a sharp and single fitted Lorentzian component in a pristine graphene whereas it can be fitted with four components in a bilayer sample with an upshifting trend for higher number of layers [236]. The 2D peak diminishes in the defected graphene structures due to discontinuous hexagonal crystal symmetry which affects the resonance [245] and the D peak has a higher intensity [246]. The position and the shape of 2D and G peaks along with their intensity ratio, I_{2D}/I_G, help deriving the number of layers [240]. In a pristine graphene sample, the D peak is not observed because of crystal symmetries, therefore, the I_D/I_G ratio is close to 0 with the I_{2D}/I_G ratio as high as 3 [247].

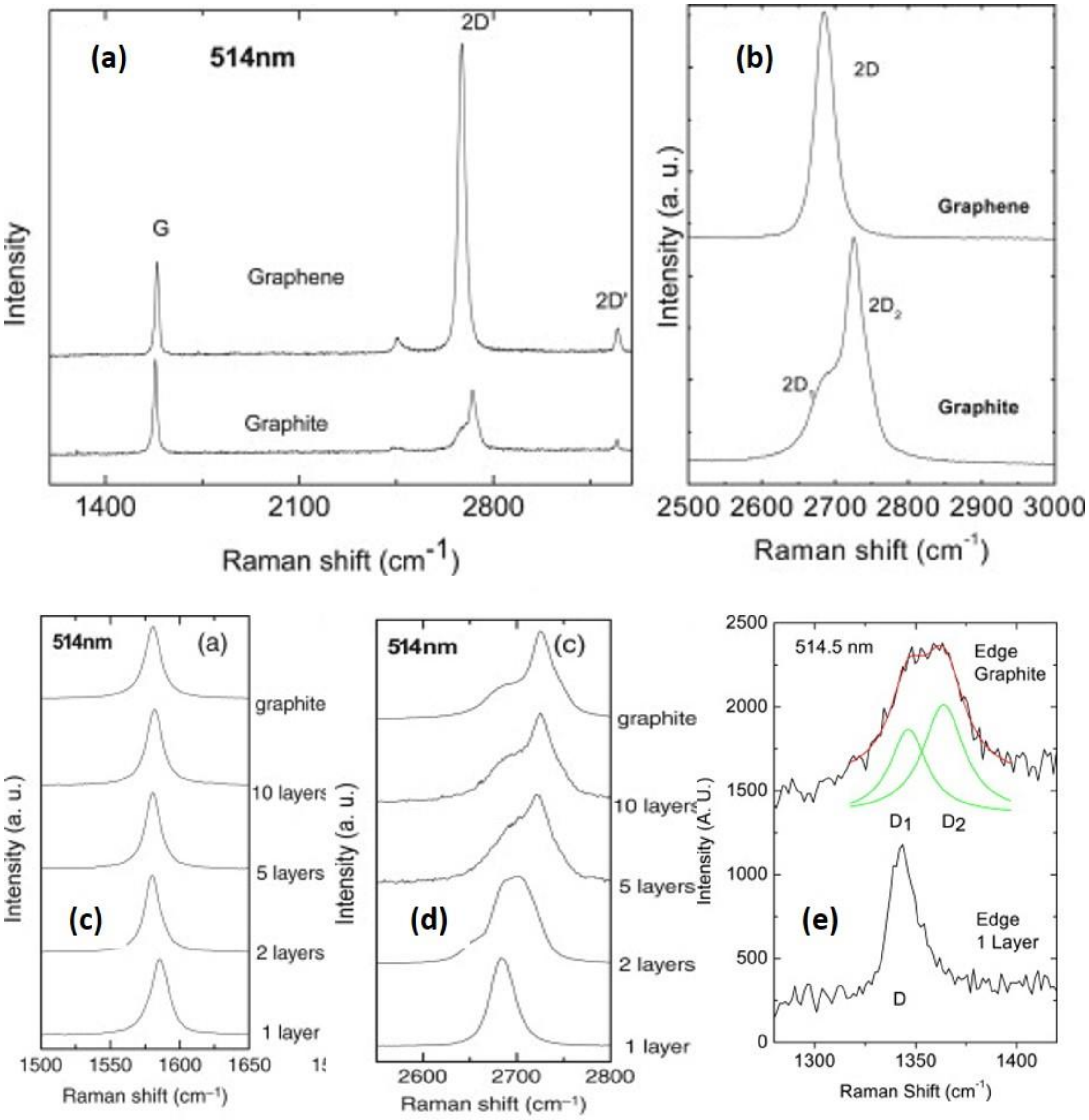

Figure 2-8: Comparison of the Raman spectra of graphene and graphite (a). Comparison of the 2D peaks in graphene and graphite (b). G peak (c) and 2D peak (d) variations with respect to number of layers. D peak obtained on the edge of graphite and graphene (e) showing defects. Adapted from [238].

Another method of graphene characterisation is to use x-ray photoelectron spectroscopy (XPS) since it is a quantitative technique that gives information about the presence of the elements at the surface together with their percentage and chemical states [248-250]. Therefore, it can also be used not only to confirm the presence of graphene but also to quantify the oxygen content for functionalisation purposes or identify any residuals following fabrication [249-253]. Using available XPS databases [254], the XPS carbon C1s spectrum can be fitted to identify the functional groups (chemical bonds) based on the peak positions. Other characterisation methods can be listed as atomic force microscopy (AFM) [190, 255] or scanning tunnelling microscopy (STM) [256]. These methods provide information on height changes by visualising the surfaces at the atomic level.

2.1.5 Applications and Future

Graphene presents the potential to improve the functionality of various fields such as energy storage, sensing, electronic, environmental monitoring and health applications [257] due to exceptional properties it accommodates e.g., room temperature high carrier mobility, light weight and transparent structure along with being stronger than steel [23]. Most of the reported properties of graphene were revealed under idealised conditions and were based on pristine material, however, under real conditions its structure is rather complex and to some extent controlled by the application [168]. Yet, with appropriate design arrangements, very high-sensitive and high-performance applications can be developed due to its profound properties which make it an unbeatable material for a variety of applications. Figure 2-9 demonstrates a summary of potential graphene applications.

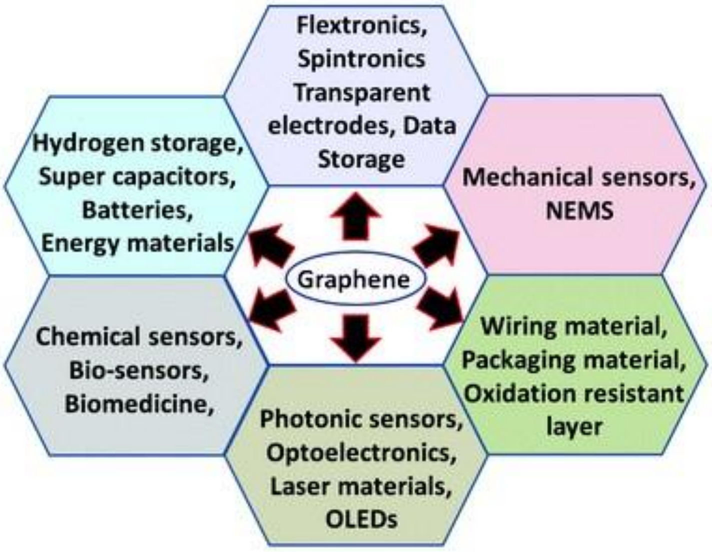

Figure 2-9: Graphene applications [258].

The mechanical properties of graphene make it a perfectly fit material for nano-mechanical applications [8, 177, 259]. Additionally, room temperature quantum Hall effect, and ambipolar field-effect characteristics along with high electrical conductivity with intrinsic low noise make it an outstanding material for electronic application development [260]. It can also be used in environmental monitoring applications as gas sensors due to its high surface area and atomic thick structure that enhances the detection limit down to single atom [15]. Food safety and clinical diagnostics are the fields where graphene has an outstanding potential to be used as an electrochemical biosensor [34]. It has potential also in optical and optoelectronic applications due to its optical transparency, flexibility and chemical resistance to acids or base [22] and it is a good candidate of fibre optic sensors since it presents surface Plasmon property [10]. A flexible organic optoelectronic device has already been reported using multilayer graphene [147]. Additionally, it is an excellent candidate for photovoltaic applications because of being stable against water and oxygen along with having large surface area and high carrier mobility. The potential of graphene has also been explored in applications such as super capacitors [9, 261] and electrochromic devices [146, 163].

Most of the peculiar properties of graphene have been revealed almost in a decade of its discovery [178]. Revealed properties so far have led to an increasing appetite of researchers to study on novel applications based on this material. Also, industrial applications of graphene are likely to appeared in near future [178]. It seems that graphene's electrical, mechanical, optical and thermal properties will enable researchers to develop high quality devices for various purposes from energy storage devices and sensor applications to bendable touch screens and logic transistors and more [25, 178]. Therefore, it holds a huge promise for future technology [262]. Figure 2-10 provides a prediction on potential electronic applications based on graphene for the future. It has a huge promise for various applications such as super capacitors, batteries, solar and fuel cells, biosensors, electronics etc., [263] due to the properties briefly summarised above.

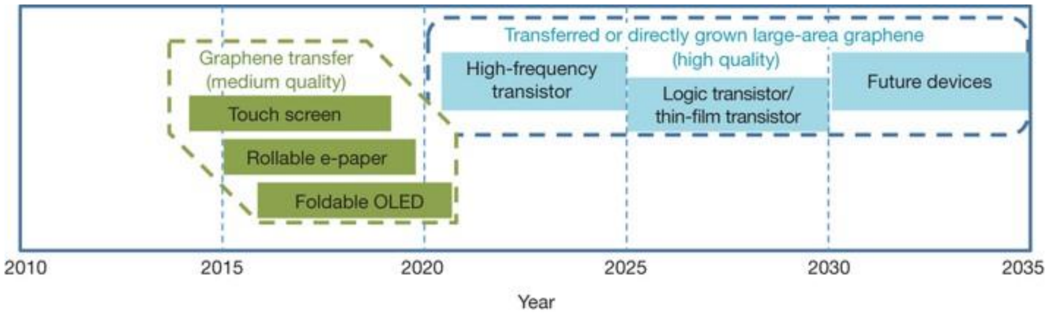

Figure 2-10: Estimation of graphene-based display & electronic devices [178].

2.2 Hall Effect

Hall effect is one of the fundamental techniques used for characterising electrical transport properties in metals and semiconductors. It was discovered by Edwin Hall in 1879 whilst he was trying to understand the mechanical force on a current carrying wire under a magnetic field [42]. The basic idea of Hall effect is to drive current through a thin layer of metal sheet or semiconductor and apply a magnetic field perpendicular to the driven current. This exerts a force which is perpendicular to both driven current and applied magnetic field. The exerted force is also known as Lorentz Force and is illustrated in Figure 2-11. This phenomenon has found important roles for many practical applications in last decades although it was employed for characterisation of electrical properties for many years.

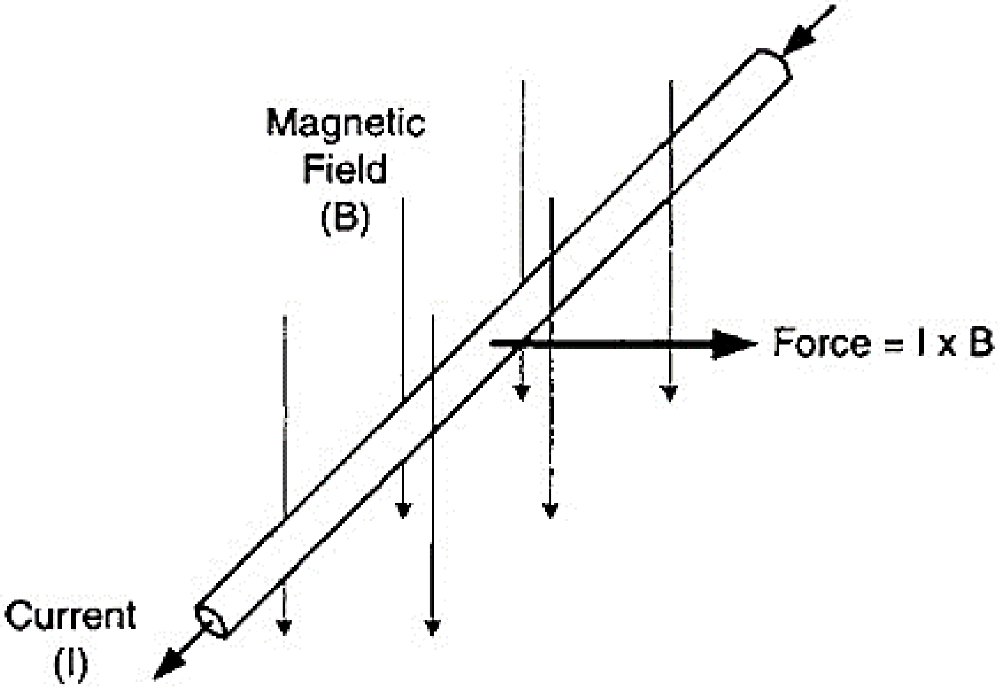

Figure 2-11: Force in a current-carrying wire due to applied magnetic field [44].

2.2.1 Properties

Hall devices are a commonly used magnetic sensors and they operate on the principle of Lorentz Force [43]. This force occurs as a result of the accumulation of moving charges to one side [118] due to a perpendicularly applied magnetic field. Consequently, a transverse voltage difference occurs. The obtained voltage is named the Hall voltage and the actual phenomenon known as the Hall effect since it was discovered by Edwin Hall [44]. Hall effect magnetic sensors are relatively easy to fabricate compared to the other magnetic device classes. Also, the ultimate goal of field implementation is achievable due to the ease of electronic integration. The relationship between exerted force, applied electric and magnetic fields can be expressed mathematically as given in equation (2-1) for a quantitative analysis.

$$\vec{F} = q\vec{E} + q\vartheta x\vec{B} = q(\vec{E}\vartheta x\vec{B}) \qquad (2\text{-}1)$$

The terms in the equation represents force ($\vec{F}$), magnitude of the charge (q), electric field ($\vec{E}$), velocity of the charge (ϑ) and the magnetic field ($\vec{B}$), respectively. This equation is also referred to Lorentz force equation. Except q, all the variables given in the equation (2-1) are vector quantities. As it is clearly seen from the equation, response of a charged particle to both electric and magnetic field has effect on exerted force. As a result of this exerted force, electrons experience resistance to their flow and this leads to an accumulation of charge carriers to one side [118]. In such a case, a transverse voltage occurs.

In addition to magnetic field (B_y) and current (I_x), the Hall voltage (V_H) at the output of a Hall device depends on geometrical shape, thickness, and material properties as well [43]. The basic relationship between Hall voltage and those properties are given below as:

$$V_H = G\frac{1}{ne}\frac{B_y I_x}{t} \qquad (2\text{-}2)$$

The term V_H represents the Hall voltage, n denotes the density of the charge carriers (carrier concentration) and it is given in cm^{-2} unit, μ is for carrier mobility with the unit of $cm^2V^{-1}s^{-1}$ and e stands for electron charge ($\sim 1.60x10^{-19}Coulombs$). These variables are related to the properties of the material apart from electron charge since it is a physical constant. Additionally, t denotes the thickness of the material in metres, I_x represents the applied current that flows through the material sheet, E_x is applied electric field and B_y is the term that represents the perpendicular magnetic field. The latter terms are the quantities that can be arranged as desired. G represents geometrical factor [119] which depends on carrier mobility and length to width ratio (*l/w*). The geometrical correction factor is defined as:

$$G = 1 - \frac{16}{\pi^2} e^{\frac{\pi l}{2w}} \left(1 - \frac{8}{9} e^{\frac{\pi l}{2w}}\right) \left(1 - \frac{(\theta_H)^2}{3}\right) \tag{2-3}$$

The relation given in equation (2-3) is valid for 0.85≤*l/w*≤∞ and $0 \leq \Theta_H \leq 0.45$ radians. Typical G values can be observed as 0.73, 0.87 and 0.924 for geometrical shapes of square, cross with narrow contacts and the cross with larger contacts, respectively [264]. The term θ_H shown in the figure is the angle between resulting electric field and current density under magnetic field and named as Hall angle. It is an indication of resistance in flow of electrons. The efficiency of Hall effect structures is expressed in terms of current or voltage related sensitivities. In addition, magnetic field resolution (or minimum detectable field) is also used to specify the ability of small field sensing. As equation (2-2) suggests, transport properties of a material such as carrier mobility, carrier concentration and carrier type can be determined by measuring Hall voltage since the values of applied magnetic field strength, flowing current and thickness of the structure is known. The voltage exerted from the system is proportional with carrier mobility and inversely proportional with carrier concentration and thickness of the material. Figure 2-12 depicts the principle of the operation with related quantities in Hall effect mechanism.

To indicate the performance of Hall devices, current-related sensitivity, S_I, is mostly used as a quantitative performance parameter for Hall devices. It is defined as the ratio of absolute sensitivity to applied current and given as:

$$S_I = \left|\frac{S_A}{I_X}\right| \tag{2–4}$$

where I_X is the applied current value. S_A represents the absolute sensitivity of a Hall device, one of the parameters used for sensitivity measurement, and it is given by the change in output voltage as a function of applied field under a certain biasing current. The latter term is given as:

$$S_A = \frac{V_H}{B_y} \tag{2–5}$$

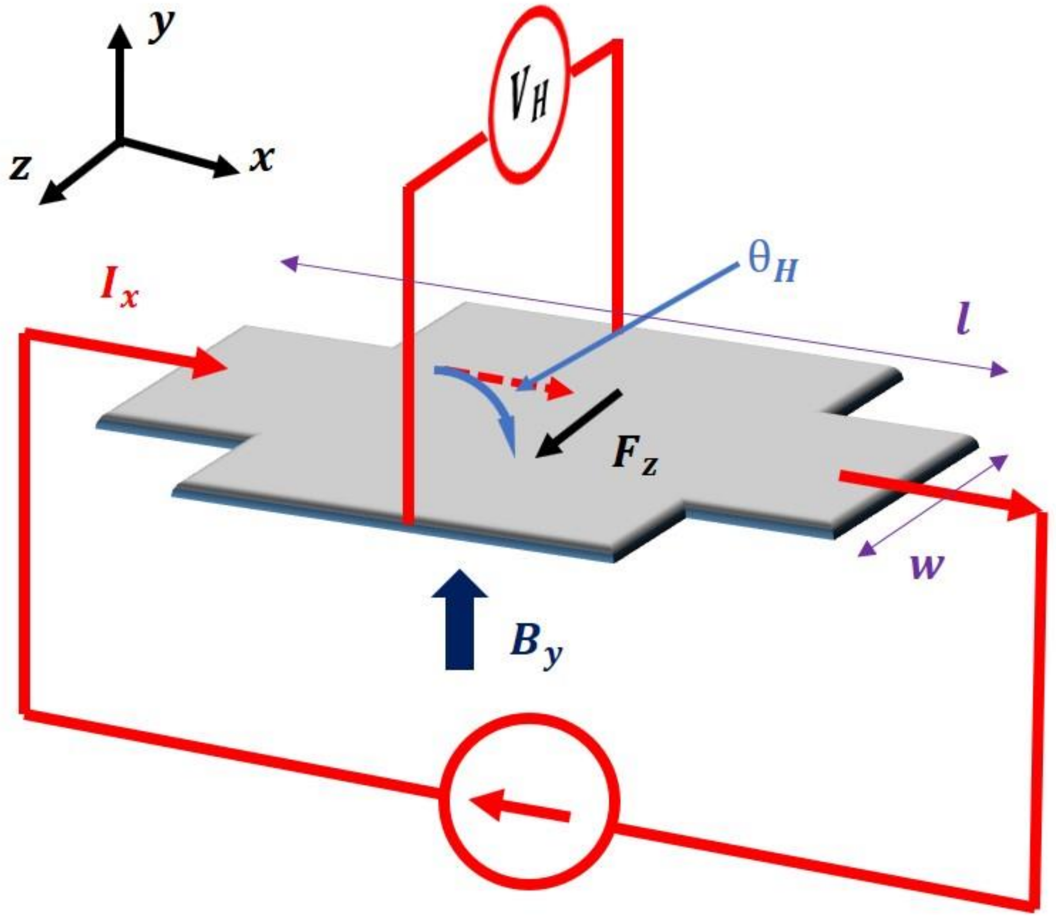

Figure 2-12: A representation of Hall effect sensing principle. A transverse voltage, V_H, is obtained in the presence of a perpendicularly applied magnetic field, By, whilst charged carriers, I_x, are flowing. Moving charges are accumulated to one side under given orientation of current and magnetic field, causing a transverse voltage to occur. The sign of the measured voltage gives an indication about the type of charge carrier in the structure.

2.2.2 The Use of Hall Effect in Characterisation

Hall effect has been used to characterise the electric properties of materials. It is used to determine the carrier mobility and density of materials as well as the dominant charge carriers. Type of the majority charge carriers (n-type or p-type) are defined by inspecting the value of Hall coefficient. This value is represented with R_H and obtained as:

$$R_H = \pm 1/nq \tag{2-6}$$

The positive sign is an indication of holes as majority charge carriers, thus, the material or semiconductor is referred to as p-type in such a case. The negative value points out that the majority charge carriers are electrons and in that case the material is referred to as n-type. Hall coefficient is also represented as in (2-7) or (2-8):

$$R_H = E_z / J_x B_y \tag{2-7}$$

$$R_H = V_H t / IB \tag{2-8}$$

Here, J_x is used for the current density and it is defined as current per unit area. Thus, the Hall coefficient could be expressed in unit of $\Omega\mathrm{m}/\mathrm{T}$ or m^3/C.

2.2.3 Applications

Hall effect sensors are magnetic type sensors that are working based on Lorentz force and uses the perpendicular magnetic field component to produce information. They are used widely in many applications as low-cost sensors. They can be seen with various names [43, 44, 53, 265, 266] in commercial field. The term Hall plate is used for the devices similar to that of Hall discovered [43] and based on different device geometries, application field and regional literature, devices whose working principle relies on the physics of Hall effect are named as "Hall device, Hall element, Hall Cell, Hall Sensor, Hall Magnetic sensor, Hall effect sensor, Hall biosensor, Hall generator or micro-Hall device etc., [43, 121, 158, 264, 265, 267-269]. In general, any shape of conductive material with four contacts could be attributed as a Hall device. However, in terms of practicality and specific applications, certain criteria should be considered to build more convenient and efficient devices.

The only application of the Hall effect principle was to determine electric transport properties of materials for many decades [43]. After its potential was realised, Hall effect mechanism has been successfully implemented to a variety of fields in terms of sensing applications which are commercially available. Devices based on the Hall effect have been investigated for more than a hundred years [43] with deployment in cars, planes, machine tools, computers and medical equipment [63]. The devices have led to a variety of applications [43, 44]; from antilock braking systems in vehicles, disk drives in computers to highly reliable position sensing with automated systems in factories. Micro power and two-wire switches, power devices and Hall integrated circuit (Hall-IC) for smart motor control are amongst developed applications. In the last decade, there has been a considerable number of reports utilizing the Hall principle for bio-sensing applications [74, 103-107, 109-115, 126, 270-281]. In terms of industrial importance, Hall devices are the most widely used magnetic sensor format [62-64] due to their ease of fabrication and implementation, small size and high linearity [70].

2.2.4 Materials

Materials with high carrier mobility, low carrier concentration and narrow band gaps are desirable for Hall effect applications since these properties provide the exact characteristics for high sensitivity Hall devices [43, 44, 158]. The existence of a band gap is the key difference between conductors and insulators. The conductors have their conduction band partially filled, therefore, electrons can move freely. As opposed to conductors, the insulators have an empty conduction band. The electrons of an insulator that has a small band gap can be activated thermally (or by doping) so that they can participate in the conduction. These types of materials are known as semiconductors and the smaller the band gap they have the easier the conduction they can provide as a result of increased mobility. As is explained in section 2.1.2, the sensitivity of a Hall device is proportional with the mobility, thus, materials with narrow band gaps are providing devices with better sensitivities. In addition, reducing the material thickness provides an exceptional advantage since the charge carriers are confined, which produces a stronger force [61, 71, 72, 159].

Materials from silicon (Si), bismuth (Bi) and indium antimonite (InSb) thin films or gallium arsenide / aluminium gallium arsenide (GaAs/AlGaAs) two-dimensional electron gas heterostructures can be used to fabricate Hall devices [117]. Currently, commercially available Hall effect sensors are dominated by silicon, due to well-developed CMOS manufacturing processes being available [63, 70, 118, 119]. However, in applications requiring higher sensitivity, heterostructures from III-V compounds are particularly more desirable due to their superior electron transport properties [120-125], but the technology can be more costly to manufacture and harder to integrate with circuits for signal processing [63]. InSb [126] and Bi [127] thin films are also used in Hall applications due to their high electron mobility properties and linear response for a wide range of field strengths. Table 2-2 provides typical sensitivities of different materials.

Material	S_I (V/AT)
CVD graphene (Ref [71])	2093
Epitaxial graphene (Ref [72])	1021
2DEG (Ref [275])	357
Silicon (Ref [282])	175

Table 2-2: Typical state of the art sensitivities for different materials.

2.2.5 Potential of Graphene

Recently, graphene has become a material of interest for many applications. It is a one-atom thick nanomaterial consisting of carbon atoms formed in a hexagonal honeycomb shape [283]. There have been many reported studies for a wide range of applications [5, 8-12, 15, 18, 21, 23, 28, 148, 163, 168, 169, 172, 260, 284-287]. The unique material properties of graphene make it a promising candidate for mechanical, electrical and optical systems [8, 12, 25, 168, 172, 174, 177, 178, 190, 288]. Possessing ultra-high carrier mobility [27, 129] and being one-atom thick makes graphene a specifically unique material for Hall effect type applications [61, 68, 71, 128] since charge carriers are constrained in a two-dimensional plane thus providing a higher sensitivity and an outstanding resolution. In addition, graphene is also an intrinsically low noise material [71, 128, 130] due to its two-dimensional structure, zero-energy band gap, high mobility and lower carrier concentration along with metallic type of conductance [289]. Therefore, there has been a number of publications exploring the potential of graphene as a Hall sensor [63, 66-69, 117, 128, 149-151, 159, 290, 291] where devices having superior sensitivities with lower noise were obtained.

2.2.6 Reported Graphene Hall Devices

Hall effect phenomena was directly or indirectly discussed in all reported studies related to electronic properties of graphene since it is used to determine electric transport properties of materials. Thus, in early studies on graphene, Hall effect mechanism was used as a tool to determine superior electric transport properties of it [292]. This was performed for single and multi-layer structures of graphene as well as for various production techniques [165, 244] such as mechanical exfoliation, epitaxial grown on silicon carbide or chemical vapour deposition methods etc. Basically, the Hall effect examples in the early studies were about describing the correlation between electric properties of graphene and the way it was obtained along with its number of layers.

Although graphene is a newly explored material, a considerable amount of papers has already been published which report on various applications of Hall effect sensor structures based on graphene [61, 63, 66-72, 145, 149, 150, 152, 159, 165, 290, 291, 293-296]. The structure of the graphene theoretically makes it an excellent candidate for such purposes. The results from graphene Hall sensors also showed that it is highly sensitive to magnetic fields and has a good linear characteristic [63, 70, 71, 297]. The excellent sensitivity of graphene is because of its high carrier mobility and its one atom thick structure which could be considered as the ultimate limit for Hall applications [71]. Noise analysis on graphene Hall devices showed that the sensitivity of a graphene Hall sensor is only limited to its intrinsic properties in addition to defects in its structure [130, 165]. This means a Hall structure out of graphene would present the same behaviour under different external conditions which makes it an ideal material for variety of Hall applications. Another advantage of graphene that should be pointed out is its tuneable electric transport properties by adjustment of gate voltage [63, 71, 128]. This helps to improve carrier mobility and lower carrier density so that it leads to devices with significant high performances [63].

Graphene was first started to be explored for magnetoresistance device fabrication in terms of magnetic applications and few studies were reported [159, 298, 299] based on this idea. The studies suggested that graphene could provide a better sensitivity even in sub-micron scales with respect to previously used materials. Hall effect was also used in one of those studies to enhance the performance of the device [298]. However, primary research on actual graphene Hall effect devices was reported on investigating transport and noise properties of micro-Hall probes for use of scanning Hall probes [165] with a high field sensitivity. A CVD grown graphene was used to pattern respective Hall probes and they were tested in temperatures ranging from 300 K to 4.2 K in the study. A scanning Hall probe microscope system [117] was developed thereafter by using CVD grown graphene and used for imaging domains of a demagnetized permanent magnet. The results suggested that graphene Hall probes are comparable with other previously reported Hall probes based on bismuth thin film or GaAs/AlGaAs hetero-structure. The studies showed that the fundamental limitation on sensitivity is only restricted by intrinsic properties of graphene and defects of its structure.

Devices based on epitaxial grown graphene on silicon carbide with micron sizes ranging from 500 nm to 20 μm were also reported [72]. These devices were used for magnetic field sensing and a minimum detectable field of 2.5 μT⁄√Hz was achieved in room temperature which makes them comparable with the same size semiconductor devices. In another study, epitaxial grown graphene was used to form micron sized Hall devices for the purpose of small magnetic moment detection as well [293]. A micro bead with a diameter of 1μm was placed on a device with a 2μm size with the aid of a nano-manipulator. Transport and noise spectrum measurements were performed in room temperature.

Hall elements with a current-related sensitivity of up to 1180 V/AT and a voltage-related sensitivity of up to 0.3 V/VT was then reported [63]. These devices were the first Hall structures reported with their current and voltage related sensitivities in addition of being the first batch fabricated high-performance graphene devices. Also, a minimum detectable field of up to 50 nT/√Hz was achieved with a frequency of 4.5 MHz which makes them far better than previously reported graphene Hall devices. Graphene devices with current-related sensitivity of up to 2093 V/AT with a magnetic resolution of around 100 nT/√Hz were then reported [71]. Further works performed to improve the sensitivity of graphene and an ultra-sensitive Hall sensors with a current-related sensitivity of up to 5700 V/AT and a voltage-related sensitivity of up to 3 V/VT was reported [70]. The latter values are much higher than not just only other semiconductor-based devices but also all reported devices based on graphene and they were achieved by encapsulating graphene in a hexagonal boron nitride.

Another interesting study was reported about a CMOS integrated circuit (IC) based on graphene/silicon structure which combines ultra-high carrier mobility of graphene with sophisticated functionality of an IC. Voltage and current related sensitivities of 0.1 V/VT and 200 V/AT were achieved, respectively. Although those results are similar with that of silicon-based Hall devices, it is not comparable with previously reported graphene devices. The reason can be attributed to defecting graphene structure during fabrication.

In conclusion, high mobility and thin structure of graphene make it the perfect candidate known to us which can revolutionise the Hall sensing applications. Due to low intrinsic noise and high stability with respect to temperature changes seems to make graphene dominating all fields of Hall applications.

2.2.7 Quantum Hall Effect and Its Observation in Graphene

The quantum Hall effect is observed in two dimensional electron gas systems under a strong magnetic field [188] and can be considered as quantum mechanics version of Hall effect. As explained in section 2.1, in classical Hall effect, electrons experience resistance to their flow while they are under magnetic field and this resistance is linear with respect to magnetic field strength. However, in quantum Hall effect, the resistance jumps up by steps with respect to magnetic field and shows integer plateaus where the longitudinal resistance vanishes. In addition, it is observed in very low temperatures (10 K - 100 K). Unlike other two dimensional electron systems, the quantum Hall effect phenomena in graphene is quite interesting as it shows half integer plateaus [6, 182, 184, 300-306] and can be observed even in room temperature [301]. Also, for different magnetic field strengths, different behaviours are also observed [307] which makes this material extremely interesting.

2.3 Other Types of Magnetic Sensors

Magnetic sensors have been useful tools for human beings to drive, store, analyse and control systems with several functions. For example, magnetic storage disks in computers, non-contact reliable switches in airplanes and automobiles, and control systems in factories for reliable and higher productivity [49]. The classification of magnetic sensors is made based on their ability to measure total (scalar magnetometers) or vector component of the magnetic field (vector magnetometers) [308]. There are several forms of magnetic sensors in terms of their principle of operations [47, 308, 309] and most commonly used types can be listed as magnetoresistive [299, 310-314], superconducting quantum interference device (SQUID) [99], spin-valve [315], and Hall effect sensors [43, 44]. The detection range and applications of magnetic sensors are summarised in Figure 2-13.

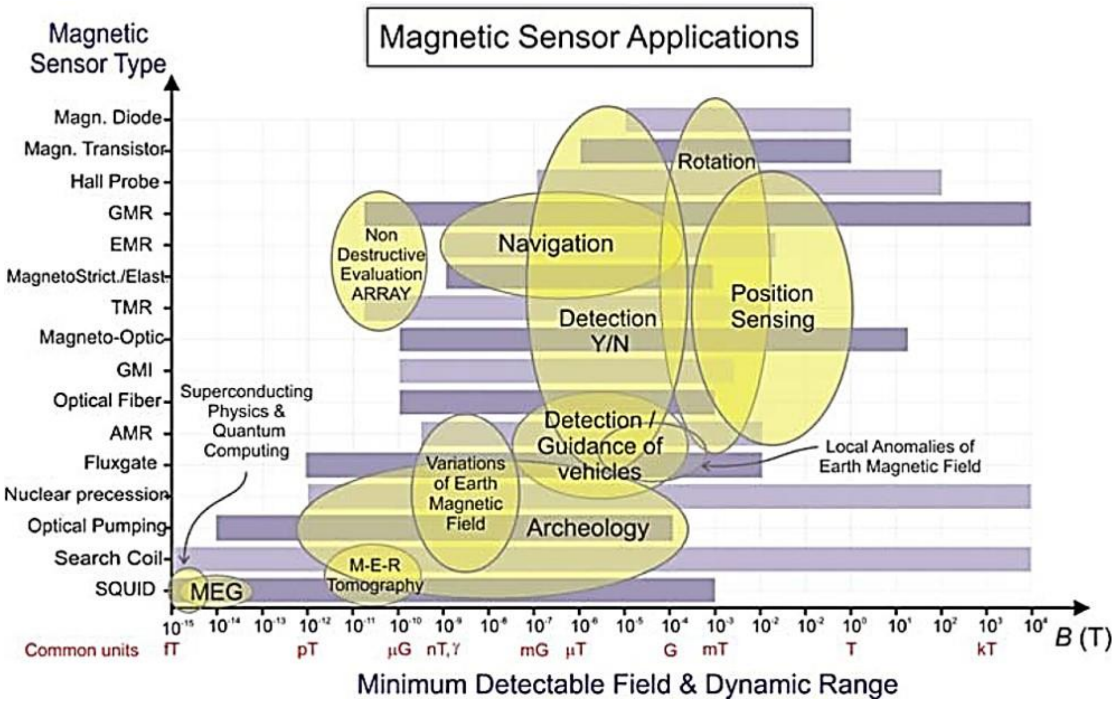

Figure 2-13: Applications and sensitivity range of magnetic sensors [48].

There are examples with excellent sensitivity [49, 308], however implementation may not be straightforward due to specific requirements, such as fabrication difficulties, operating conditions and specific temperature requirements [48, 49, 118, 309, 316-318]. For example, SQUID sensors are the magnetometers that exploit the superconducting properties of certain materials under low temperatures that are below superconducting transition range. If materials are cooled below that temperature, their resistance to the flow of electricity is eliminated and they become superconductors. The sensitivity of those types of sensors is limited by magnetic noise and the range is from 10^{-6} nT to 10^{-5} nT for commercially available sensors [49]. Although they are perfect for detecting field strengths that are below the earth’s magnetic field, the system requirement makes it hard to implement. Another magnetic sensor example is search-coil magnetic sensors. Those sensors work based on Faraday’s induction law. The voltage of the output leads changes proportional to the amount of the magnetic flux applied to the coil. Those magnetometers can detect fields up to $2x10^{-5}nT$ in a frequency range of 1 Hz to 1 MHz [49]. Meanwhile, the electronic read-out circuit has a limiting effect on the sensitivity and frequency range of those type of sensors. Likewise, flux-gate magnetic sensors can be listed as another type of magnetic sensor and they are formed from a drive and a sense coil along with a wound of ferromagnetic material. The working principle relies on magnetic induction and the saturation property of ferromagnetic materials at high fields. They have a sensitivity range of $10^{-2}nT$ to $10^{7}nT$ [49]. Besides magnetic sensor types briefly explained above, there are several types of magnetic sensors also available with various detection capacity. The detailed information of all types of magnetic sensors can be found in literature with in depth analysis [47-49, 62, 96, 99, 118, 119, 159, 298, 308-311, 316-322].

2.4 Biosensors

A biosensor is a combination of two components, bio-receptor and transducer, integrated in such a way to allow the detection of specific target molecule. A bioreceptor is a specific recognition element for detecting desired chemicals and biomolecules. The transducer is used to convert the detection event into a meaningful description by means of electrical, mechanical or optical signals. The definition of IUPAC (International Union of Pure and Applied Chemistry) for a biosensor is “A device that uses specific biochemical reactions mediated by isolated enzymes, immunosystems, tissues, organelles or whole cells to detect chemical compounds usually by electrical, thermal or optical signals” [323]. Biosensors are used in various fields such as food safety, environmental monitoring and medical diagnostics. Basic structure of a biosensor is shown in Figure 2-14.

Historically, the field of biosensor research traces back to 1962 with enzyme electrode development by Lenard C. Clark [1, 41] for testing glucose levels in blood and since then the bio-sensing field has been contributed by scientists from different research backgrounds. Thus, it has created a multidisciplinary research field. In 1970s, the first generation of biosensors was commercialised [324]. Further developments followed by describing a bio-recognition system for the use of whole cell [325]. Research and developments on the field has continued, particularly over the last decade. Using carbon nanotubes [79], nanowires [326, 327], nanoparticles [328-330] and novel materials such as graphene [4, 18, 28, 30, 32, 284, 331-333] could lead to incredible advancement.

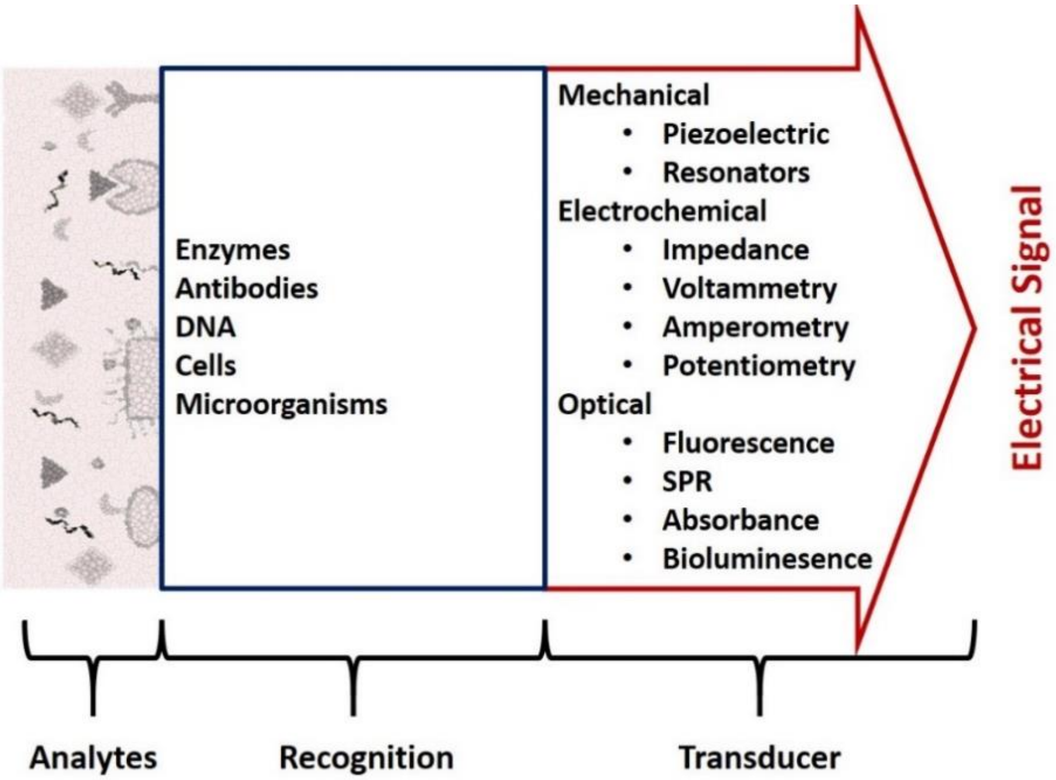

Figure 2-14: Basic structure of a biosensor.

The biosensors market is expected to reach $21.17 billion by 2020 [334]. It is likely that the biosensors will have a huge impact on point of care diagnostics [335] because they have potential to be simplified and reduced in size, thus providing easy to use products. Therefore, this field needs to be improved based on new materials and design implementations to achieve a detection range of very small concentrations. However, it is worthy of note that the commercialisation of biosensors is slow despite having the huge potential. This can be attributed to cost required for development, optimisation and fabrication from research to commercial products.

2.4.1 Detection Principle

In order to detect a specific desired biological element, the sensor surface should be functionalised and this is usually done with complementary molecule [40]. In the presence of desired biological element, a capture process occurs. This process refers to the recognition step. A transducer is then used for converting the recognition event into a measurable electrical signal. A desired target molecule is captured by bio-receptor and this event creates a physical change in the transducer. The physical change can be measured as electrical [155], mechanical [336], optical [337] or electrochemical [338] based on transducer type. This change is converted to an electrical signal for a meaningful interpretation of the detection. The signal from output of the transducer is usually very small and needs to be amplified. In addition to amplification, any noisy harmonics should also be removed. Figure 2-15 is a representation of complete bio-sensing system depicting recognition (a), transducing (b), signal amplification (c) and processing (d) with recording/displaying (e) steps.

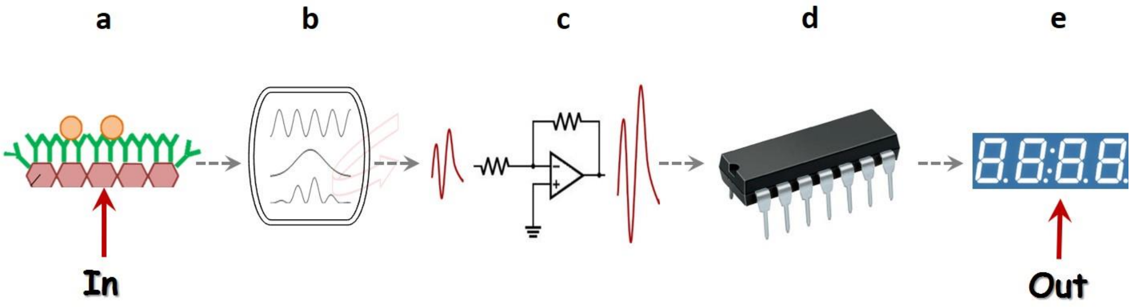

Figure 2-15: Schematic of biosensor with recognition (a), conversion (b), signal amplification (c), processing (d), recording and displaying (d) steps.

2.4.2 Classification

There are different types of bio-receptors (enzymes, antibodies, nucleic acids, cells), and biosensors can be classified according to which type bio-receptor is used. Meanwhile, they can be classified based on their transducing element such as mass-based, optical-detection, electrochemical, electrical etc. Detailed overview on biosensor types can be found in refs [2-4, 40, 41].

2.4.3 Hall Effect in Biosensing

The principle of Hall effect was well-developed for defining material properties of solids and magnetic field measurements and it was successfully applied to several systems based on engineering-oriented applications. The applicability of Hall principle has been investigated quite recently for biomedical purposes [339] and a considerable number of reports have been devoted to employability of Hall principle for biosensing applications [65, 103-115, 126, 154, 271, 272, 275, 280, 282, 340-347]. Hall effect-based biosensors have been shown to be successful with the aid of magnetic particles [73, 81, 153, 276, 277, 348-350]. In this type of detection, magnetic beads are used to measure magnetic susceptibility [81]. Basically, a combination of alternating and non-alternating magnetic field is applied in-plane and perpendicular to the sensor surface, respectively. The detection is achieved via observing an output signal which has the same frequency of the in-plane excitation signal.

Magnetic beads are promising tools for target molecule detection in human fluid since they could be used as magnetic labelling of biological molecules [272] and provide a low cost technique. Also, they have the advantage of negligible interference and long-term stability [272, 351]. However, there are some restrictions that limit the sensitivity of the Hall sensor if magnetic beads are used. It is crucial to consider the separation between surface of the sensor and magnetic bead as magnetic field from the beads decreases proportional to $\sim 1/s^3$ where s represents the separation distance [115]. This parameter must be treated carefully for an optimised signal to noise ratio.

$$B_{dipole} = \frac{\mu_0 m}{2\pi s^3} \tag{2-9}$$

Additionally, magnetic moment of a magnetic bead is another important parameter that must be considered since those parameters are affecting the magnetic field provided by magnetic beads. Equations (2-9) and (2-10) explain the relationship of those parameters. Here, m, M_s, V and ρ represent magnetic moment, saturation magnetization, volume and density of superparamagnetic beads, respectively. The term μ_0 is used for the permeability of vacuum.

$$m = M_s . V . \rho = M_s . \left(\frac{4\pi}{3}\right) . r^3 . \rho \tag{2-10}$$

A Dynalbead with 1 μm diameter has a typical magnetic moment of ≈4×10^8 μ [107]. This value corresponds to a B_{dipole} of 640 μT at a distance of 50 nm. This can easily be detected by fabricated devices since a minimum field detection of 162 nT/√Hz was obtained (see section 6.4.2). In fact, this resolution makes the sensor capable of detecting beads even at a separation distance of 0.5 μm successfully.

In terms of application point of view, Hall effect sensors have been used for detecting [105, 107, 110, 114, 282, 352-355] or counting magnetic beads [106]. The beads were used as a label and those sensors have been adopted to manipulate biological species, perform medical imaging [356, 357] or map the trajectory of moving particles [104]. A successful magnetic bead detector using a silicon Hall sensor, having an active area of 2.4 × 2.4 μm^2, was demonstrated for detecting a single magnetic bead with diameter of 2.8 μm [282]. This was fabricated using CMOS technology and a current related sensitivity of 175 V⁄AT with a magnetic field resolution of about 200 nT⁄√Hz was achieved. The ability of a similar structure was then tested as an actual biosensor in another study [351] by functionalizing beads. It was applied to immunoassay and a detection limit of 0.1 ng ⁄ ml was achieved. These studies followed by several reports of CMOS fabricated sensors that manipulate or detect magnetic beads for various biological species [269, 276, 342, 351, 358, 359]. The advantage of a Hall biosensor in CMOS structure is its ability of combining the sensor structure with required manipulating and signal processing circuitry such as biasing, reading, amplifying, sampling and control logic on a chip which provides an advanced functionality [277, 281, 360]. However, there are certain limitations that restricts the sensitivity such as the material being used, since silicon is not the best option to obtain a high sensitive Hall effect sensor, and the separation distance between sensor surface to bead. Therefore, thin film structures with high carrier mobility, such as thin films of InSb [273] or 2DEG systems of InAs , AlGaAs/InGaAs [361] and InAs/GaSb [275], have also been preferred since their sensitivity is better than silicon competitors and the signal of interest can be provided even in longer separations. For example, a micro-Hall sensor based on InSb thin film was reported as a potential platform for bio-screening applications which was capable of detecting beads as small as 100 nm even at a distance of 200 nm between particle and sensor surface [115]. In a further study based on InSb thin films, the detection of DNA [272] has been explored using devices with an active area of 30 × 30 μm^2. The detection process was performed by functionalizing magnetic beads of sizes around 200 nm diameter. A layer of gold (200 nm) was used on the surface of the sensor for immobilization process and the sensor was isolated with silicon nitride [271] and promising results have been obtained. In addition, the feasibility of a potential biosensor was also demonstrated by placing 2.8 µm beads on an array consisting of devices with 5 µm × 5 µm active areas [113]. More studies followed by using InSb for similar sensing purposes [112, 113, 126]. 2DEG heterostructures have also shown promising results in terms of bead detection as a biosensing platform [111, 274]. The advantage of using such systems is their adjustable high mobility during fabrication which provides the flexibility of sensitivity adjustment. In terms of graphene, micron-sized devices were fabricated from epitaxial graphene [293] and their promise was assessed using a Dynal bead with a size of 1 µm. The results demonstrated an improved performance compared to standard semiconductor devices which suggests graphene as a highly important material for biological substance detector using beads as a label. In addition, in a sensitivity modelling work, the performance of graphene has also been confirmed for such applications via performing simulations [362].

2.4.4 Graphene in Biosensing

Graphene demonstrates good stability, high sensitivity and selectivity, negligible capacitive current, and great electro-catalytic activity [7]. Various appealing properties can be observed in graphene such as high transparency, unbeatable mechanical strength, flexibility, good electrical and thermal conductivity, large surface area, ambipolar electric field effect and superior electronic properties [4]. Due to unique material properties, graphene is considered as a highly promising candidate for optical, electrical and mechanical systems [8, 12, 25, 168, 174, 177, 178, 190, 288]. It is particularly promising for electrical sensing applications [363] because of its high carrier mobility [27, 166] and low intrinsic electrical noise [11, 364]. It may seem to be an ideal choice as a biosensing element due to its large surface area and excellent electrical conductivity, however, a monolayer pristine graphene is chemically an inert material [176] which presents a drawback in terms of electrochemical sensing point of view. Because, the main characteristics of an electrochemical sensing system is that on the surface, reduction or oxidation reaction can occur so that it causes the transfer of electrons from or to the sensing surface, thus, providing a change that can be measured in terms of voltage, current or impedance [365].

Nonetheless, graphene can be used in biosensing field in two different ways [30]. The first method involves charge biomolecule interactions at π-π domains, electrostatic forces and charge exchange that lead to electrical variations [366]. The other method is to employ structural defects [38], so that functional groups can be obtained, and using chemical functionalization for immobilizing the molecular receptors on graphene and then make use of highly conductive characteristics of graphene [187, 367-370]. To achieve enhanced biosensing performance, graphene is often functionalized using biomolecules, enzymes, polymers, metals and metal oxide nanoparticles [7, 371]. Graphene can allow the development of new electrochemical sensors for detection of glucose, nucleic acids, hydrogen peroxide, protein markers etc., [260] due to its distinguished electrochemical structure. The unique electronic band structure of graphene leads to incredible charge transport and electrical properties. The large surface area [13, 372] of graphene particularly distinguishes it amongst existing nanomaterials and allows direct interaction with a wide range of biomolecules available [373]. In addition, engineering graphene with structural defects is possible using low-cost fabrications techniques [374].

To perform a label-free detection, a covalent binding process can be employed for surface modification from benefitting the structural defects, however, the incredible electric transport properties of graphene diminishes in such an arrangement due to discontinuity in the structure of graphene. To overcome this issue, a high-quality graphene film can be used with pyrene which allows the surface modification process to be performed non-covalently [375]. A non-covalent binding occurs between graphene and pyrene through π-stacking [376] due to charge interactions between them which leads to a change in carrier density [155]. Through this mechanism a label-free detection can be performed. In this work, this mechanism was employed to create a label-free biosensing system.

Graphene has already been adopted in various sensing applications such as clinical (for detections of glucose, cholesterol, ascorbic acid, uric acid, H_2O_2, dopamine), environmental (detections of pesticides, hydrogen and metal ions), and food (detections of staphylococcus and tryptamine) [32]. Comprehensive reviews on this topic can be found in refs [16, 19, 28, 30, 33, 284] since the details on those structures are beyond the scope of this work.

Chapter 3. Test Rig Design

A specific setup in a specific order is required for successfully obtaining accurate results from measurements. First, a voltage or a current source is required as a biasing source to operate a Hall device. The operation mode of a Hall device is named as current-mode or voltage-mode of operation depending on which source is used to bias the device [44]. Secondly, a magnetic field source is necessary. The latter source must be introduced in such a way that the field lines are applied perpendicularly to the driven current. Then, the simple rule for obtaining Hall voltage is to form at least four contacts on a thin sheet of metal or semiconductor and bias it via preferred choice of source. This is, in principle, sufficient for obtaining any Hall voltage which occurs due to applied perpendicular magnetic field. A voltmeter can then be used to acquire the output across the remaining contacts that are not used for biasing. However, Hall voltages are typically quite small and therefore require amplification. This means that the output needs to go through an amplification step. Apart from driving sources and reading circuitry, external noise sources have certain limitations on the sensitivity of the system. Therefore, it is also important to consider minimizing the effect of the external noise sources for increasing the sensitivity. In this chapter, required biasing and magnetic field sources with relevant design arrangements for control circuitry are discussed to obtain the output of interest in real-time with an accurate measurement.

3.1 Rig Design

A Hall effect sensor can be thought of as a combination of three major parts; the transducer itself, power supply to bias the transducer and data acquisition stage for acquiring relevant output. However, those parts require to be used in conjunction with specially designed electronics to perform properly and to present the data to end user. Adopting specially designed electronics significantly improves the system capability by maintaining the performance and providing application specific data, thus, leaving no concern to the end user. A test rig, including biasing sources and specific electronics, was designed and constructed to obtain a sensor with desired performance parameters. The following sections provide a detailed outlook to constructed rig to operate devices.

3.1.1 Biasing Source

A Hall transducer can, in principle, be used simply by adding a stable power supply to it and biasing can be achieved either with a voltage or a current source. Each biasing source has its own advantage and disadvantage. A simple setup for biasing a Hall device is demonstrated in Figure 3-1. In case of a voltage source, the temperature coefficient of the transducer sensitivity will be as high as 0.3% / °C [44], meaning that the output will vary significantly with respect to temperature change. Therefore, some additional front-end circuitry is required to limit the current that will be sourced from the voltage supply and provide more stable output in case of voltage mode of operation [44, 267]. Limiting the current is particularly important to reduce the power consumption, hence, preventing device from thermal heat effect. Figure 3-1 illustrates the simplest way of biasing a Hall device.

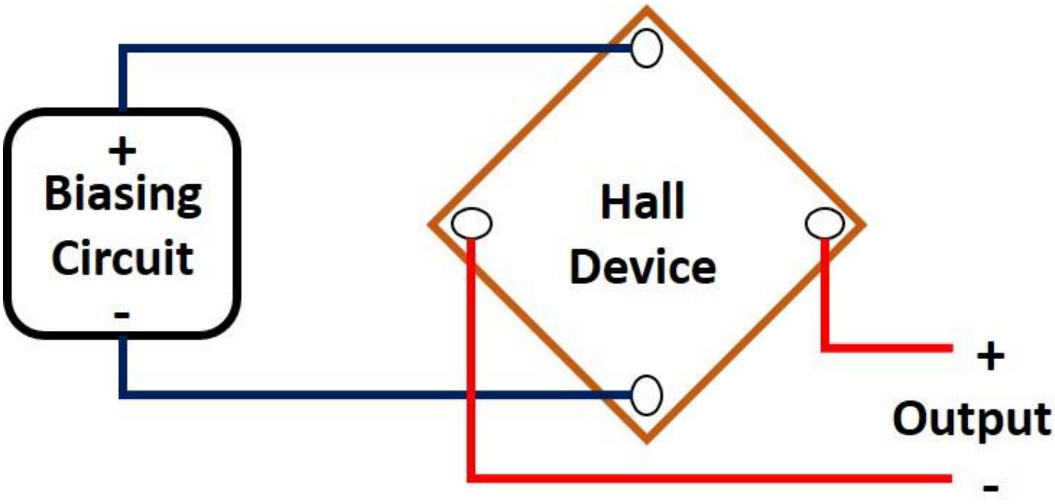

Figure 3-1: An illustration of a Hall plate biasing.

To obtain a stable output in case of temperature changes, the voltage source or the gain of the amplifier can be made temperature dependent [43] to maintain a stable output, thus, making the system less sensitive to variations of temperature. In terms of implementation, a buffer must be placed in between voltage reference and the Hall transducer for low current transducers where an additional transistor can be added in between the buffer and the device for the transducers requiring high currents.

Another way of reducing the output variations with respect to temperature changes is to bias the transducer via a current source. Current mode of operation provides a reduction as low as 0.05 % / °C in temperature coefficient [44]. As a result, current source biasing is preferable in most cases as it provides more stable working conditions due to significant reduction in temperature coefficient [43, 44, 158]. In terms of current mode of operation, a power supply can simply be used with a combination of resistors for biasing devices. A constant current biasing circuit can be achieved by placing simply a resistor in between voltage reference and the transducer. It can also be obtained via using a transistor by connecting it to the transducer as shown in Figure 3-2.

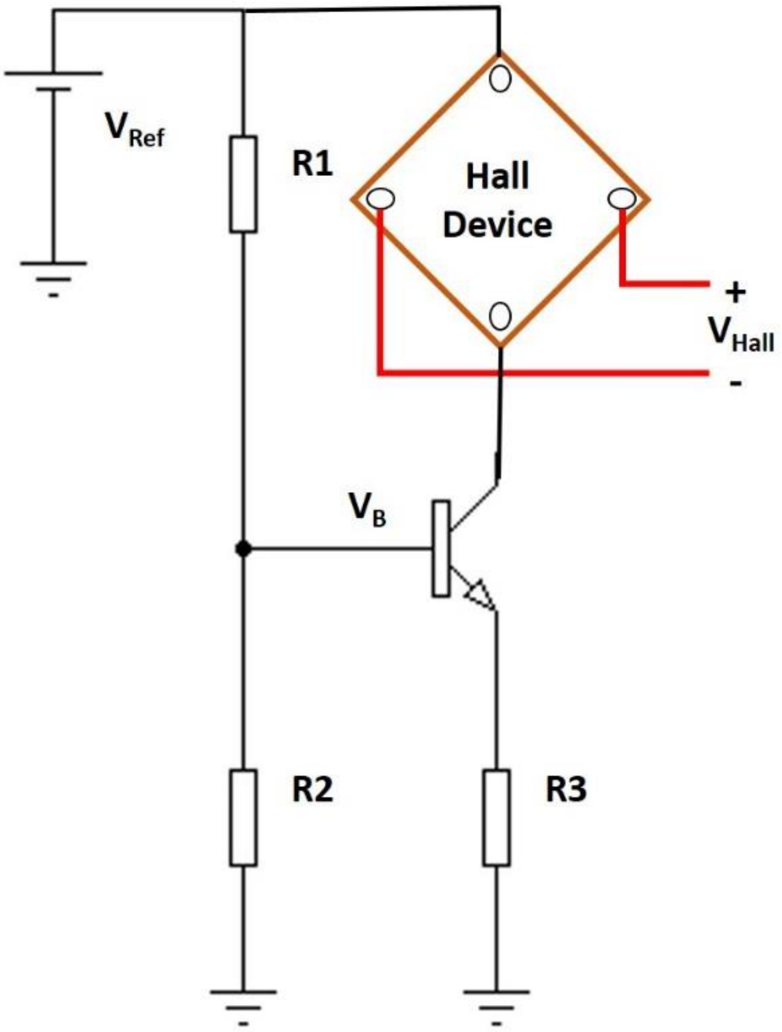

Figure 3-2: Biasing Hall transducer via a constant current source using a transistor.

3.1.2 Magnetic Field Source

A magnetic field source is required for applying a force on moving charges, thus, creating a transverse voltage. An electromagnet could be made simply by winding a current carrying wire on a piece of ferromagnetic material such as iron and can be used as a magnetic field source that can be varied. Another approach is to use a permanent magnet as a constant magnetic field source. In both cases, the magnetic field lines should be applied perpendicular to the surface plane of the device and needs to be able to provide a uniform field.

Strong rare earth magnets (First4Magnets-UK) were used as constant magnetic field source. To apply a strong and uniform field in a perpendicular orientation a ‘c-core shape’ was designed as shown in Figure 3-3 (a) and made from pure iron for applying field lines perpendicularly as uniform as possible. Then, neodymium magnets (First4Magnets-UK) with various thickness and radius were used as constant magnetic field sources.

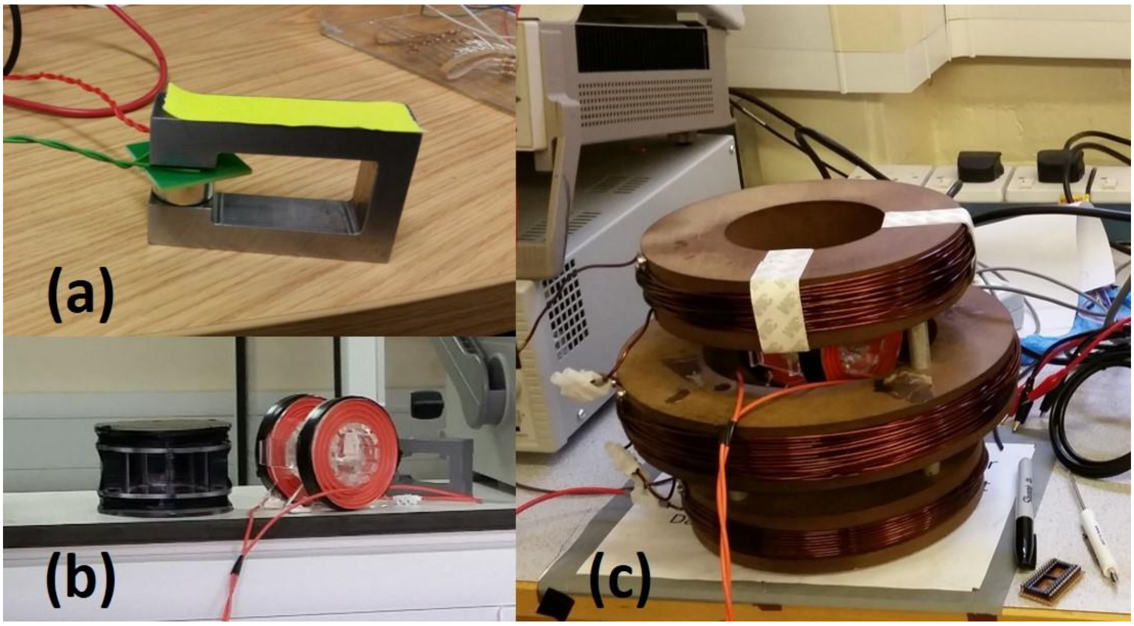

Figure 3-3: Magnetic field sources. A rare earth magnet in a designed c-core shape and made of pure iron (a). Two rare earth magnets in a designed plastic holder (b - left) and arranged for providing constant magnetic field. A Helmholtz coil (b – right) and Maxwell coil (c) for providing variable magnetic field. The c-core shape was also used as a variable magnetic field source by winding a current carrying wire without including rare earth magnet.

Using magnets in such a geometry made the magnetic field even stronger and a field strength of up to 750 mT was obtained and used as a high field providing source. Moreover, Helmholtz coils was also designed and constructed by using laser cut acrylic pieces (Figure 3-3 (b)). The latter setup provided a constant field strength of 120 mT (Figure 3-3 (b) – black shape on the left containing two neodymium magnet) along with a variable field of up to 20 mT (Figure 3-3 (b) – orange shape on the right containing a wire). The specification of permanent magnets used in this study is summarised in Table 3-1.

Magnet	Diameter	Thickness	Pull Force
N42 Neodymium Pot Magnet	60 mm	14.5 mm	136 kg
N52 Neodymium "Strongest Grade" Magnet	20 mm	10 mm	14.8 kg
N42 Neodymium Magnet	10 mm	10 mm	3.9 kg

Table 3-1: Specification of permanent magnets used in this study (All magnets were purchased from First4Magnets-UK.)

In addition, a Maxwell coil (Figure 3-3 (c)), designed and made in Newcastle University as part of a previous PhD project [377], was used as a uniform and variable magnetic field source. This coil was made of double insulated Magnetemp CA200 copper transformer wire which had 1 mm diameter. This wire was wound on to a custom made Tuffnall formers by hand. The field response of this magnet was calculated to be 1.159 mT/A. A cross-sectional view of used Maxwell coil is given in Figure 3-4.

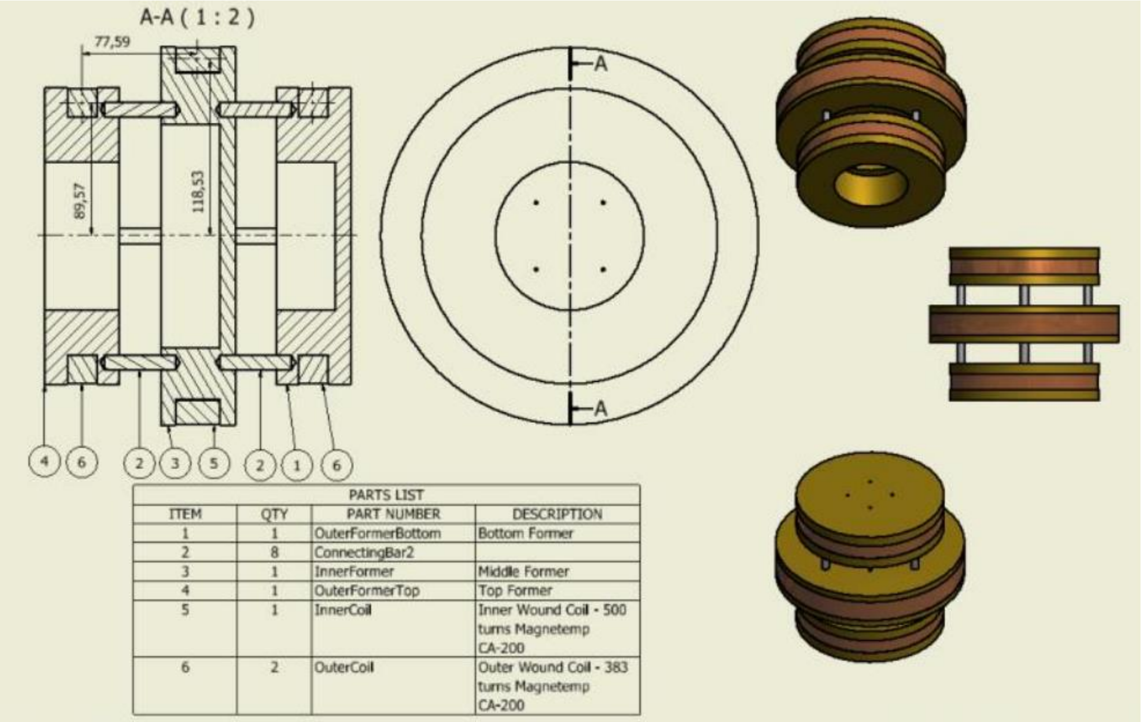

PARTS LIST			
ITEM	QTY	PART NUMBER	DESCRIPTION
1	1	OuterFormerBottom	Bottom Former
2	8	ConnectingBar2	
3	1	InnerFormer	Middle Former
4	1	OuterFormerTop	Top Former
5	1	InnerCoil	Inner Wound Coil - 500 turns Magnetemp CA-200
6	2	OuterCoil	Outer Wound Coil - 383 turns Magnetemp CA-200

Figure 3-4: Cross-sectional view of the Maxwell Coil. Adapted from [377].

All these sources were used to characterise the response of graphene devices for varying magnetic fields as well as for its sensitivity to low level field strengths. The provided quantitative values were obtained by using a commercially available gauss meter (Hirst Magnetics GM08 Gauss Meter).

3.1.3 Amplification

In general, Hall voltages are quite small and therefore require amplification meaning that the output needs to go through an amplification stage. Therefore, it is necessary to implement an amplification process since the output of such systems are in millivolt or microvolt ranges. Depending on the structure of the devices, the Hall voltage might be even smaller. For instance, Hall voltage obtained from output of the devices made on PCB (see section 4.4.1) was in nanovolts range. This can be explained by high carrier density and relatively thick structure of the materials that were used to form those devices. The smaller ranges make it difficult to measure since it is below the detectable range of most of the acquisition systems. To overcome the issue, an amplification stage is required in order to bring the Hall voltage to a level that can be measured easily. In the amplification stage, an instrumentation amplifier is desired since the Hall devices have differential outputs as seen in Figure 3-5. Therefore, a zero-drift, precision programmable instrumentation amplifier, LMP8358 (see Figure 3-6), with a high gain (x10 - x1000) was used to amplify the differential output signal from the device.

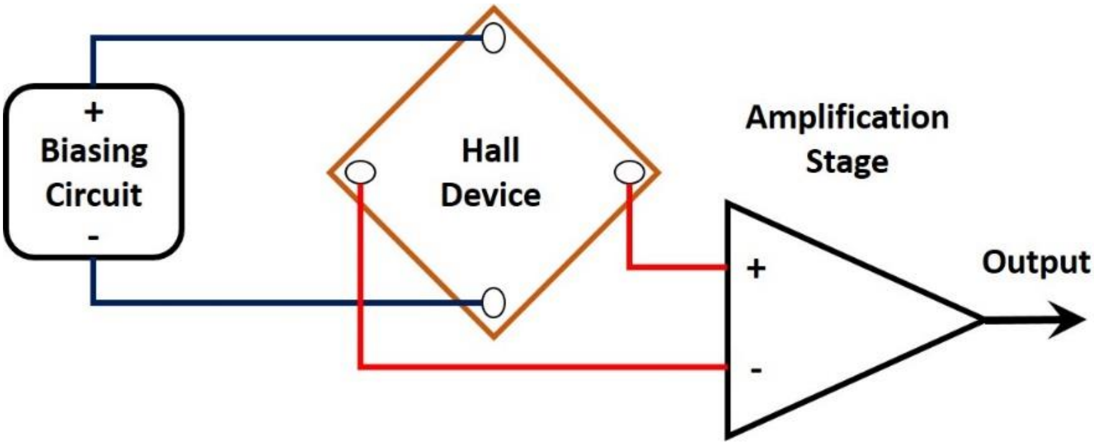

Figure 3-5: Implementation of an amplification stage.

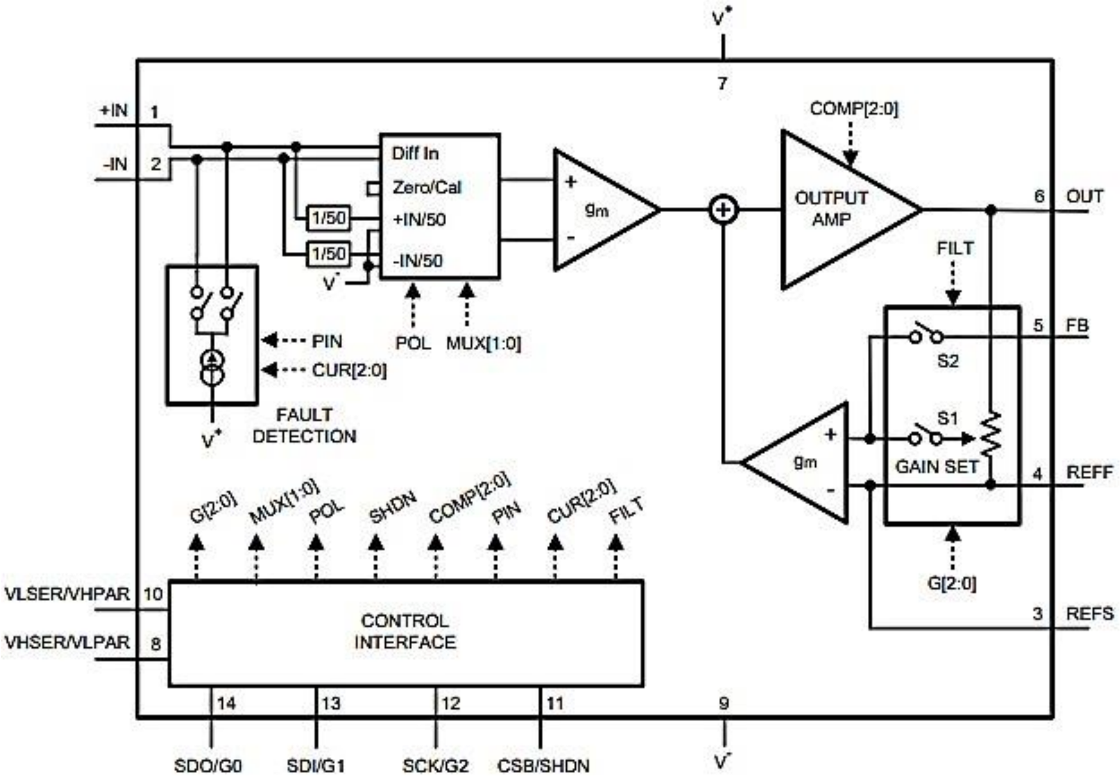

Figure 3-6: The structure of LMP8358MA instrumentation amplifier (Texas Instruments).

3.1.4 Offset Removal

The offset voltage is an undesired effect which occurs due to contact misalignments, poor surface roughness or non-homogeneous device structure [43, 44, 378] and introduces a non-zero voltage value for the cases of zero magnetic field and keeps increasing with increased current under constant magnetic field. In most cases, this voltage could be even higher than the actual Hall voltage that is point of interest. Figure 3-7 represents the parameters that causes the offset voltage.

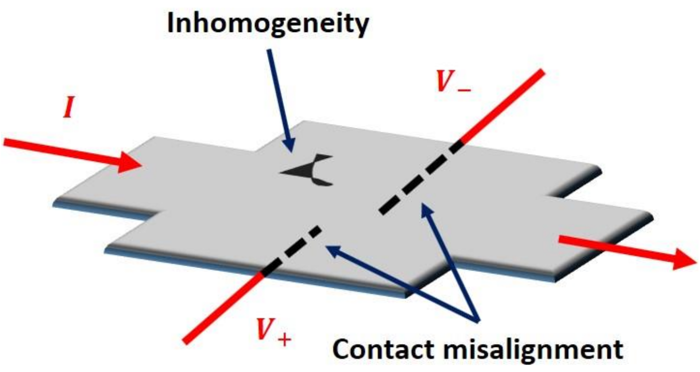

Figure 3-7: The parameters that causes offset voltage.

The amplification stage increases the output and help better understanding of the voltage change; however, it still has the limitations in terms of the ability of accurate measurement since the output is amplified together with offset voltage. That means the amplification process also causes the amplification of the offset voltage, as well. A potentiometer can be used as a tool for eliminating offset voltage by being connected to the output of the amplification circuit as shown in Figure 3-8 and could be arranged to provide zero offset. However, this will work for a specific biasing current and will require an adjustment if the amount of biasing current changes. Additionally, thermal effects will be dominant since a potentiometer is in use.

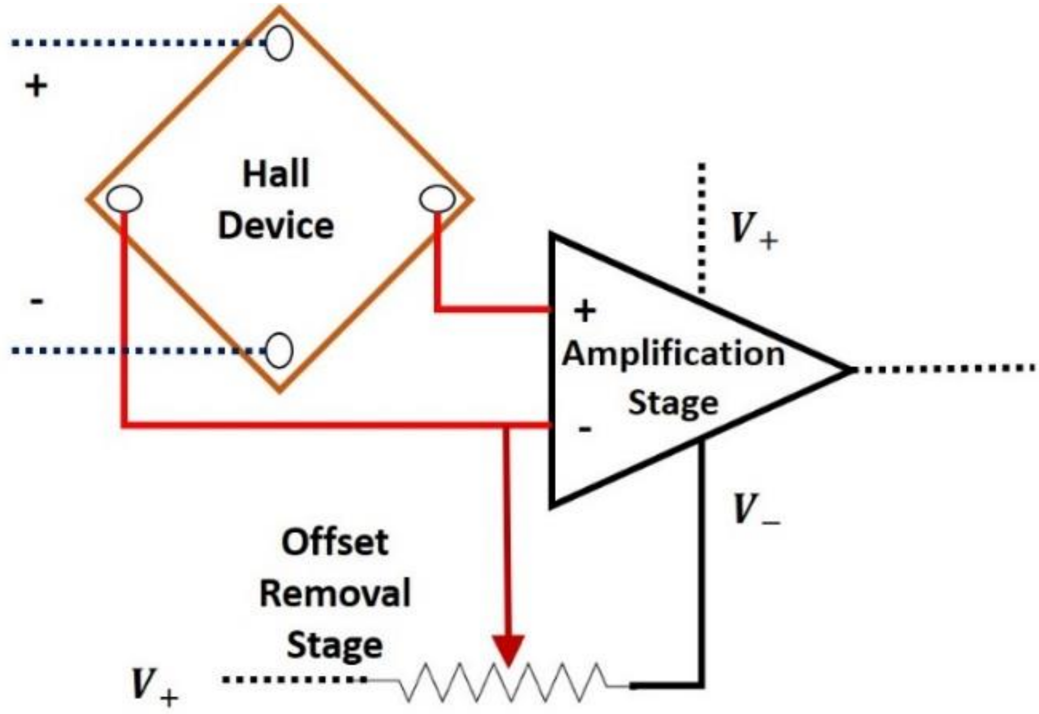

Figure 3-8: A basic offset removal stage for Hall devices using a potentiometer.

3.1.5 External Noise Cancellation

External noise sources have certain limitations on electronic circuits. Likewise, the developed system is prone to external noise sources which needs to be dealt with. In addition to implemented stages given in previous sections, a shielded aluminium enclosure (RS Components, UK) was used to serve as a Faraday cage. As shown in the Figure 3-9, it is a closed dark box and helped eliminate external noise sources such as RF and ambient light etc. The external connections to inner medium were made via BNC connectors.

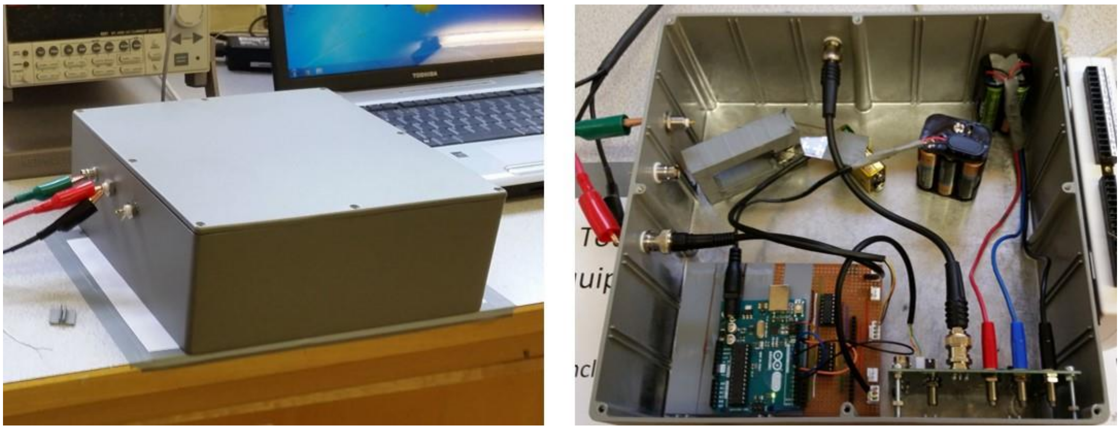

Figure 3-9: Outer (left) and inner (right) view of the shielded aluminium enclosure.

3.1.6 Data Acquisition

Data acquisition can be performed after the amplification and offset removal stages. As was mentioned in section 3.1.4 the amplification increases the offset voltage as well, however, this can be eliminated via the procedure explained. The amplification stage introduces another issue which might cause a deteriorating effect on actual signal of interest since it leads to a similar amount of amplification of noise signals. Therefore, the output of the amplifier must be filtered with a low pass filter for removal of undesired frequency components. Figure 3-10 shows the implementation of a filtering stage. A filter having a specified cut-off frequency can simply be integrated to the circuit via passive components such as capacitors and resistors. Meanwhile, it can also be filtered using a software after acquisition.

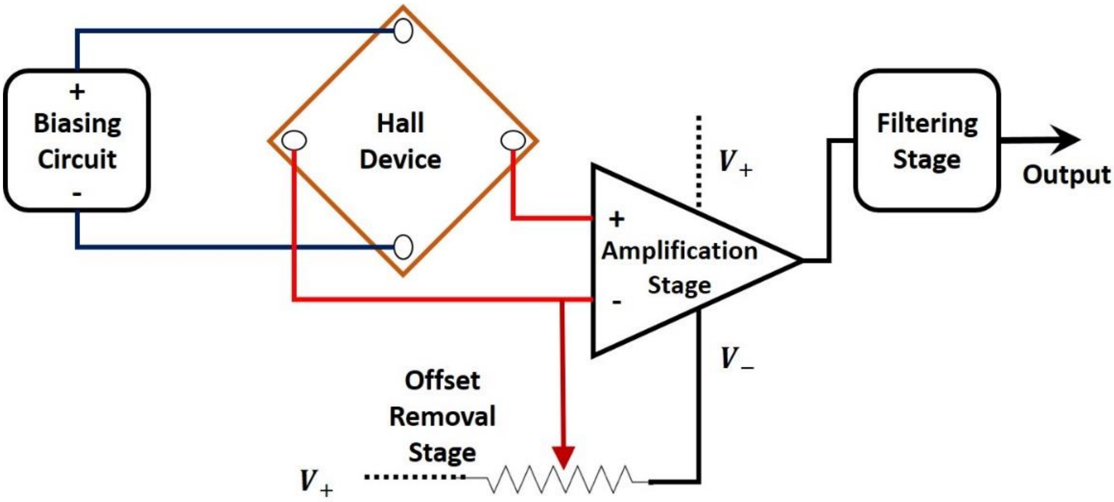

Figure 3-10: A basic biasing, amplifying and offset removal stages along with filtering stage for Hall devices.

A portable multimeter (Fluke 189 True RMS Multimeter) capable of measuring microvolts and a Keithley 6517B electrometer with Digimess DM200 digital multimeter was used to observe the output behaviour of the devices. In cases where the voltage was too low to measure by those equipment, a Keithley 2182A nanovoltmeter was used. In addition, a data acquisition card (National Instrument USB6221 DAQ) was also used to record the output for further analysis using LabVIEW software. The USB6221 DAQ is a high-performance multifunction data acquisition module that was optimised for fast sampling rates with superior accuracy. It can easily be connected to a PC via USB Port. It provides 16 analog inputs (16-bit, 250 kS/s) and 2 analog outputs (16-bit, 833 kS/s) along with 24 digital I/O (8 clocked) and 32-bit counters.

3.2 Implementation of an Integrated System

The simple rule for obtaining a Hall voltage is to form at least four contacts on a thin sheet of metal or semiconductor. This is, in principle, sufficient for capturing any Hall voltage which occurs due to the applied perpendicular magnetic field. However, Hall voltages are typically quite small and therefore require amplification. In addition, offset voltages may be significantly higher than the Hall voltage. The offset voltage is an undesired outcome that occurs due to contact misalignments or poor surface roughness and non-homogeneous device structure [44]. This must be eliminated when forming a system with high sensitivity. The approaches presented in above sections will not be able to remove the offset dynamically since any change in the biasing current leads to a change in output regardless of magnetic field. More importantly, the output is prone to thermal effects in such a design since it becomes very sensitive to temperature changes. To remove the offset voltage a technique called ‘current spinning’ was employed [379] which can remove the offset voltage dynamically. Figure 3-11 is a representation of a cross shaped Hall device which will be used to explain the spinning method between contacts.

Basically, the idea can be explained by a simple approximation of a Hall device structure by using four resistors connected to each other in a Wheatstone bridge structure. In this case, an offset voltage can easily be introduced by using three resistors with the same values and one with a different value. Once the current is applied from one connection to the other non-neighbouring connection a voltage will be measured between other two non-neighbouring connection points. If this setup is rotated by 180°, the measured voltage will change in sign but remain as the same value.

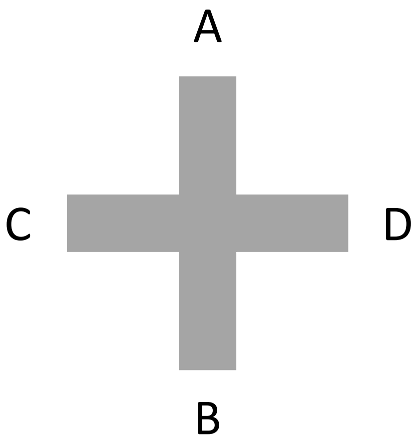

Figure 3-11: A representation of cross shape Hall device.

In case of a Hall device, the Hall voltage would not change since it depends on the exerted force (given in equation (2-1)) due to applied current and magnetic field. Once the outputs for 0° and 180° are obtained, the Hall voltage can easily be calculated by doing a simple mathematical operation on them. This method is summarised in Table 3-2 by considering the current rotation between all contacts.

Current	Measure	Obtained Output
From A to B	Between C and D	$V_H + V_{offset1}$
From C to D	Between B and A	$V_H + V_{offset2}$
From B to A	Between D and C	$V_H - V_{offset1}$
From D to C	Between A and B	$V_H - V_{offset2}$

Table 3-2: Biasing configurations and relevant outputs for a cross shape Hall device (see Figure 3-11 for cross shape).

In general, it is relatively simple to integrate Hall devices with on-chip circuitry for actuation and read-out, however, this is not straightforward when using graphene materials. The theoretical sensitivity of the system reduces significantly during implementation – as demonstrated by a previous attempt to integrate Hall effect graphene devices on a CMOS chip [291]. In the reported work, the achieved sensitivity limit (200 *V/AT*) [291] was similar to silicon based Hall devices (310 V/*AT*) [380]. This may be due to introducing defects in the graphene during the processing steps.

To address the issue, a bespoke circuitry was designed and constructed on a PCB board, by employing a 'current spin model' [378], and integrated with the graphene Hall effect sensors for biasing and processing the output. The circuitry was used to correct the output by eliminating non-desired offset voltages and reducing noise levels thus providing an improvement on the sensitivity of the overall system. The schematic in Figure 3-12 demonstrates the steps that were implemented for driving devices and reading the outputs.

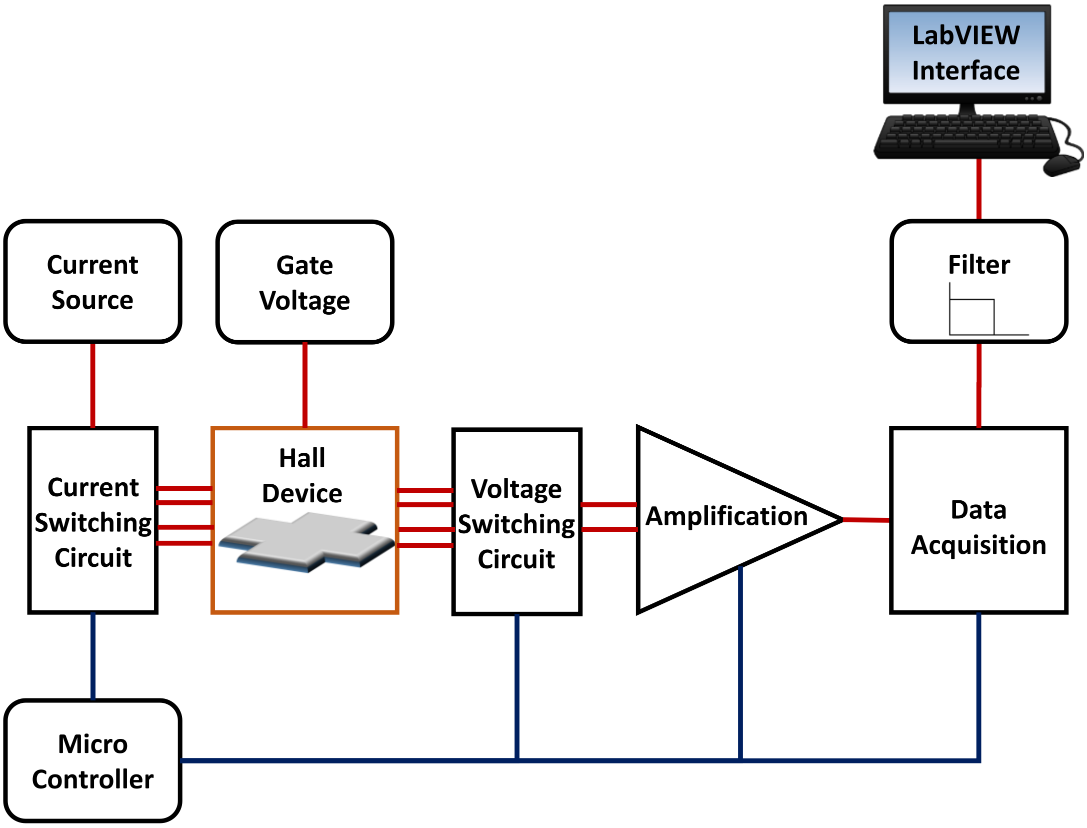

Figure 3-12: Schematic of developed driving and processing circuitry for rotating the current between contacts and reading the output simultaneously. Current and voltage switching circuits are simultaneously operating with the help of a microcontroller and the output is amplified before being read by the data acquisition card. Then, the obtained output is filtered and visualized via a user interface created via LabVIEW. The entire system synchronously operates to provide a smooth elimination process.

Fundamentally, the current is driven from one of the contacts to a non-neighbouring contact and simultaneously the produced output voltage is measured across the remaining two contacts (e.g. current flows from the top contact to the bottom and the voltage difference between left and right contacts is measured – see Figure 3-11 and Table 3-2)). In such a case, the produced output includes both Hall voltage (V_H) generated by applied perpendicular magnetic field (B_y) and offset voltage (V_{off}). To be able to remove the offset voltage, the current flow is rotated 180° and passes through two new non-neighbouring contacts whilst the voltage across the remaining contacts is measured. The current flows from left contact to the right contact and the voltage difference between bottom and top contacts are measured (see Figure 3-11 and Table 3-2). In this case, the measured output includes Hall voltage subtracted by offset voltage. For a more robust elimination, this procedure continues for one complete cycle meaning that the current is driven between all contacts for a complete cycle following 90° rotation steps. Averaging the obtained outputs eliminates the offset and reveals the Hall voltage. A typical processed output of the device for one cycle is given in Figure 3-13. Each region indicated in the figure corresponds to the specific cases mentioned above, e.g., region 1 is the measured output between left and right contacts whilst the current flows from top to bottom.

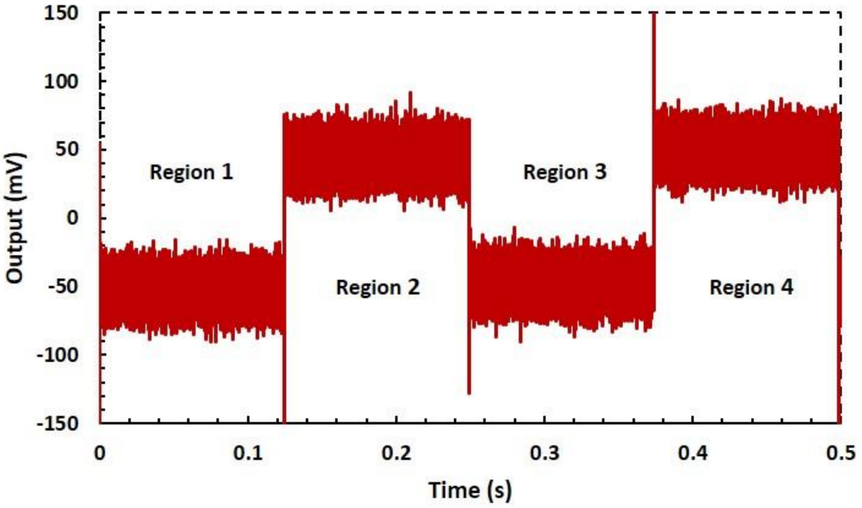

Figure 3-13: A Typical output obtained after one cycle with a rotation frequency of 2 Hz. Each region corresponds to a specific obtained output of which current flows between two non-neighbouring contacts.

The constructed PCB has an on-board constant current source, which can easily be adjusted from 1 µA to 10 mA and can bias the sensor in floating or grounded mode of operation. Due to the controllable sensitivity of graphene, an optional input for gate voltage was also included. Current and voltage switching mechanisms were connected to the current source and the amplifier along with the connections to device contacts as shown by the circuit diagram in Figure 3-14. A microcontroller simultaneously manipulates the current rotation and output reading for various frequencies up to 1 MHz, however, due to the lack of reading capacity of data acquisition device the system was operated in a maximum frequency of up to 50 kHz. Amplification was performed via a high-performance instrumentation amplifier (LMP8358). The image in Figure 3-15 shows the designed system built on a PCB board.

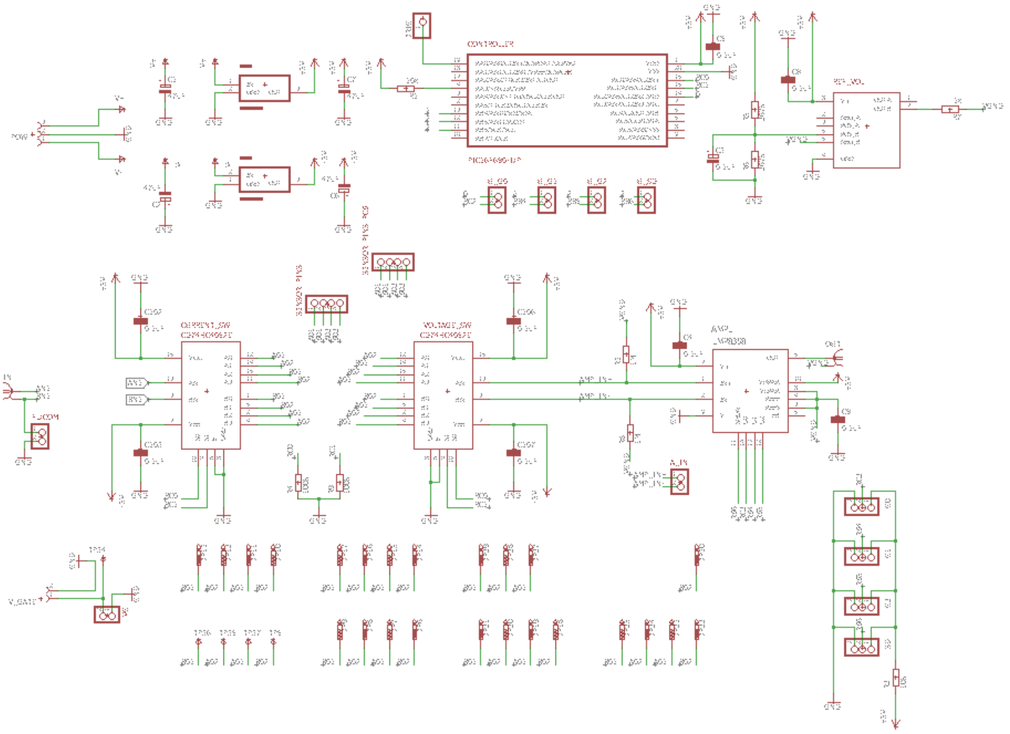

Figure 3-14: Circuit diagram of the constructed system.

The whole setup was synchronized with a data acquisition card for obtaining the output and a LabVIEW interface was created for saving and analysing the obtained data. The sensors can be integrated by being mounted on the board via the tongue shaped tip shown. Connections can also be made remotely using the relevant connection pins on the board. Assembling the driving and read-out system on a PCB is beneficial since there are challenges to integrate graphene on a single chip which encompasses all the electronic functionalities required for operation. As was demonstrated in a previous study [291], the complexity and temperature requirements of fabrication makes it difficult to integrate the graphene devices with a chip having biasing and read-out functionality. Figure 3-16 shows the setup which was used to operate devices.

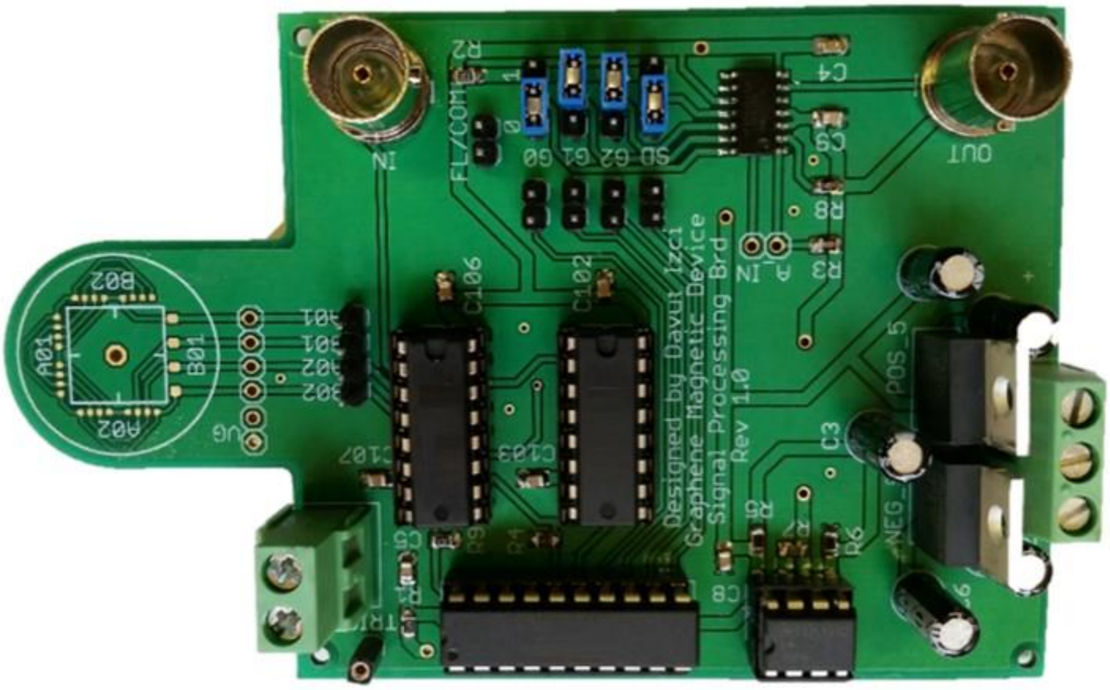

Figure 3-15: Constructed system board PCB. The sensors can easily be mounted on the tongue shaped tip or can be remotely connected via specified pins provided. The on-board current biasing mechanism can be used for biasing the Hall elements. The PCB also allows a current source to be connected externally for biasing.

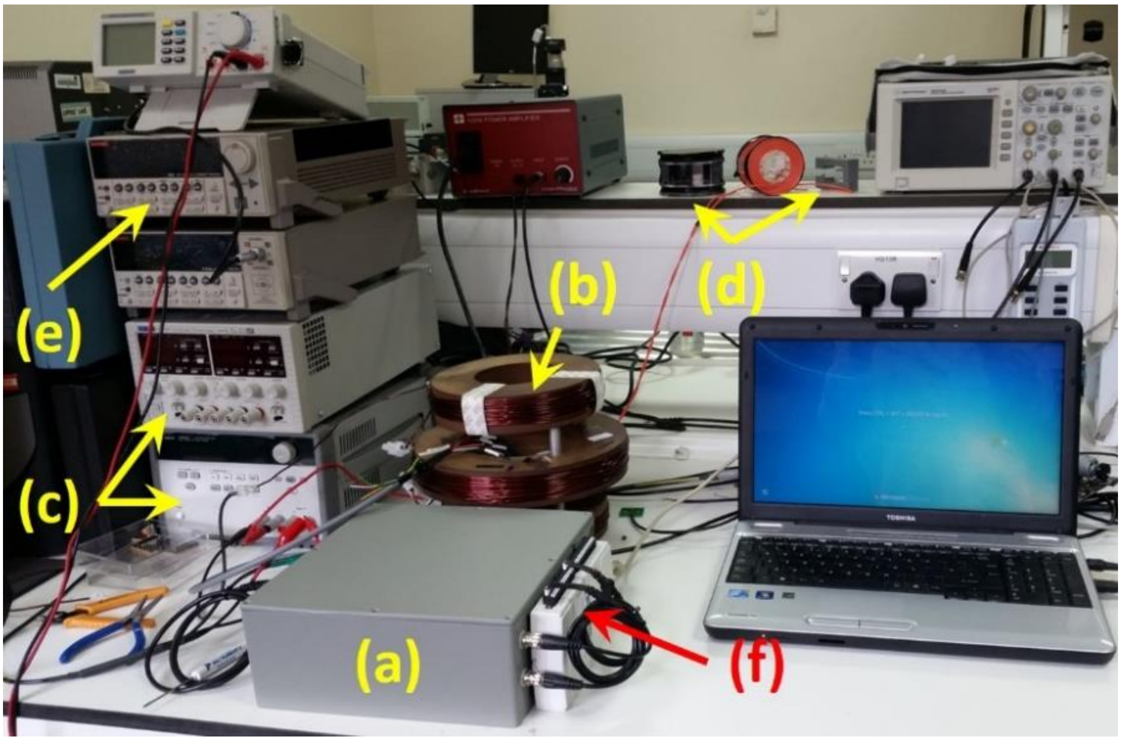

Figure 3-16: Measurement setup including a Faraday box (a) for eliminating external noise sources, a Maxwell coil (b) with power supplies (c) and permanent rare earth magnets (d) for obtaining variable and constant magnetic fields uniformly and a Keithley 6221 current source (e) for biasing with DAQ device (f) for data acquisition.

3.2.1 Offset and Noise Reduction

The developed driving and processing board was tested for its dynamic offset removal ability. The results obtained from the output of the devices with and without circuit implementation was assessed for cases of no magnetic field with a variable current source (Figure 3-17 (a)) and constant current flow with variable magnetic field (Figure 3-17 (b)). The implementation of the circuitry helped reducing the offset voltage by 99%.

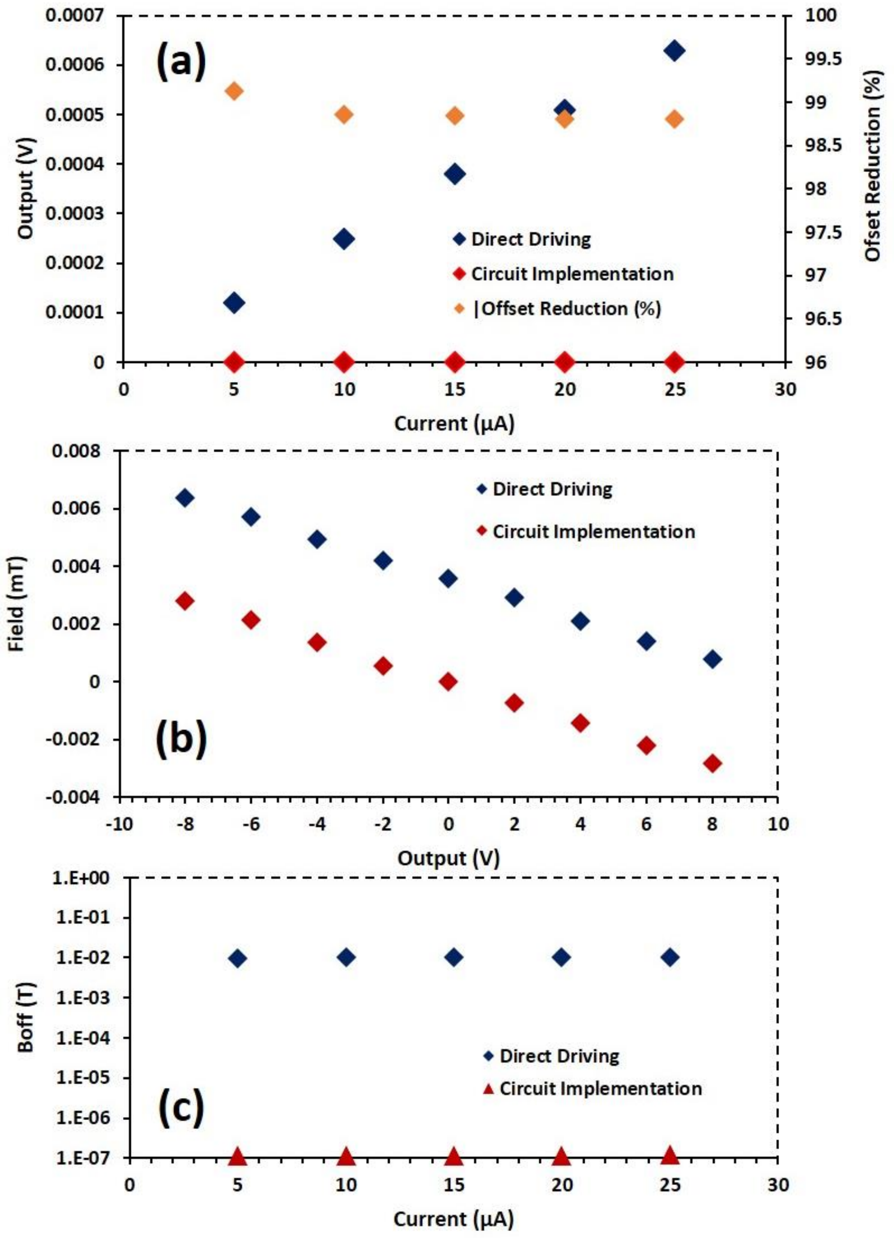

Figure 3-17: Demonstration of offset removal utilising graphene devices (see section 6.4.1). Direct driving of the sensor under no magnetic field (a). The data shown with yellow gives the reduction ratio. The response of the sensor under variable magnetic field with constant current source of 15 μA (b). Residual magnetic offset values obtained for both processed and non-processed output (c).

The offset equivalent magnetic field is defined as the ratio of offset voltage to the absolute sensitivity and given as:

$$B_{off} = \frac{V_{off}}{S_A} \tag{3–1}$$

where B_{off} stands for offset equivalent magnetic field and V_{off} represents offset voltage. The negligible residual offset shown in Figure 3-17 (c) corresponded to an offset equivalent magnetic field value of 100 nT thus providing a significant improvement in terms of the system accuracy.

Also, fast Fourier transform measurements on devices with and without biasing and driving circuitry showed that the noise level is reduced considerably by employing the developed circuitry. The power spectral density figures showed that the higher frequency operation leads to lower noise effect, thus, providing devices with better sensitivities. Figure 3-18 shows power spectral density measurements with respect to frequency of rotation.

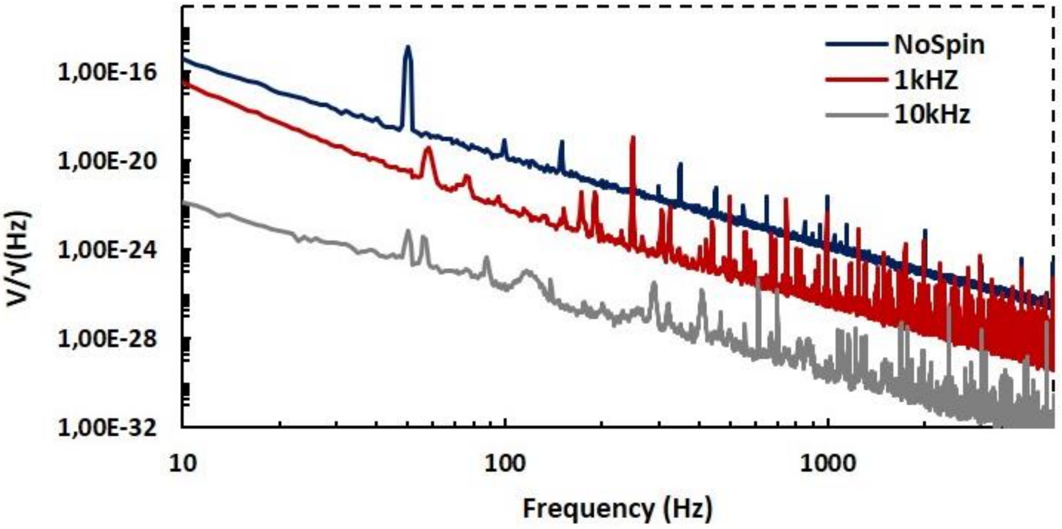

Figure 3-18: Power spectral density measurement with respect to rotation frequency showed a considerable amount of reduction in noise.

3.3 Bead Detection

Magnetic beads have been mostly used in biosensing platforms that utilise Hall mechanism as detection scheme [102, 105, 109, 115, 153, 272, 276, 282, 340, 348, 349]. This is most commonly preferred method for performing biological measurements [154] in Hall effect based biosensors. Adopting beads in Hall sensors require a different scheme for detection. Basically, magnetic micro/nano beads are used as a label to achieve the detection by covering the surface with a desired target analyte. Then, the sensor surface is functionalized in such a way to capture those target analytes. This method is also known as 'ac susceptibility measurements' [154] and is preferred commonly for performing biological measurements. The idea in ac susceptibility measurement is to create an alternating magnetic field with a certain frequency. This field is then applied in the plane of the sensor in the direction of the applied dc current. A perpendicular constant magnetic field is applied after the in-plane alternating field is created. If the beads are on the sensor surface then an output signal that has the same frequency of the in-plane ac excitation field must be observed, otherwise, there will not be any output. In other words, the output should be observed in case of binding event. The detection scheme is demonstrated in Figure 3-19 via a constructed system for potential future works.

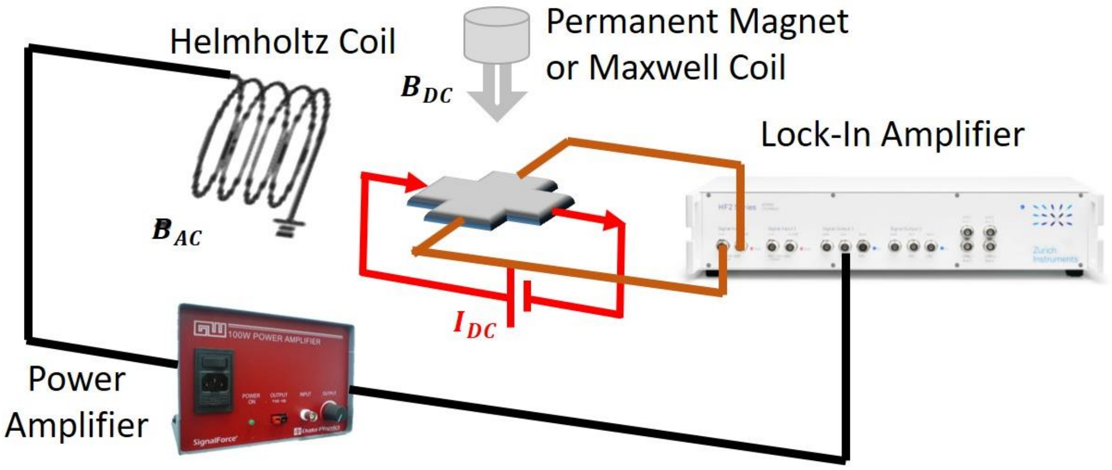

Figure 3-19: Schematic view of the measurement setup for ac susceptibility measurements. The setup contains Zurich HF2LI Lock-in amplifier, Signal Force (Data Physics) power amplifier, Maxwell coil or permanent magnet for dc field and Helmholtz coil for ac field creation.

In order to achieve such a scheme, a lock-in amplifier (Zurich Instruments HF2LI) was used to drive a power amplifier (Signal Force – Data Physics). The power amplifier fed a handmade Helmholtz coil for creating an alternating field having the same frequency of the excitation signal produced by lock-in amplifier. The Helmholtz coil was designed to include a base for placing the sensor chip in the right orientation so that in plane magnetic field can be applied. A high current power supply (Aim-TTi CPX400D) was used to create constant magnetic field by employing a Maxwell coil. The sensor output was connected to lock-in amplifier for achieving the detection of the same frequency of the driven signal. A Keithley 6221 DC and AC current source was employed to bias the sensors and a Keithley 6517B electrometer with a DM 200 multimeter were used for confirmation. Meanwhile, due to necessity for real-time monitoring, this method has not been used for measurements. However, the setup for this scheme was created, as shown in Figure 3-20, for potential future applications where beads may be used. Moreover, the complexity in this scheme does not make it attractive in terms of practicality.

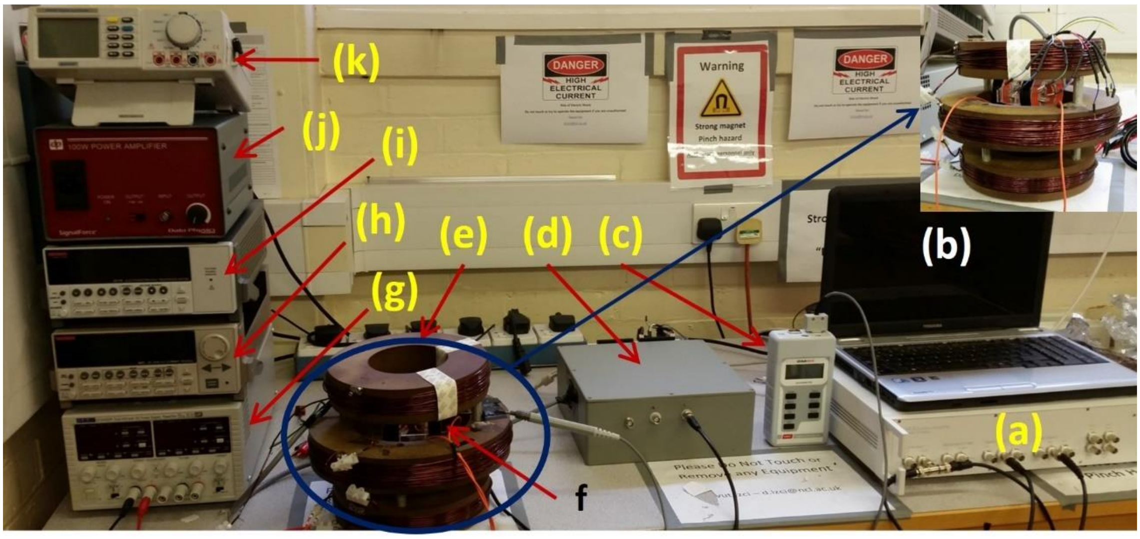

Figure 3-20: Test rig setup for measurements including lock-in amplifier (a), LabVIEW interface (b), Hirst Magnetics GM08 gauss meter (c), Faraday cage (d), Maxwell coil (e), Helmholtz coil (inside Maxwell coil) (f), high current power supply (g) to produce magnetic field, Keithley 6221 DC and AC current source (h), Keithley 6517B electrometer (i), Signal Force (Data Physics) power amplifier (j) and Digimess DM 200 Digital Multimeter (k).

Chapter 4. Gold Hall Devices

Any thin layer of metal or semiconductor in a simple rectangular shape with four contacts could be considered as a Hall device although they would suffer from significant small potential difference produced at the output due to their electric transport parameters. As is mentioned in section 2.2, certain requirements such as carrier mobility, density of charge carriers etc., should be satisfied in materials to have effective and sensitive Hall devices. In fabrication of gold devices, the aim was to explore a cheaper and easier way of implementation for biosensors as gold can easily be functionalised for biosensing purposes [381-385]. This Chapter presents entire steps that were undertaken from design and manufacture to measurements of Hall devices made of gold.

4.1 Design

Hall devices are basically devices that are producing information, with respect to applied field, as an output voltage. As is given in equation (2-2), Hall voltage output is proportional with carrier mobility and inversely proportional with carrier concentration. However, the geometrical structure has certain effects in terms of produced output [43, 264, 267, 386]. Therefore, designing a suitable geometrical structure [43, 44, 264, 267, 387] has a huge influence in terms of produced output. Scaling those structures are also affecting the output voltage [387, 388]. Several devices with different geometrical structures (Greek cross, square, cauliflower, round etc.,) and dimensions.

Figure 4-1 is a sketch of basic geometrical structures with corresponding dimensions (in terms of length and width) on the masks. Active areas that were ranging from 1 mm to 3 mm were designed to be used for devices on PCB. The reason of designing devices with relatively large sizes (millimetre range) was due to PCB fabrication limits. The corresponding shapes were designed as a gerber file (.gbr extention) in order to fabricate appropriate geometrical structures.

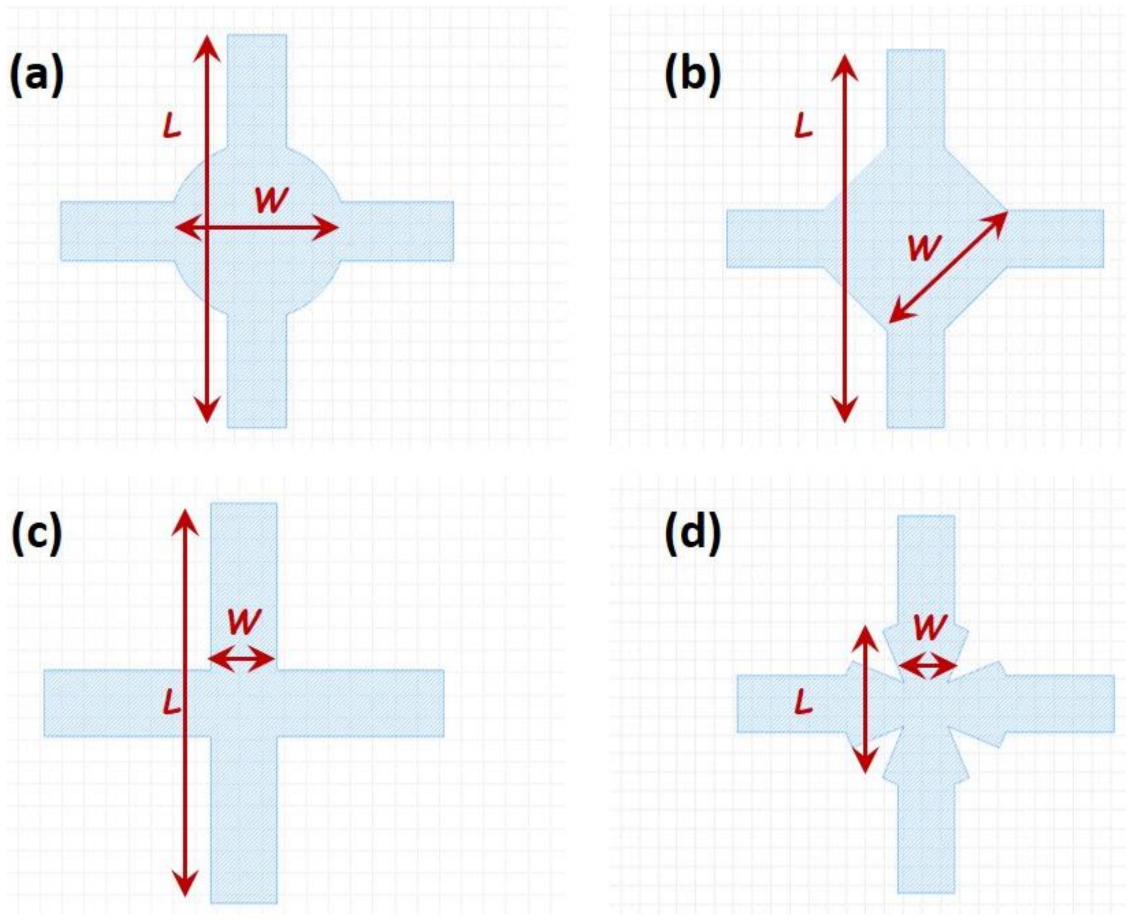

Figure 4-1: A representation of basic shapes of circle (a), square (b), cross (c) and cauliflower (d) with corresponding dimensions as length (L) and width (W).

A second design including cross structures with relatively smaller sizes (500 µm) was also prepared as dxf file (.dxf extension). This was used to operate laser machine (HPC Laserscript) to create masks for gold sputtering on a glass substrate. The reason of choosing the latter dimension was because of the limit that the laser cutting machine can reach for obtaining a clear mask from acrylic. Due to thermal distortion in acrylic, smaller dimensions with clear shapes were not feasible.

To fabricate micro-scale gold devices on a silicon substrate, a mask was designed with several geometrical forms (cross, square, circle, cauliflower) along with various length to width ratios (l/w) greater than 3 and made on a 4-inch glass to form devices having active areas of 10 µm, 20 µm, 40 µm and 60 µm. An integrated circuit design software (Tanner Tools – L-edit) was used to design the mask with geometrical structures to form devices along with contact pads. Figure 4-2 shows the designed mask.

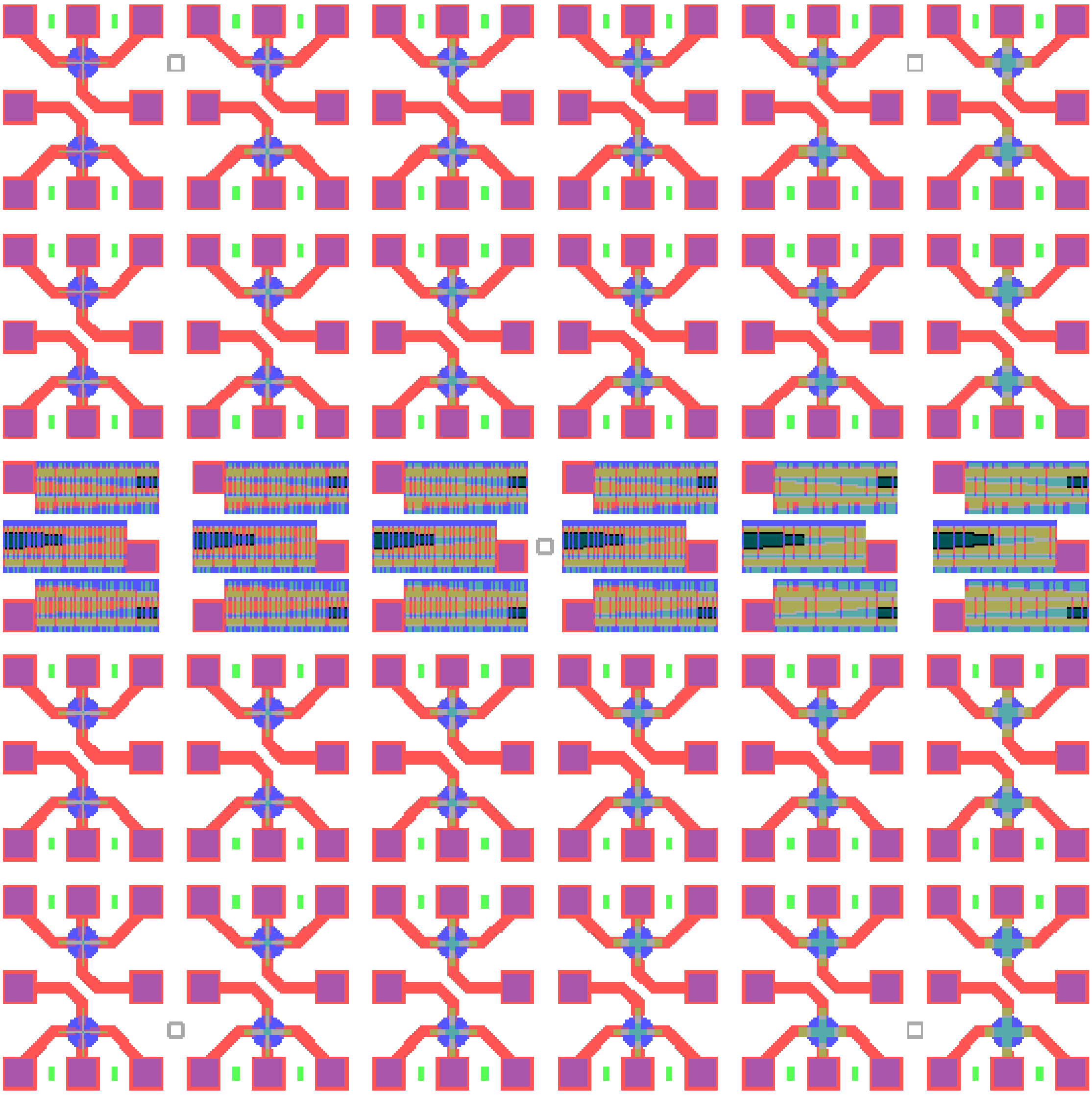

Figure 4-2: Designed mask with several Hall devices from 10 microns to 60 microns along with beams and cantilever structures having various sizes.

4.2 Materials

Thin films [124, 127, 389, 390], 2DEG heterostructures [121, 123, 391-394] or single layer atomic structures such as graphene and its derivatives [63, 71, 72, 128] are the excellent choices since they meet the required criteria for better Hall devices. However, working with those materials requires familiarity of microfabrication processes which could be expensive to a certain extent and could cost time. Because, every stage of the process, from design to actual manufacturing, must be well-defined. Additionally, the manufactured devices should be planned as part of a system that is easy to be biased with current or voltage sources and allows reading the output without causing confusion. Therefore, it was decided to work with relatively easy to fabricate devices.

4.2.1 Devices on PCB

Initially, gold devices were planned to be made on a traditional PCB in combination with nickel and copper. Those devices are not practical for the Hall device structures; however, it was used to help in experimental setup described in Chapter 3. The aim was to optimise sensing circuitry although PCB Hall devices are not viable for sensing purposes.

4.2.2 Devices on Glass

The second approach was to form gold structures directly on a glass substrate. This approach was simple in terms of fabrication with feasibility as Hall sensors. However, they presented a disadvantage in terms of biosensing which occurs due to adhesion issue. Since no adhesion layer such as chromium or titanium was used, the gold layer was prone to delamination in wet environment.

4.2.3 Devices on Silicon Substrate

The last approach was to implement microfabrication steps and form gold based micro-Hall devices in combination of chromium on a silicon die. This method of fabrication was more complicated to make devices and leading to slightly less sensitive sensors for relatively bigger sizes, yet, can be applied to biosensing applications.

4.3 Fabrication

4.3.1 Fabrication on PCB

This approach was an unusual way of fabrication for Hall structures as they are commonly made via microfabrication techniques mostly using semiconductors due to the advantage of being able to control the material parameters which are crucial for Hall effect applications. The aim was to use an alternative and easier way of device fabrication and practically observe the response of an inhomogeneous combination of metals along with different shapes and sizes. Additionally, and more importantly, they were used to develop the Hall measurement system that is mentioned in section 3.2. The devices were made of single-sided PCB with no plated-through holes and were built on 1.6mm FR4 epoxy glass fibre substrate along with three layers of different materials using PCB fabrication techniques. It was consisted of 1 oz (35 μm) of copper (Cu) layer, 3-5 μm nickel (Ni) layer, and 0.3 μm of gold (Au) layer. A cross-sectional view of the design is given in Figure 4-3.

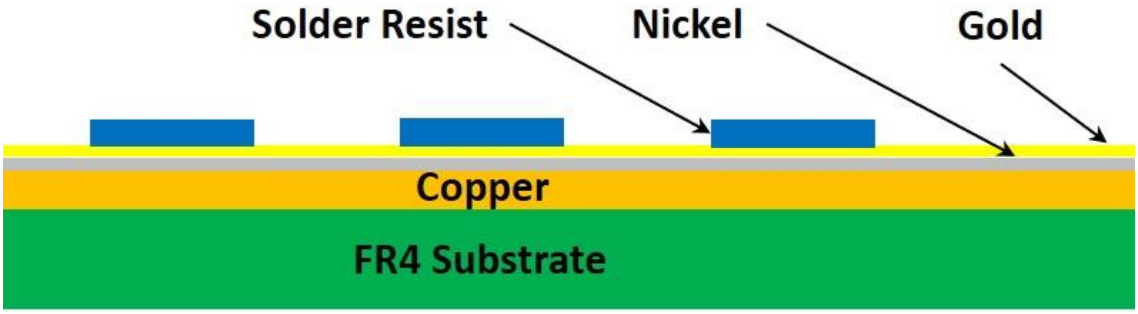

Figure 4-3: Cross-sectional view of designed Hall devices on PCB.

Several devices with different geometrical structures (Greek cross, square, cauliflower, round etc.,) and dimensions ranging from 1 mm to 3 mm were fabricated for each shape (see Figure 4-4). The reason of designing devices with relatively large sizes (millimetre range) was due to PCB fabrication limits. Most of the devices consisted of 4 contact points; 2 for biasing and other 2 for reading, respectively. The devices with 6 contacts (Figure 4-4 (e) and Figure 4-4(f)) were aimed to be used for quantum Hall effect or magnetoresistance effects. However, they were not tested for quantum Hall effect since it requires too strong magnetic field which was not practical at this stage.

The areas covered by solder resist was designed for potentially limiting any bead attachment to the required areas of devices meaning that the functionalisation process can be performed only on active areas of the devices. Meanwhile, those devices were used as a test step to create a relevant electronic circuitry for further works rather than functionalising for specific purposes. This was due to high carrier concentration and relatively thick and large structure of the devices which makes them not practical for such a purpose. The fabricated PCB Hall devices with various structures is shown in Figure 4-4.

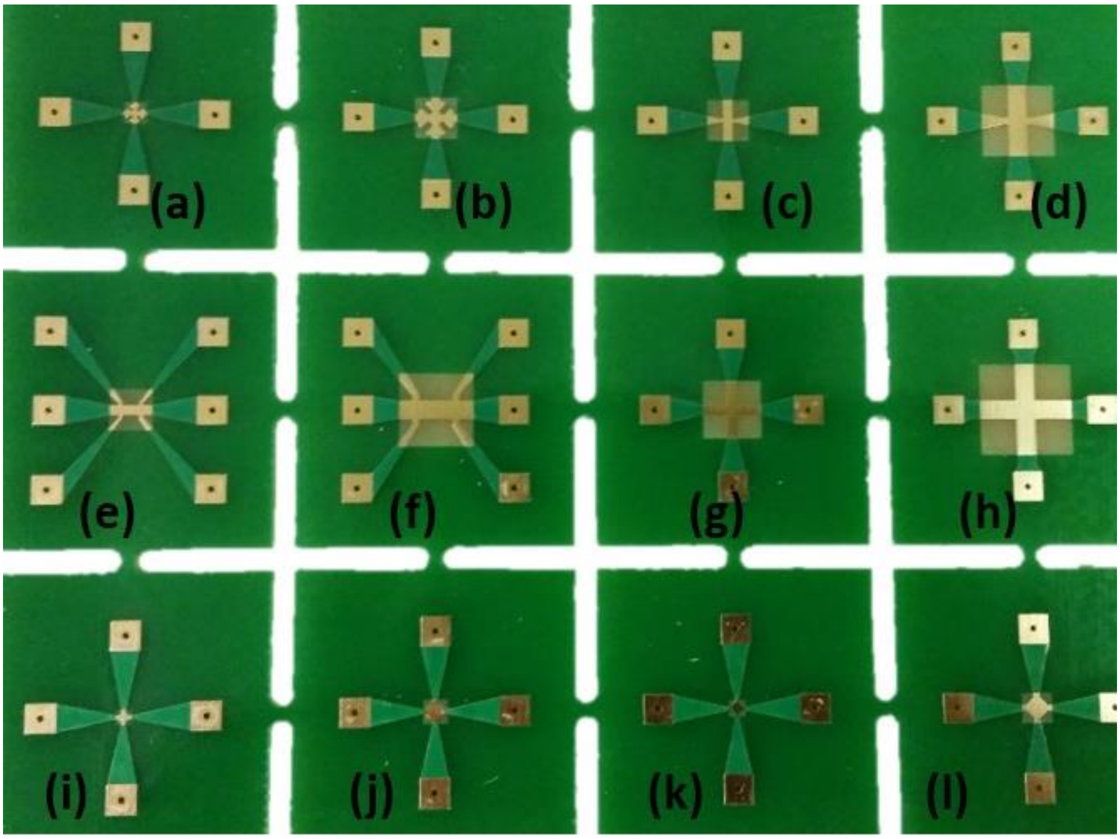

Figure 4-4: Fabricated Hall Devices. Cauliflower shapes with 1 mm (a) and 3 mm (b). Hall bar with 1 mm (c) and 3 mm (d). Hall bar with two legs having 1 mm (e) and 3 mm (f) shapes. Cross shapes with 1 mm (g) and 3 mm (h). Circle shapes with 1mm (i) and 3 mm (j) diameters. Square shapes with 1 mm^2 (k) and 3 mm^2 (l).

4.3.2 Fabrication on Glass

Devices that are explained in previous section had non-homogeneous structures since they included three different layers of materials. Additionally, surface roughness was not as smooth as desired. Therefore, additional structures were designed and made on a thin acrylic mask by cutting relevant structures with laser cutting machine (HPC Laserjet). Then a gold layer of around 30 nm were formed by sputtering technique using a Bio-Rad Microscience Division SC500 sputter machine. Those devices had relatively large sizes (500 µm and more) due to the limitation in laser beam size and thermal distortion issue in the acrylic. Figure 4-5 shows the sputter machine used for forming gold structures (a) along with the created acrylic masks on glass slides (b) and one of the slides with formed Hall devices (c).

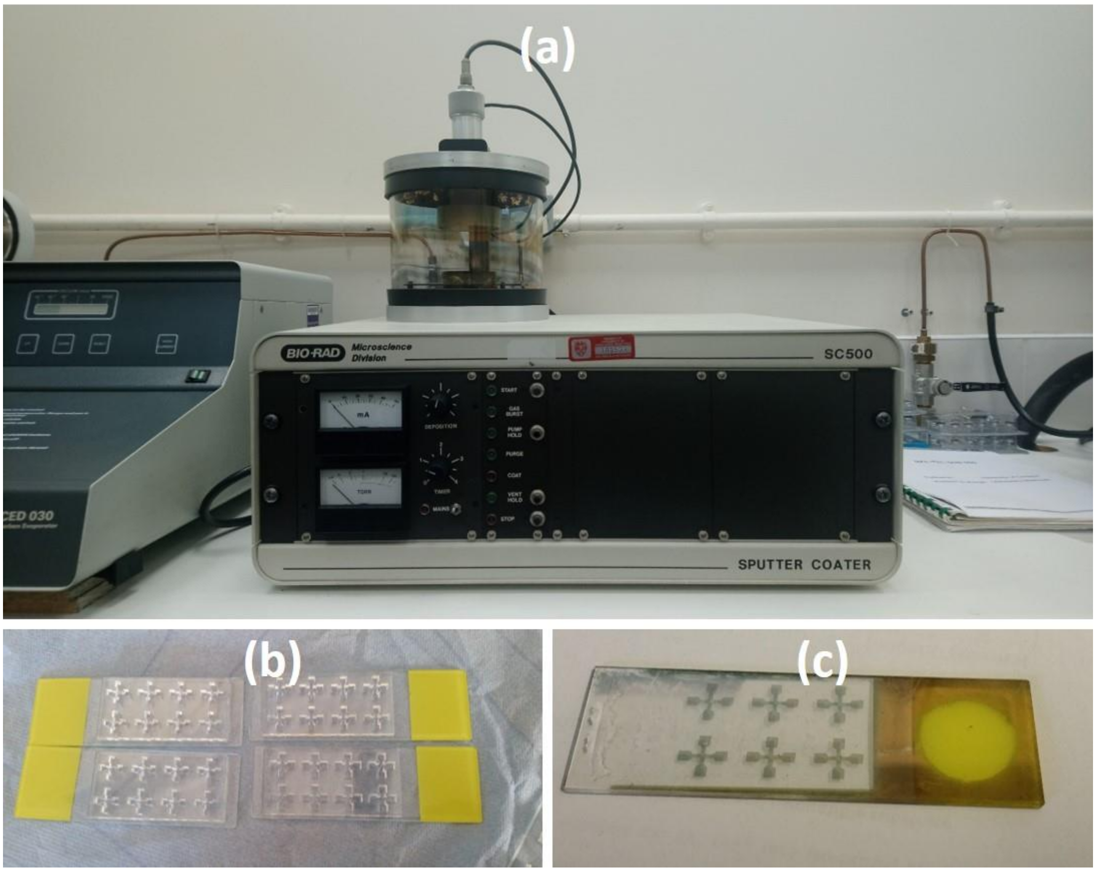

Figure 4-5: Gold sputter coater (Bio-Rad Microscience Division SC500) used for gold sputtering on glass (a) with designed acrylic masks (b) and obtained devices (c).

4.3.3 Fabrication on Silicon Substrate

Gold devices on glass were found to be feasible as Hall devices, however, there was an issue regarding the adhesion between gold layer and the substrate implying that the devices will work in dry air only, and in case of a liquid environment they will be detached from the surface of the substrate. This was practically tested and confirmed meaning that they were not suitable for biosensing due to adhesion issue. Therefore, it was decided to fabricate gold devices with an adhesion layer. As a result, in addition to those devices made on PCB and glass, micro-Hall devices from 10 µm to 60 µm were also fabricated using microfabrication techniques including lithography and lift-off processes by employing a SiO_2/Si substrate. A chromium layer was used to aid the adhesion. Figure 4-6 demonstrates the microfabrication steps designed for device manufacturing.

The fabrication started with cutting silicon substrates of around 10 × 10 mm^2 and cleaning before any process. The cleaning procedure took place initially by doing ultrasonic bath at 80 °C using NMP (N-methyl-2-pyrrolidone) and IPA (propan-2-ol) for 10 and 5 minutes, respectively, followed by rinsing with ultra-pure water. This was carried out as an initial step for organic clean. Then, further cleaning process was taken place using piranha solution (a mixture of H_2O_2 (hydrogen peroxide) and H_2SO_4 (sulphuric acid)) to remove any residue. The last step in cleaning was to employ RCA cleaning method (steps including NH_4OH (ammonium solution), H_2O_2 and BHF (buffered hydrofluoric acid)). After wet-chemical cleaning procedure, the substrate was dried using nitrogen gun.

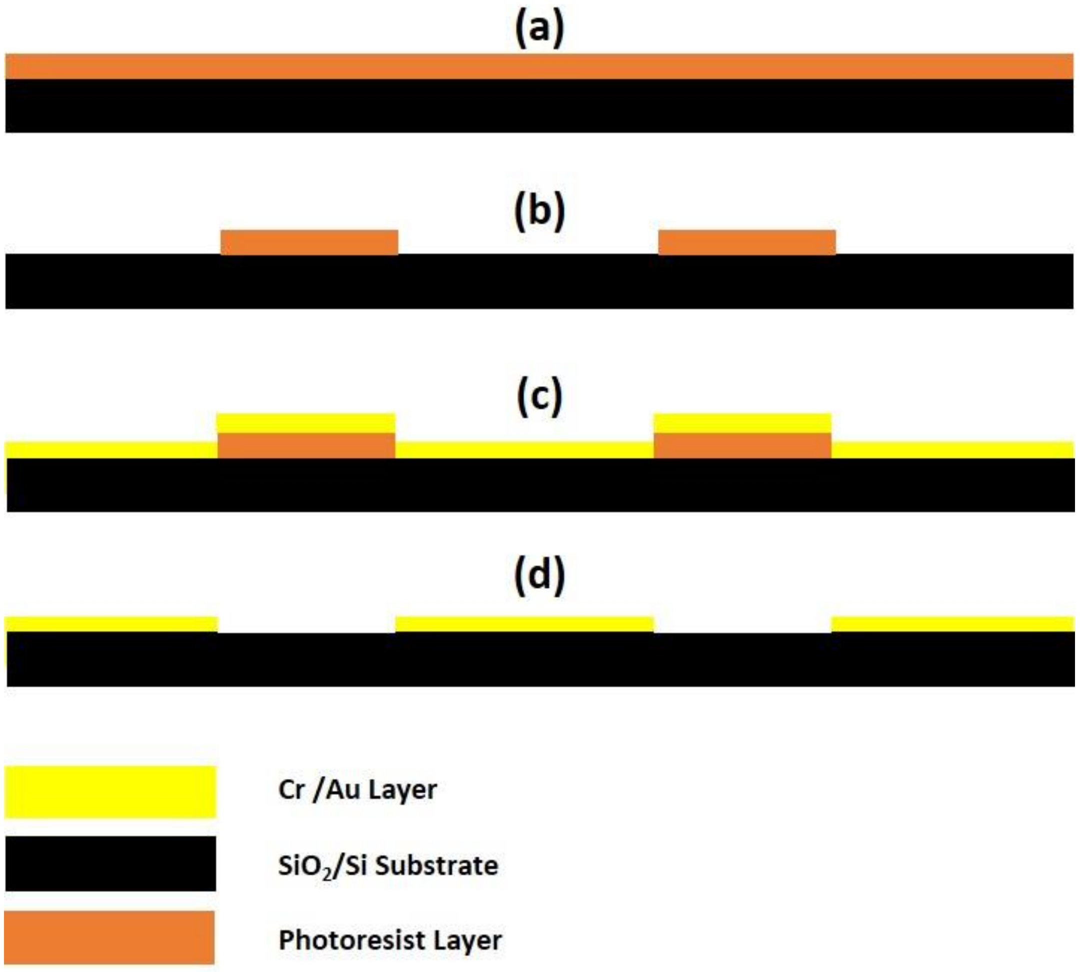

Figure 4-6: Lithography and lift-off process for micro-Hall gold devices. Positive photoresist cover (a), lithography and developing resist stages for constructing the pattern (b), chromium (Cr) and gold (Au) evaporation using e-beam evaporator (c), and lift-off process (d).

The substrate was covered with negative photoresist (AZ5214E) by using a spin coater (EMS 6000 spin coater) and pre-baked at 90 °C for 10 minutes, following the cleaning procedure. Then, the lithography process was performed with the aid of patterned glass mask. The sample was exposed to UV for 4 seconds using

KarlSuss MJB-3 mask aligner. A post-bake stage took place by using a hot plate (Electronic Micro Systems Ltd Model 1000-1 Precision Hot Plate) at 120 °C for 30 seconds followed by a blank UV exposure for 8 seconds. The latter process was performed to use the photoresist as an image reversal. After lithography, patterns were obtained by developing the photoresist using AZ 326 MIF developer. A chromium layer of 7 nm and gold layer of 35 nm were evaporated using e-beam evaporator (Edwards 306 e-beam evaporator) after developing relevant structure. These thicknesses were decided to be adequate for visibility and adhesion. In addition, the stated thicknesses were decided to be sufficient for potential biosensing applications in liquid medium. The last step was to do lift-off process in order to remove unnecessary parts. Figure 4-7 shows the obtained device structures after following the steps explained above.

Figure 4-7: Patterned photoresist after lithography and developer (a), obtained device structures after lift-off (b).

A similar process was carried out to form contacts on the obtained structures. Meanwhile, it is worth to note that the steps given in Figure 4-6 are for forming the Hall features using negative photoresist. To obtain contacts, positive resist was used instead of negative resist due to feature arrangements on the mask, therefore, the process took place in the reverse meaning that the features were formed on the areas where exposed to UV directly. In this case, the same photoresist was used, however, it was pre-baked at 90 °C for 15 minutes and the exposure time was 4 seconds without performing post-bake and blank exposure. The same developer was used to develop the resist and a layer of chromium with 30 nm along with a layer of gold with 250 nm were evaporated using e-beam evaporator. The fabrication was completed by doing the second lithography.

Figure 4-8 shows the developed features aligned with previously formed Hall structures (a) and the devices with contacts after lithography process (b) along with the fabricated devices on a 10 × 10 mm^2 die (c).

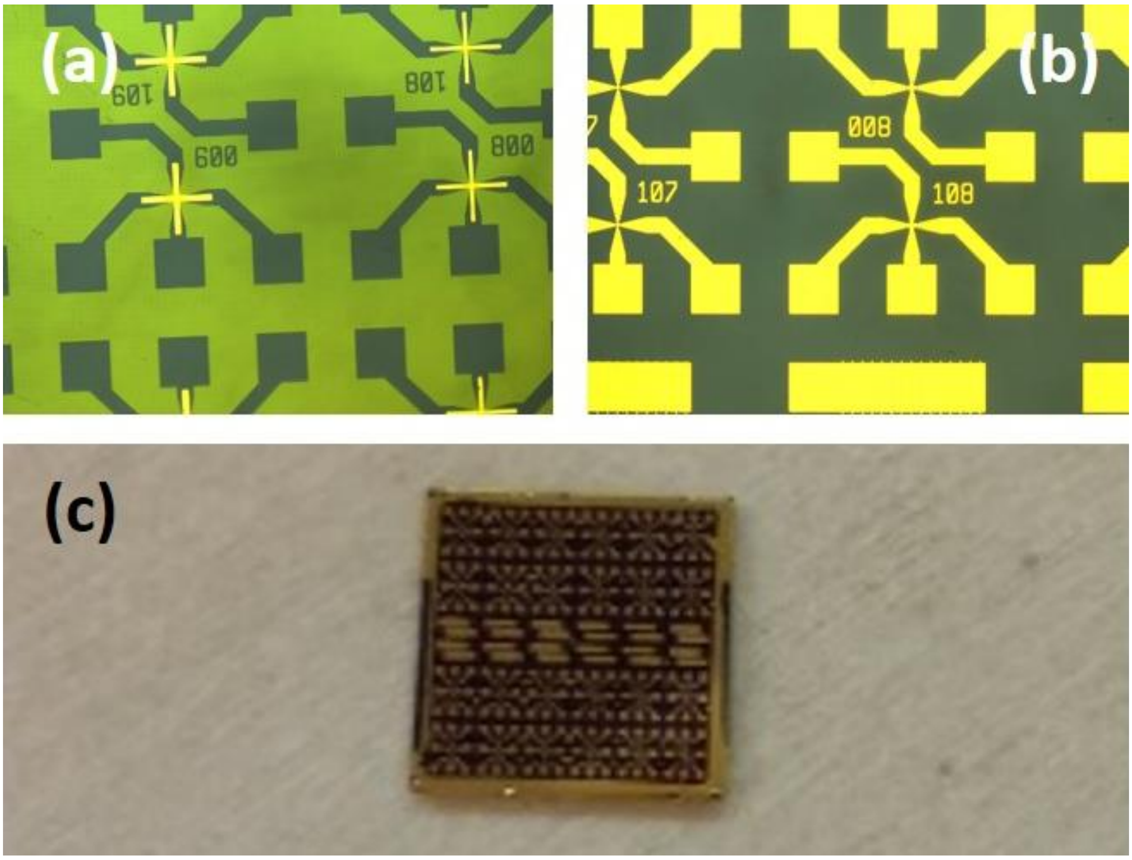

Figure 4-8: Patterning contact locations and alignment with photoresist (a), formed contacts after second lift-off (b). A silicon die used as a substrate with the fabricated devices on.

4.4 Measurements and Results

4.4.1 PCB Hall Devices

As was mentioned in previous sections, Hall devices on a PCB substrate is not an ideal way of device formation. Because of non-homogeneous material combination along with relatively thick and large structures, these types of devices required high current and high magnetic field to produce considerable output. Initially, a low noise linear DC power supply (Farnell E30-28T) was used to drive the devices. The reason of not using a switching power supply was to minimize any noise caused by biasing source. The linear power supply was used in combination with high power resistors to obtain a current source with higher ranges (up to 3A). Apart from this power supply, a Keithley 6221 AC and DC current source was also used for operating devices. It can provide a DC current range of −100 mA to +100 mA and is able to provide current in nano-amp precision. Additionally, it can provide an AC current range of up to 2 mA, as well. To allow current flow, the contacts of the device were soldered using a screened cable. The reason of using the screened cable was to eliminate external noise effects. The PCB Hall device was placed in between designed c-core structure as shown in Figure 4-9 in order to apply a perpendicular magnetic field.

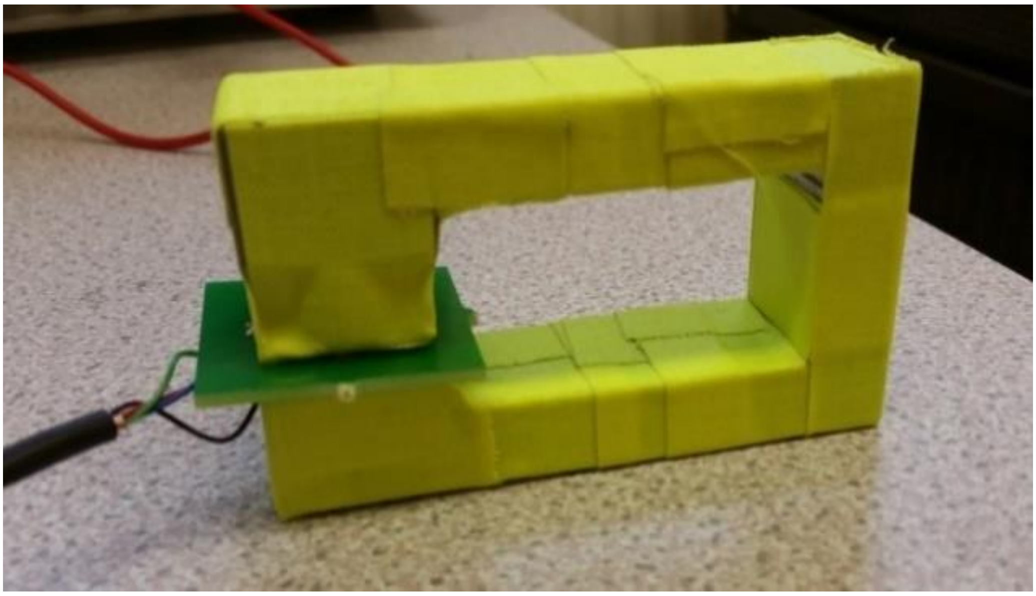

Figure 4-9: A PCB Hall device placed in the designed c-shaped structure which consists of a rare earth magnet and iron core to perform Hall measurements.

The Hall voltage is not affected from the misalignment of the contacts along the length of the device. Because the electrons would feel the same amount of resistance to their flow and a voltage value due to the exerted force would occur at the location where the transverse contacts are placed. A typical output obtained from fabricated PCB devices is shown in Figure 4-10 as an example. The zero-magnetic field line should have been on zero-horizontal line instead of being a negative value with a voltage gradient. This was because of the offset voltage effect as explained in section 3.1.4. However, if the no-field line is taken as a reference, the response of the device is highly linear for both positive and negative magnetic field strengths since a voltage gradient is observed for positive and negative values of current and magnetic field. This was a good sign in terms of linearity point of view. Nevertheless, this response must be corrected as it introduces complexity if the device is intended to be used for specific purposes.

The PCB Hall devices were designed and fabricated with the aim to create a circuitry for offset removal initially. Because, they were expected to have low performance parameters as Hall sensors, however, the idea was still to obtain an accurate measurement from them both for constructing a working circuitry for graphene devices and adopting PCB devices as biosensors in future works. The integrated circuitry explained in section 3.2 was designed and constructed with the aid of fabricated PCB devices. Figure 4-11 presents the corrected version of the results given in Figure 4-10.

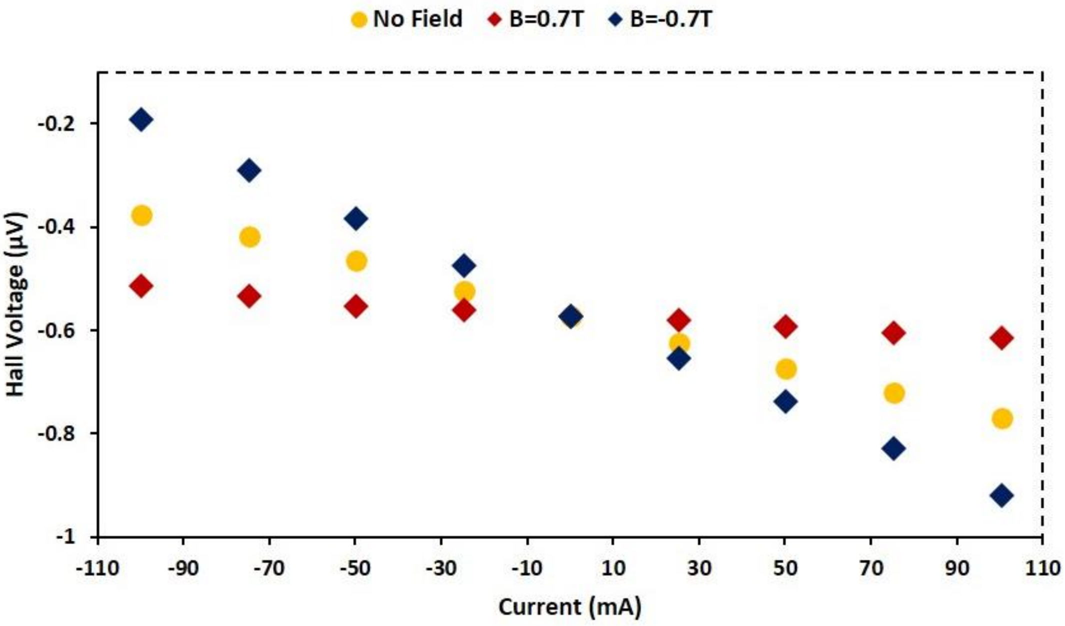

Figure 4-10: A typical output obtained from devices made on PCB without correction.

The output voltages in few hundreds of nanovolts were obtained from PCB based Hall devices. In order to be able to achieve an output of around few hundreds of microvolts range, the system must at least be driven with no less than 1 A with the employment of high magnetic field. Meanwhile, applying high current is particularly not convenient for safety reasons. It also causes more power consumption which consequently leads to disruptive working behaviour due to thermal heat effects.

A current-related sensitivity of 3 μV ⁄ AT was calculated which proved that the sensitivity of those type of Hall sensors are not in a desired range as was estimated due to its relatively large and thick structure along with its non-homogeneous structure.

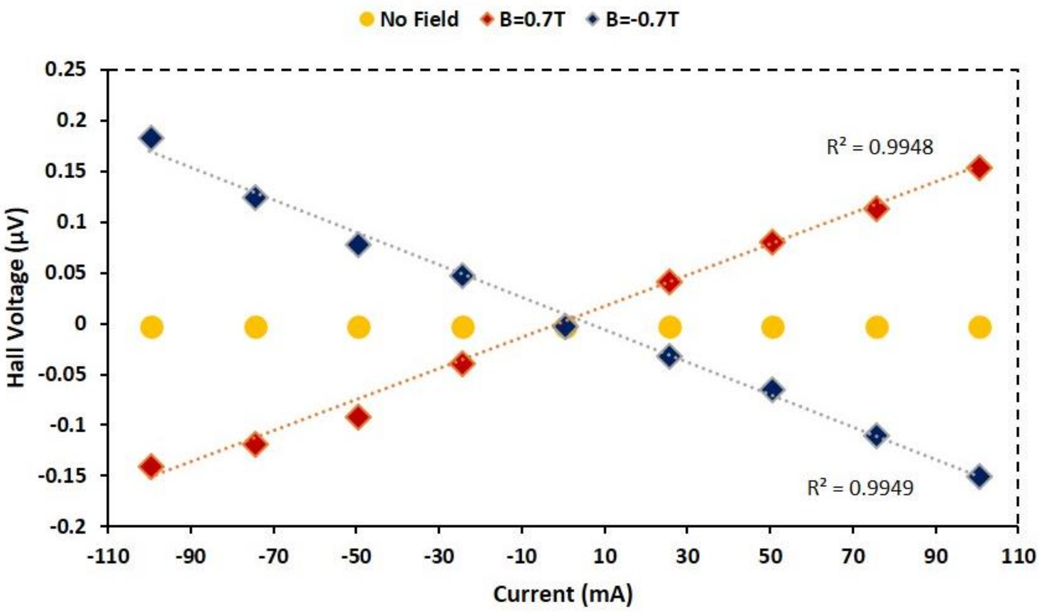

Figure 4-11: Corrected Hall output after removing offset voltage.

4.4.2 Devices on Glass Substrate

The gold devices on a glass substrate were designed and fabricated to eliminate the non-homogeneous structure issue so that the sensitivity could be improved. To perform measurements, a screened cable was connected to the device's contacts with the aid of silver paint (RS Pro Silver Conductive Adhesive Paint). Similar to the case in the PCB devices, the magnetic field was provided using the same iron core and rare earth magnet as shown in Figure 4-12.

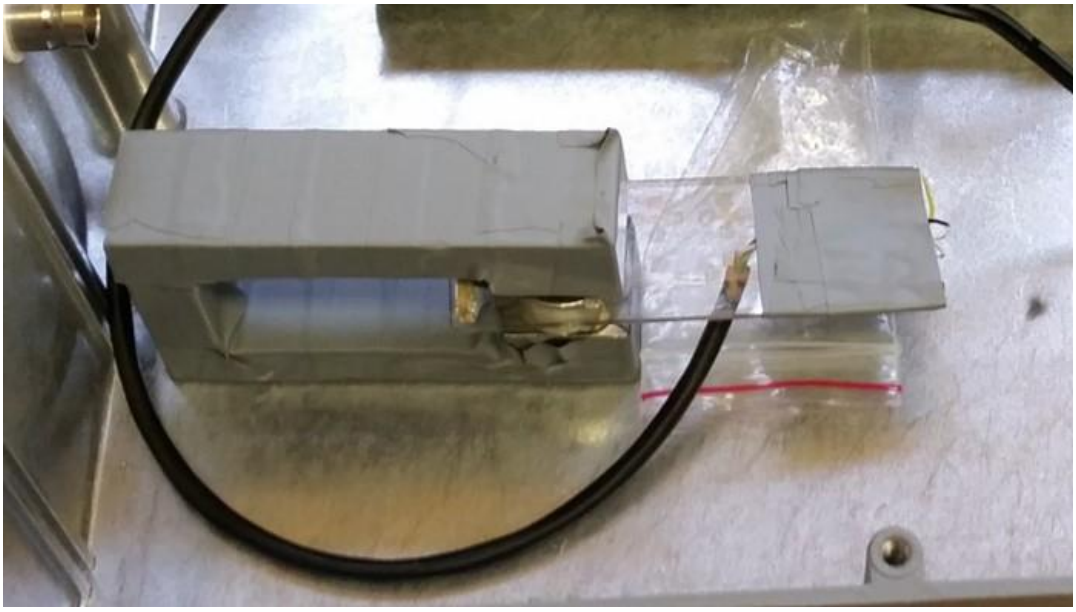

Figure 4-12: Au Hall device on glass substrate placed in magnetic field.

As was expected, this type of devices showed better sensitivity characteristics compared to PCB ones. Because, it did not include different material combination and had thinner gold layer. They also presented a good linearity behaviour. Outputs in microvolt range were obtained from those devices as shown in Figure 4-13. The obtained values were better than the PCB based devices by about an order of magnitude.

The behaviour they presented suggests that they can be adopted for applications where high sensitivity is not required. A current-related sensitivity of 5 mV ⁄ AT was obtained which confirms the improvement of the performance comparing PCB based Hall sensors. However, in terms of biosensing applications, they are not suitable due to lack of adhesion to the substrate which consequently causes delamination when a liquid inserted on them.

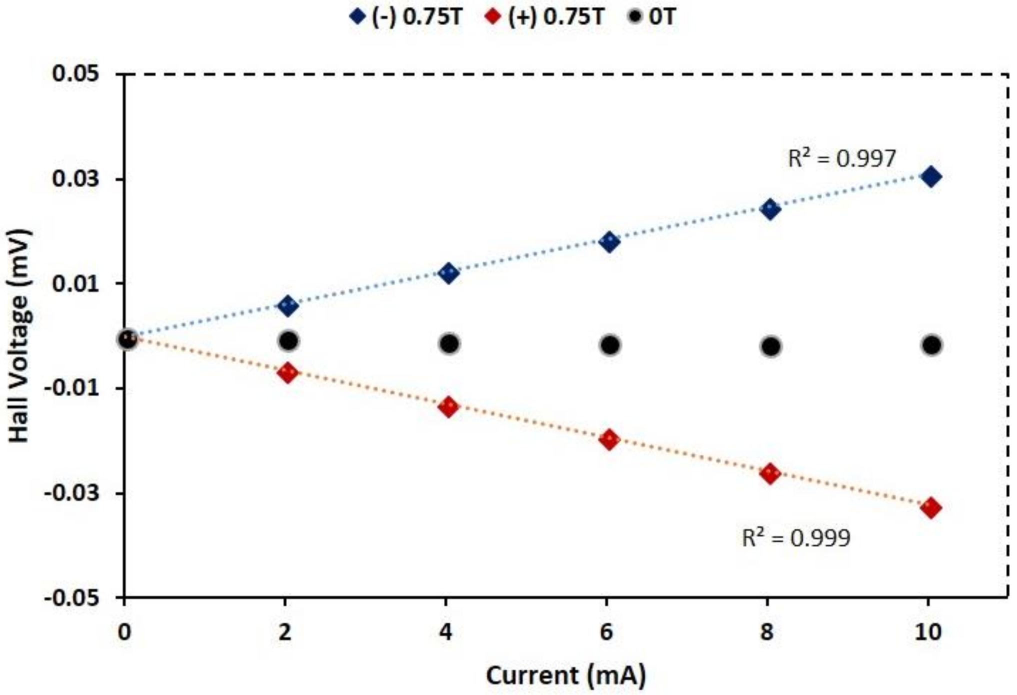

Figure 4-13: Response of a gold-based Hall device on gold substrate to positive and negative field polarities along with no magnetic field cases under varying current.

4.4.3 Devices on Silicon Substrate

Micro-fabricated gold devices were employed as an alternative to gold-based Hall devices on glass substrate to improve the adhesion. To do so, a layer of chromium was used as was explained in section 4.3.3. However, addition of this extra layer means that the performance of the device would decrease. To overcome this issue, the size of the sensors was decreased to compensate the reduction of the performance due to adhesion layer. The fabricated devices were wire-bonded to a 28-pin DIP chip, as demonstrated in Figure 4-14, using a wire bonder (Kulicke & Soffa Industries Model 4700 Wire Bonder).

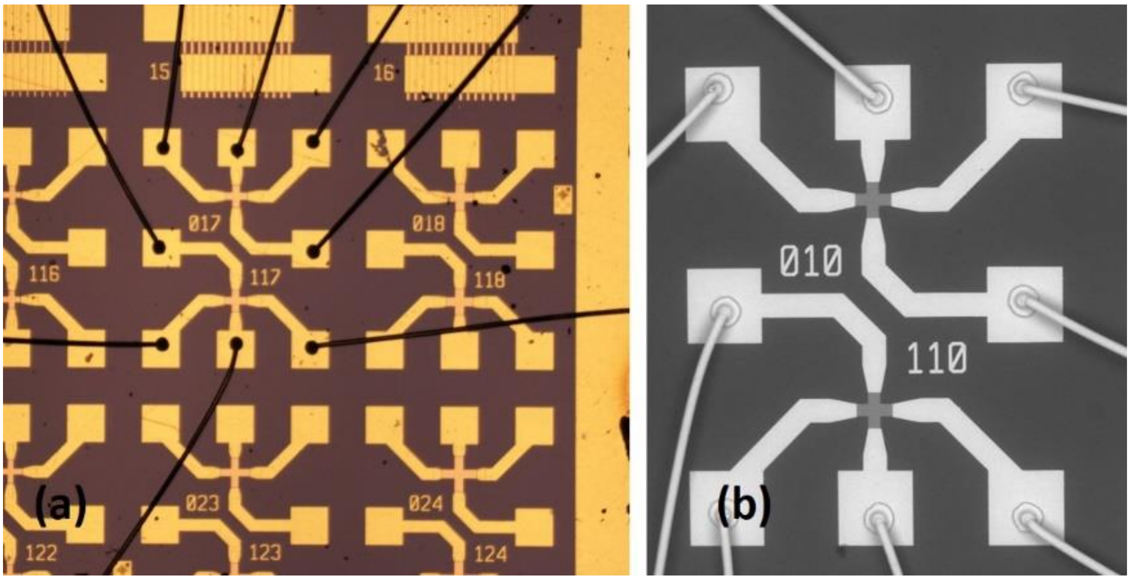

Figure 4-14: A optical (a) and SEM (b) image of wire-bonded contacts to a chip.

The initial measurements were performed on devices with 60 μm sizes. The performance parameters with those devices were no better than gold devices on glass substrate. This was an expected reduction since micro-Hall gold devices were fabricated with an additional layer of chromium. A current-related sensitivity of 3 mV/AT was obtained from those devices which verified the reduction in performance. Figure 4-15 shows the output change of a 60 μm device with respect to magnetic field.However, the following measurements on devices with 10 μm active areas presented a considerably better performance. This was attributed to the size effect [43, 264, 267, 316, 387] meaning that the smaller the size the better the performance. A current-related sensitivity of 27 mV ⁄ AT was calculated for those devices. In Figure 4-16, the output characteristic of a 10 μm device is presented with respect to varying current (a) and magnetic field (b).

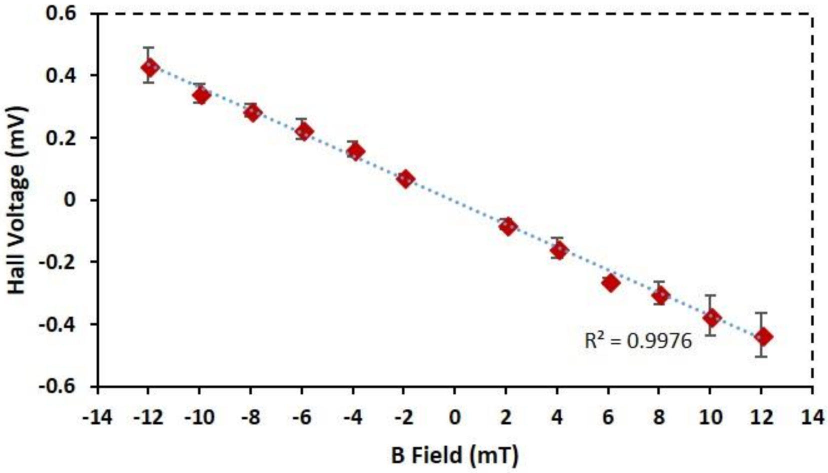

Figure 4-15: The output of a Cr/Au device on silicon substrate with 60 µm active area. The device was biased with 1 mA driving current.

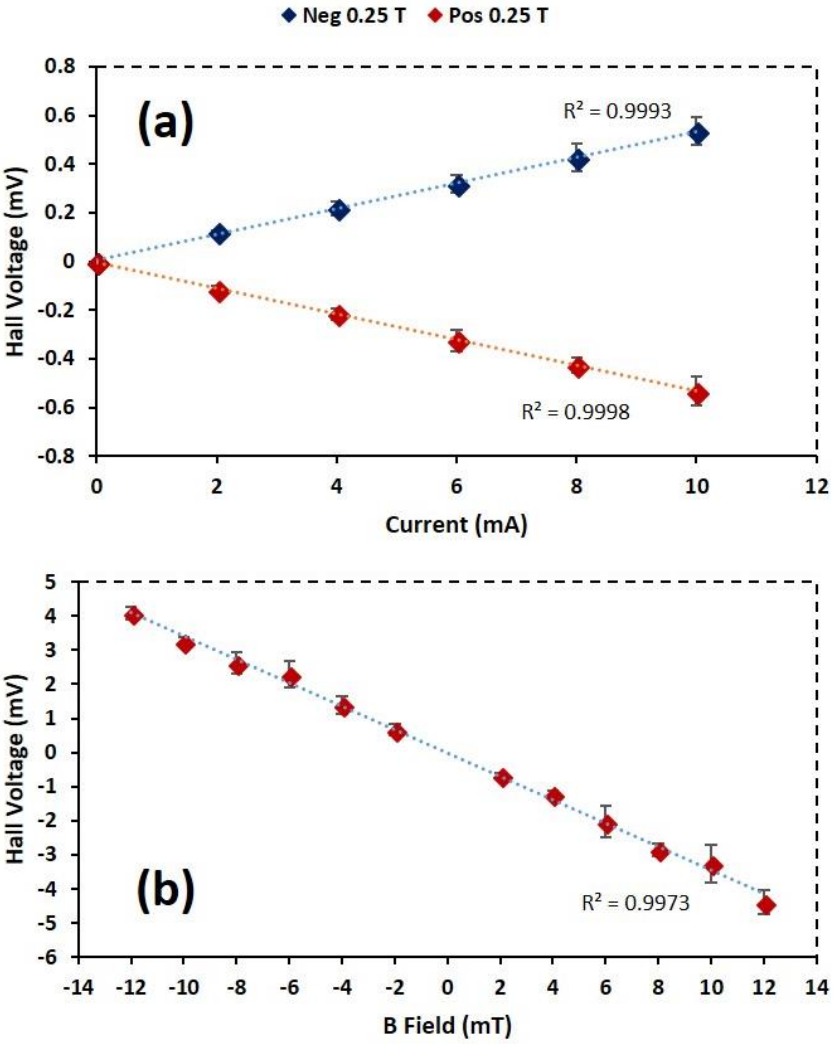

Figure 4-16: The output of a Cr/Au device on silicon substrate with 10 µm active area. The device output with respect to varying current for positive and negative magnetic fields (a). The output of the device with respect to varying magnetic field with a biasing current of 1 mA.

4.5 Summary

In general, gold-based Hall devices on PCB cannot be considered for high sensitivity applications due to their electric material properties and non-homogeneous structure. However, reducing the layer sizes has merit for applications not requiring high sensitivity as was shown with gold devices on glass substrate. In reality, the performance parameters for the latter type of Hall sensors can significantly be improved if they can be made in smaller sizes as confirmed by gold devices on silicon substrate with 10 μm active areas. In this work, the aim was to discover a cheaper and easier fabrication method, thus, the devices on glass substrate were made with larger sizes, due to limitation of laser size and distortion in acrylic because of thermal heat effect. Moreover, sputtering technique is not convenient for creating a smooth surface as it is bombarding the gold all around the surface. Therefore, employing an appropriate glass mask with smaller features and implementing lithographical processes would allow smaller sizes. Using electron beam evaporation can improve the surface smoothness which will consequently lead to devices with much better performances. Meanwhile, it is worth to note that creating devices with only a thin gold layer will not be suitable for biosensing applications although they might be used for applications requiring dry air. Because, the material is removed from the surface when it is introduced in liquid environment. This is due to the lack of the adhesion layer. In the meantime, employing an adhesion layer will cause distortion in the performance as was shown by Cr ⁄ Au devices with 60 μm active sizes. Nevertheless, this issue can be overcome by decreasing the feature size as was confirmed by Cr ⁄ Au devices with 10 μm active areas. The performance parameters for the devices explained in this chapter is summarised in Table 4-1.

Devices	Current-related Sensitivity
Au / Cu /Ni on PCB (1 mm size)	3 μV/AT
Au on Glass Substrate (500 μm size)	5 mV/AT
Au / Cr on SiO_2/Si Substrate (60 μm size)	3 mV/AT
Au / Cr on SiO_2/Si Substrate (10 μm size)	27 mV/AT

Table 4-1: Comparison of performance parameters for gold-based devices.

Chapter 5. Graphene Preparation

In terms of graphene, the aim was initially to prepare graphene so that it can be used to fabricate Hall sensors on a substrate. In addition, it was also aimed to prepare graphene in such a way that it can be adopted to form suspended Hall sensors. Then, the plan was to fabricate Hall devices from both suspended and supported graphene sheets and explore their behaviour in terms of sensitivity and repeatability. Therefore, different techniques such as epitaxial graphene growth on silicon carbide and CVD grown graphene were employed to prepare graphene so that it can be used to form supported and suspended structures. CVD grown graphene on copper and on polymer were employed for graphene transfer process since this method provides large area of graphene coverage. Epitaxially graphene growth method was implemented using various options to obtain high quality films with good electrical properties. This chapter presents various options that were adopted to achieve supported and suspended graphene with the feasibility along with the strength and weakness of each method.

5.1 Materials

CVD and epitaxially grown graphene sheets were initially used for graphene preparation. CVD grown single layer graphene sheet on copper (Graphene Supermarket) and on polymer (Graphenea) were used for obtaining actual suspended structures whereas other form of graphene was used to explore the feasibility of implementation. To obtain suspended graphene sheets from CVD grown graphene, pre-patterned substrates were used. To explore the manufacturability of epitaxially grown graphene, a conductive silicon carbide was used by implementing thermal decomposition and laser heating procedures.

5.2 Epitaxial Graphene

5.2.1 Thermal Decomposition

The silicon face of an n-type 4H silicon carbide sample was used to implement the growth process. The reason of employing this type of silicon carbide crystal was because of its hexagonal unit cell structure [213]. They consist of 4 and 6 bilayers of silicon and carbon atoms, respectively. The lattice structures of these types are shown in Figure 5-1.

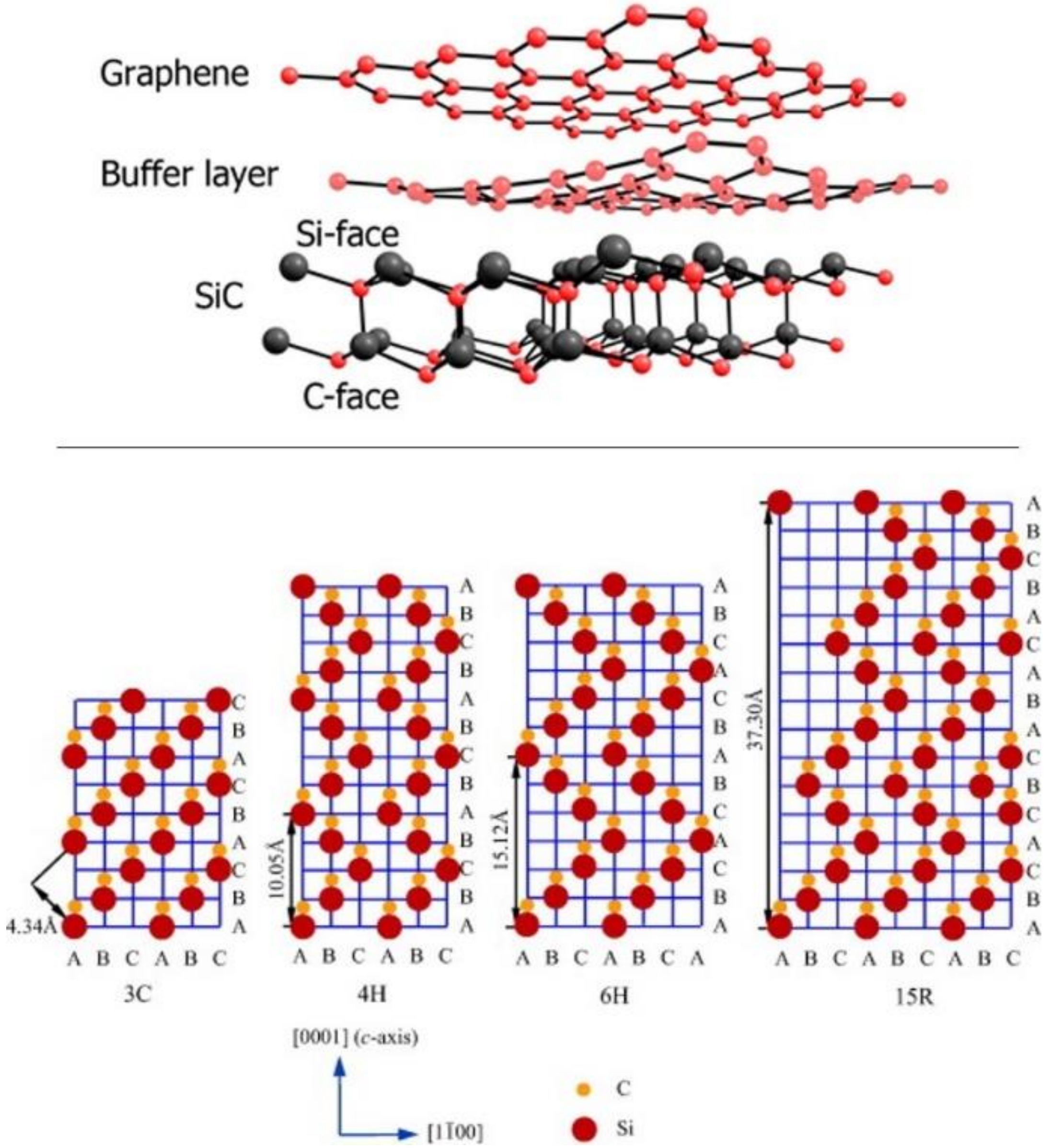

Figure 5-1: A Silicon carbide bilayer atoms and demonstration of a formed single layer graphene along with buffer layer (Top) [395]. Lattice structure for 3H-SiC, 4H-SiC, 6H-SiC and 15R-SiC (Bottom) [396].

The silicon carbide sample should not have any scratches on it for a successful growth process. Therefore, polished samples need to be used for the process. Also, the surface must be cleaned [213] for a successful growth. The surface cleaning procedure included a set of chemical process also known as RCA clean. Briefly, N-Methyl-2-pyrrolidone (NMP), isopropanol (IPA) and ultrapure water were used with the aid of ultrasonic bath for initial organic clean at 80 °C. After this initial step, the samples were further treated with piranha solution (25% hydrogen peroxide – H_2O_2, 75% sulphuric acid – H_2SO_4) and hydrofluoric acid (HF) to remove any residues. Lastly, the samples underwent final cleaning steps including ammonium solution (NH_4OH), hydrogen peroxide and buffered hydrofluoric acid. A nitrogen gun was then used to dry the samples. After cleaning the samples, an etching process was performed under argon / nitrogen (95% / 5%) gas flow for about 20 minutes in a temperature around 600 °C. Then, the growth process was done by using a high temperature furnace (JIPELEC), as shown in Figure 5-2, which was heated up to 1725 °C.

Figure 5-2: High temperature vacuum furnace (Newcastle University, School of Engineering).

The latter process was performed in two steps under high vacuum (on the order of 10^{-5} - 10^{-6} torr). First, the sample was heated up to 1200 °C for 20 minutes to allow surface reconstruction of silicon carbide. Once this process was completed, it was further heated up to 1725 °C for 1 hour to grow graphene. It was reported [214] that graphene growth rate is slower on silicon terminated face (0001) than carbon terminated face ($000\bar{1}$), thus, the graphene was grown on silicon face for obtaining potentially single layer graphene. Figure 5-3 depicts the formation of graphene both on silicon and carbon faces of silicon carbide sample.

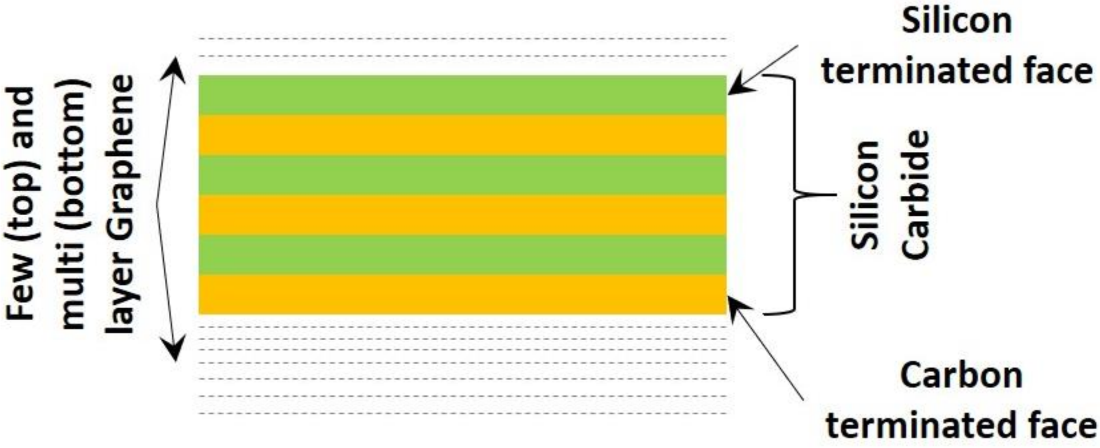

Figure 5-3: Graphene formation on both faces of silicon carbide.

The Raman spectrum shown in Figure 5-4 was taken as one scan and the arbitrary units were referenced to the same baseline. A ratio of 0.95 was calculated for 2D/G from Raman spectroscopy measurements, shown in Figure 5-4, which confirmed the existence of double layer graphene [165, 236, 237, 239, 240, 397] after implementation of thermal decomposition process. Meanwhile, the cost of the production is also important in addition of the quality. This requires alternative ways of implementations. Therefore, a relatively new technique was reported as an alternative process for obtaining epitaxial growth of graphene [258, 398-401]. Detailed exploration of this alternative method is given in the following section.

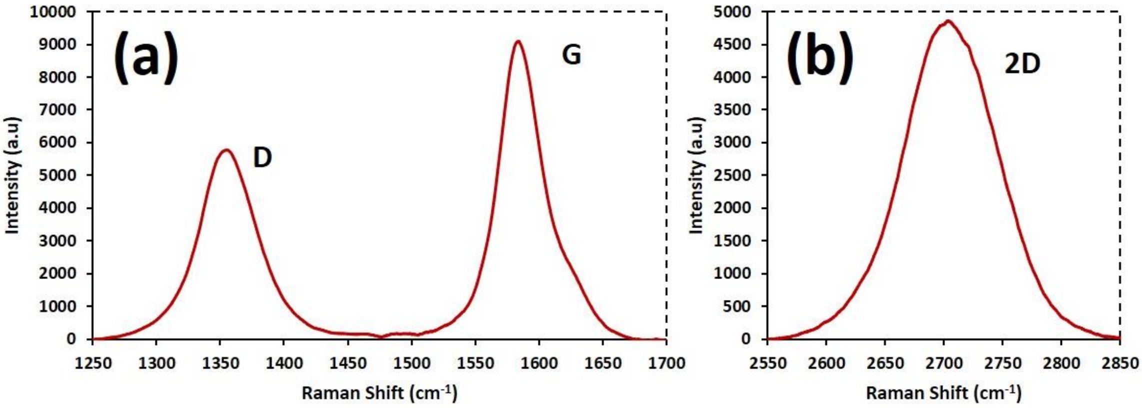

Figure 5-4: Raman spectra of epitaxial graphene on silicon carbide. D and G peaks (a) with 2D peak (b).

5.2.2 Laser Heating

Recently, promising results were reported based on laser beam irradiation [25, 398-401] for graphene manufacturing purposes. This technique provides the advantage of performing the task under atmospheric pressure and lets the formation of graphene to occur just in seconds scale. In addition, depending upon the beam size, the patterning can also be performed simultaneously during the growth process [400]. Additionally, it does not require a thorough cleaning procedure. Thus, the growth process was decided to be performed by using a laser beam as a heating source because of being cost effective, time saving and simplicity of implementation.

In order to implement such an experiment, a chamber was designed to be made of stainless steel. The cross-sectional view of the design is given in Figure 5-5 (a). This was manufactured in mechanical workshop of the School of Engineering. Basically, it has an adjustable sample holder for arranging the distance between the sample and laser source and has a sodium chloride window to prevent back reflection of the beam before it reaches the sample. Additionally, it has a pressure gauge to monitor the pressure inside the chamber as it was designed to be capable of handling a certain amount of pressure. However, it was used only with free flow of argon gas during the experiments as it has to be done in an inert atmosphere. The actual view of the manufactured chamber is shown in Figure 5-5 (b).

In a previously reported study, an n-type 6H silicon carbide sample was used and a CO_2 laser source was used to heat only a spot of beam diameter for 10 seconds [398]. However, it was not suitable for growing graphene uniformly on the substrate since the growth area was limited to the diameter of the beam size. Therefore, it was decided to scan the entire substrate using laser beam in order to have a uniformly grown graphene. To do so, a 60 W CO_2 laser cutting machine (HPC Laserscript) was used in engrave mode with a scanning speed of 300 mm/min and 80% of power to heat the entire surface of the sample. A piece of n-type 4H silicon carbide was placed on the top of the adjustable sample holder and an argon gas bottle was connected to chamber. The gas was allowed to flow freely under atmospheric pressure and the sample was scanned via laser beam for 25 times. Figure 5-6 shows the entire experimental setup including laser machine, argon gas bottle along with the manufactured chamber (inset).

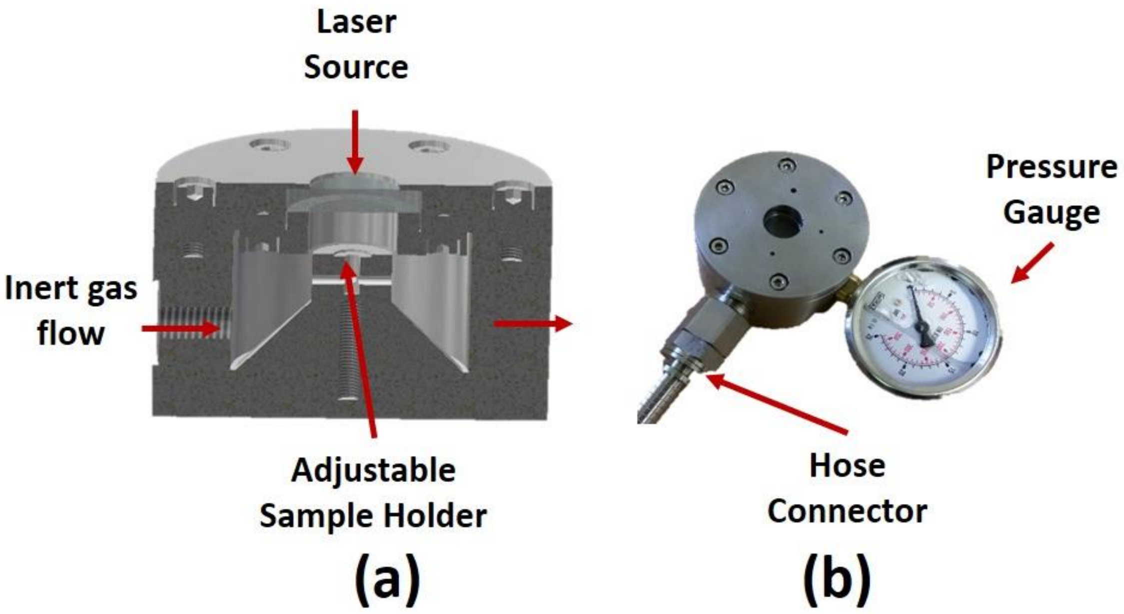

Figure 5-5: Cross-sectional view of the designed chamber for implementation of laser heating (a). The chamber was made of stainless steel and a pressure gauge was fitted with required hose connectors for gas connection (b).

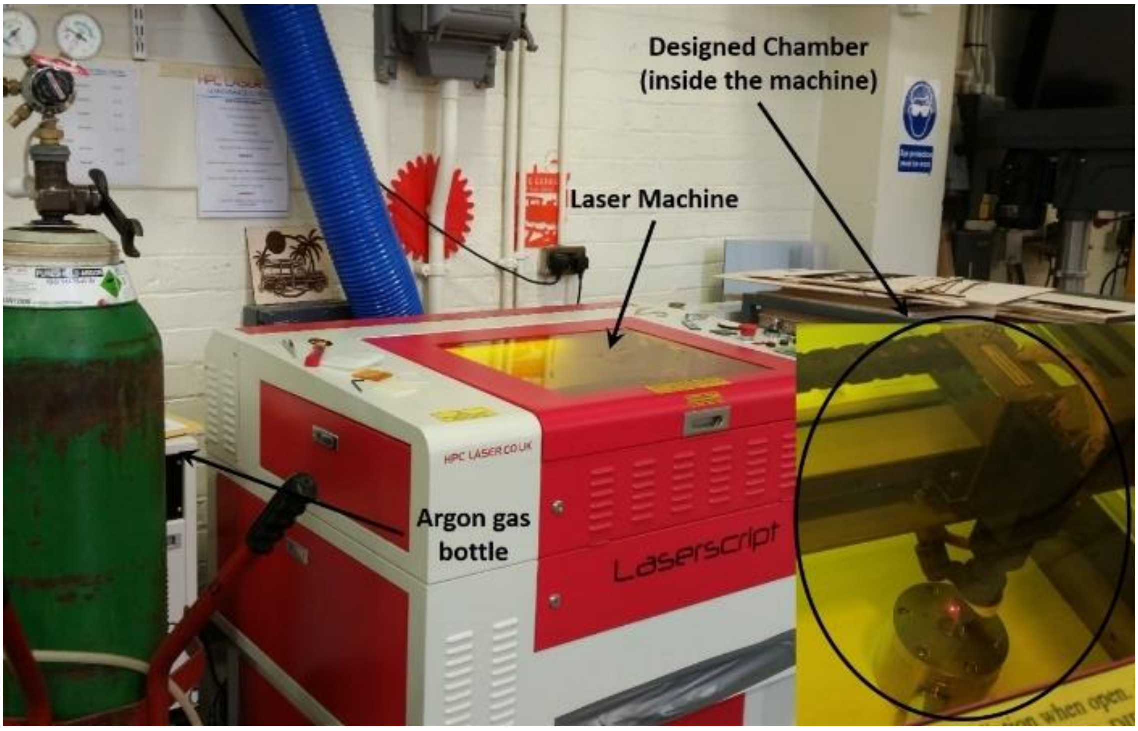

Figure 5-6: Laser heating setup.

Raman measurement, given in Figure 5-7, showed that D, G and 2D peaks of graphene were obtained. However, 2D peak of graphene had a full width half maximum of almost 180 cm^{-1} which is too broad for monolayer graphene. Meanwhile, it still has promise for graphene formation since other two peaks (D and G) are in corresponding locations and have satisfactory shapes. This could lead potentially single layer graphene on a large scale after optimizing the setup and, consequently, could either reduce the fabrication costs or reduce the time required for epitaxial growth process. Few rearrangements such as laser power, flow rate of the gas or pressurizing the chamber could make the process an applicable approach. Due to limited time of the project, the optimisation works have not been carried out.

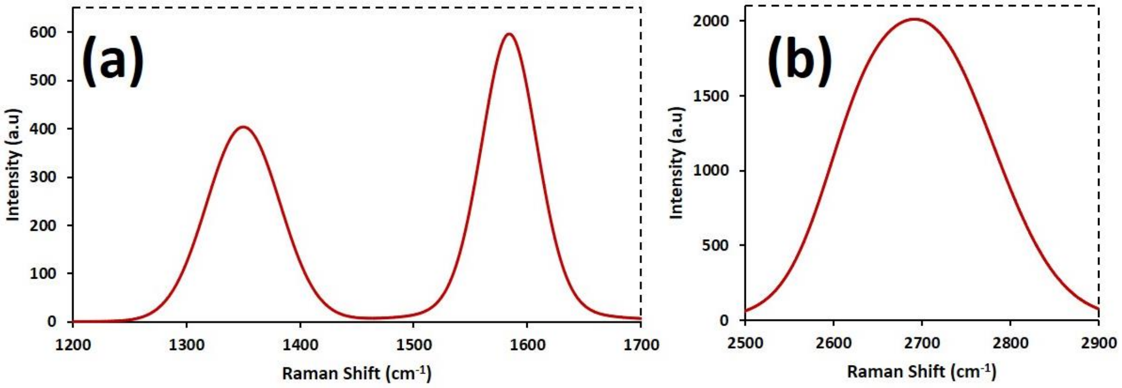

Figure 5-7: D and G (a) with 2D (b) peaks obtained from laser heated silicon carbide.

5.2.3 Silicon Carbide Etch

In the former two sub-sections, the ways to obtain epitaxially grown graphene samples was discussed along with the undertaken work to achieve it. Those samples could be used directly to form devices by masking the substrate and implementing lithography and/or a set of chemical processes. However, to have suspended graphene structures, further treatment requires to under etch respective areas on the substrate. A photoelectrochemical process has been implemented which is similar to a previously reported study [402] in order to successfully etch the silicon carbide. An illustration of the process is given in Figure 5-8.

To implement the illustrated process given in Figure 5-8, a holder was designed which consisted of slots for Fresnel lens to accommodate the best focal length and a stand for UV light source. The distance from Fresnel lens to UV source and the Fresnel lens to sample can be arranged by changing the location of lens using the slots in order to have a better focus on a specific area of interest on the sample. A 100 W mercury lamp was used as a UV light source. Fresnel lens were aimed not only to focus on a specific part but also to increase the concentration of UV light source. The setup for the experiment is shown in Figure 5-9.

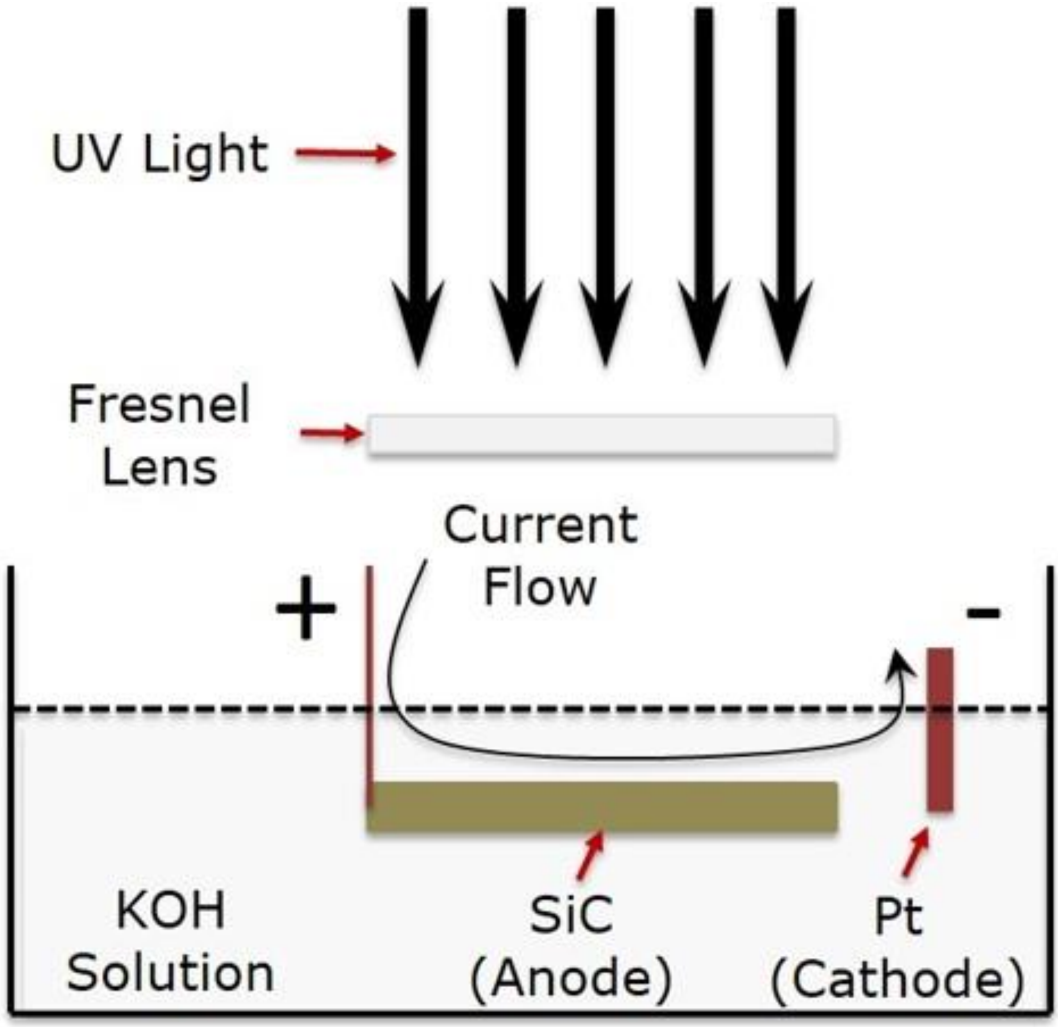

Figure 5-8: An illustration of the photoelectrochemical etching process for silicon carbide.

A chemical solution of potassium hydroxide (KOH) with 1% concentration was prepared as an etchant. To handle it during the process, a Teflon plate was used. A conductive silicon carbide sample was adhered on the surface of the plate with the aid of a nail varnish. Silver paint was used to contact the sample to current source from one of its edge. The contact point was insulated by melting a drop of wax on the silver paint in order to prevent any chemical reaction on that region.

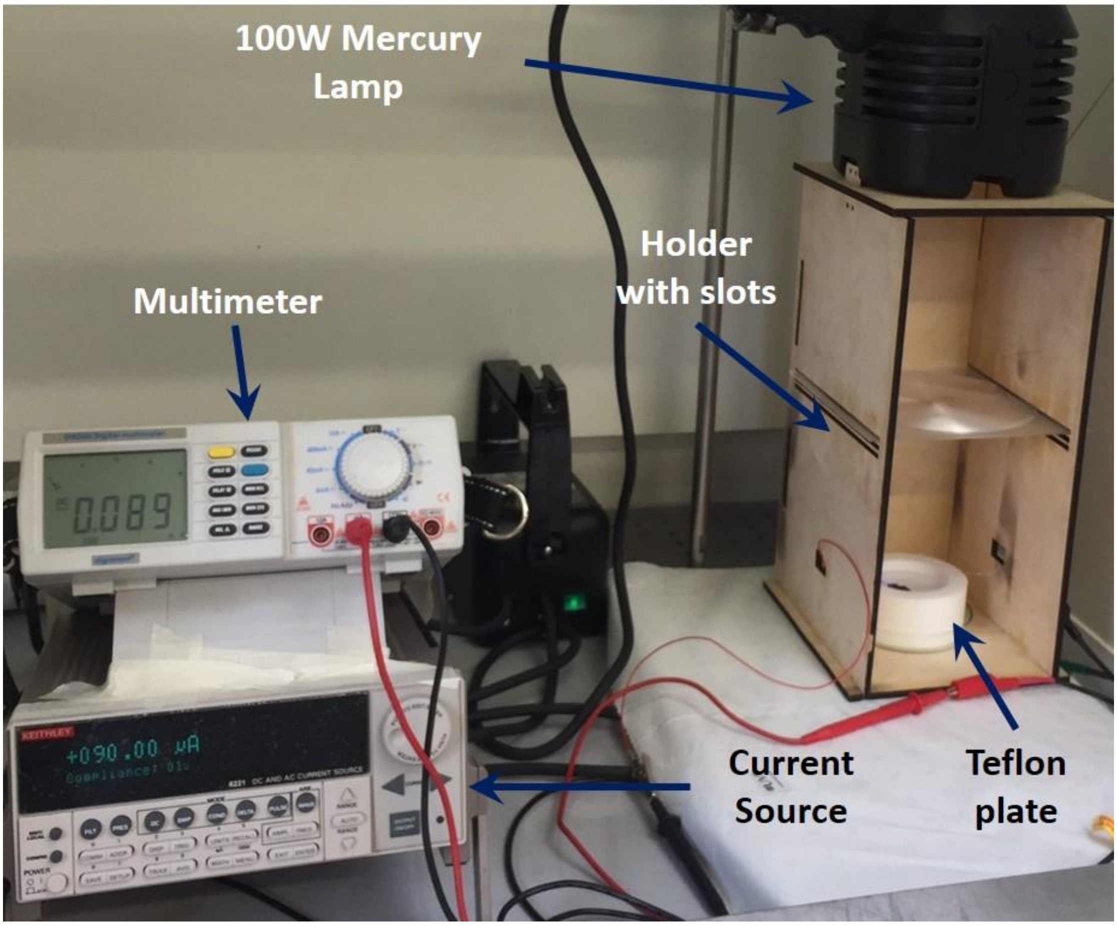

Figure 5-9: Setup for photo-electrochemical etching of silicon carbide.

A platinum wire was attached to Teflon plate and one side of it was put inside the KOH solution directly to serve as an anode contact. The current value was set to 5 mA initially and observed throughout the entire process. It was found that the current level started to decrease dramatically in the beginning and the decreasing ratio slowed down after around 20 minutes and became stable at a level of around 70 μA towards the end of the experiment. The change in the current was not reported in previously reported study, however, it was attributed as the reason of resistance change throughout the process. One of the reasons, why they did not report, might be because of only relying on the adjusted value on the source rather than observing the actual current value throughout the experiment. The etching process was performed continuously for 2 hours. The sample was then cleaned with acetone and isopropanol and rinsed with deionized water. Zygo profilometer was used to check any changes on the sample. Initial result was promising since it was confirmed that the sample was etched around 5 nm as it is seen in Figure 5-10.

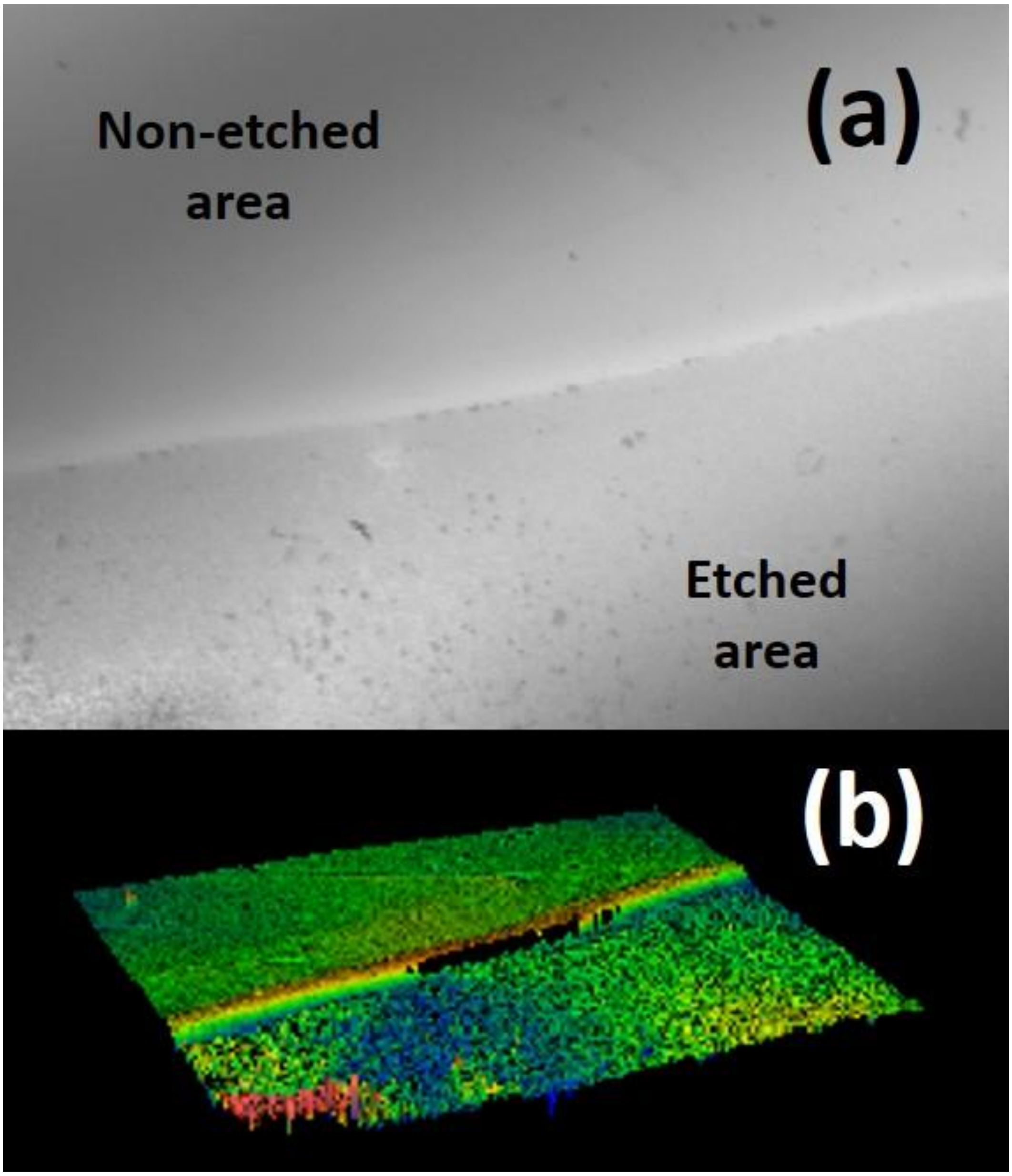

Figure 5-10: The sample was characterized using Zygo profilometer. Etched silicon carbide sample after the process (a). 3D view of the step created after etching process (b).

The same setup was used to etch an n-type semi-insulating silicon carbide sample as well. However, this type of sample did not allow the current to start at a value of 5 mA. The maximum sourced current was 22 µA, however, after 2 hours it was observed that the current limit could be increased as high as 10 times of initial value and stays stable at a value around 210 µA. This was attributed as the resistance drop as opposed to the case in the conductive sample. Nonetheless, no considerable change was observed in the latter sample after it was checked with Zygo profilometer. This was attributed to low level of current value which requires more time to achieve a considerable amount of etching.

5.3 Graphene Transfer

5.3.1 Transfer from Copper to SiO_2/Si Substrate

CVD grown graphene on copper is a method that is widely used for obtaining graphene sheets covering large areas. To take the advantage of graphene, it needs to be transferred on to a SiO_2/Si substrate. A sheet of 2 × 2 cm^2 graphene grown on copper foil was used (Graphene Supermarket) as a single layer graphene to create suspended graphene devices. The graphene sheets were transferred on a substrate which was drilled with the aid of focused ion beam milling technique. The drilling process can be defined briefly as focusing beam of gallium ions at a high beam current for opening holes on a specific area of interest [403]. Circle structures having diameters that vary from 3 μm to 5 μm along with a depth of 1 μm were designed to be created on a SiO_2/Si substrate. The drilling procedure started with covering the substrate with a thin layer of gold. Then, it was drilled with a configuration of 3 sets of 5 x 5 having 10 μm separation between each hole. As shown in Figure 5-11, the first, second and third sets consisted of 3 μm, 4 μm and 5 μm diameters, respectively. Meanwhile, the substrate having smaller holes (down to 400 nm) has also been made.

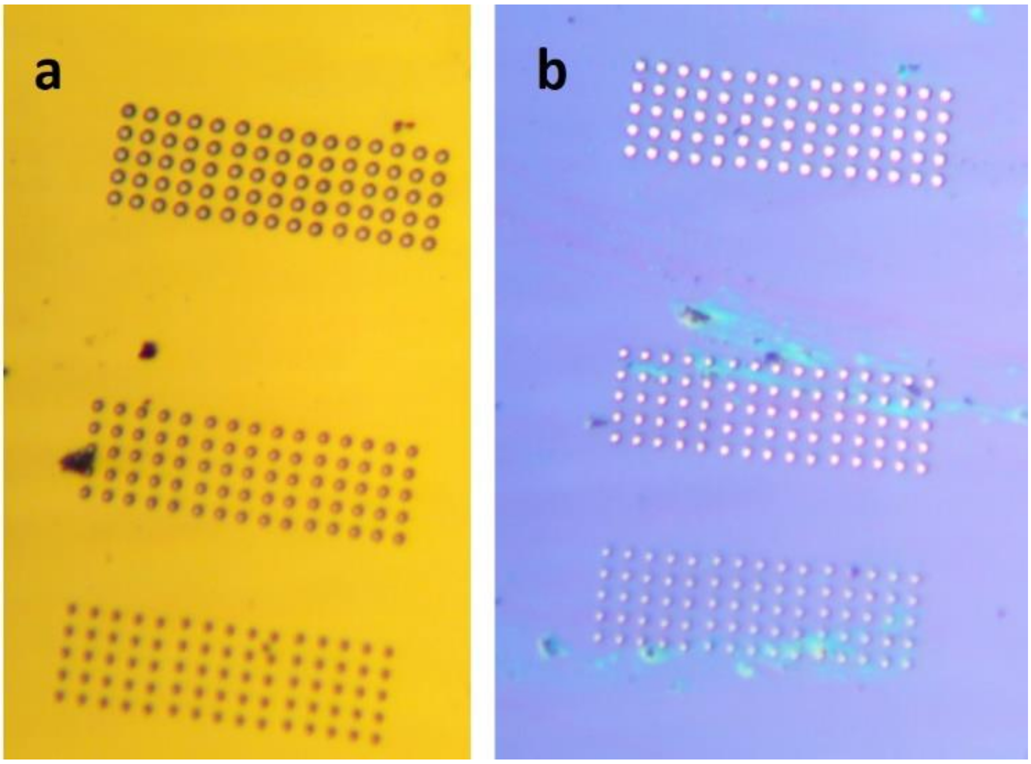

Figure 5-11: Formed features on the substrate using ion-beam milling. The surface covered with gold and drilled (a). Gold layer was etched away chemically (b).

The drilling task has been performed using facilities in Birmingham University, UK. After successful substrate drilling, the gold layer was etched, and the sample was cleaned. The gold on the surface of the substrate was removed via potassium iodide (KI) gold etchant (1:4:40 I_2/KI/H_2O) solution. After etching process, the sample was cleaned using acetone, isopropanol and piranha (a mixture of hydrogen peroxide (H_2O_2) and sulphuric acid (H_2SO_4)) solution. Then, the substrate further cleaned for any organic residuals via oxygen plasma etch. After completion of cleaning process, the substrate was dried using nitrogen gun. Figure 5-11 shows the sample with holes after drilling process (a) as well as after gold removal stage (b).

The transfer process has been performed following the cleaning procedure. This was basically implemented by using a purchased CVD grown monolayer graphene on copper (Graphene Supermarket). A thermal release tape (purchased from Graphenea as a sheet of 200 mm x 200 mm) was adhered to the copper foil which had graphene on both sides. This tape can be released in a temperature of 100 °C. A piece of double-sided tape was attached on to a glass slide and then a piece of thermal release tape was stuck on the other side of the double-sided tape where a piece of copper foil was deposited on the thermal release tape. This was pressed down firmly for 5 minutes. Then, an etchant was prepared by using 40% iron (III) chloride solution for etching the copper. The glass slide with copper attached was put into prepared solution for 50 minutes until all the copper was etched away. The slide was then placed into ultrapure water for 5 minutes and then left to dry for 1 hour. After that, it was placed onto a clean SiO_2/Si die (thermal release tape face down) and pressed firmly. The attached slide and die were placed in the oven together at 120 °C for 10 minutes until the thermal release tape became unstuck. Figure 5-12 shows them implementation of the transfer process.

Several techniques were implemented to characterize the fabricated suspended graphene devices. SEM and EDX were used to have an initial assessment of the transfer to image devices and observe the carbon atoms for validating the existence of graphene on the holes. However, imaging graphene via the available SEM was not managed.

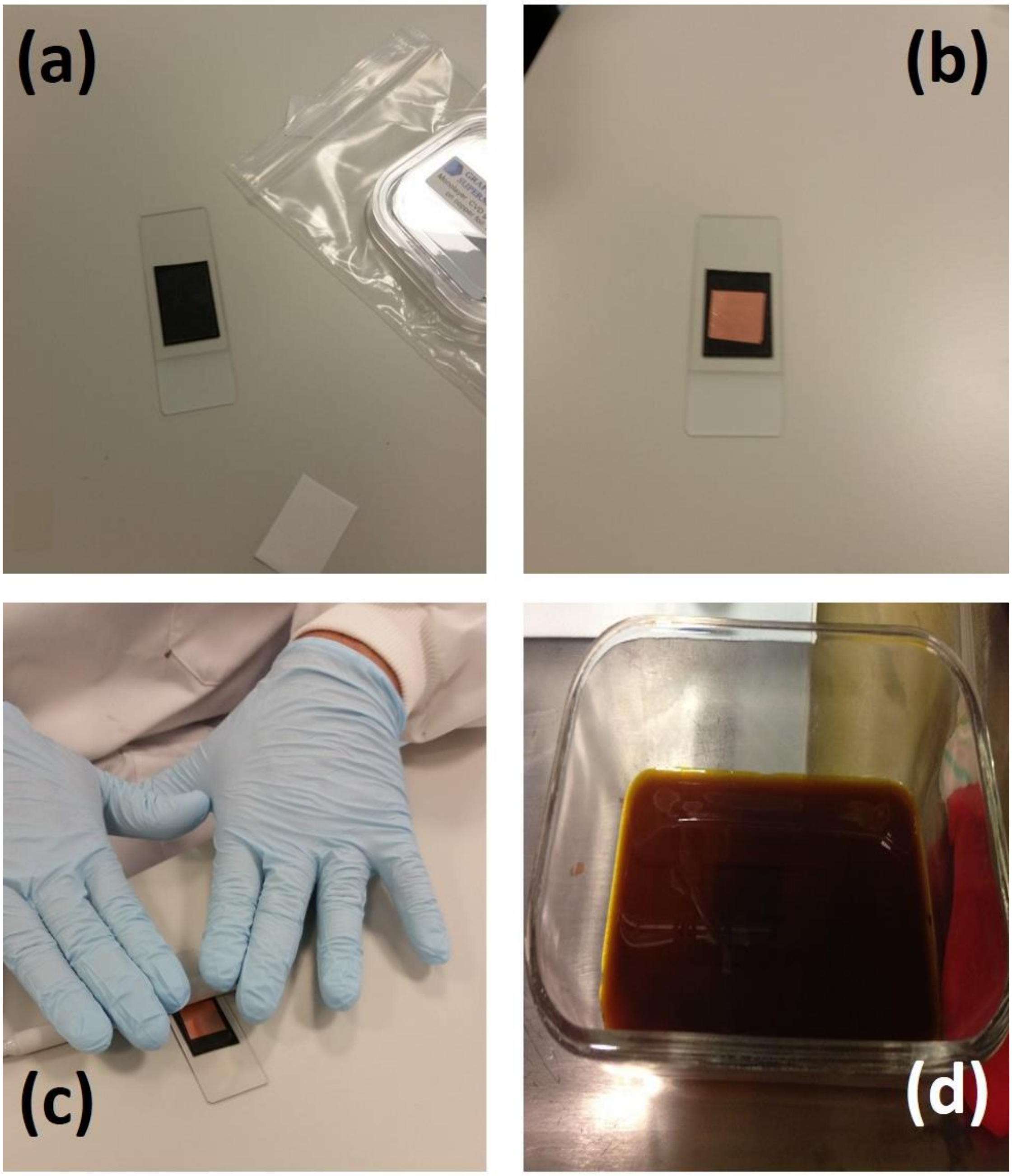

Figure 5-12: Transfer process for fabrication of suspended graphene. A double-sided tape was stuck to a piece of glass slide (a). The copper foil having graphene was stuck to a thermal release tape and put on the prepared glass (b). Then, it was firmly pressed (c). Finally, the sample was placed in a chemical etchant to remove the copper (d).

Nevertheless, the EDX result given in Figure 5-13 confirmed the existence of carbon (C) atoms, which was attributed as graphene on related regions. The other peaks related to silicon (Si) and oxygen (O) were because of the substrate. Gallium (Ga), iron (Fe) and aluminium (Al) atoms were also detected which were attributed as the elements that were used in the processes of focused ion beam milling and copper etching.

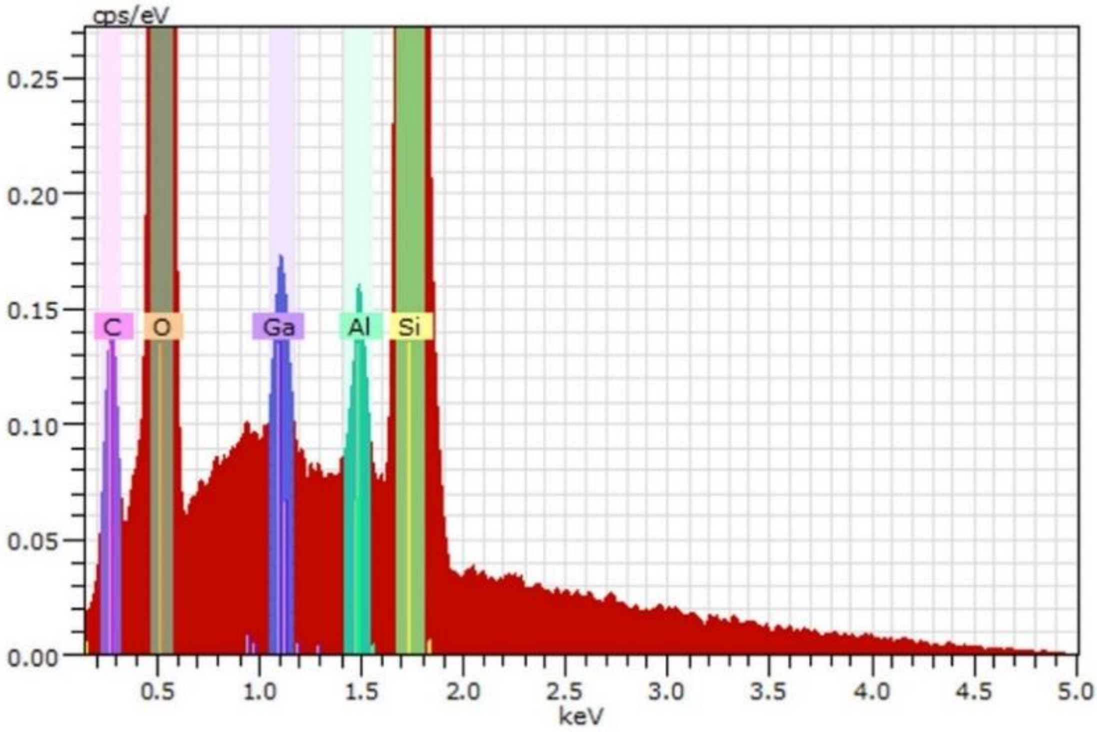

Figure 5-13: A typical EDX result on transferred graphene from copper to SiO_2/Si Substrate.

Then, sample was further characterised by Raman spectroscopy using a Horiba Yvon Raman Spectrometer with a laser excitation of 514 nm. The initial results confirmed the existence of graphene on both supported and suspended locations of the substrate. As seen in Figure 5-14 (a), a sharp 2D peak was obtained with a 2D/G ratio of 2.4 meaning that single layer graphene was obtained. Additionally, a Raman mapping was also performed on and around several holes to examine the structure for any considerable difference in Raman peaks for supported and suspended locations (Figure 5-14 (b)). This was carried out to have a better appreciation of the distribution of graphene. Therefore, a MATLAB script was used to fit the peaks and image them based on their locations and widths as well as their intensities as shown in Figure 5-14 (c-d-e). In a previous study [259], it was reported that there are differences in Raman results such as reduced energies and increased widths for suspended graphene locations for suspended portions compared to supported ones. However, they might have measured the differences due to strain or any other mechanical effect since any considerable difference was not observed in the obtained sheets in this work.

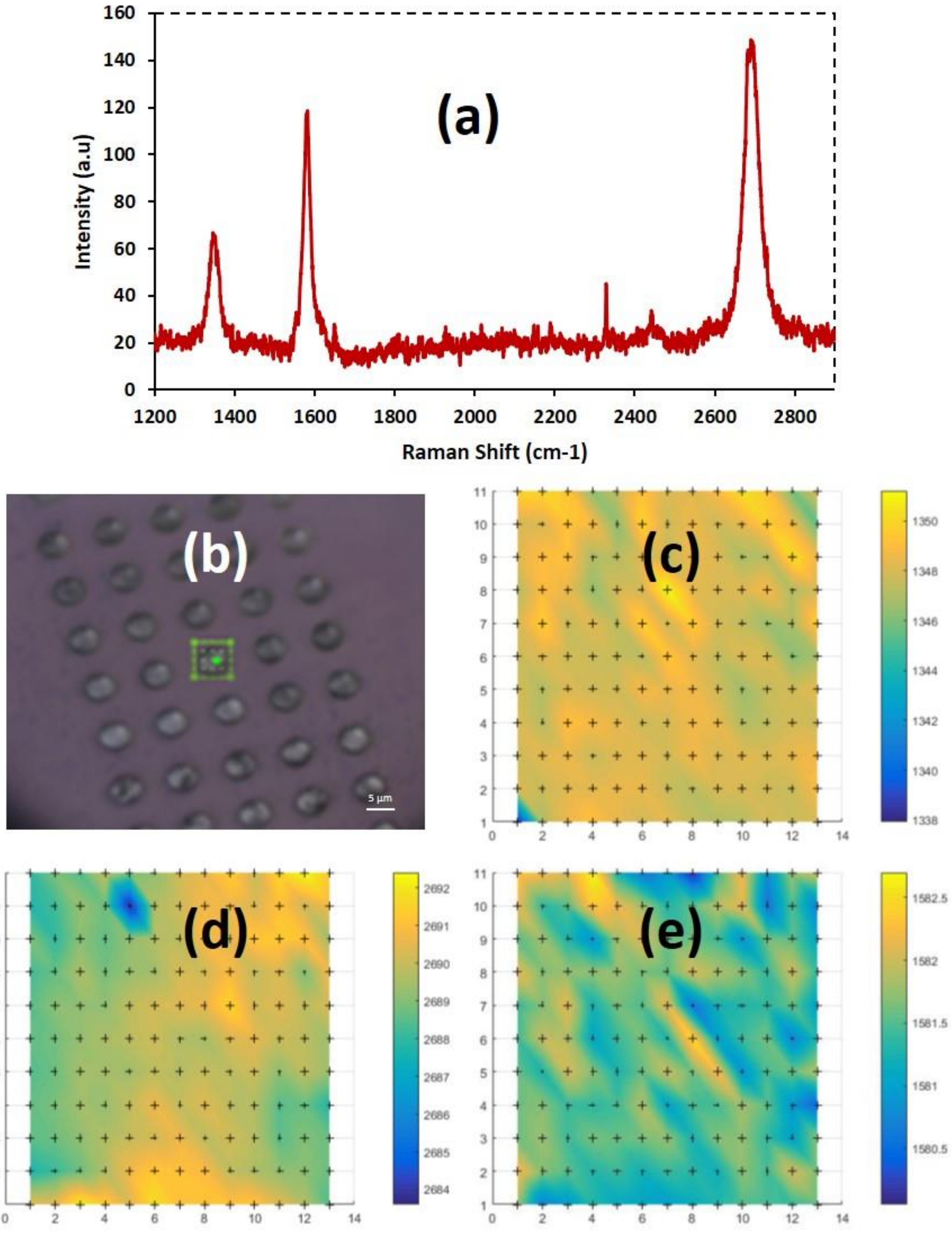

Figure 5-14: Raman mapping for the location of graphene peaks on and around a suspended structure. Typical Raman Spectra after transfer process (a). Silicon substrate with holes (b). Raman peak distribution around a hole for D (c), 2D (d) and G peaks (e). The surface was scanned with a laser having spot size of 1 µm. The hole does not appear to affect the graphene Raman spectra.

In addition to imaging the devices via Raman mapping, helium ion microscopy (ORION NanoFab – 3-in-1 Multibeam Ion Microscope for Sub-10nm Nanostructuring – see Figure 5-15) was also used as part of the visualisation process. This imaging technique allowed individual graphene flakes to be seen. This imaging technique was found to be the best solution for monitoring single layer graphene sheets amongst other methods that were mentioned so far because, it presented a clearer view of the structure even in large magnification.

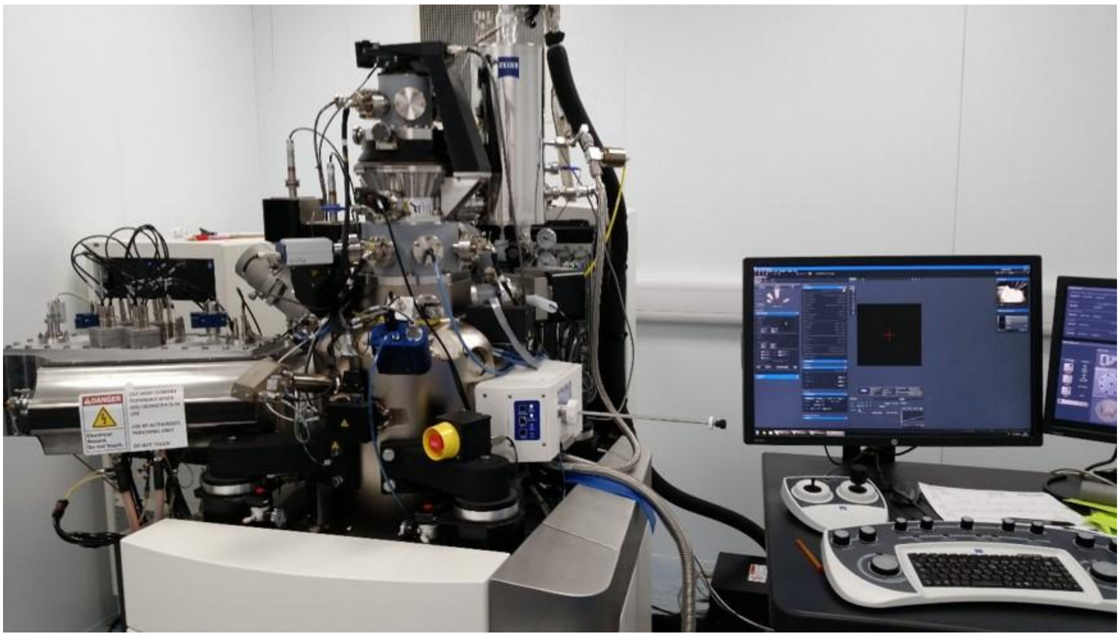

Figure 5-15: ORION NanoFab Multibeam Ion Microscope for Sub-10nm Nanostructuring (Newcastle University, NEXUS).

Graphene layers on some of the holes were found to be ruptured as pointed in Figure 5-16. This was attributed to any trapped gas inside the holes which has led to a blast because of the vacuum during imaging process. Shining bits on the supported locations are graphene flakes. The holes which are covered with graphene can easily be distinguished as shown with red circle. The illustration of the suspended structures via helium ion microscopy together with the Raman spectroscopy confirmation proved the successful achievement of the suspended graphene structures. The obtained suspended graphene structures could then be patterned with the aid of an appropriate mask and lithographic process to form desired Hall devices. Undesired parts of the graphene can easily be removed via oxygen plasma etch.

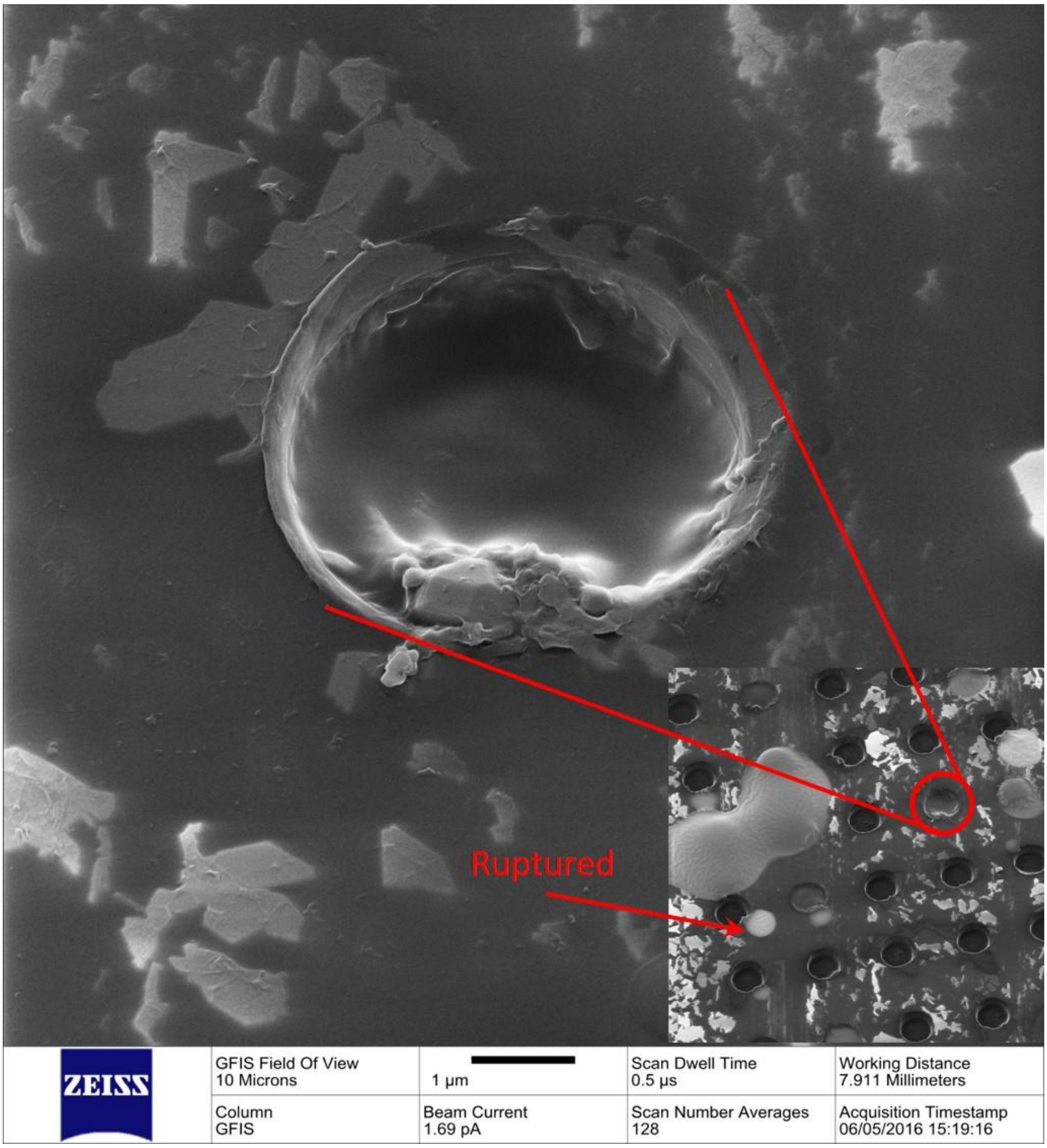

Figure 5-16: Helium ion microscope image of suspended graphene sheets.

5.3.2 Transfer from Polymer to SiO_2/Si Substrate

As a newly developed method (Graphenea), easy transfer monolayer graphene form provides easier transfer option and prevents from using dangerous chemicals explained above. The structure consists of three layers as shown in Figure 5-17 (a). Instead of a copper foil, this type of graphene comes on a polymer layer. The graphene is also protected with a sacrificial layer that is placed on top of it. Employing this type of graphene provides more flexibility and eliminates exhausting chemical processes to etch copper, clean surface and perform the actual transfer operation as described in section 5.3.1.

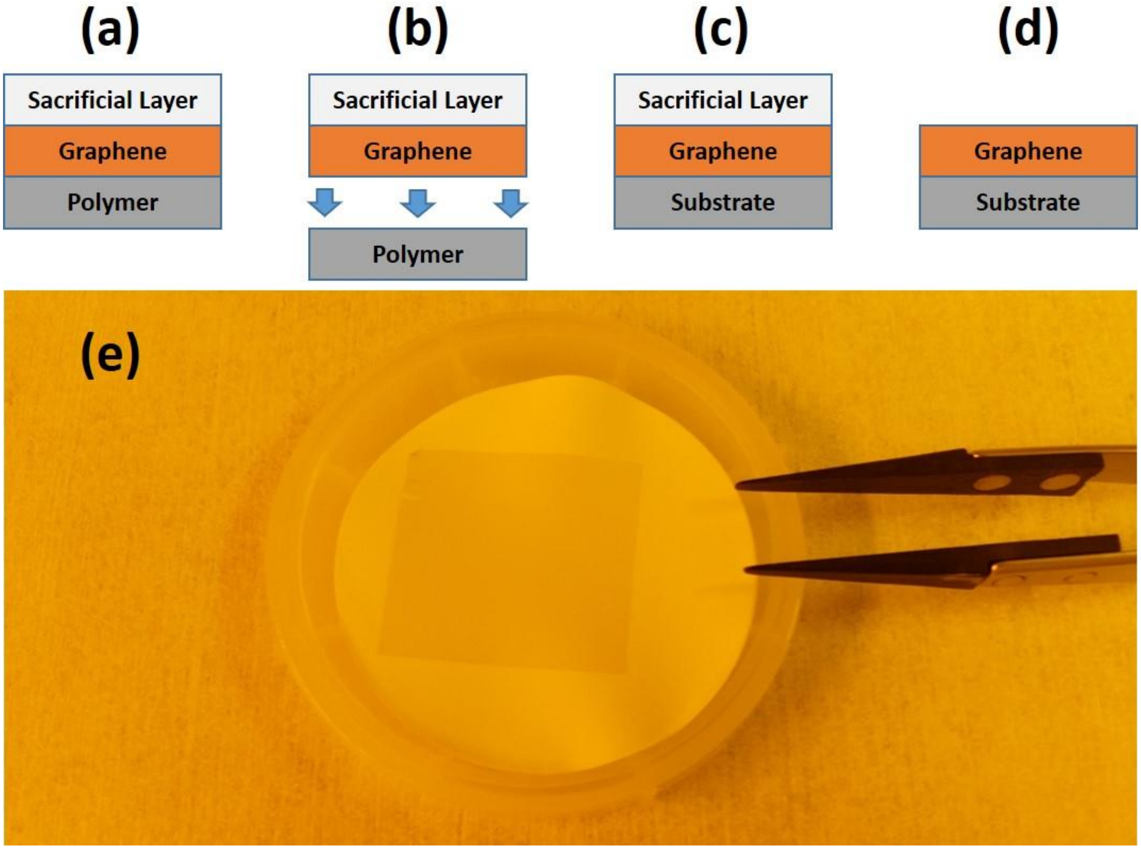

Figure 5-17: Easy transfer monolayer method. Graphene is in between a polymer and sacrificial layer (a), polymer is removed via deionized water (b), Substrate is introduced (c) and the sacrificial layer is removed (d). 1 × 1 inch2 graphene film on polymer (e).

To perform the transfer process, silicon substrates were prepared to have rectangular trenches which are continuous along the sample lateral size. Creating these features instead of holes was because of avoiding any rupture that was explained in section 5.3.1. Four rectangular geometries (1.5 mm wide and 9 mm long) were prepared to have a separation distance of 0.5 mm between each and made by using the facilities in Birmingham University, UK. Each of the four rectangles had depths of 20 μm.

A monolayer graphene film in between a polymer and sacrificial layer with a dimension of 6.5 × 6.5 cm^2 was used for performing transfer process. The polymer layer was detached easily only by putting the structure in deionized water (Figure 5-17 (b)). Then, graphene and sacrificial layer was floating on the surface of water once the polymer was removed. The transfer was achieved by introducing the substrate in the water and fishing the floating graphene with sacrificial layer (Figure 5-17 (c)). The substrate was then taken out of the water and left in air for 30 minutes to let it dry (Figure 5-17 (d)). After that, a hot plate with a temperature of 150 °C was used to anneal the substrate in order to allow better adhesion. The actual view of substrates with graphene and sacrificial layer after initial annealing process is depicted in Figure 5-18.

Figure 5-18: Graphene samples with sacrificial layer on the substrates after initial annealing process at 150 °C using hot plate.

To improve the adhesion, the samples were placed in vacuum and kept for 3 days. Then, the samples were annealed at 450 °C under nitrogen flow for at least 2 hours to remove the sacrificial layer (suggested by the supplier – Graphenea). Meanwhile, the removal could have also been performed by implementing wet chemical treatments, however, since there were trenches on the substrate, it might have caused the suspending graphene portions to adhere the sides and the bottom of the trenches, thus, preventing the formation of suspended structures. Therefore, high temperature treatment was considered as a safer way of implementation.

The samples were imaged using helium ion microscopy following the removal of sacrificial layer. Initial assessment verified the formation of suspended graphene sheets as shown in Figure 5-19. Examining the surface via this method showed that the formation is arbitrary instead of continuous coverage. This was attributed to excessive trench widths (1.5 mm wide) which causes fractures in the graphene. However, this method was proved to be feasible and a safer way of obtaining suspended graphene sheets. To achieve a higher coverage, the width of the trenches should be reduced so that the fracture is prevented.

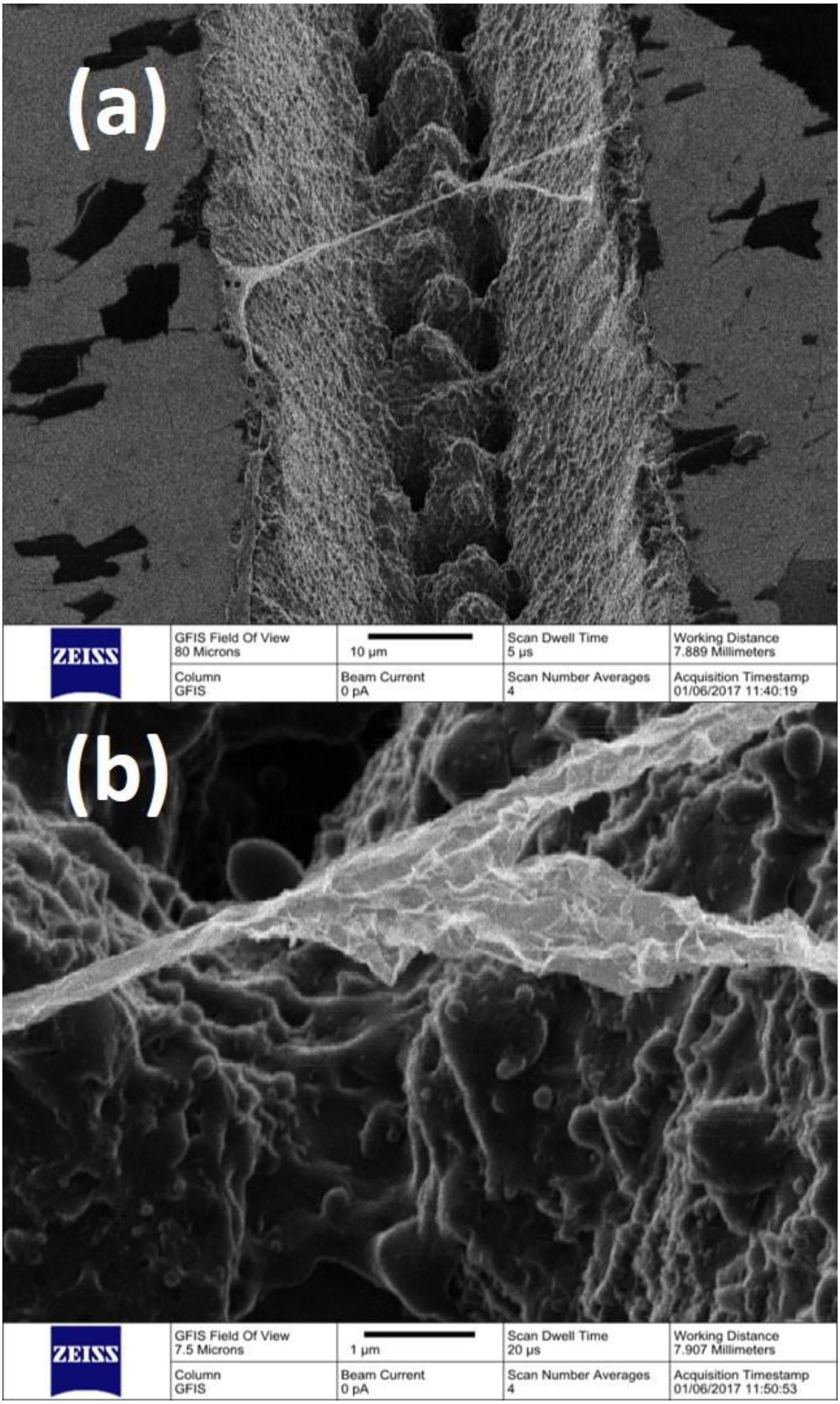

Figure 5-19: Suspended graphene on a pre-created trench (a). A closer view showing wrinkled graphene sheet (b).

5.4 Summary

The initial assessment for silicon carbide suggested that the methodology given under section 5.2.2 has potential for graphene production as a cheaper and faster way of implementation. The undertaken work regarding silicon carbide etch showed the promise for suspended sheet formation. However, achieving an optimum solution for graphene formation and suspension would require a significant amount of time which was beyond the time allowed for this study. Therefore, the optimization work has been left for the following future projects.

Although suspended graphene is shown to be feasible following different techniques using CVD grown graphene (given under section 5.3), there was not enough project time to optimise the presented methods for suspended sensors. Therefore, the work focused on buying commercially available CVD grown graphene samples on SiO_2/Si substrates. The details about device fabrication using commercially available CVD grown graphene samples is presented in the following chapter. The next chapter is also presenting an alternative way of obtaining suspended graphene structures during microfabrication which may eliminate the steps requiring for graphene preparation.

Chapter 6. Graphene Hall Devices

The main focus of fabricating Hall devices was to use CVD grown graphene, on a Si/SiO_2 substrate. Commercially available graphene samples were purchased, and different microfabrication processes were defined to achieve micron-sized Hall devices. Moreover, the defined procedures were arranged so that it may also be used for suspended devices, if required in future applications. In addition, reduced graphene oxide printed on a glass substrate was also explored as an easier and cheaper fabrication approach. This chapter presents, design and manufacture steps to obtain graphene micro-Hall devices by following different techniques along with the obtained results.

6.1 Design

Two different microfabrication processes were designed to allow the fabrication of graphene Hall devices. The first method was designed to be performed by employing a protective layer whereas the second approach was designed to perform microfabrication without coating the surface with a protective material. In addition to those two approaches, an alternative way of device fabrication was also planned for microfabrication by adopting printed graphene oxide for direct patterning of devices without need for additional procedures.

For the first method, a mask having the same design presented in section 4.1 was used (gold-based devices on silicon substrate). However, an optional layer for oxide etch was included to this mask. As opposed to potential ways for obtaining suspended graphene sheets presented in Chapter 5, an additional insulation layer was designed on the mask to allow a second way of implementation for obtaining potential suspended structures after device fabrication. The third layer on the mask were created to avoid further treatment after graphene preparation which may provide more robust solution for future projects. However, this would require a careful planning and handling since dangerous chemicals such as hydrofluoric acid is needed. Moreover, additional features as depicted in Figure 6-1 was also placed on the mask so that the substrate can be patterned chemically for graphene transfer applications. The latter features were designed to create an alternative option for focused ion beam milling technique. This mask was designed to perform microfabrication on a die scale.

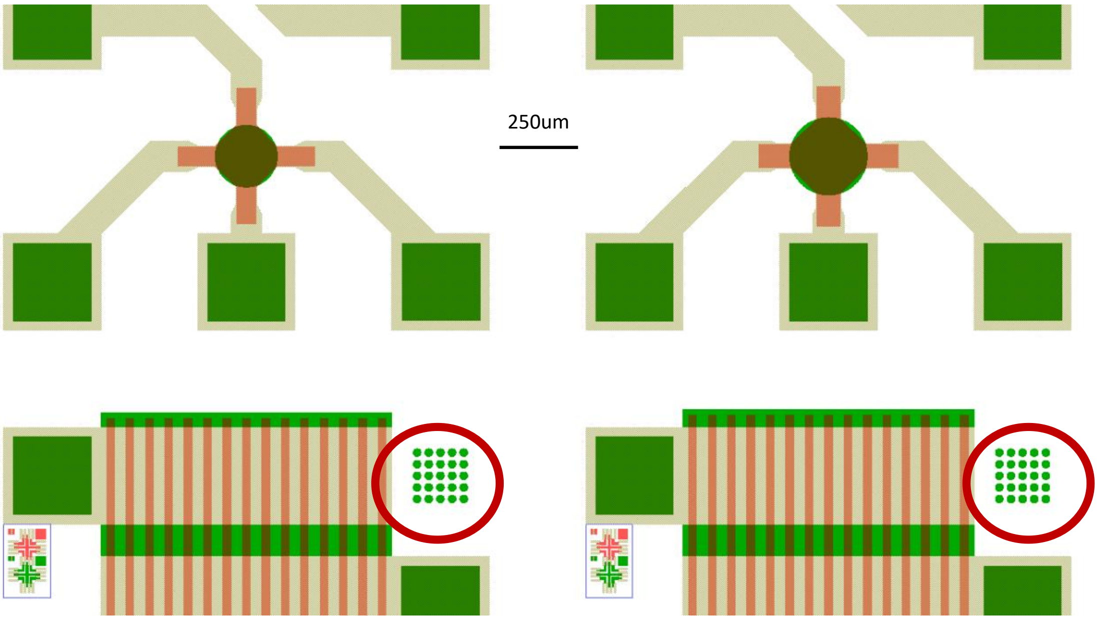

Figure 6-1: Designed mask with additional features to allow implementation of further fabrication. The features encircled with red are for creating the holes and then transfer graphene to form suspended structures.

In addition, a wafer scale manufacturing procedure was also designed to achieve bulk fabrication. To do so, another mask was designed which includes several cross structures having active areas of 10 μm, 20 μm and 40 μm. Figure 6-2 shows layout of an individual die of 5 × 5 mm^2 placed on the mask. The latter mask was made of plastic and designed to form devices to allow the wire bonding of the contacts on a chip and make insulation easier. This mask was also created to be used for manufacturing devices without any protective layer. Moreover, the features on the mask was arranged so that the fabricated devices can perform within a liquid medium for biosensing applications.

Apart from the first two methods, printing graphene oxide was planned to be used as an alternative and cheaper way for device fabrication. In terms of material point of view, the latter approach may not be the best option for Hall device manufacturing, however, biosensors with better performances could be obtained.

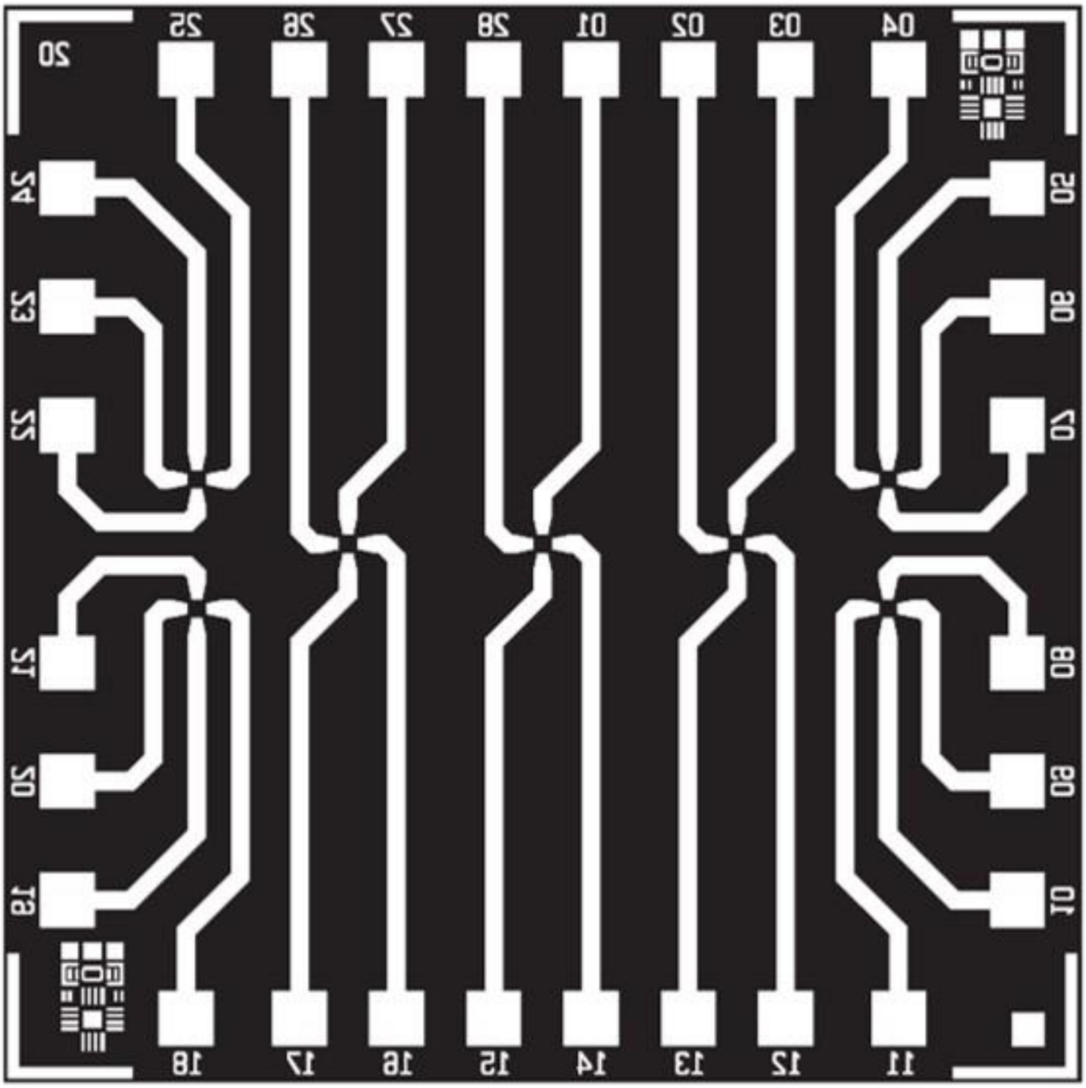

Figure 6-2: Layout of an individual 5 mm × 5 mm die on a 4-inch mask for wafer-scale fabrication.

6.2 Materials

CVD grown single layer graphene samples on SiO_2/Si substrate Graphenea (had a substrate thickness of 525 μm with an oxide layer of 300 nm) and Graphene Supermarket (had a substrate thickness of 525 μm with an oxide layer of 285 nm) were used for microfabrication of Hall devices. The reason of using CVD grown graphene was because of its high-quality electrical properties and large area coverage (>95%). The samples from Graphenea were used for microfabrication using a protective layer whereas the samples from Graphene Supermarket were employed for implementation of microfabrication with no-protective layer. Moreover, multilayer graphene samples (Graphene Supermarket) were also used to manufacture devices without adopting a protective layer. Besides, graphene oxide (Graphenea) was employed as an alternative approach to achieve an easier fabrication method to manufacture devices.

6.3 Fabrication

To obtain devices out of graphene, the substrate needs to be masked and be exposed to lithographic and chemical processes. The following sections provides information about several steps that were undertaken to achieve microfabrication. Most of the fabrication process took place in clean room environment. However, the works related to derivatives of graphene were partly performed outside of the clean room using different laboratories within the School of Engineering and the Institute of the Cellular Medicine. Figure 6-3 shows some of the laboratories used for fabricating devices.

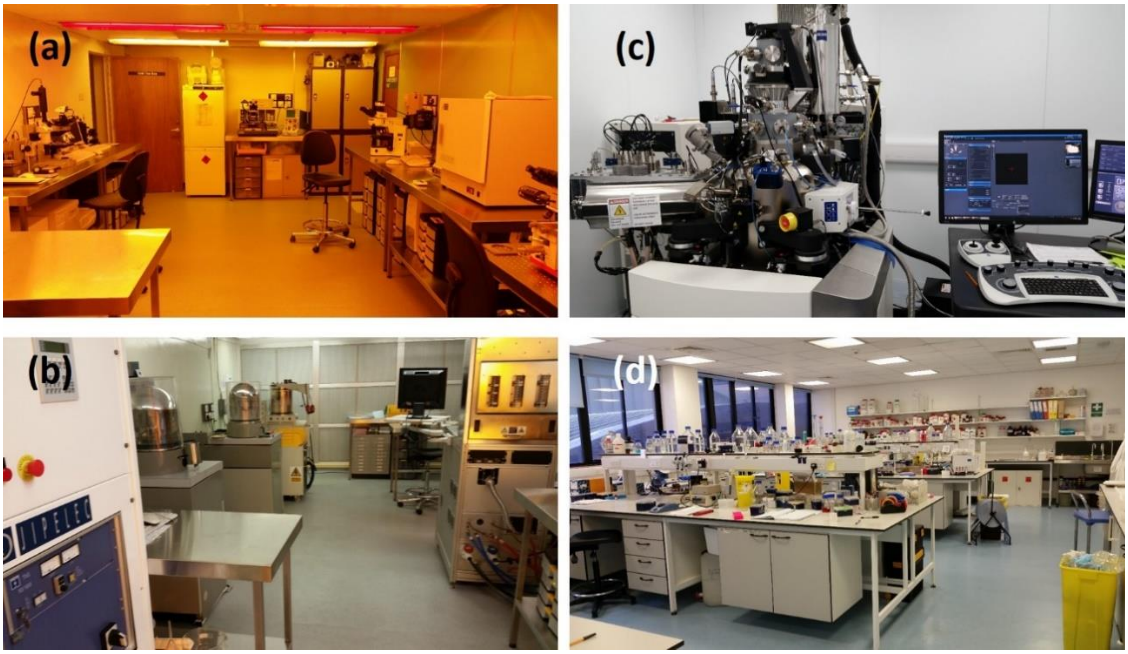

Figure 6-3: Partial views from some of the labs used for fabrication. Clean room facilities for lithographical (a) and thermal processes (b). Nexus facilities for nano-scale fabrication and imaging processes (c). Facilities under Institute of Cellular Medicine for surface modification and bio-measurements (d).

Two microfabrication routes were defined for manufacturing devices using monolayer graphene samples. The initial work carried out by adopting a protective layer using titanium as a cover. This was followed by fabrication process without employing a protective layer which was demonstrated to be easier and more robust. Multilayer graphene devices were also manufactured following the route for no-protective layer. In terms of derivatives of graphene, devices were manufactured with reduced graphene oxide by directly printing them on a glass substrate. This had then reduced chemically to obtained devices from reduced graphene oxide.

6.3.1 Monolayer Graphene Using Protective Layer

Due to issues related to visualising graphene under optical microscope, a layer of titanium was decided to be employed for covering the surface of graphene, initially. The aim was to make formed structures easy to see during the fabrication. In addition, graphene would have been protected during wet chemical processing. Moreover, it was thought to provide an adhesion layer for the contacts, as well. Therefore, the surface was covered with 15 nm titanium using e-beam evaporator shown in Figure 6-4 (Edwards 306 e-beam evaporator).

Figure 6-4: Edwards 306 e-beam evaporator in CLR4 (Newcastle University, school of Engineering).

After titanium evaporation, the plan was to etch the titanium using buffered hydrofluoric acid (BHF with a concentration of 5:1) as is defined in Figure 6-5 to remove areas not required for device formation. Graphene was planned to be used for protecting the underlying oxide layer since it was shown to be resistant to BHF [175, 404]. The rest of the steps were planned as graphene etch, photoresist spin, lithography, developing photoresist, chromium/gold evaporation and lift-off for obtaining complete set of devices. The devices should have been successfully manufactured up to this point (up to step 10, see Figure 6-5). To allow the formation of suspended structures, devices were planned to be further processed by implementing the remaining steps shown in Figure 6-5 by exposing the substrate to further wet chemical etching process mainly using BHF.

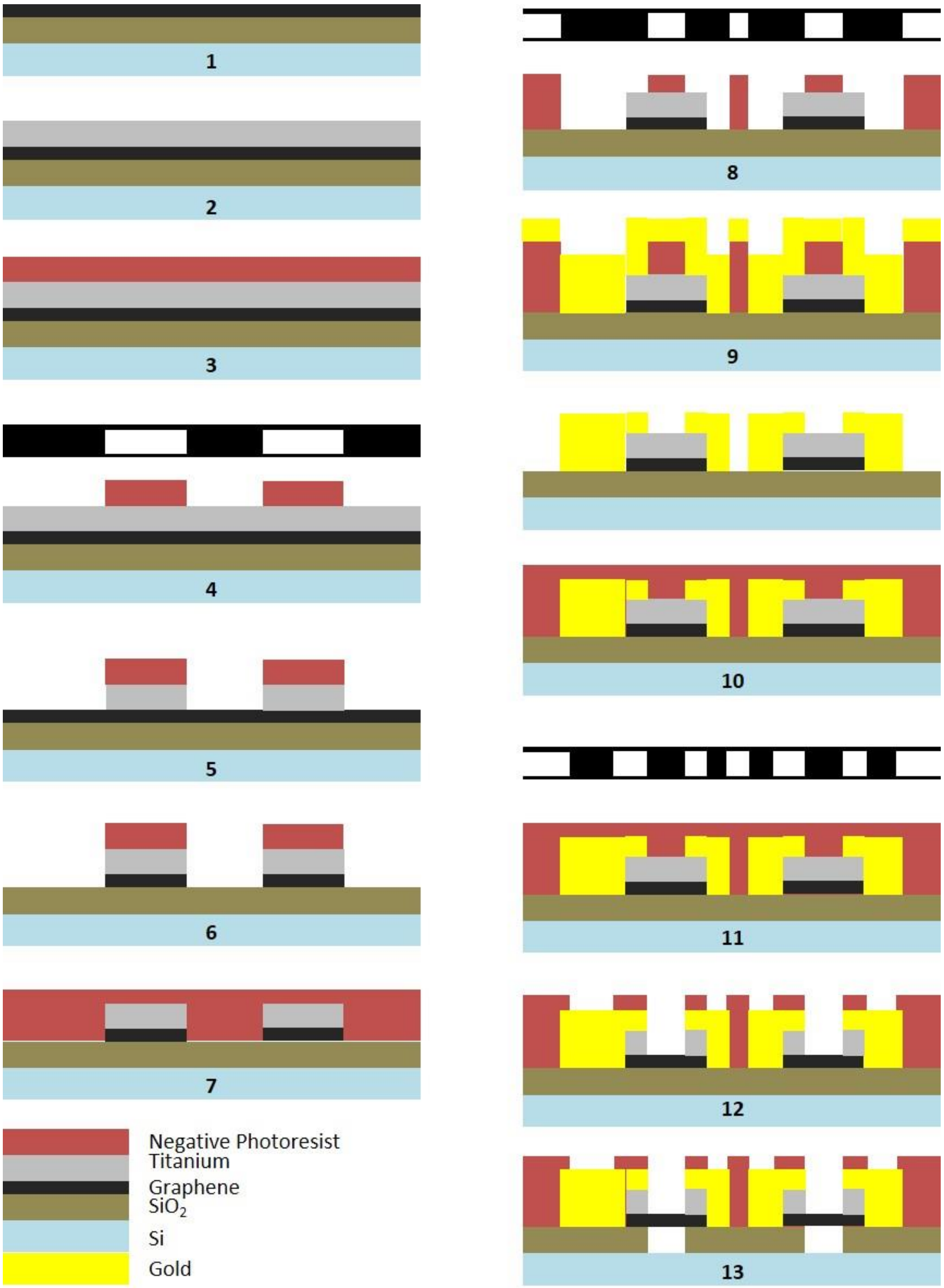

Figure 6-5: Microfabrication process. (1) CVD graphene on a SiO_2/Si Substrate. (2) Titanium deposition. (3 & 4) Photoresist cover and developing it for forming device structures. (5) Etching titanium. (6) Graphene etch. (7 & 8) Photoresist cover and developing it for forming contacts. (9) Chromium and gold evaporation using e-beam. (10) Lift-off. (11) Photoresist deposition. (12) Lithography. (13) Titanium etch. (14) SiO_2 etch. The steps from 1 to 10 is designed for forming supported devices whilst the rest of the steps are further steps for forming suspended structures.

After titanium coverage, the substrate was spun with photoresist (AZ5214E image reversal resist), using EMS 6000 Spin Coater (Figure 6-6 (a)), and the lithographical process was performed via Karl Suss MJB-3 Mask Aligner (Figure 6-6 (b)).

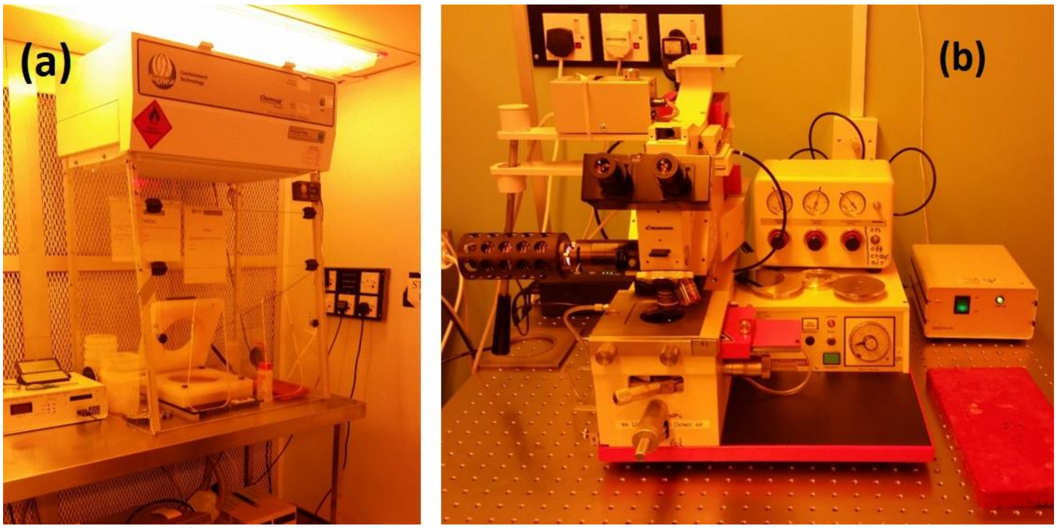

Figure 6-6: Spin coater (EMS 6000) (a) and mask aligner (Karl Suss MJB-3) (b) (Newcastle University, school of Engineering).

A spin speed of 4300 rpm was used to coat the surface of the sample with 1 μm thick photoresist. This was pre-baked for 10 minutes at 90 °C and then exposed to UV for 4 seconds. This procedure followed by a post-bake step which took place on a hot plate for 30 seconds at 120 °C. A final UV exposure was performed for 8 seconds to obtain features on the surface. Figure 6-7 shows an optical microscopy image of the substrate with titanium layer (a) and the formed geometries after resist development. The process was shown to be fully successful up to the first resist development stage.

After lithography process, titanium was etched chemically using HF for removing the locations not required for device formation. However, it was found that most of the substrates were cleared, as shown in Figure 6-8 (a), which was attributed as a consequence of oxide layer etch by HF. The graphene on the remaining parts of the samples was observed to be mostly delaminated (Figure 6-8 (b)). Employing HF to etch titanium yielded only a small number of survived features (Figure 6-8 (c)).

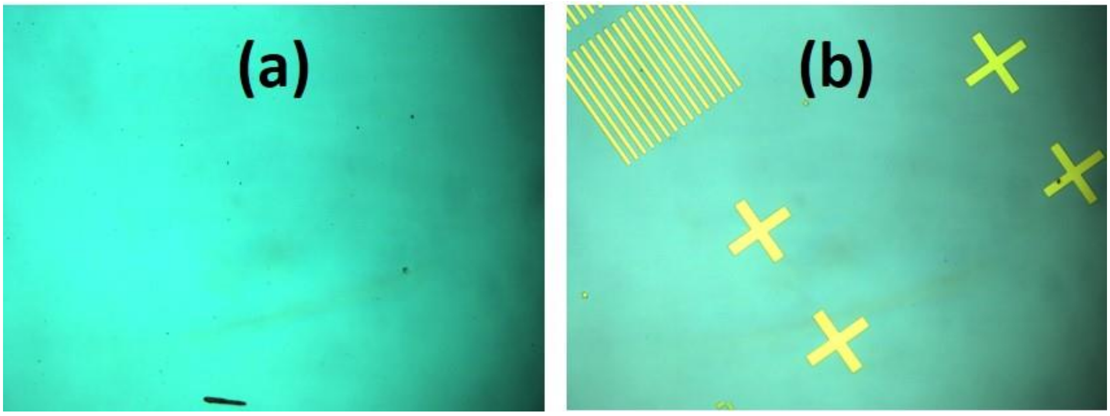

Figure 6-7: Optical microscopy images of microfabrication process using titanium as a cover. The substrate was covered by evaporating titanium (a). Created structures after lithography (b).

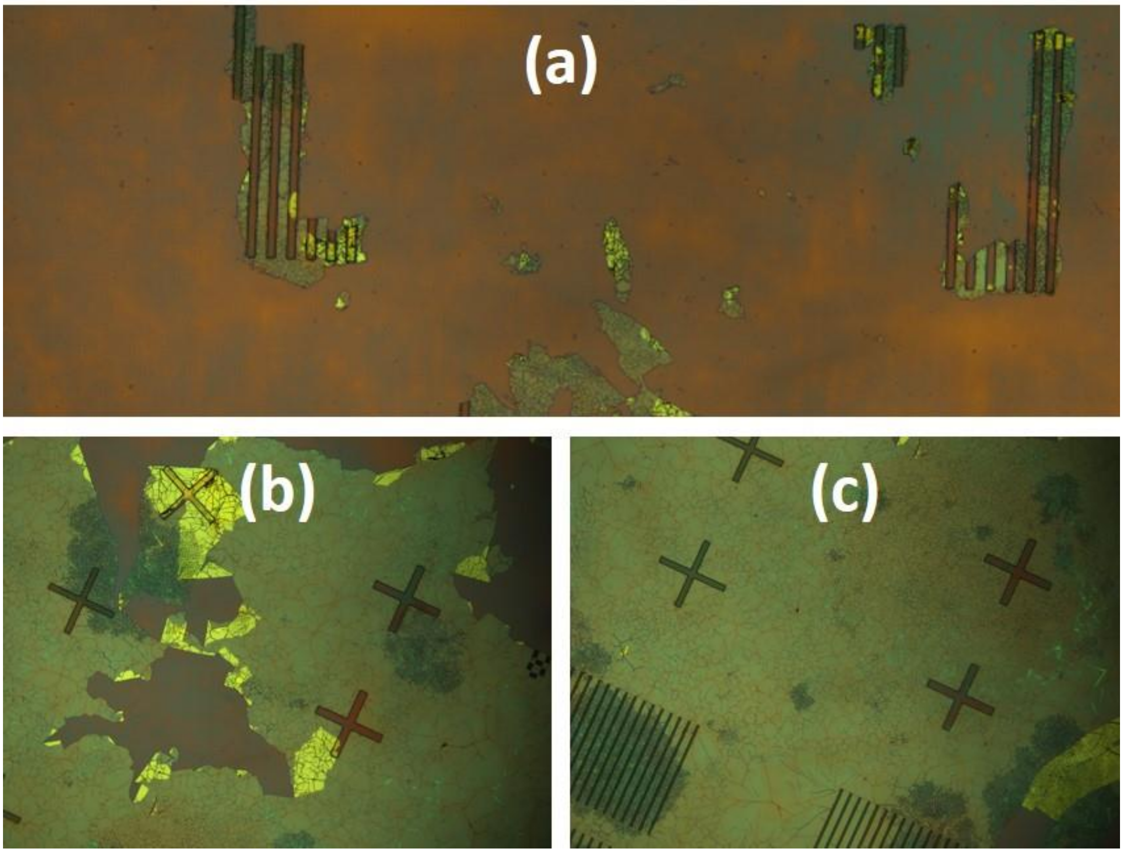

Figure 6-8: Wiped (a), delaminated (b) and partially obtained structures after titanium etch (c).

Meanwhile, successfully survived features were characterised for existence of graphene, thus, SEM imaging with EDX was performed using a bench-top SEM Microscope (Hitachi Tabletop TM3030) as shown in Figure 6-9. SEM images clearly showed the remaining patterns and the EDX results suggested that there were some bits of the titanium around the surface of the substrate which means few more seconds require for wet chemical etching process. However, it was observed that exposing the substrate to HF for a bit longer time eventually caused the features to be wiped.

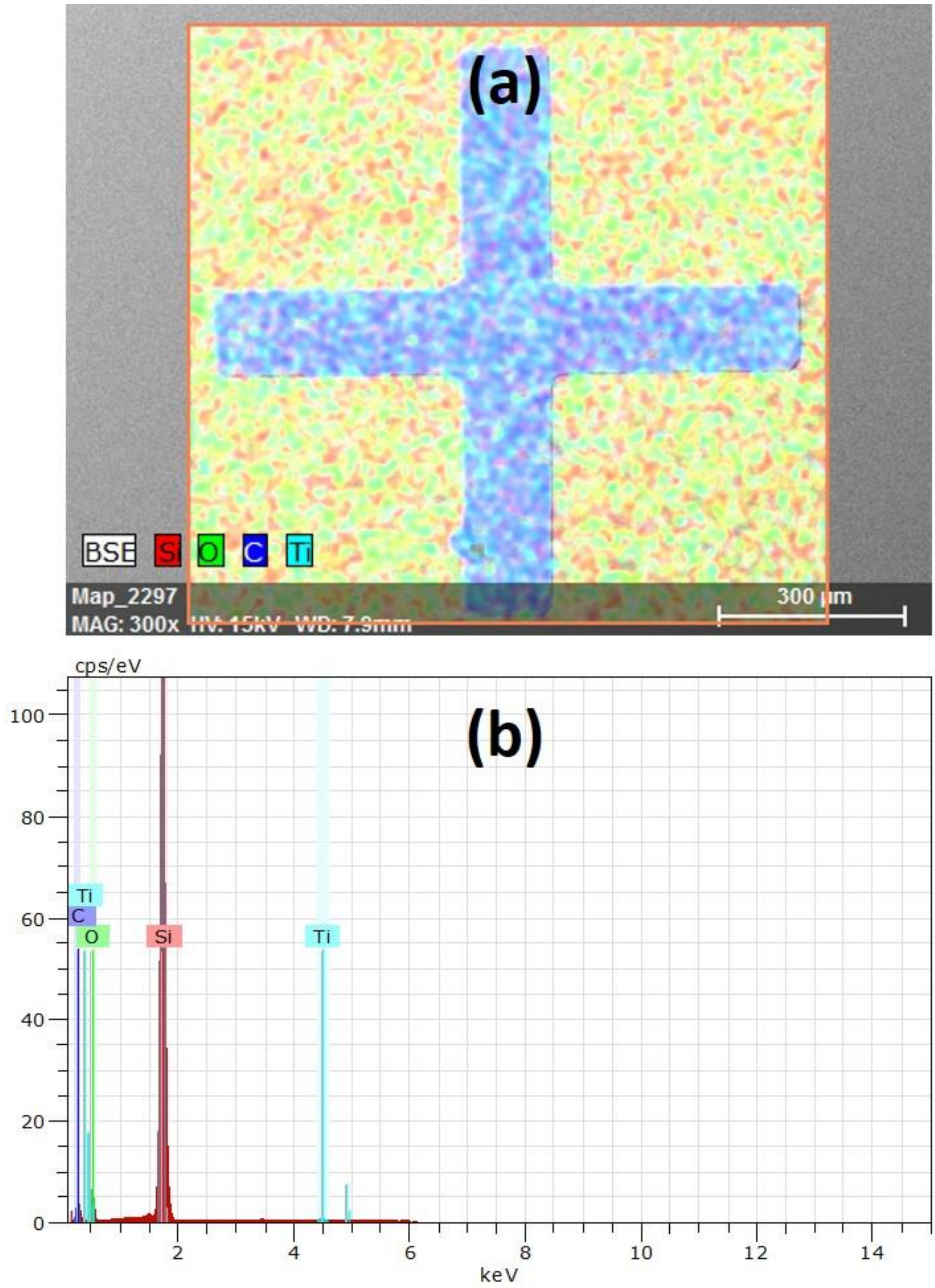

Figure 6-9: SEM image (a) and EDX (b) on patterned structure of titanium/graphene.

In addition, Raman spectroscopy of the samples was obtained using a Horiba Yvon Raman microscope. As was explained in section 2.1.4 the D peak is an indication of defects in graphene samples. The measurement showed a high D peak which refers to defected structure of graphene as shown in Figure 6-10.

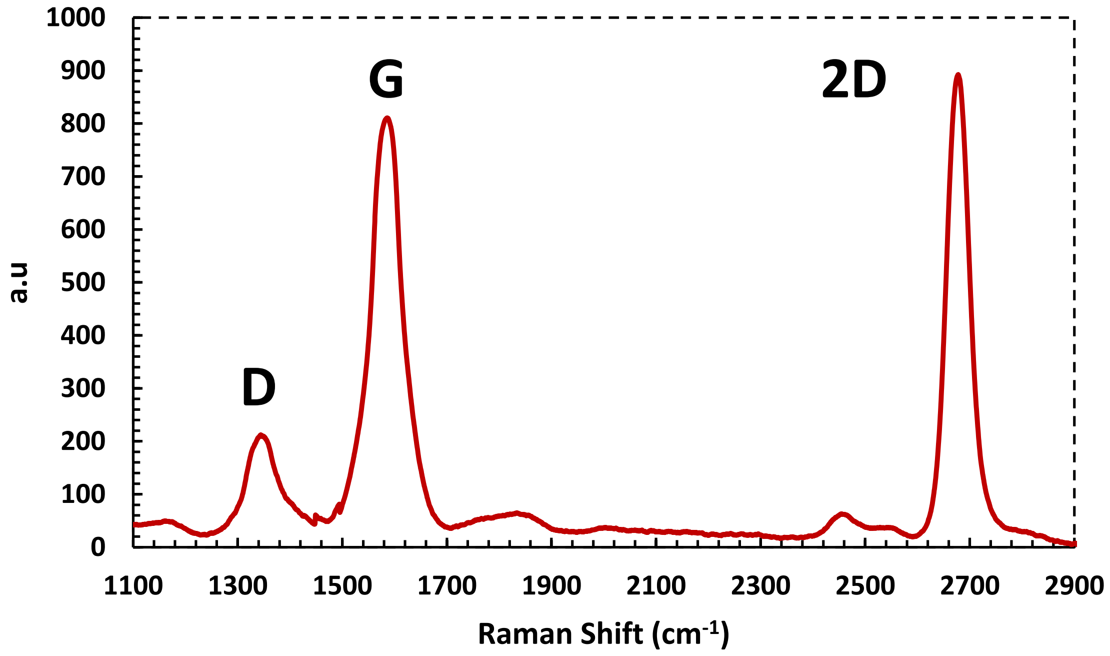

Figure 6-10: Raman spectra of remained graphene structures.

It was also realized that the delamination was not only due to oxide layer etch by HF but also because of poor adhesion of graphene to the surface. Wet chemical processing caused the delamination since the adhesion was not strong enough. It was further observed that even diluting the sample in pure water without any treatment caused the same issue. In order to overcome this issue, the samples were pre-treated, and the microfabrication took place without employing a protective layer as is explained in the next section.

6.3.2 Multilayer Graphene

It was observed that the adhesion of multilayer graphene is stronger than the single layer one which makes the fabrication process easier. Therefore, the same mask mentioned in section 6.3.1 was used for patterning multilayer graphene and evaporating metal contacts, however, without adopting any protective layer. The multilayer samples were consisted of randomly distributed graphene flakes of 3 to 5 layers along with various lengths. The primary reason of using multilayer structure was due to its easier visibility. Apart from implementing steps for covering the surface with a protective layer, similar steps given in Figure 6-5 were adopted by excluding the procedure defined for suspending the structures.

Similar to the operation explained in previous section, a photoresist was spin coated and baked following by a UV exposure. The features were obtained after resist development. Then, desired patterns were revealed by implementing an oxygen plasma process using a TEGAL Co. PLASMOD microwave asher. It was found that the time required for implementing some steps was slightly longer than monolayer graphene. For example, etching this type of graphene using oxygen plasma took longer time (around 45 minutes) due to relatively thicker structure of multilayer graphene. The photoresist has successfully survived during plasma etch process. In reality, it was also etched during the operation, however, due to its higher thickness (>1 μm) a longer time was going to require for sweeping all of it. In addition, it was also more resistant than expected since it was baked prior to operation. Figure 6-11 shows the view of a multilayer graphene sample after each step from bare sample (a) to lithography and resist development (b) along with patterning (c-d) process.

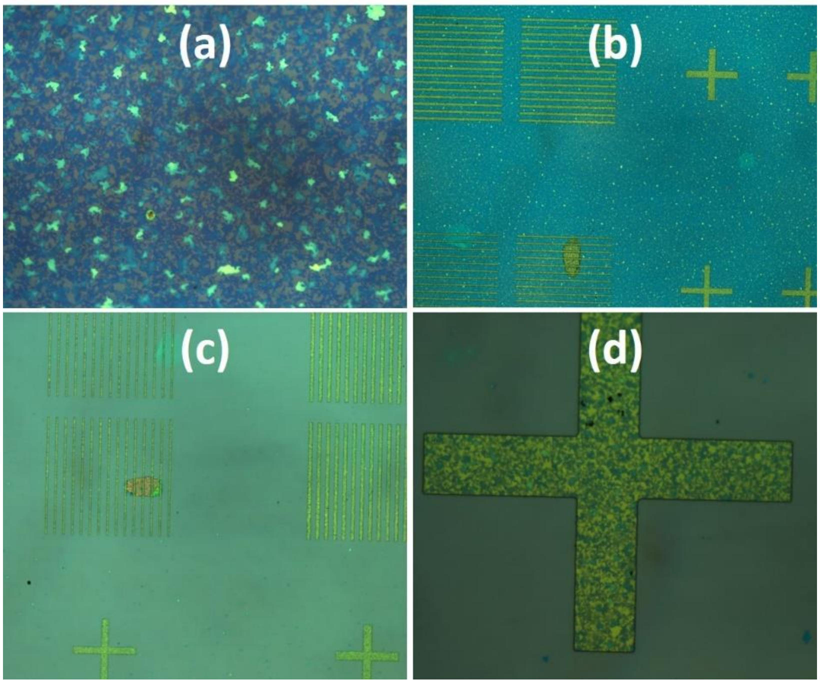

Figure 6-11: Fabrication steps for patterning multilayer graphene. Multilayer graphene (a) and the view after lithography and developing process (b). The patterning was achieved by performing plasma etching (c). A closer look at the patterned structure after etching process (d).

To obtain actual devices, another lithographical process was performed using similar techniques for contact formation depicted in Figure 6-5. Therefore, a second resist coating and lithographical process took place following by a photoresist development stage. The contact features were formed and a layer of chromium (30 nm) along with a layer of gold (250 nm) was evaporated using e-beam evaporator. Devices with contacts were formed after lift-off. The alignment during the lithography process was more straightforward since it was easier to visualise multilayer graphene. Figure 6-12 demonstrates the images of contact formation on the patterned structures.

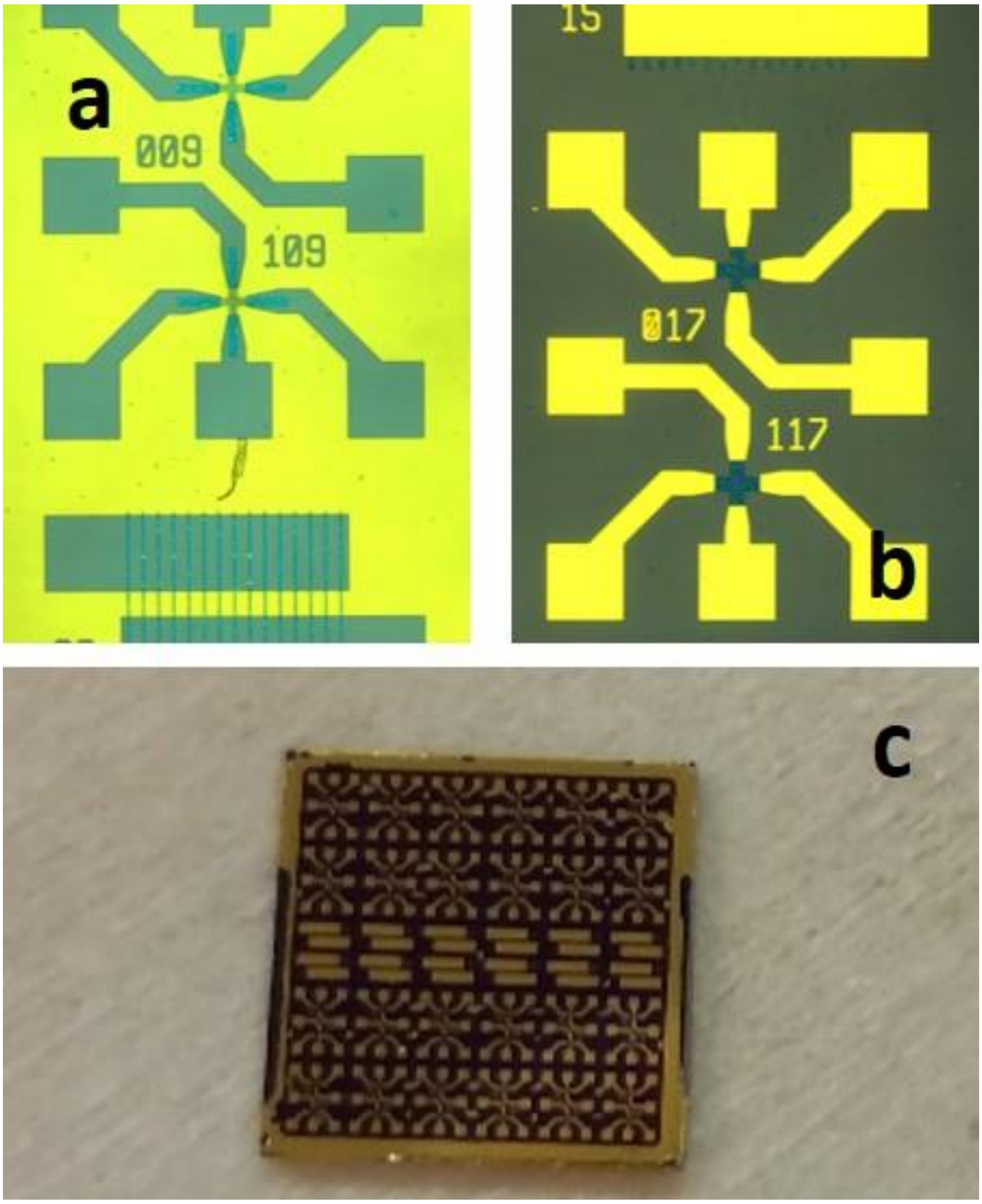

Figure 6-12: Micro-fabricated multilayer graphene. The view after lithography and developing (a) and after lift-off (b). Devices were placed on 10 mm × 10 mm substrate (c).

Raman spectra measurement of the devices after fabrication is shown in Figure 6-13. The peaks characteristic to graphene were assessed and peak intensity ratio between 2D and G (2D⁄G) bands were calculated to be 0.6 indicating multi-layer graphene [405].

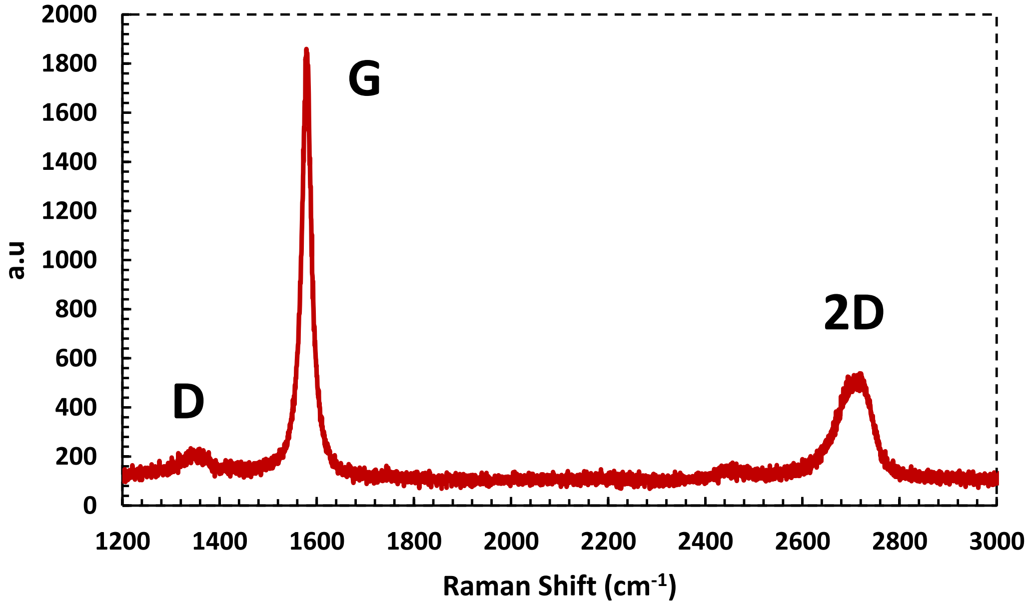

Figure 6-13: The Raman spectrum of multilayer graphene after fabrication.

6.3.3 Monolayer Graphene (No Protective Layer)

To avoid the issues mentioned in the section 6.3.1, another microfabrication process was carried out by directly processing CVD grown graphene without any protective layer. To help better adhesion of the graphene to the Si/SiO_2 substrate and prevent any delamination, the samples were annealed at a temperature of 300 °C under free flow of nitrogen for 3 hours. Meanwhile, single layer graphene presents difficulties in terms of visualisation which causes misalignments of contacts and patterned geometries. The visualisation issue was the reason why a protective layer was employed in the section 6.3.1. To overcome this issue, a sub-micron manipulator (FINEPLACER® lambda Sub-Micron Bonding System) shown in Figure 6-14 was used to mark certain areas on the wafer in order to allow the alignment marks to be visible, therefore, making the alignment easier during the lithography. Lithographical process became relatively easier by employing this method. Apart from visualisation, this approach was designed to be performed as a wafer-scale, thus, preventing the time-consuming tasks required for die-scale manufacturing.

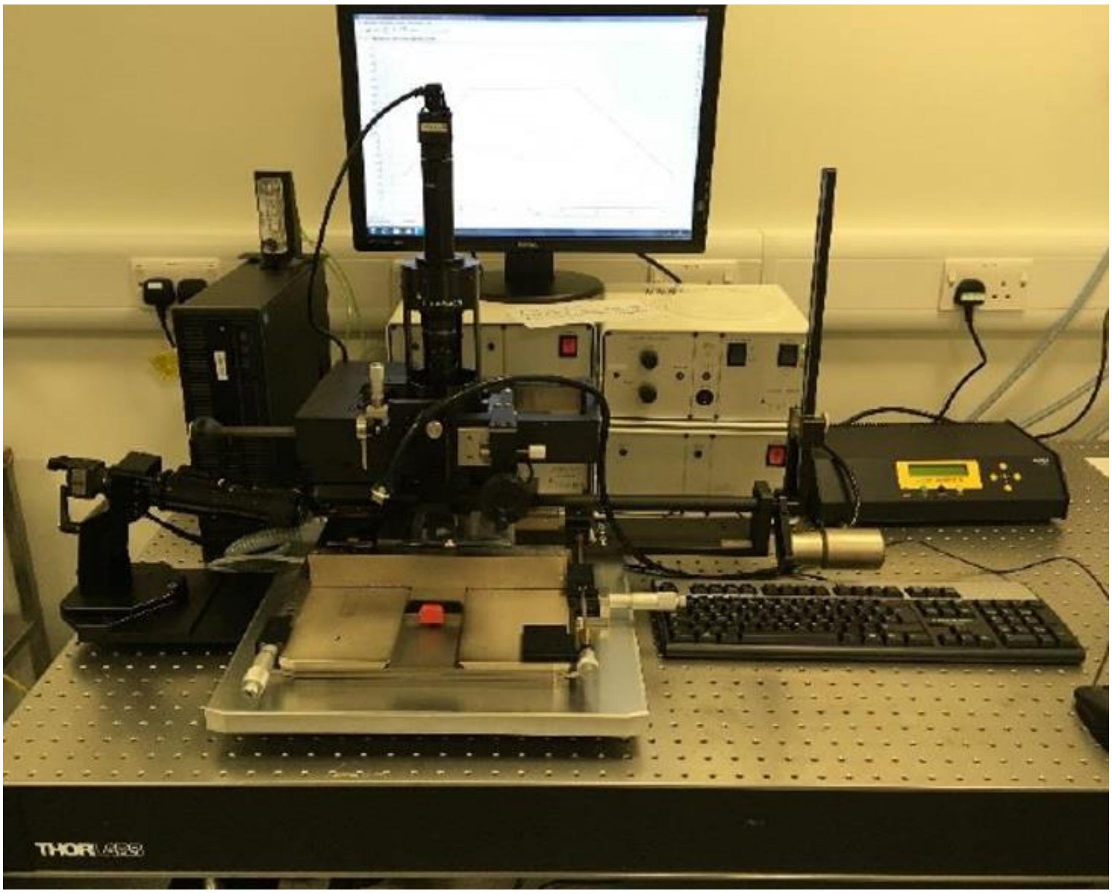

Figure 6-14: FINEPLACER® lambda Sub-Micron Bonding System used to mark certain areas on the wafer for alignment. (Newcastle University, School of Engineering).

An array of single graphene Hall devices with an active area of 10 μm × 10 μm were designed for manufacturing on 5 mm × 5 mm dies using the following microfabrication process highlighted in Figure 6-15. A photoresist layer was spin coated to cover a 4-inch silicon wafer containing a 285 nm surface oxide layer with a CVD grown and transferred graphene layer (Graphene Supermarket). Desired patterns were obtained by implementation of a lithography process. The wafer then underwent a dry etching process via oxygen plasma (by using TEGAL Co. PLASMOD microwave Asher) for 13 minutes to remove the graphene not protected by photoresist. After removal of photoresist, a similar lithography process was performed for defining the contacts. A 30 nm layer of chromium and 250 nm layer of gold were deposited with electron beam evaporation following the lithography steps. The desired contact patterns were formed after the lift-off. Lastly, the processed wafer was diced into 5×5 mm^2 dies which include several individual micro-Hall elements. Devices having an active area of 10 μm × 10 μm were formed in a cross-like geometry as shown in Figure 6-16.

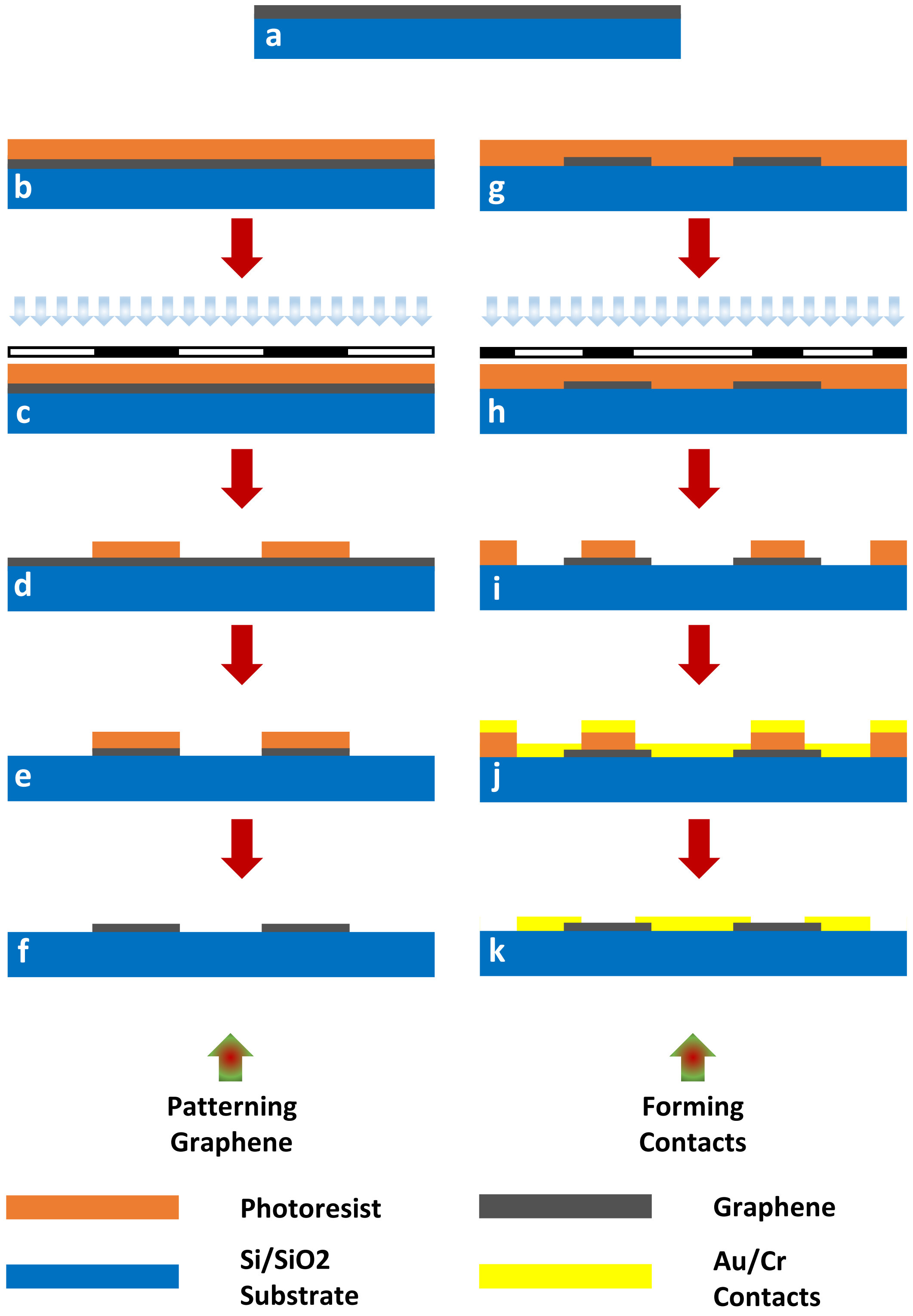

Figure 6-15: Schematic for microfabrication process to form graphene micro-Hall devices. (a) High quality CVD grown graphene situated on a Si/SiO_2 wafer. (b) The wafer was covered with AZ5214E photoresist and pre-baked at 90° C for 15 minutes. (c) UV exposure for 14 seconds using a patterned mask. (d) Developing the photoresist for obtaining relevant patterns. (e) Etching process via oxygen plasma to remove graphene not protected by the photoresist layer. (f) Photoresist removal. (g) Another layer of photoresist was spin-coated onto the sample and pre-baked. (h) Second UV exposure for defining contacts. (i) Photoresist development. (j) Chromium and gold evaporation. (k) Lift-off.

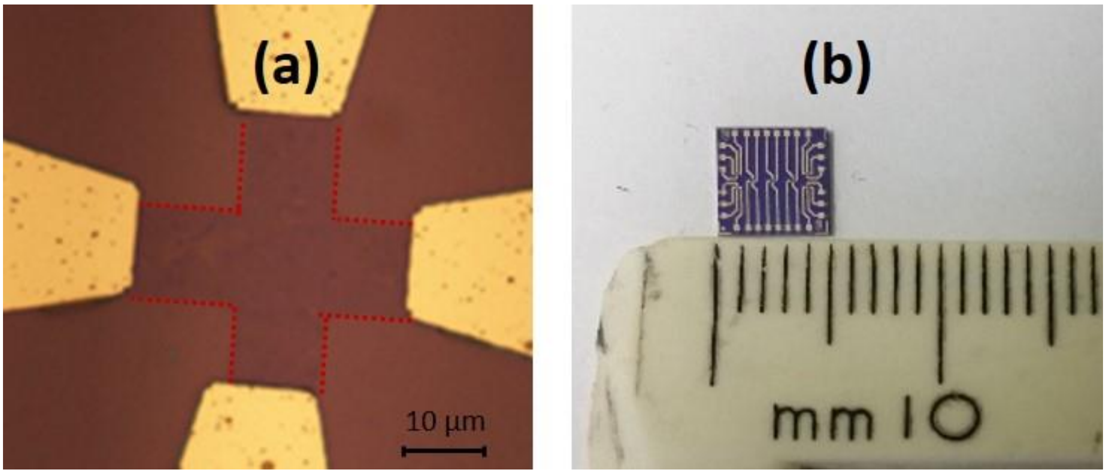

Figure 6-16: (a) An optical image of a graphene Hall effect device with Cr/Au contacts. Graphene layer is highlighted with red-dotted lines. (b) A view of one of the fabricated 5x5mm^2 dies containing several devices.

The length to width ratio was designed to be greater than 3 in order to avoid weakening the Hall effect due to geometrical factor [43, 118, 128]. To assess the quality of the graphene, Raman spectroscopy measurements were performed. The Raman data, shown in Figure 6-17, was obtained after completion of the fabrication procedure. The peaks characteristic to graphene were assessed. A sharp 2D peak and quite small D peak were obtained with a calculated *2D/G* intensity ratio of around 2.5 which indicates a high quality single layer graphene [165, 236, 237, 239, 240, 397].

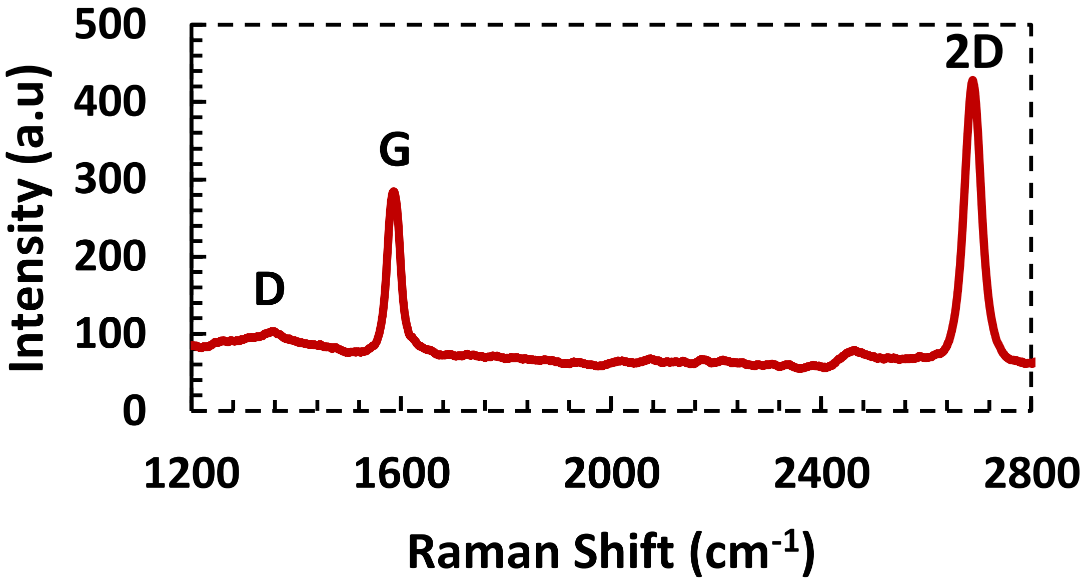

Figure 6-17: The Raman spectrum of graphene after the microfabrication process.

6.3.4 Printed Graphene

The intention in employing printed graphene was to develop an alternative way of device manufacturing which can both make the fabrication easier by eliminating most of the steps given in above sections and provide better devices for biosensing purposes. The idea behind the printed graphene was to employ graphene oxide solution by printing it on the surface of a glass slide. The fabrication of those devices was performed using facilities in Chemical Nanoscience Laboratory within the School of Natural and Environmental Sciences (Newcastle University). The sensors were printed at a temperature of 75 °C with a setup that provides a material having around 5-layer thickness. Meanwhile, graphene oxide is not conductive due to high resistance, thus, cannot be used as Hall device normally. However, reduced graphene oxide is relatively better and can be used as a conductive material. Therefore, the devices were reduced chemically after they were formed directly without using any mask. Figure 6-18 shows one of the printed graphene oxide devices after being reduced.

Figure 6-18: Printed and chemically reduced graphene oxide Hall device.

The printed devices require to have contacts to allow performing measurements. Therefore, silver contacts were also printed on those Hall devices so that they can be connected to the testing equipment. A silver ink was used with a cartridge that blocks UV-light to avoid silver degradation. Meanwhile, the printing process for contacts was performed after chemical reduction of graphene oxide to maintain the resistance between contacts and device. The printed silver contacts on a Hall device is shown in Figure 6-19.

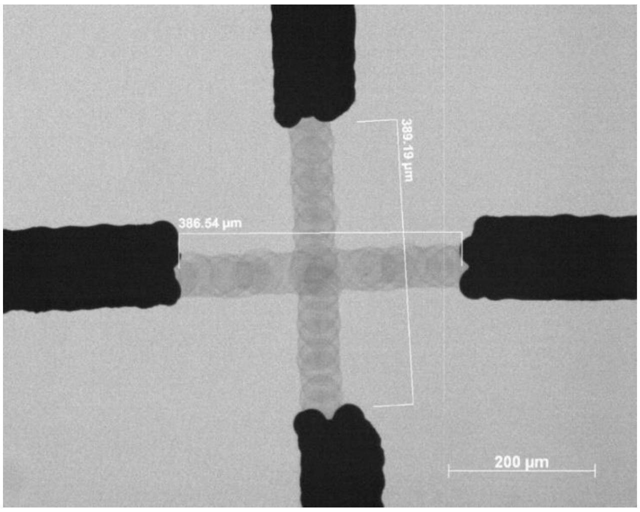

Figure 6-19: An optical microscopy image of reduced graphene oxide Hall device with printed silver contacts.

In a graphene oxide sample the oxygen content is higher which gives rise to C-O peak (≈286.7 eV) comparing to C=C peak (≈284.5 eV) [406]. However, in a reduced graphene oxide sample, the content of oxygen is decreased significantly [407]. The existence of the graphene oxide on the glass substrate was confirmed via performing XPS as shown in Figure 6-20. The XPS spectra showed that the relative percentage of C=C bonds is extremely higher than C-O bonds which verifies the reduction in oxygen content. Moreover, it did not show any elements other than carbon and oxygen which indicates the absence of impurities.

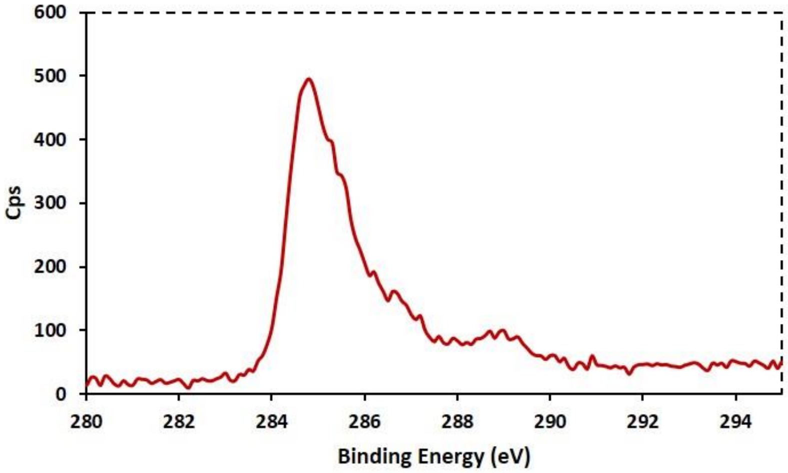

Figure 6-20: XPS Spectra of reduced graphene oxide.

6.4 Measurements and Results

The measurements were carried out via integrating samples to the processing board. Samples were placed either on the specified part (tongue shaped) of the board (see Figure 3-15) or on a chip, as shown in Figure 6-21, and then measurements were performed.

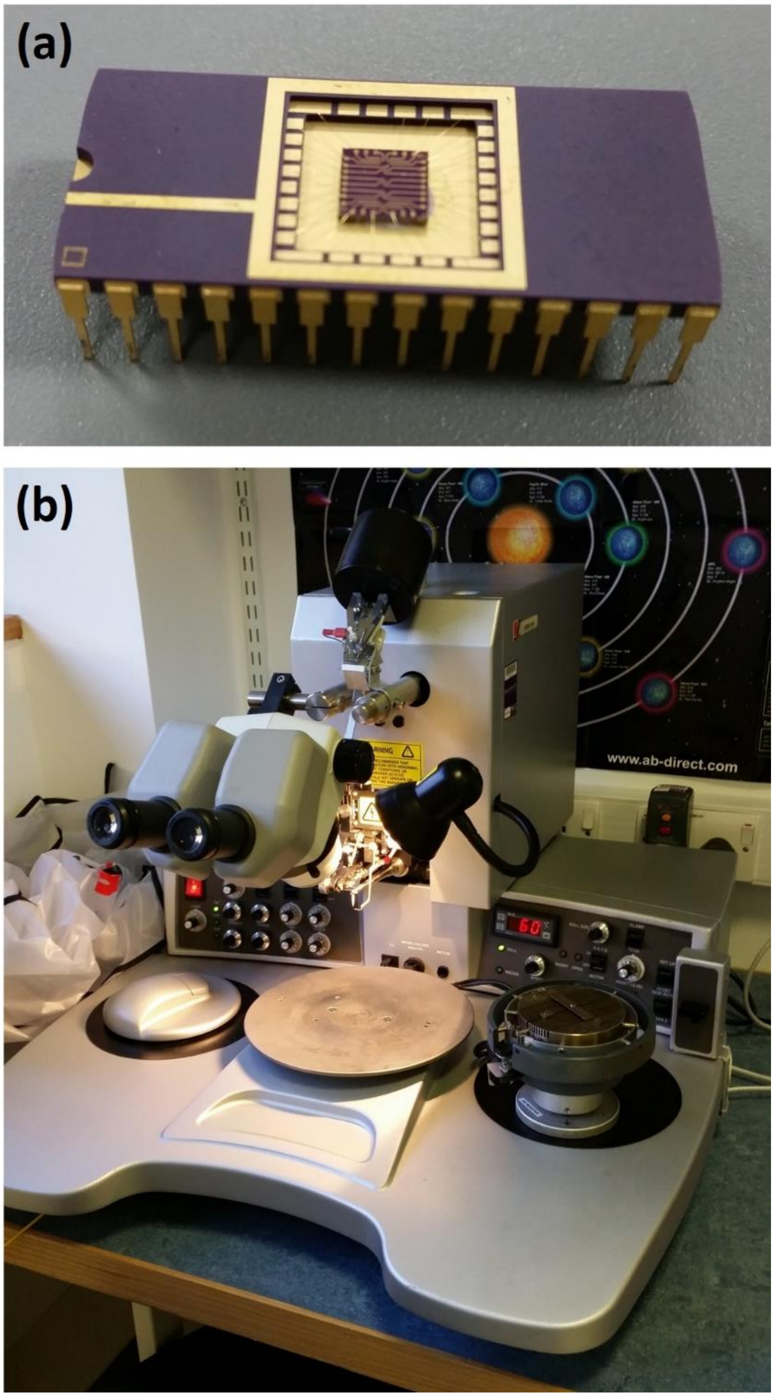

Figure 6-21: A fabricated die with several graphene Hall devices placed on a chip (a) and the wire bonder (Kulicke & Soffa Industries Model 4700 wire bonder) used for assembling devices to the chip (b).

6.4.1 Multilayer Graphene

Structures having cross-like geometries with an active area of 40 μm and length to width ratios of 3 were tested for characterising the performance of multilayer devices. The ability of detecting magnetic field change is one of the key parameters for determining the performance of Hall devices [43]. As was expected, graphene was proved to be significantly better than gold-based devices mentioned in Chapter 4. The Hall voltage obtained from output of the graphene devices was higher than the gold-based ones even with less driving current about three orders of magnitude and less field strengths about an order of magnitude. This is due to the unique structure of graphene which consists of high carrier mobility and atomic-level thickness. A current of few μA and a field strength of few mT were sufficient for obtaining outputs. Figure 6-22 demonstrates a typical output from a multilayer graphene sample with respect to varying field.

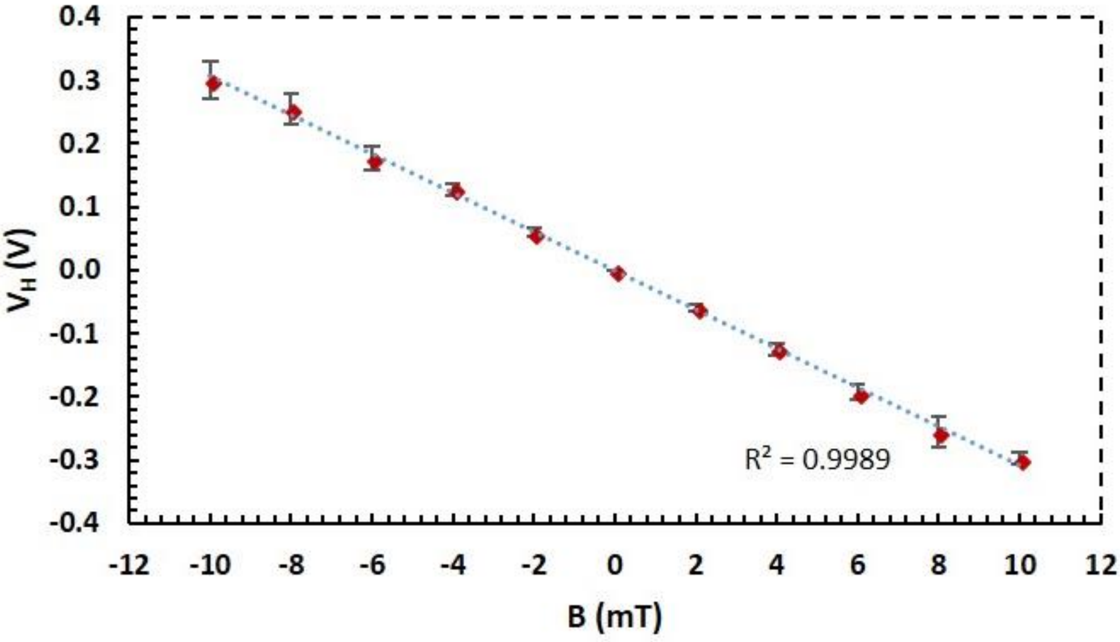

Figure 6-22: A typical Hall voltage obtained from output of a multilayer graphene device (n=4) with respect to varying magnetic field using 50 μA of driving current by employing current-spinning circuitry. The device had an active area of 40 μm.

Presenting a linear behaviour with respect to field change is another key parameter in Hall devices for applicability of applications. Multilayer graphene samples also showed good linearity across devices as shown in Figure 6-23.

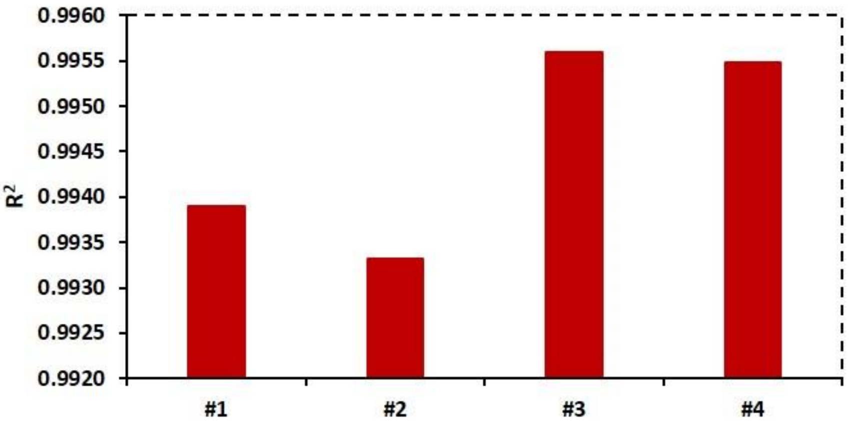

Figure 6-23: Linearity across several devices made of multilayer graphene.

A current-related sensitivity of up to 200 V/AT was obtained from multilayer devices which is better than gold-based devices about five orders of magnitude and comparable with the silicon based competitors [408]. The current-related sensitivity with respect to varying magnetic field is given in Figure 6-24 (a) along with the sensitivity parameters across multilayer graphene devices.

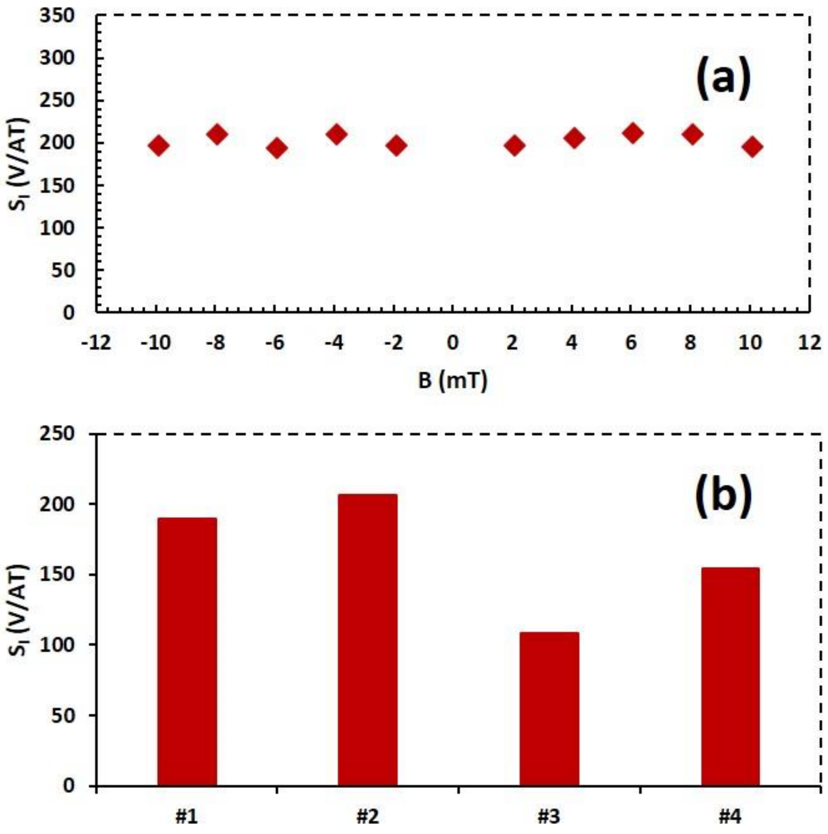

Figure 6-24: Current-related sensitivity with respect to varying magnetic field for device #2 (a). Current-related sensitivities across multilayer graphene Hall devices (b).

The obtained results suggest that graphene-based materials have the promise for Hall effect type applications and better performance parameters can be reached by adopting single layer graphene devices. The extraordinary capability of single layer graphene Hall devices is presented in the following section.

6.4.2 Monolayer Graphene

Several micro-fabricated Hall elements with the same geometries, having length to width ratios of 3.5, were tested to observe the output characteristics of devices. Unlike the design for multilayer graphene (given in section 6.4.1), the length to width ratio was designed to be greater than 3 in order to avoid weakening the Hall effect due to geometrical factor [43]. Quantitative analysis was performed both under constant magnetic field with variable current and under constant current with variable magnetic field. To achieve devices with the capability of low field sensing, the offset equivalent magnetic field needs to be optimized first. Reducing this parameter is important for sensitivity improvements and consistency. Eliminating this parameter also considerably increases the sensitivity of the devices. Therefore, a circuitry was constructed on PCB as explained in section 3.2.1. As shown in that section, a residual offset corresponding to an offset equivalent magnetic field value of 100 nT was obtained using the developed circuitry for offset removal. Together with detection capability, a linear performance is also desirable for practical implementation of Hall effect devices. As seen from Figure 6-25 the Hall voltage of fabricated graphene devices showed a highly linear behaviour with respect to both applied field strength and driving current. The demonstrated highly linear response ($R^2 > 0.99$) is comparable with those reported in previous studies on graphene devices [63, 291, 296].

A maximum current-related sensitivity of 2540 V/AT was obtained with no gate voltage applied. As seen from Figure 6-26, the sensitivity varies across devices. The sensitivity variations across those devices can be explained by non-uniform adhesion of graphene to the substrate, defects and ruptures or residuals caused the by fabrication process [165]. Differences in the input resistances of devices may also play a role in sensitivity variations [394]. Nevertheless, thanks to the excellent electrical properties of graphene, fabricated devices with even the worst performance (323 V/AT) still provide better sensitivities compared to Si based competitors (310 V/AT) [380].

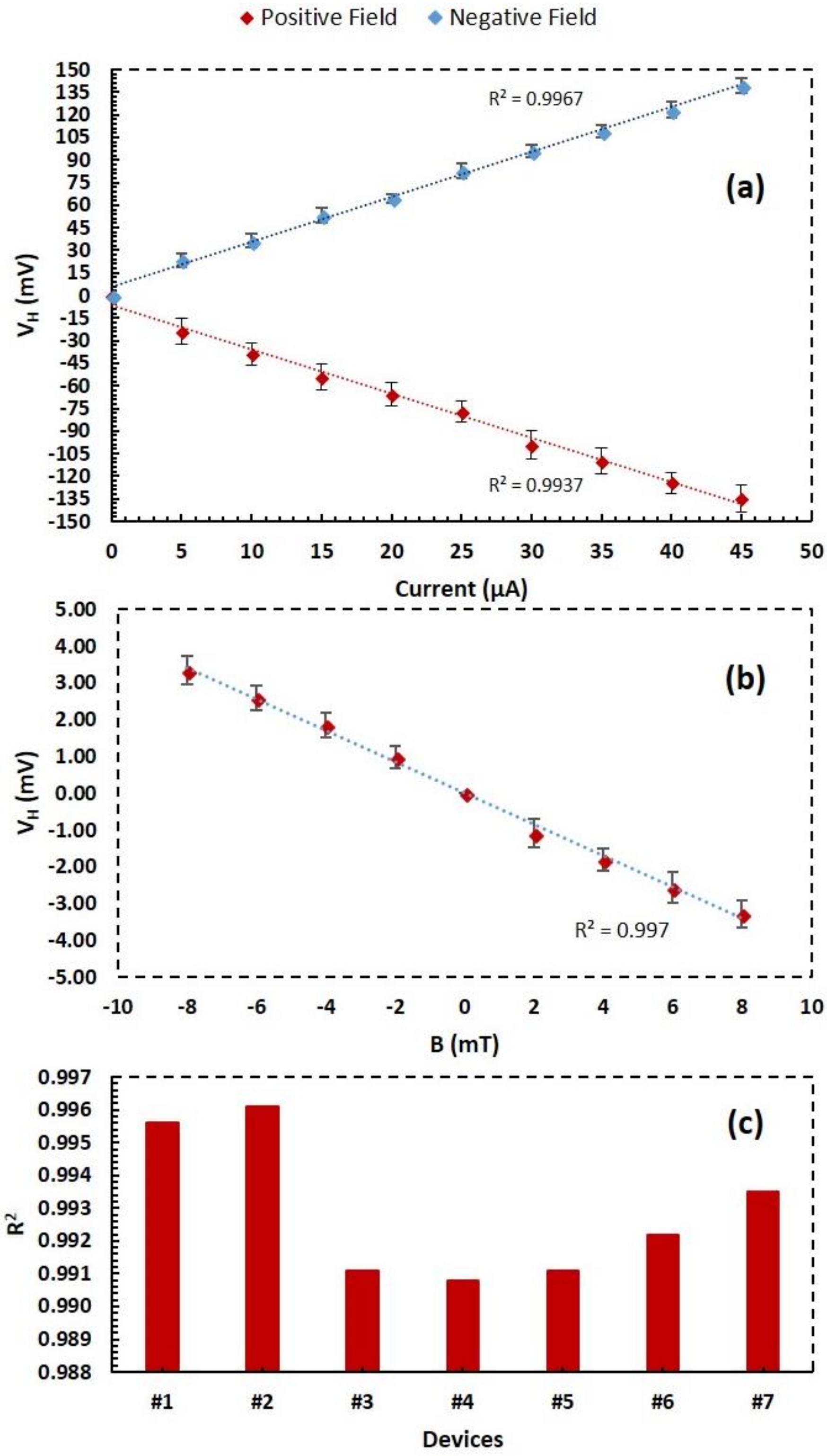

Figure 6-25: The response of the graphene sensor shows highly linear behaviour. Hall voltage under constant negative (red) and positive (blue) field strength of 120 mT with variable driving current (a) and under variable magnetic field with constant driving current of 15 µA (b). The repeatability (n=3 for (a) and n=6 for (b)) tests showed that devices are highly stable in terms of providing corresponding outputs. Good linearity is shown across all devices (c).

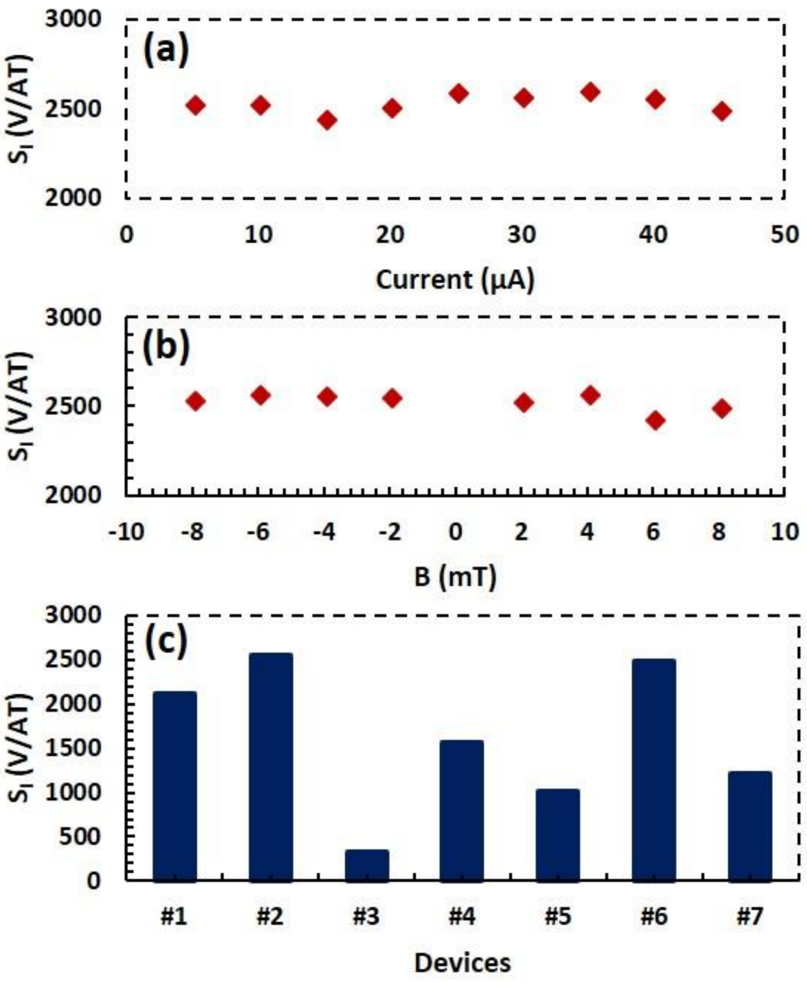

Figure 6-26: Current-related sensitivity for variable current (a) and variable magnetic field (b) for device #2. Current-related sensitivities across different graphene Hall devices (c) with the same geometry and sizes under the same operating conditions (15 μA biasing current and 2 mT field).

In addition of representing high sensitivity, graphene also has low noise intrinsically [11]. Having a combination of low noise and high sensitivity leads to devices with high resolutions. Magnetic field resolution is the parameter that is used for determining the minimum detectable field capability of the sensor and given as:

$$B_{min} = \frac{\sqrt{4k_B T R_s \Delta f}}{R_H I_x} \qquad (6–1)$$

where, k_B is the Boltzmann constant, T temperature, R_s series resistance and Δf measurement bandwidth. The minimum detectable magnetic field parameter can also be determined according to equation (6–2), where B_{min} is the field resolution and V_n represents the spectral density of the voltage noise.

$$B_{min} = \left|\frac{V_n}{S_A}\right| \qquad (6\text{–}2)$$

The latter equation states that the resolution can be calculated by dividing the noise spectra by absolute sensitivity. To determine this value, the FFT tool of LabVIEW software was used to measure voltage noise spectra by adopting a National Instruments' data acquisition device (NI-DAQ USB). The data of measured noise spectra (V/√Hz) was divided by absolute sensitivity, during the operation, to obtain the minimum detectable field (T/√Hz). Magnetic field resolution of the sensor with respect to frequency was obtained as shown in Figure 6-27. Meanwhile, it is worth to note that the minimum detectable field is defined by the thermal noise region. That means the maximum achievable value is considered as the magnetic resolution of a particular device within the thermal noise region.

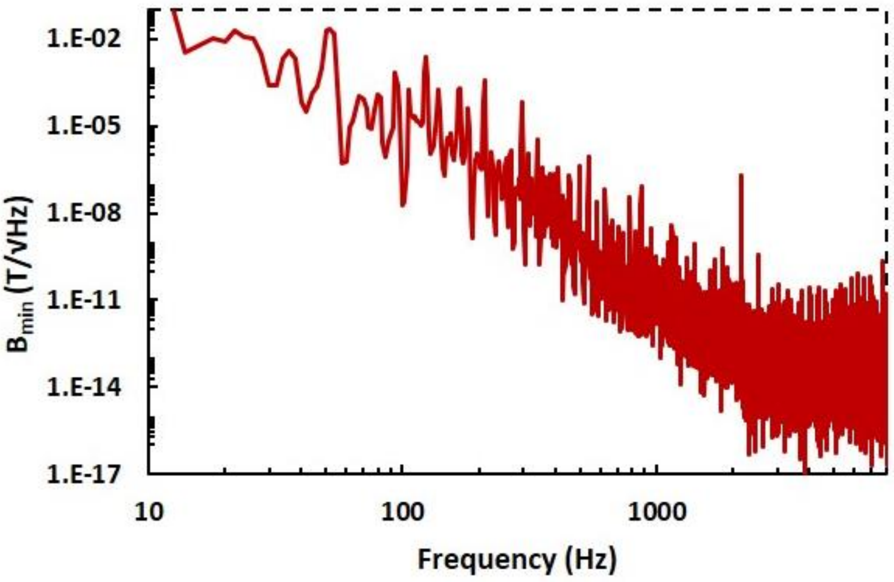

Figure 6-27: Magnetic field resolution of a graphene Hall sensor as a function of frequency.

As seen in Figure 6-27, the noise level decreases with respect to increasing frequency, representing a 1/f dependence. Around 2 kHz, the noise level is dominated by thermal noise only. A minimum field resolution of 162 nT/√Hz was extracted from fast Fourier transform measurements. Assessing the current related sensitivity together with the minimum detectable field, it can be seen that the developed devices demonstrate the highest S_I and the second lowest B_{min} as given in Table 6-1. The field resolution is higher than that of calculated for offset equivalent magnetic field presented in section 3.2.1 since another sensor was used.

Material	S_I (V/AT)	B_{min} (nT/√Hz)
CVD graphene (Ref [63])	1200	800
CVD graphene (Ref [71])	2093	100
CVD graphene (Ref [117])	1800	20000
Silicon (Ref [282])	175	200
Epitaxial graphene (Ref [72])	1021	2500
CVD graphene (Ref [130])	800	500
2DEG (Ref [275])	357	500
Silicon (Ref [408])	143	250
CVD graphene (Ref [165])	1200	43000
This work	2540	162

Table 6-1: Comparison of current related sensitivities and minimum detectable field resolutions.

6.4.3 Printed Graphene

Apart from the microfabricated devices presented in the above sections, an easier alternative of device manufacturing was also explored as was explained in section 6.3.4. The measurements on this type of devices were not performed thoroughly due to an extreme decrease in their performance after being driven with the current for a short period of time. To carry out the measurements, a silver paint and an extremely thin wire were used as shown in Figure 6-28 to arrange the connection between testing equipment and the sensors.

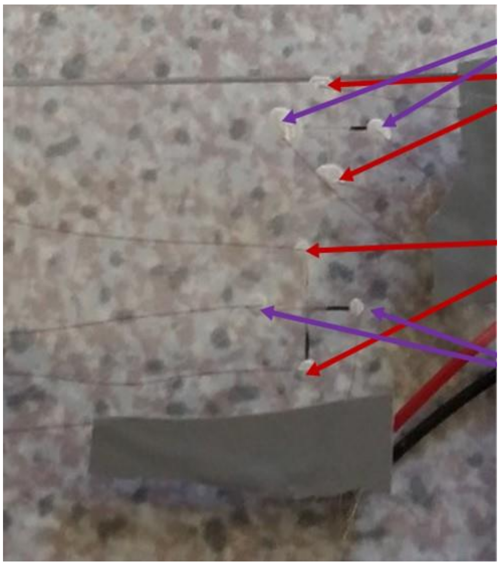

Figure 6-28: The connection between reduced graphene oxide Hall sensors on glass substrate and test equipment with the aid of silver paint and a thin wire.

Initial assessment showed that they can reach a current-sensitivity of around 64 V/AT, however, keeps decreasing and finally does not provide any reusable output. The reduction in the performance was attributed to the oxidizing effect caused by electrical stimulus [409]. The performance of the devices may be maintained by employing a reversible electrical modification process defined in ref [409]. However, implementation of this technique was left for potential future projects since this approach was not the main focus of this work.

6.5 Summary

Design, fabrication and performance parameters of graphene-based Hall sensors were discussed. It was shown that single layer graphene can be fabricated without need to a protective layer by implementing a high temperature treatment under free flow of nitrogen gas. The performance of single layer graphene was also demonstrated to be better than other competitor materials such as InSb or 2DEG systems. In addition to single layer, the multi-layered graphene structures were also shown to have comparable performances to silicon-based Hall sensors. Table 6-2 demonstrates the current-related sensitivities obtained across graphene devices with different structures.

Devices	Current-related Sensitivity
Monolayer Graphene	2540 V/AT
Multilayer Graphene	200 V/AT
Printed and reduced Graphene Oxide	64 V/AT

Table 6-2: Current-related sensitivities obtained from fabricated devices.

Novel techniques were also investigated to obtain Hall devices from derivatives of graphene. Printed and chemically reduced graphene oxide was explored for potential Hall effect biosensor applications which would eliminate most of the microfabrication steps. It was shown that the fabrication and reduction is feasible with this method. However, a significant loss of performance was observed which was attributed to oxidizing effects. Potential solution for this issue was recommended which is worth to be investigated in future.

Chapter 7. Forming Graphene Hall Effect Biosensor for Real-time Label-free Detection

In terms of utilising the fabricated devices as biosensors, a protocol has been prepared to modify the surface of the sensors for the recognition of specific biomolecule. The fabricated devices were placed on a chip and a well was formed on the top in order to serve as a reservoir. This chapter presents the steps for fabrication of devices that can operate in liquid environment along with the process for functionalization and the results of bio-measurements.

7.1 Design

Similar design steps for monolayer graphene given in section 6.1 were used for construction of devices. To form a biosensing system which can operate in real-time, the fabricated devices should be able to operate in liquid environment. To do so, further steps were designed to form a well on the surface of the devices. An epoxy glue was employed for insulating the contacts. In addition, acrylic masks were designed to be created using laser cutting machine to protect the active areas of the devices with the aid of photoresist during insulation process. The cross-sectional view of the design presented in Figure 7-1 shows the process of insulation.

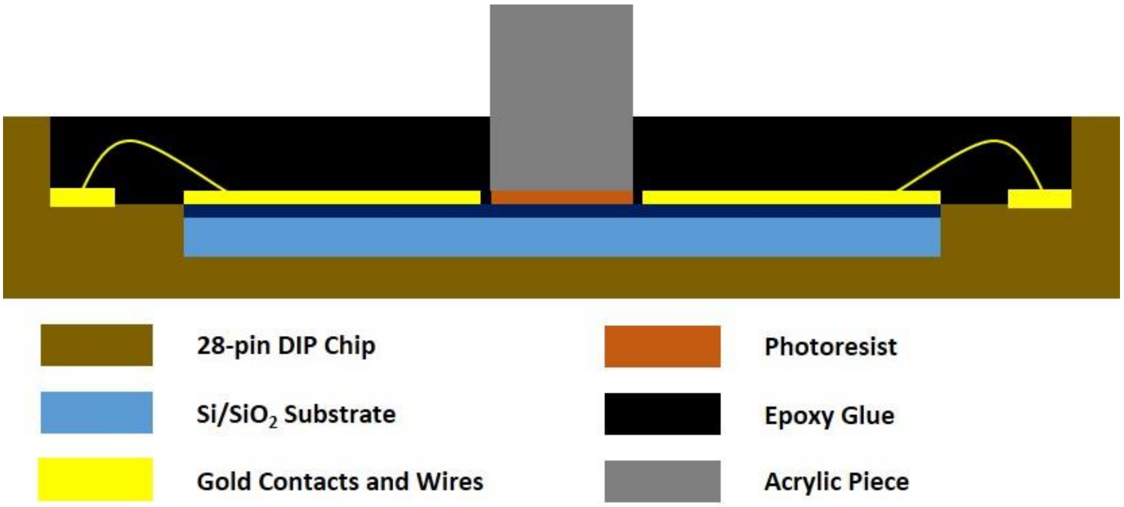

Figure 7-1: Schematic of design of the system (Cross-sectional view). The well is obtained once the acrylic piece is removed (after the drying process of the epoxy glue). The photoresist is cleaned using acetone after removal of acrylic piece.

7.2 Materials

Devices were built using monolayer CVD grown graphene (Graphene Supermarket). Chemicals that were used for this study were purchased from Sigma-Aldrich, UK, unless otherwise stated. In order to maintain a constant pH of 7.4, a phosphate buffered saline (PBS) was prepared (500 mL) using 0.4 g of sodium chloride (NaCl), 0.1 g of potassium chloride (KCl), 0.71 g of sodium phosphate dibasic (Na_2HPO_4) and 0.1 g of potassium phosphate monobasic (KH_2PO_4). This buffer is a salty solution and has an ionic concentration that matches with the solution of the human body. The reason of using this buffer was to maintain a constant pH for IgG molecules to survive. It was also used as a reference point between different stages during the measurements to observe if there were any change in output of the devices. Due to high conductivity of graphene and the aid of the insulation shown in Figure 7-1, the conduction occurs on the surface of graphene, thus the Hall phenomena can be observed in this solution.

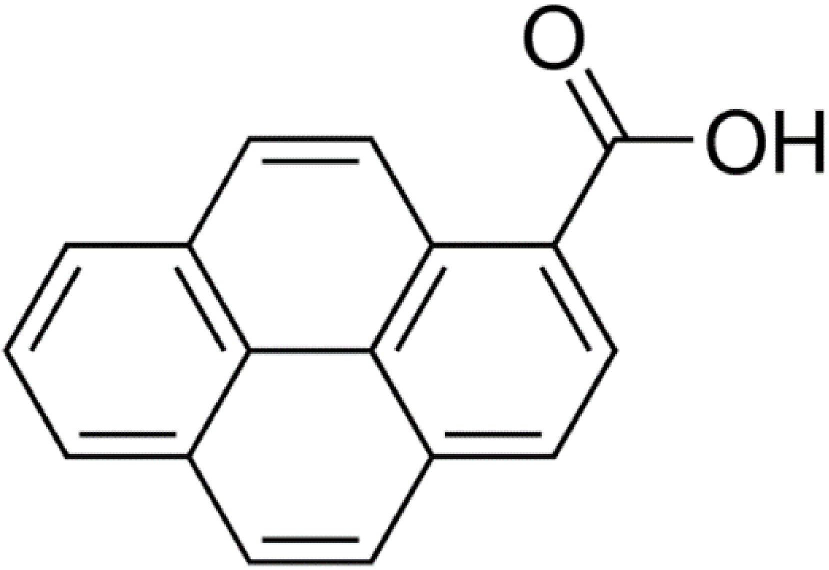

Figure 7-2: The structure of 1-Pyrenecarboxylic acid. Adopted from Sigma-Aldrich.

Another prepared solution was MES buffer which has a pH of around 6. The reason of using MES was because of its amine free structure which can be employed for carboxy to amine crosslinking using carbodiimide crosslinker, thus, would not create additional bonds with pyrene. To prepare the buffer solution of 500 mL; 100 mM of MES hydrate ($C_6H_{13}NO_4S \cdot xH_2O$) and 500 mM of sodium chloride were used. Since Raman and XPS spectra showed that the formed graphene devices are good quality and has no considerable defects, pyrene was decided to be used to modify the surface non-covalently. Therefore, 1-Pyrenecarboxyilic acid ($C_{17}H_{10}O_2$) was employed which can help reduce the distance between the binding area and the surface of the device due to its shorter chain (see Figure 7-2). The charge interaction between graphene and pyrene causes a change in carrier concentration through π-stacking which consequently leads to a Hall voltage change. This mechanism was adopted to create a label-free detection. Therefore, a pyrene solution of 5 mM was prepared using methanol (CH_3OH) (Fisher Scientific). In order to facilitate the amine group for carboxyl to form an amide bond, EDC (N-(3-Dimethylaminopropyl)-N'-ethylcarbodiimide hydrochloride) and sulfo NHS (N-Hydroxysulfosuccinimide sodium salt) was used. EDC was used as a carboxyl and amine reactive crosslinker and sulfo-NHS was used to enhance the coupling efficiency. The solution was prepared in 1:1 ratio by using 0.6 mg of EDC and 1.1 mg of sulfo NHS with 1 mL of MES buffer. Immunoglobulin G (Mouse IgG) was used to interact with this structure and serve as a capture antibody. To prevent non-specific binding of antigens and antibodies, bovine serum albumin (BSA) was used as a blocking agent. It was prepared in 2 % of concentration using PBS solution. Lastly, anti-mouse IgG and anti-goat IgG were used as specific and non-specific antigens, respectively, to observe the behaviour of the biosensor.

7.3 Fabrication

Devices were fabricated by microfabrication techniques similar that of the explained in section 6.3.2. Basically, the microfabrication process was performed by directly processing graphene without a protective layer. The graphene was sourced from Graphene Supermarket^{TM}, which was grown by chemical vapour deposition (CVD) and situated on a 4-inch silicon wafer containing a 285 nm surface oxide layer. To improve the adhesion of graphene to the substrate and to prevent the possibility of delamination, the samples were annealed at 300 °C under free flow of nitrogen for three hours. Devices having an active area of $20 \times 20\ \mu m^2$ were fabricated on dies of $5 \times 5\ mm^2$ by implementing the following microfabrication process shown in Figure 7-3.

Devices having sizes of 10 × 10 μm^2 were used to develop a high-sensitive magnetosensing system as explained in section 6.3.3. These devices were also used to find and optimum way for a biosensing system development and had damages during the process. Therefore, remaining devices with the 20 × 20 μm^2 sizes were used for performing biosensing measurements.

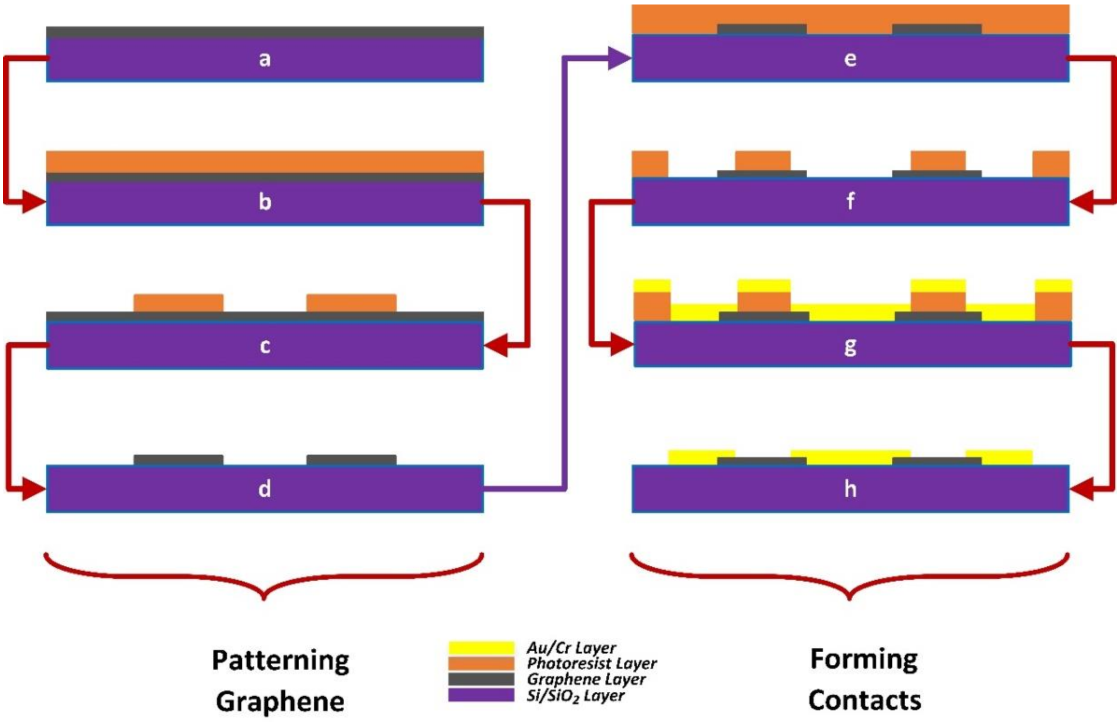

Figure 7-3: The fabrication steps to form sensors. CVD grown graphene on Si/SiO$_2$ substrate (a). Photoresist spin (b). Lithography and resist development processes (c). Graphene etching using oxygen plasma (d). Another photoresist spin for contact formation (e) with lithography and development processes (f). Cr/Au evaporation (g) and lift-off (h).

A photoresist layer was first spin-coated onto a 4-inch wafer containing graphene layer and then patterned by a lithography process. A dry etching process was performed via oxygen plasma for 13 minutes to remove the graphene parts that were not required. Then the photoresist was removed, and a lift-off process was performed to define the gold contacts. For the deposition, a layer of 30 nm chromium (Cr) followed by a layer of 250 nm gold (Au) was evaporated by electron beam (e-beam) evaporation. To form the desired gold contacts, the wafer was then placed in acetone for 30 minutes to remove the remaining photoresist and metal not adhered to the graphene surface. Figure 7-4 shows Raman and XPS spectra of graphene after fabrication. The obtained data showed that graphene is of high-quality single layer with low defects.

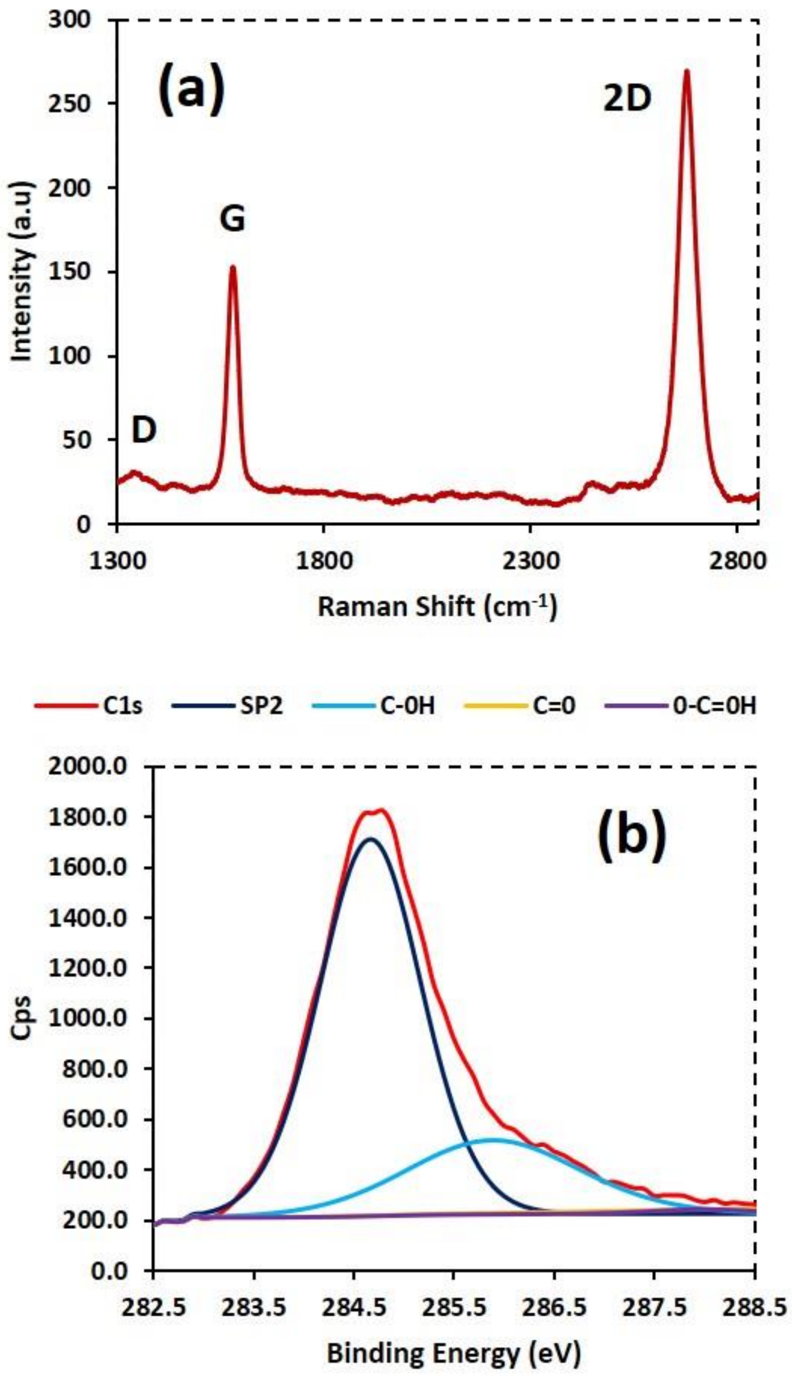

Figure 7-4: Raman (a) and XPS (b) Spectra of fabricated devices.

To form a system which can operate in real-time, the fabricated devices should be able to operate in liquid environment. To do so, a reservoir needs to be formed on the surface of the devices. Therefore, devices went through further steps in order to host solution analytes. The obtained 5 × 5 mm^2 dies were placed on 28-pin DIP chips and all relevant connections between device contacts and the chip were made using a wire bonder (Kulicke & Soffa Industries Model 4700). Then the contacts were isolated by using an epoxy glue (Epoxy Technology Inc. EPO-TEK® 302-3M Black) for forming a reservoir, as shown in Figure 7-5.

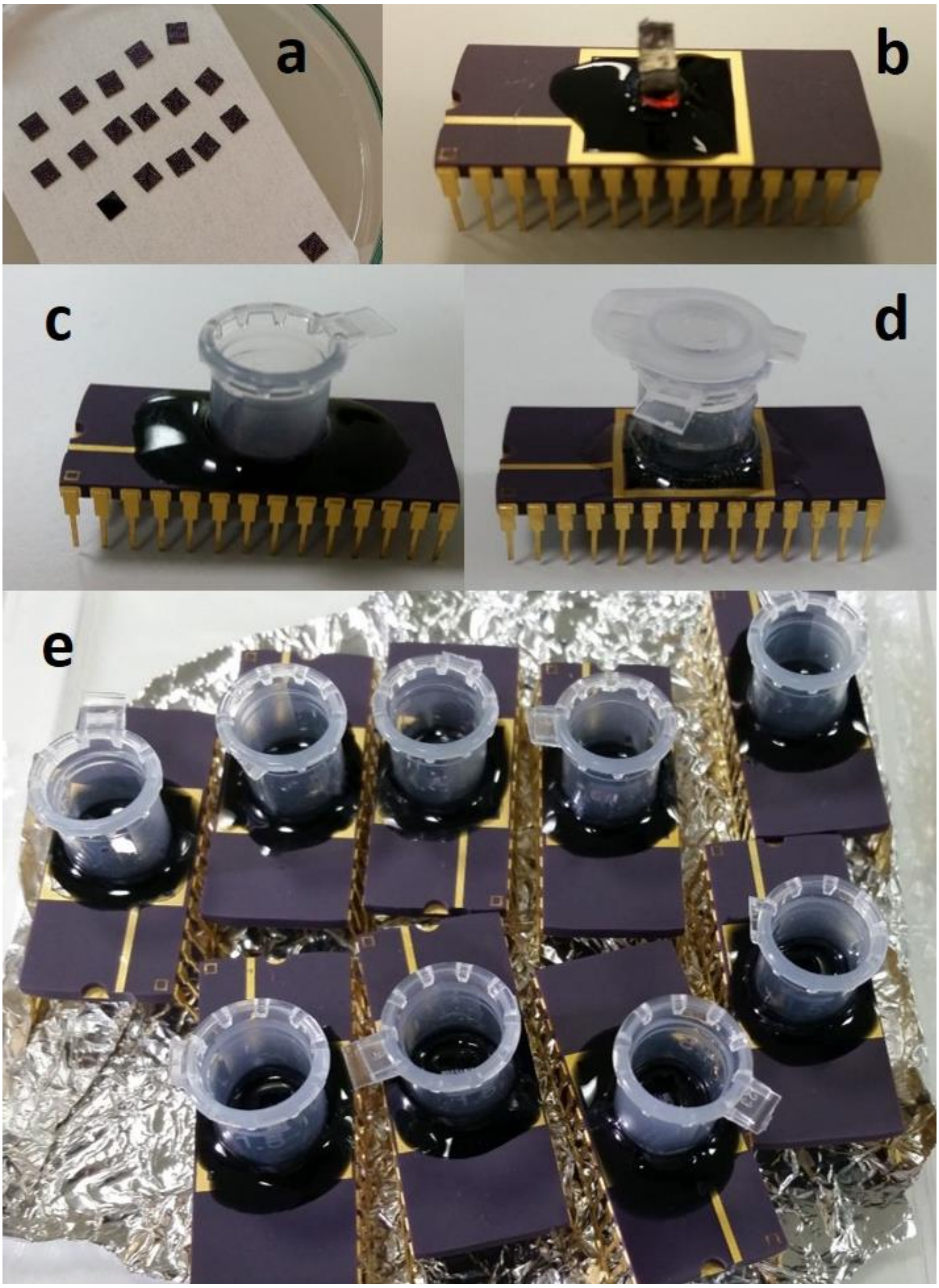

Figure 7-5: Fabricated devices (a) with placement on a chip and coverage of epoxy glue using laser cut acrylic tool (b). A reservoir was placed on the top of the formed well (c) and it was fitted with a lid (d) to prevent vaporization of the liquids if the process requires longer time. Several devices were fabricated to observe the behaviour of the devices for different conditions (e).

To keep the active areas of the devices clear, related patterns were designed and made from acrylic by cutting them using laser cutting tool (HPC Laserscript). The active areas were covered by photoresist and acrylic patterns were placed on them. Then, they were kept for few hours to let drying before being covered by the epoxy glue. Devices were left to dry overnight after application of epoxy glue and then a plastic reservoir was placed on top of the created wells. Lastly, the photoresist was removed, and devices were left to dry before being modified and tested.

7.4 Experimental

7.4.1 Functionalization

In principal, it is sufficient for a receptor part of a biosensor to be highly selective to specific biomolecular element. However, it has to be interfaced with a transducer for operation and the transducer requires to be sensitive enough and reproducible and, ideally, can operate in real-time for reliable measurements [30]. A labelled approach is normally implemented to obtain a stronger signal in the presence of biological specificity to an analyte or chemical binding, thus, improving the precision. However, this approach requires the labelling process including nanoparticles, quantum dots, fluorescent dyes, chemiluminescent molecules [20, 75, 410-416] and may not allow real-time monitoring or may increase the time for detection as is the case for magnetic particles used in Hall effect type biosensors [269]. A label-free detection approach can alternatively be implemented using electrical, mechanical and optical properties or charge interaction to monitor binding activities in real-time, thus, providing direct information about target molecules more and preventing the negative impacts of interference effects which may occur during the labelling process [30]. Therefore, in this study, graphene Hall effect devices were decided to be used for biosensing purposes by employing a label-free detection approach in order to be able to observe the response of the devices in real-time as well as reducing the need for costly electronics which require for labelled detection scheme [107].

Covalent binding approach can be employed to achieve label-free detection, however, the electronic structure of graphene is disturbed if the binding event takes place with this method since the it occurs at carbon atoms near grain boundaries and defects [375] meaning that there must be considerable amount of defects to adopt covalent binding. However, as it can be seen from Raman and XPS spectra presented in previous section (Figure 7-4), the fabricated devices consist of monolayer of graphene with no considerable functional groups. Pristine graphene is considered to be an oxide free material and demonstrates π–π stacking, non-covalent interaction and strong electrostatic force besides providing a vast surface area at molecular level [30]. Therefore, the functionalization can be performed non-covalently for binding the functional groups of graphene [417-419] which will also prevent the disruption of electronic properties. Non-covalent modification includes ionic bonds, Van der Waals forces, π–π stacking interactions, hydrogen bonding and coordination bonds [19]. To be able to achieve non-covalent functionalization, pyrene derivatives can be adopted since it was discovered to interact with graphene non-covalently via π-stacking [376]. Therefore, 1-pyrenecarboxylic acid was used in this study for surface modification and this helped creating a label-free detection scheme as explained in the following section.

7.4.2 Detection Protocol

Detection protocol was designed to include two main approaches, namely, positive and negative control. Positive control procedure was designed to observe the behaviour of devices in the presence of specific antigen. In this study, anti-mouse IgG was chosen to be used as specific target analyte. On the other hand, negative control was designed under two headlines. The first approach for negative control was to test the device response in the vicinity of non-specific target antigens. For this study, anti-goat IgG was employed for this purpose. The second approach for negative control was to observe the behaviour of the devices where there is no capture antibody immobilized on the surface. To do so, surface was modified but without adding capture IgG on and the rest of the procedure was the same as positive control scheme.

The assessment procedure began with implementing the steps defined by positive control procedure. Initially, 100 µL of PBS buffer was added on the surface and the output of the device was recorder under the presence of this solution without implementing any surface modification process. Then, PBS solution was removed from the surface and it was rinsed with methanol. After rinsing, 5 mM of 1-Pyrenecarboxylic acid was inserted on the surface and kept for 1.5 hours to allow interaction with graphene. The surface was then rinsed with methanol and PBS respectively, following the interaction process. The output of the device was observed in PBS medium for the second time to check for any change after graphene and pyrene interaction. The procedure followed by rinsing the surface with MES buffer and adding NHS/EDC solution in 1:1 ratio. The device was kept under this solution for 15 minutes and then it was quickly rinsed with PBS solution. Mouse IgG, having a concentration of 20 µg/ml, was immobilized to the surface of graphene by adding it on the surface and leaving for 1 hour. The latter bio-element was used as capture antibody for specific biomolecule recognition. The immobilization was followed by PBS rinse and observing the device output under the presence of this solution for the third time to analyse for any signal change. To prevent any non-specific binding event, BSA was used as a blocking agent (2 %) to block any binding sites. It was added on the surface and remained for 1 hour followed by another PBS rinse. The output of the devices was observed for the fourth time in PBS. Lastly, anti-mouse IgG of 20 µg/ml was injected on the surface and kept for 1 hour to allow binding. The last step was followed by PBS rinse and the output observation for the fifth time under PBS presence. The protocol for positive control scheme is demonstrated in Figure 7-6. It is worth to note that this figure illustrates the procedure only for positive control in a brief manner. Therefore, observing an output change is of importance. The process needs to demonstrate a measurable change to confirm a successfully performed stage. As a result, the process was defined to include verification steps so that in case of the observation of no change, the initial stage would be performed from the beginning by cleaning devices or using new ones.

The procedures for non-specific antigen and no capture antibody cases were designed to be slightly different than that of shown in Figure 7-6. To observe the behaviour of the devices for non-specific biomolecules, anti-goat IgG was used instead of anti-mouse IgG. Apart from employing anti-goat IgG, all other steps were the same as given in the figure. Meanwhile, in the last step of the process (before record the output), the output needs to be recorded whether there is any change or not. In other words, the process would not return the initial stage if a change is observed although a non-specific binding should not occur for an appropriately performing device which would not produce a measurable difference. If, for any reason, non-specific binding occurs, then it would be easier to observe by following the latter procedure. Therefore, the performance of the devices would clearly be presented in terms of sensitivity and selectivity of specified targets.

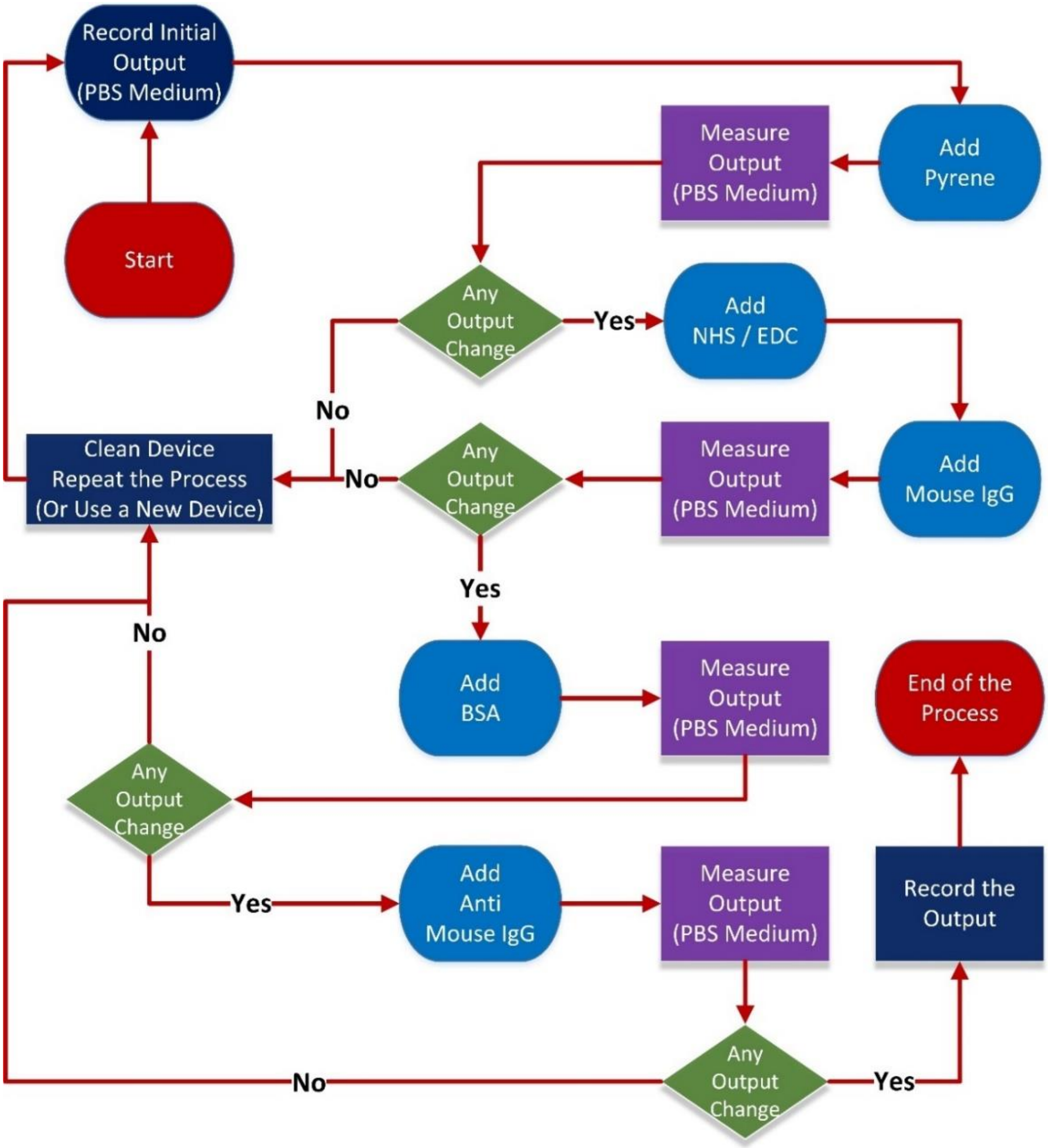

Figure 7-6: Positive control protocol for detecting IgG.

For the case where there is no capture antibody, the stage shown for surface modification with capture antibody was not performed, instead, blocking agent (BSA) was used to block any available binding sites. To clarify, the stage depicted as “add mouse IgG” in Figure 7-6 should be used as “add BSA” followed by the actual BSA stage shown in the figure. The second blocking stage was to make sure that the blocking stage was performed thoroughly. At the end of the process, anti-mouse IgG was used to assess the selectivity of the devices.

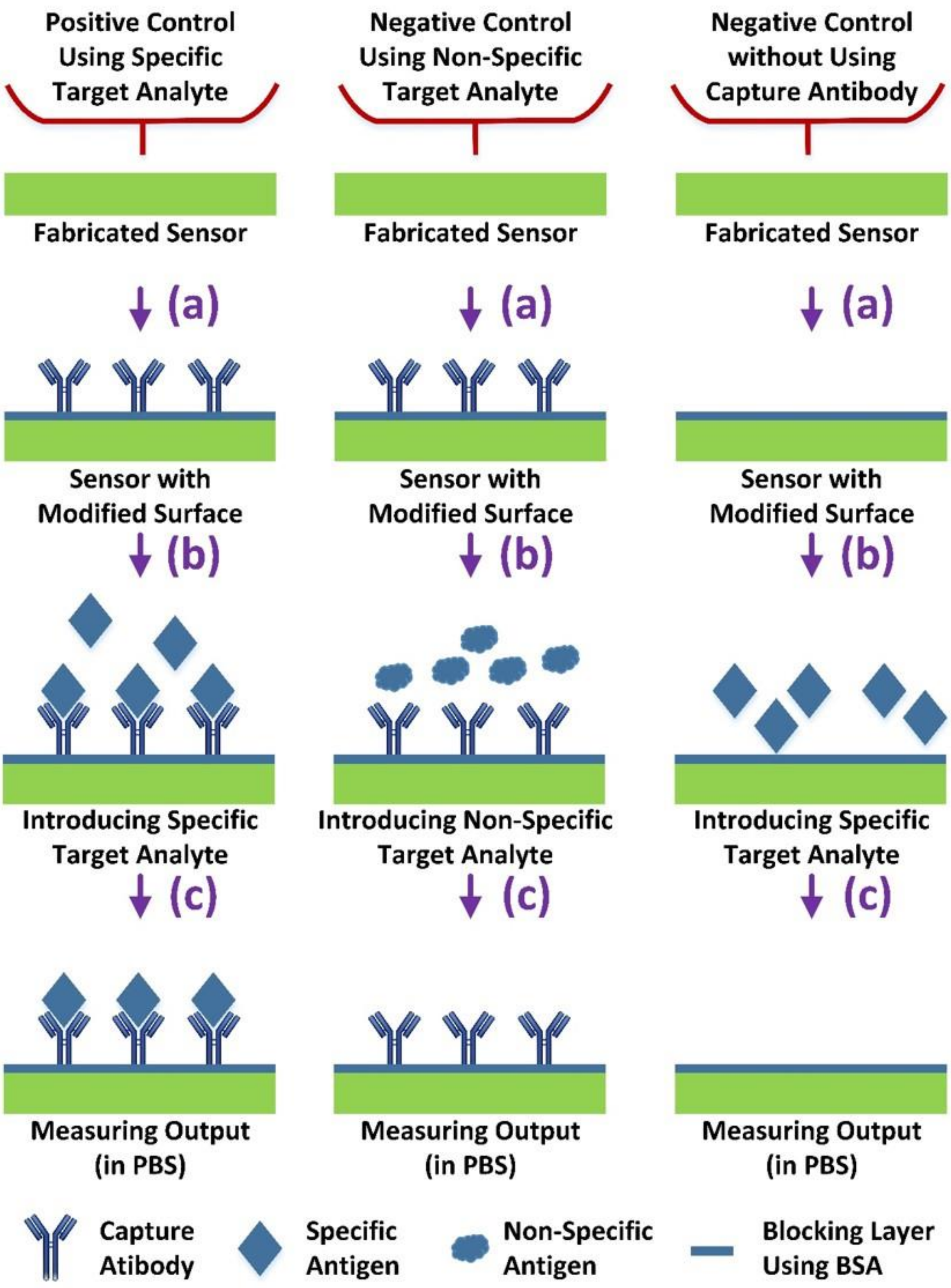

Figure 7-7: The illustration of control steps for specific (left column) and non-specific (middle column) antigens along with no-capture antibody (right column) cases. All three cases include surface modification with blocking stage (a), injection of target analytes (b) and observation of behaviour by measuring the output (c).

As was the case for the previous negative control scheme, in the last stage no output change should be observed for an appropriately functioning device.

However, the procedure was designed to record the output without looking whether there is any change or not to ensure the capability of devices for assessing the sensitivity and the selectivity thoroughly. Figure 7-7 illustrates antibody-antigen interactions which was expected to occur by employing the methods explained for positive and negative control schemes. The left column in the figure is an interpretation of the positive control steps that were used to check the sensor output in the presence of specific target analyte. Likewise, the middle and the right columns are representing interactions between non-specific antibody-antigen and surface-analyte in case of no capture antibody, respectively.

7.5 Results and Discussion

The next challenge was to illustrate how sensitive are the developed biosensors in terms of detecting the specified bio-elements. This section provides a quantitative analysis in terms of selectivity, sensitivity and repeatability. Initially, devices were assessed in terms of their feasibility to operate in liquid environment. To do so, ultra-pure water was injected on the surface of the sensor with the aid of formed reservoir. As can be seen from Figure 7-8, the obtained output presented a desirable characteristic meaning that the polarity of the output changes whilst the magnetic field is applied in the reverse polarity which follows the characteristic behaviour of a Hall device.

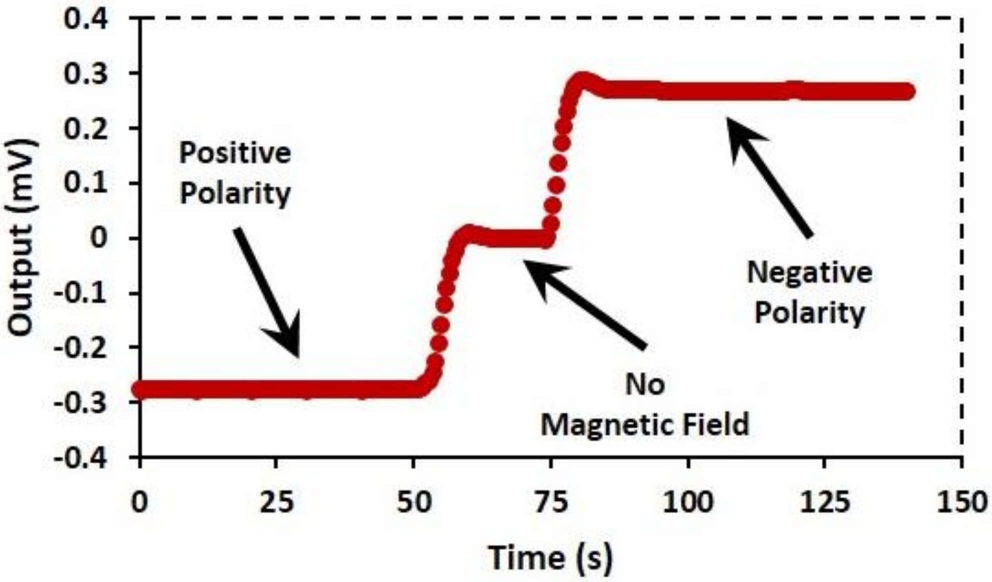

Figure 7-8: The behaviour of the sensor with respect to polarity of the applied magnetic field.

Secondly, the devices were evaluated with respect to the concentration of the solution to observe whether there is any significant change depending on the concentration. Glycerol (w ⁄ v changing from 0 % to 40 %) was employed in order to satisfy this requirement. The change in the output with respect to concentration of glycerol is shown in Figure 7-9. As is seen, the output tends to rise with the increase of concentration. The latter case suggests that there must be a base solution to observe any difference after performing each stage explained in section 7.4.2. Therefore, PBS solution was used between different stages to examine the characteristics of the devices.

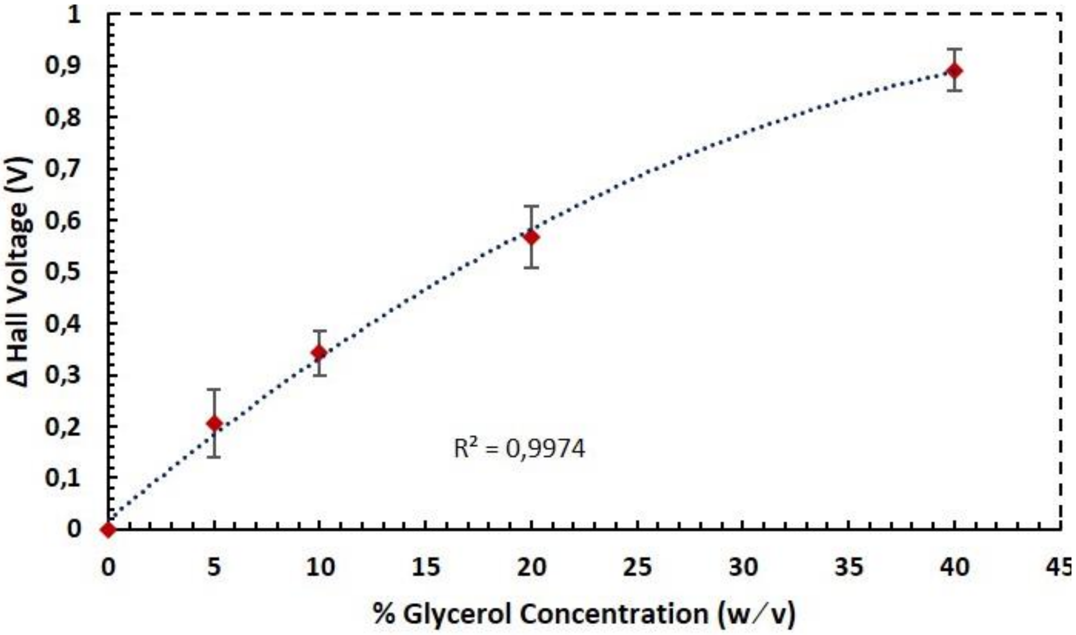

Figure 7-9: Change in Hall voltage with respect to glycerol concentration (weigh / volume) showing rising output (n=3).

The behaviour of the devices was assessed by employing the control mechanisms described in the previous section to discover the feasibility as a biosensor and to determine the performance in terms of detection capability of specific target analytes. The main expectation in a biosensor is to observe a measurable signal change whilst specific target antigens are introduced which should occur due to antibody-antigen interaction. To confirm the signal change, PBS solution was used as a reference base and the sensor output was recorded after each step. All measurements were performed under 10 μA driving current with a magnetic field of 120 mT. Due to performance variation across fabricated devices (see section 6.4) data was normalised with respect to the change observed in the first step. Figure 7-10 shows the normalized data with respect to pyrene change for each step indicated in the figure. After each step, a measurable signal change has been observed with respect to the sensors previous stage which both confirmed the surface modification and antibody-antigen interactions.

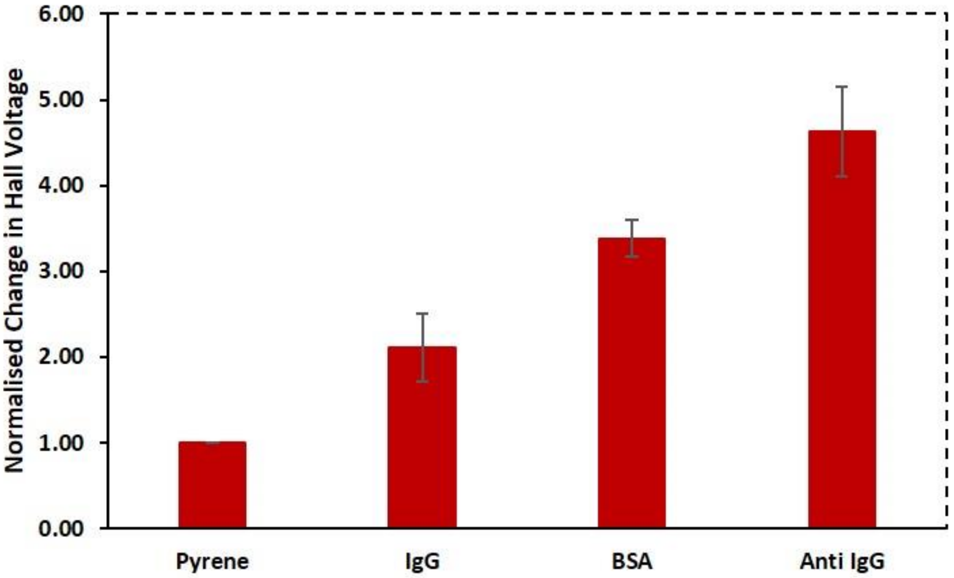

Figure 7-10: The obtained data by normalising all steps with respect to pyrene change (n=6) using positive control scheme.

Furthermore, the verification was performed by observing the output of the device in real-time during each step as indicated in Figure 7-11. The figure shows the real-time data which presents the change of the output with respect to initial measurements of each step. As can be seen from the figure, a change is observed in each stage from pyrene addition (a) and surface modification with capture antibody (b) to blocking the surface for non-specific targets (c) along with the addition of specific antigens (d). The change in the voltage can be explained by charge interactions between graphene and the added materials which consequently altering the performance of the Hall devices and creating a considerable difference with respect to sensor's initial state during each step.

The second requirement in a biosensor is not to allow the binding of the non-specific target analytes and consequently not to produce any measurable signal difference compared to its previous stage. To assess the behaviour for this requirement, the approach given in the middle column of the Figure 7-7 has been employed as a negative control scheme using non-specific target antigen. Similar to the positive control scheme, the sensor surface was modified so that it contained mouse IgG as capture antibody. However, non-specific target analyte (Anti-goat IgG) was introduced instead of specific antigen (middle column, after process (b)).

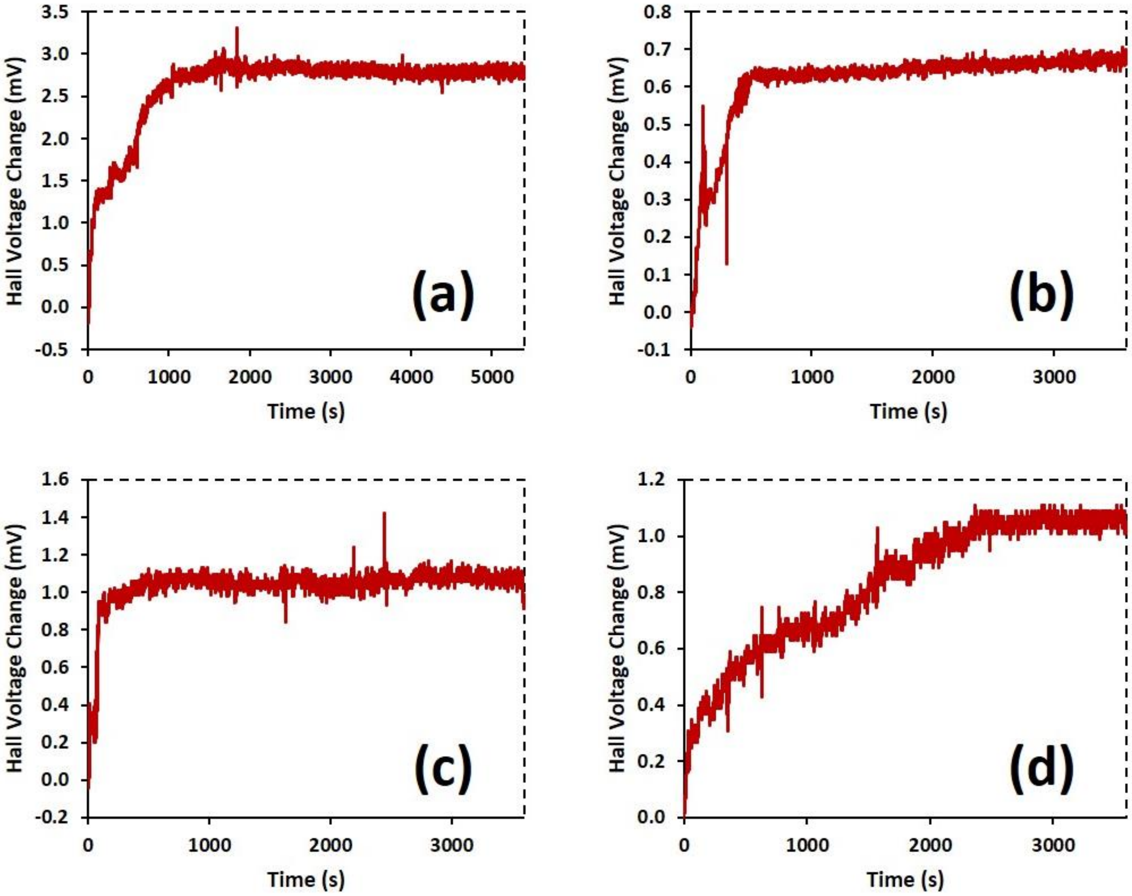

Figure 7-11: Real-time data showing the output change with respect to the initial measurement of each process. A clear change can be observed for pyrene addition (a), surface modification with capture mouse IgG (b), blocking with BSA (c) and anti-mouse IgG (d) for specific target analyte processes.

The output of the devices was recorded in PBS medium after each step and related data were normalised with respect to pyrene change, as shown in Figure 7-12, for a better representation. It is clearly seen that there is not any considerable measurable signal comparing with the recorded output of the previous stage after addition of non-specific antigen. This confirms that no interaction occurred between capture antibody and non-specific target antigen. The observed behaviour of the devices indicated that they are sensitive to specified biomolecule. Similar to the positive control scheme, real-time data were also used in conjunction with the PBS base measurements for further verification. As can be seen from Figure 7-13, the surface modification processes have led to an output change (a, b, c) whereas no change was observed during the stage where non-specific antigen was introduced (d).

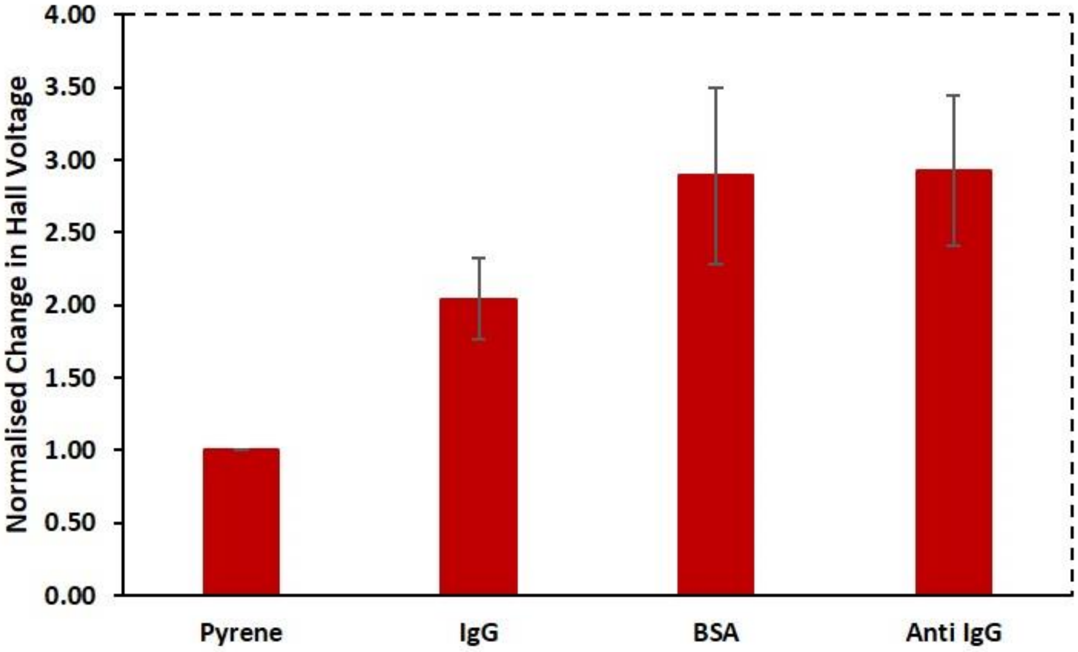

Figure 7-12: The obtained data by normalising all steps with respect to pyrene change (n=4) using negative control scheme which employs non-specific target antigen.

Meanwhile, further investigation was carried out to fully characterise the behaviour of devices. The output of the sensors was also checked if any considerable change can be obtained while there is no capture antibody. The latter case was adopted as another negative control procedure which is not using capture antibody. This case must be examined to verify that the sensor is not just producing random output in the presence of any analyte. Therefore, as shown in the right column of the Figure 7-7, the surface of the sensor was modified using pyrene, however, without employing capture antibody. Apart from using mouse IgG as bioreceptor, the remaining steps were the same as explained for the positive control scheme. The obtained data for the latter case were normalised with respect to pyrene change as shown in Figure 7-14. The data clearly demonstrates no signal change after blocking stage which can be explained by no interactions between the surface of the sensor and the target analyte.

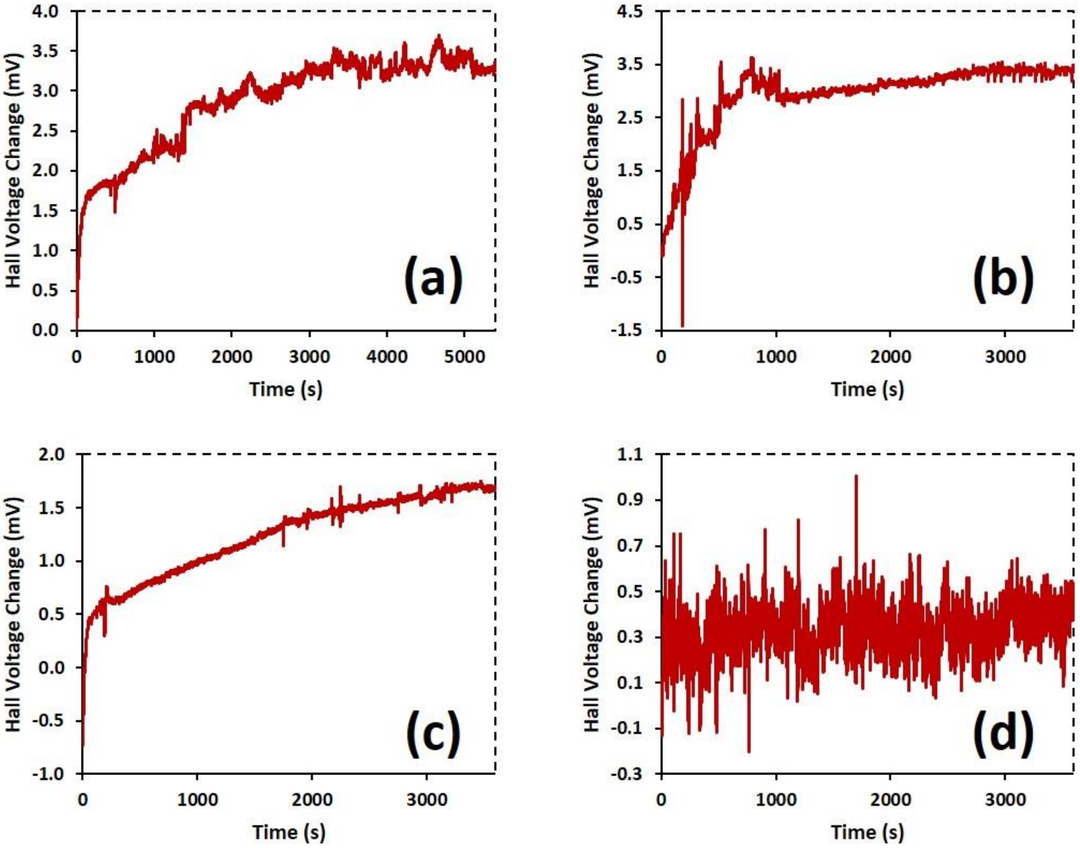

Figure 7-13: Real-time data showing the output change with respect to the initial measurement of each process. A change can be observed for pyrene addition (a), surface modification with capture mouse IgG (b) and blocking process with BSA (c). However, introducing anti-goat IgG (d) has led to no change during the process which confirms no interaction occurred between capture antibody and non-specific antigen.

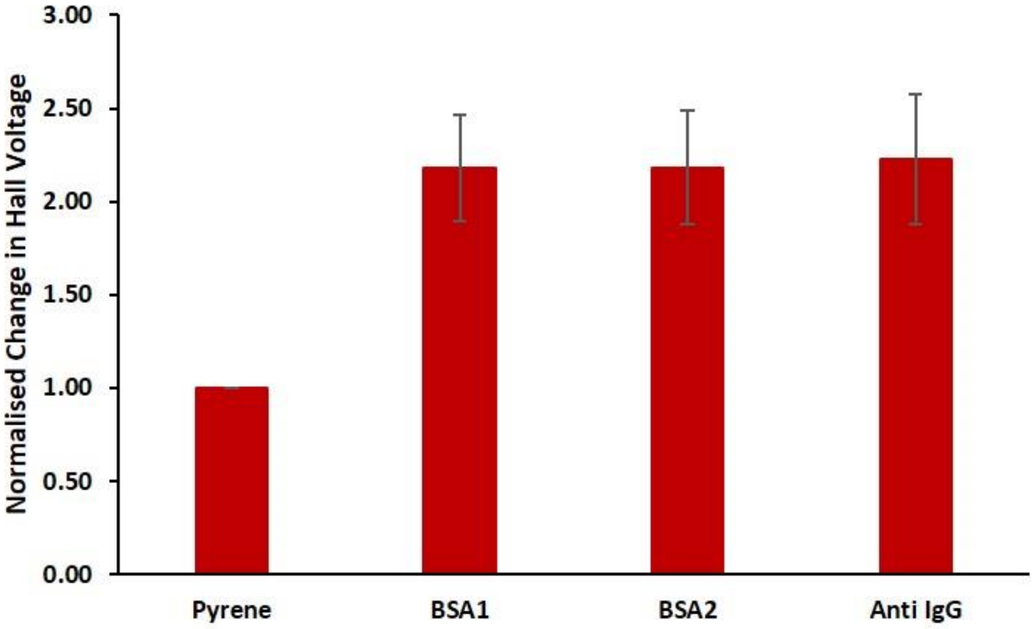

Figure 7-14: The obtained data by normalising all steps with respect to pyrene change (n=4) using negative control scheme which does not employ any capture antibody.

Similar to the case in specific and non-specific antigen detection schemes, the output characteristic of the devices was also monitored in real-time as shown in Figure 7-15. A clear change can be seen for pyrene addition which occurred due to pyrene-graphene interaction (a). Likewise, a change can be observed in surface modification (b). In this stage no capture antibody was used, instead, BSA was used to block any available binding sites. This stage was followed by one more blocking process (c) to ensure the blocking was successfully implemented. No signal change was observed for the second blocking stage which verifies the blocking process. Similarly, addition of analyte (d) did not caused any signal change which also validates the selectivity of the devices. Overall, the real-time data showed the sensor’s selectivity and verified that there is no measurable change in the output whilst there is no capturing antibody which makes the devices feasible to be used as biosensors for the specified task.

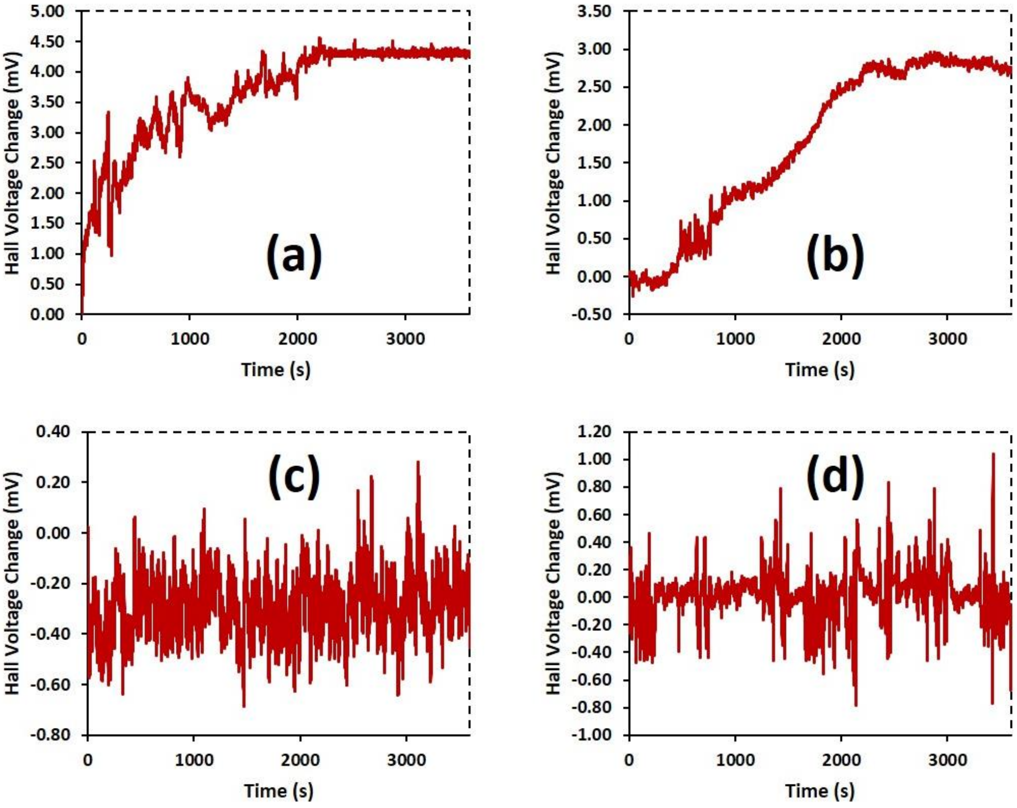

Figure 7-15: Real-time data showing the output change with respect to the initial measurement of each process. A change can be observed for pyrene addition (a), surface modification without using capture mouse IgG (b). In modification step, BSA was used to block any available binding sites instead of using capture antibody. To ensure successful blocking operation, another blocking process was performed using BSA (c). The second blocking process shows no change which verifies the successful operation. Meanwhile, introducing anti-mouse IgG (d) has led to no change during the process which confirms no interaction occurred between sensor surface and target analyte since there was no available bioreceptor on the surface.

Figure 7-16 is a 3D plot considering all the data together and demonstrates the output change per step which validates the devices to be good in terms of sensitivity and selectivity to the specific binding. Taking all the data into account, it is clear that the developed system can be used as a biosensor which is sensitive and selective to specified biomolecule and can operate in real-time without need for any labelling procedure.

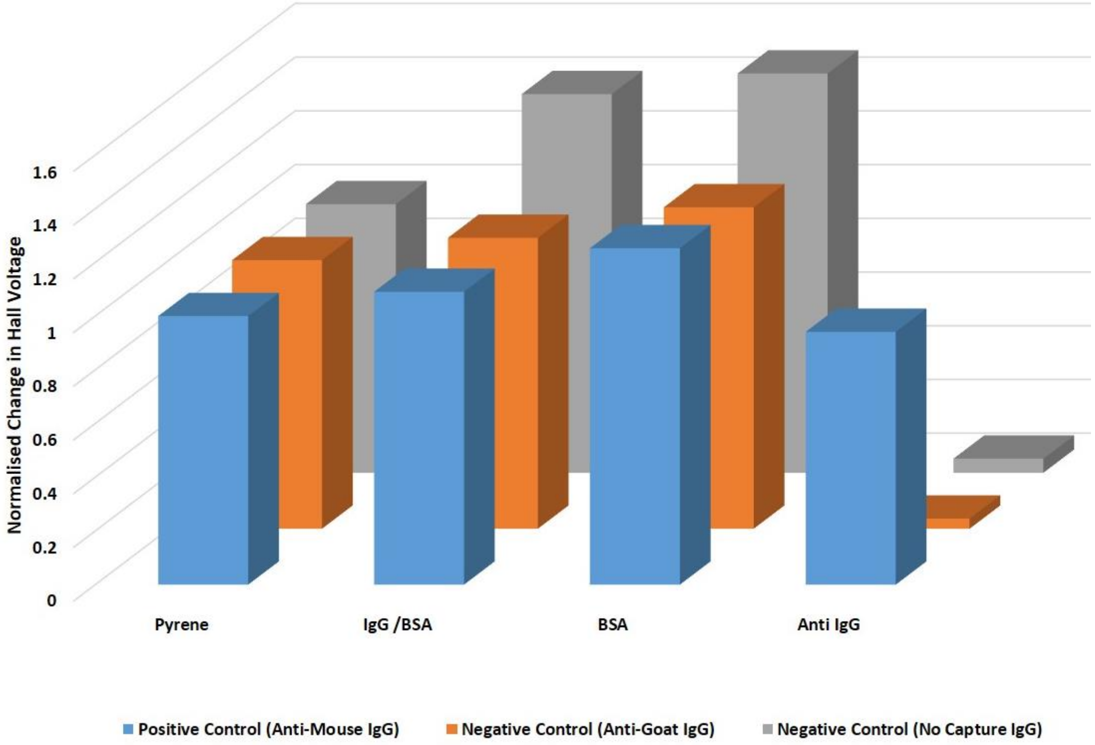

Figure 7-16: Normalised data with respect to pyrene change showing change per step with respect to its previous stage. The figure clearly demonstrates the devices to be good in terms of being sensitive only to the specific binding required.

Lastly, developed biosensors were assessed for their dynamic detection range with respect to molar concentration. To do so, similar steps given in positive control scheme were implemented using 20 µg/ml coverage of mouse IgG, however, in the last step where injection of specific antigen is required, anti-mouse IgG was added to the surface in such a way that the molar concentration changes as shown in Figure 7-17. The specific antigens were added in different molar concentrations (starting from 0 nM and keeps increasing) step by step so that the output can be observed with respect to different concentrations. Increasing molar concentrations have led to a change of the output. The resolution is reduced in higher concentrations due to saturation. A dynamic range of 1 nM to140 nM was demonstrated with potential for a wider dynamic range since the data seem to fit well to a 3rd order polynomial. The obtained minimum detection limit corresponds to 150 ng/ml.

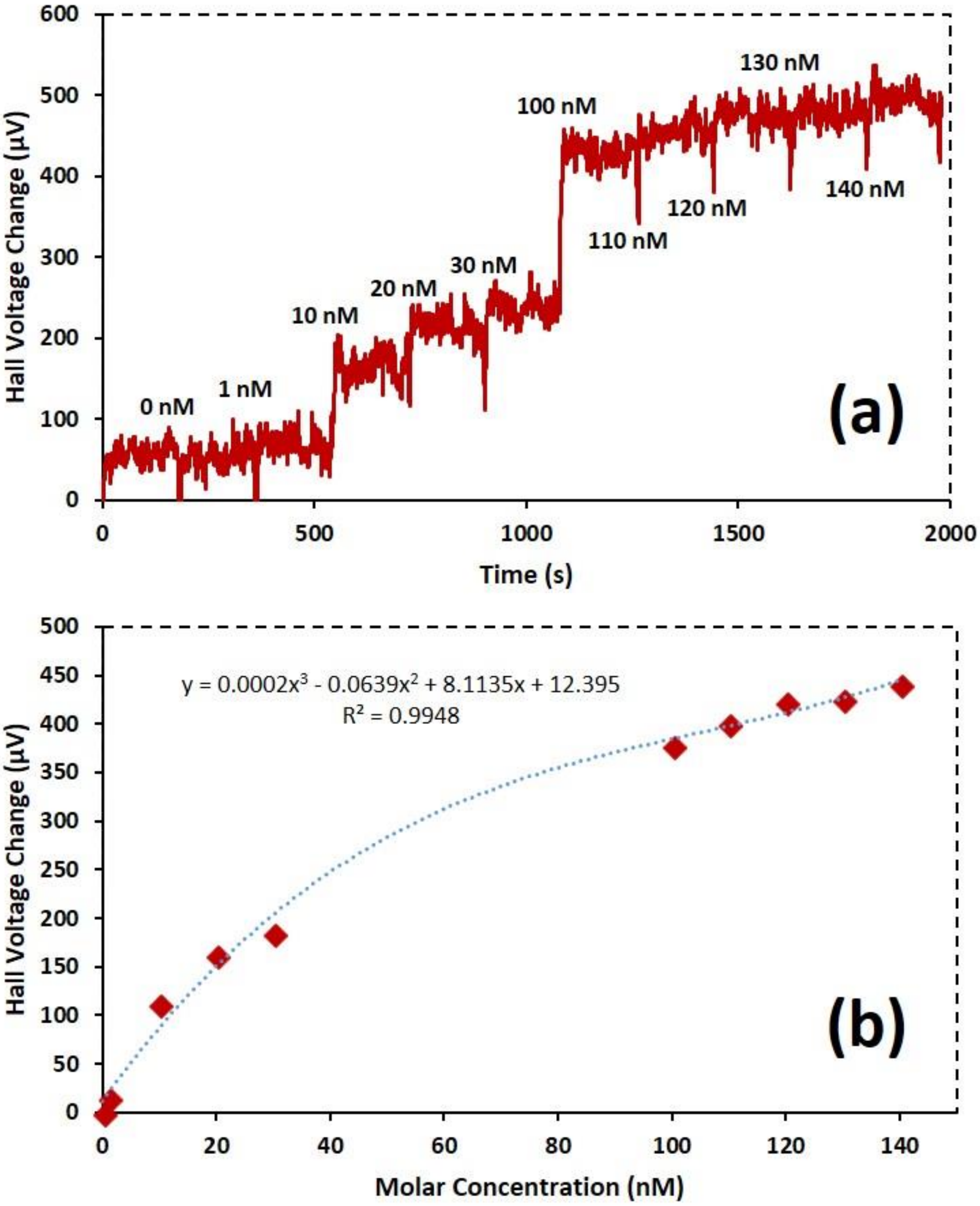

Figure 7-17: Data representing change in the output with regards to added concentration of anti-mouse IgG through the time (a). A better representation showing output change with respect to molar concentration of anti-mouse IgG (a).

As was mentioned in section 2.4.3, the Hall effect biosensors were mainly used to detect the existence of beads. Therefore, a detailed analysis which encompasses the saturation was not found in the literature to compare the results related to calibration curve. To the best of author's knowledge, this is the first work related to Hall effect biosensors which performs a thorough analysis from specific and non-specific target response to the output change with respect to concentration change.

7.6 Summary

In this work a non-covalent modification approach was employed due to low defective structure of devices. This approach was also adopted to maintain the good electronic properties of graphene samples. A label-free detection scheme was designed and implemented. It was shown that real-time monitoring of the output is feasible. Eliminating magnetic beads in such applications also helped reduce costly equipment to drive and process the output of the system. In addition, extra steps for functionalizing labels were also eliminated which preserving a considerable amount of time. A covalent functionalization approach may be considered in future for samples that have considerable number of defects. It can also be implemented by creating local defects in pristine graphene. However, this would certainly cause a deterioration in electronic properties of graphene which may consequently reduce the sensitivity of such biosensors.

In conclusion, the feasibility of a label-free graphene Hall effect biosensor was demonstrated by fabricating devices in micro-scale and developing an appropriate bio-chemical procedure. The developed biosensors were shown to be good in terms of sensitivity and selectivity of specified target molecules without need for any label. It would be expected that an optimisation of the sensor fabrication would help to reduce the current lower detection limit to below 1 nM. The upper limit looks to be higher than that of the demonstrated range since the data fits well to a 3rd order polynomial. Therefore, it appears to have a wider dynamic range towards higher concentrations.

Chapter 8. Conclusion and Future Work

8.1 Conclusion

In this work, Hall effect magnetometers were fabricated from a range of approaches. Relatively large-scale PCB sensors were used to develop the system electronics. Gold devices were then fabricated to obtain bench mark performance figures for micro fabricated devices. Finally, a range of graphene devices were developed to allow an assessment of their performance. Apart from actual device manufacturing, several routes were employed for easier graphene production and suspension. Therefore, thermal decomposition and laser heating options were investigated for epitaxial graphene growth from silicon carbide and a photoelectrochemical etching process was adopted to obtain potentially suspended graphene. Meanwhile, alternative avenues were also explored using CVD grown graphene sheets by transferring on pre-patterned substrates for suspended graphene formation. Different options such as graphene on copper and on polymer were used for the transfer process and their promise was examined in terms of applicability.

A reservoir was formed on surface of devices in order to obtain a biosensing system. An epoxy glue was used to isolate the contacts with the aid of a laser cut acrylic mask which was adopted to protect the active areas of devices during isolation process. The isolation process allowed the biosensors to operate in liquid environment. To functionalize devices, a non-covalent surface modification process took place by employing pyrene. A protocol consisting of three control steps was defined to assess the behaviour of devices. The developed biosensors have shown to be sensitive and selective to specified target molecules.

8.2 Contribution

Various options were investigated for preparing graphene and micro fabricating devices. Devices from single layer graphene samples were shown to be the best material for magnetosensing applications. To reveal potential of fabricated graphene Hall devices, a circuitry was designed and made on PCB which was used to actuate devices and process the output by dynamically removing undesired effects. The circuitry helped reduce the offset equivalent magnetic field down to 100 nT, thus, improved the accuracy of the devices significantly. Integrating this circuitry with fabricated devices, have led to a highly sensitive magnetometer [420] which reached a current-related sensitivity of 2540 V/AT [421] along with good linear behaviour.

In addition, the feasibility of suspending graphene was demonstrated which can be adopted for future device fabrication. Moreover, printed graphene oxide devices were shown to have merit for easier and cheaper device manufacturing. The most important contribution of this work was to demonstrate the feasibility of a label-free graphene Hall effect biosensor. The feasibility was demonstrated by adopting a protocol including control mechanisms to assess the performance of the developed system. This demonstration showed that the elimination of additional steps in fabrication and operation of Hall effect-based sensors are feasible which can help to develop cost-effective biosensors. The devices showed the promise which can be taken forward for future applications.

8.3 Future Work

A range of other options for device fabrication were explored, several of which showed potential for further development. Inkjet printing of graphene oxide is one of the most promising method that could be taken forward for potential future device developments. It was shown to be feasible for direct device manufacturing without need for any additional fabrication step. A thermal reduction method could be performed to reduce the oxygen content of the structure [422]. To prevent the degradation in the performance of those devices, a reversible electrical modification process presented in ref [409] could be employed to maintain the efficiency for potential biosensor development. Likewise, heating silicon carbide samples via a laser beam is another promising option for potential graphene fabrication. Optimisation works on laser power, scanning speed, and manufactured chamber could provide uniformly grown graphene sheets. The promise of this method has already been shown in a quite recent work [423] which suggests the method is feasible for future electronic device applications. Further improvement is feasible by adapting an onboard analog to digital converter (ADC) and a display along with a small magnet which will make the system more compact and eliminate all lab equipment, thus, making the system convenient to be used for end users.

References

[1] L. C. Clark, Jr., and C. Lyons, “Electrode systems for continuous monitoring in cardiovascular surgery,” *Ann N Y Acad Sci,* vol. 102, no. 1, pp. 29-45, Oct 31, 1962.

[2] A. P. Turner, “Biosensors: sense and sensibility,” *Chem Soc Rev,* vol. 42, no. 8, pp. 3184-96, Apr 21, 2013.

[3] S. Vigneshvar, C. C. Sudhakumari, B. Senthilkumaran *et al.*, “Recent Advances in Biosensor Technology for Potential Applications - An Overview,” *Front Bioeng Biotechnol,* vol. 4, no. 11, pp. 11, 2016-February-16, 2016.

[4] G. Maduraiveeran, M. Sasidharan, and V. Ganesan, “Electrochemical sensor and biosensor platforms based on advanced nanomaterials for biological and biomedical applications,” *Biosens Bioelectron,* vol. 103, pp. 113-129, Apr 30, 2018.

[5] K. S. Novoselov, D. Jiang, F. Schedin *et al.*, “Two-dimensional atomic crystals,” *Proc Natl Acad Sci U S A,* vol. 102, no. 30, pp. 10451-3, Jul 26, 2005.

[6] K. S. Novoselov, A. K. Geim, S. V. Morozov *et al.*, “Electric field effect in atomically thin carbon films,” *Science,* vol. 306, no. 5696, pp. 666-9, Oct 22, 2004.

[7] X. Yu, W. Zhang, P. Zhang *et al.*, “Fabrication technologies and sensing applications of graphene-based composite films: Advances and challenges,” *Biosens Bioelectron,* vol. 89, no. Pt 1, pp. 72-84, Mar 15, 2017.

[8] X. N. Zang, Q. Zhou, J. Y. Chang *et al.*, “Graphene and carbon nanotube (CNT) in MEMS/NEMS applications,” *Microelectronic Engineering,* vol. 132, pp. 192-206, Jan 25, 2015.

[9] P. Xu, J. Kang, J. B. Choi *et al.*, “Laminated ultrathin chemical vapor deposition graphene films based stretchable and transparent high-rate supercapacitor,” *ACS Nano,* vol. 8, no. 9, pp. 9437-45, Sep 23, 2014.

[10] J. N. Dash, and R. Jha, “Graphene-Based Birefringent Photonic Crystal Fiber Sensor Using Surface Plasmon Resonance,” *IEEE Photonics Technology Letters,* vol. 26, no. 11, pp. 1092-1095, Jun 1, 2014.

[11] J. S. Moon, D. Curtis, D. Zehnder *et al.*, “Low-Phase-Noise Graphene FETs in Ambipolar RF Applications,” *IEEE Electron Device Letters,* vol. 32, no. 3, pp. 270-272, Mar, 2011.

[12] E. W. Hill, A. Vijayaragahvan, and K. Novoselov, “Graphene Sensors,” *IEEE Sensors Journal,* vol. 11, no. 12, pp. 3161-3170, Dec, 2011.

[13] M. D. Stoller, S. Park, Y. Zhu *et al.*, “Graphene-based ultracapacitors,” *Nano Lett,* vol. 8, no. 10, pp. 3498-502, Oct, 2008.

[14] J. T. Robinson, M. Zalalutdinov, J. W. Baldwin *et al.*, “Wafer-scale reduced graphene oxide films for nanomechanical devices,” *Nano Lett,* vol. 8, no. 10, pp. 3441-5, Oct, 2008.

[15] F. Schedin, A. K. Geim, S. V. Morozov *et al.*, “Detection of individual gas molecules adsorbed on graphene,” *Nat Mater,* vol. 6, no. 9, pp. 652-5, Sep, 2007.

[16] J. Singh, A. Rathi, M. Rawat *et al.*, “Graphene: from synthesis to engineering to biosensor applications,” *Frontiers of Materials Science,* vol. 12, no. 1, pp. 1-20, Mar, 2018.

[17] J. Shi, and Y. Fang, "Biomedical Applications of Graphene," *Graphene*, pp. 215-232: Academic Press, 2018.

[18] P. Salvo, B. Melai, N. Calisi *et al.*, “Graphene-based devices for measuring pH,” *Sensors and Actuators B-Chemical,* vol. 256, pp. 976-991, Mar, 2018.

[19] Q. Zhang, Z. Wu, N. Li *et al.*, “Advanced review of graphene-based nanomaterials in drug delivery systems: Synthesis, modification, toxicity and application,” *Mater Sci Eng C Mater Biol Appl,* vol. 77, pp. 1363-1375, Aug 1, 2017.

[20] M. Hernaez, C. R. Zamarreno, S. Melendi-Espina *et al.*, “Optical Fibre Sensors Using Graphene-Based Materials: A Review,” *Sensors (Basel),* vol. 17, no. 1, pp. 155, Jan 14, 2017.

[21] R. Forsyth, A. Devadoss, and O. J. Guy, “Graphene Field Effect Transistors for Biomedical Applications: Current Status and Future Prospects,” *Diagnostics (Basel),* vol. 7, no. 3, Jul 26, 2017.

[22] Y. Xu, and J. Liu, “Graphene as Transparent Electrodes: Fabrication and New Emerging Applications,” *Small,* vol. 12, no. 11, pp. 1400-19, Mar, 2016.

[23] N. A. A. Ghany, S. A. Elsherif, and H. T. Handal, “Revolution of Graphene for different applications: State-of-the-art,” *Surfaces and Interfaces,* vol. 9, pp. 93-106, Dec, 2017.

[24] X. Wan, Y. Huang, and Y. Chen, “Focusing on energy and optoelectronic applications: a journey for graphene and graphene oxide at large scale,” *Acc Chem Res,* vol. 45, no. 4, pp. 598-607, Apr 17, 2012.

[25] N. O. Weiss, H. Zhou, L. Liao *et al.*, “Graphene: an emerging electronic material,” *Adv Mater,* vol. 24, no. 43, pp. 5782-825, Nov 14, 2012.

[26] A. H. Castro Neto, F. Guinea, N. M. R. Peres *et al.*, “The electronic properties of graphene,” *Reviews of Modern Physics,* vol. 81, pp. 109-162, 2009.

[27] K. I. Bolotin, K. J. Sikes, Z. Jiang *et al.*, “Ultrahigh electron mobility in suspended graphene,” *Solid State Communications,* vol. 146, no. 9-10, pp. 351-355, Jun, 2008.

[28] R. Kumar, R. Singh, D. Hui *et al.*, “Graphene as biomedical sensing element: State of art review and potential engineering applications,” *Composites Part B-Engineering,* vol. 134, pp. 193-206, Feb 1, 2018.

[29] G. H. Yang, D. D. Bao, H. Liu *et al.*, “Functionalization of Graphene and Applications of the Derivatives,” *Journal of Inorganic and Organometallic Polymers and Materials,* vol. 27, no. 5, pp. 1129-1141, Sep, 2017.

[30] P. Suvarnaphaet, and S. Pechprasarn, “Graphene-Based Materials for Biosensors: A Review,” *Sensors (Basel),* vol. 17, no. 10, Sep 21, 2017.

[31] G. Reina, J. M. Gonzalez-Dominguez, A. Criado *et al.*, “Promises, facts and challenges for graphene in biomedical applications,” *Chem Soc Rev,* vol. 46, no. 15, pp. 4400-4416, Jul 31, 2017.

[32] C. I. L. Justino, A. R. Comes, A. C. Freitas *et al.*, “Graphene based sensors and biosensors,” *Trac-Trends in Analytical Chemistry,* vol. 91, pp. 53-66, Jun, 2017.

[33] N. Chauhan, T. Maekawa, and D. N. S. Kumar, “Graphene based biosensors-Accelerating medical diagnostics to new-dimensions,” *Journal of Materials Research,* vol. 32, no. 15, pp. 2860-2882, Aug, 2017.

[34] Y. Song, Y. Luo, C. Zhu *et al.*, “Recent advances in electrochemical biosensors based on graphene two-dimensional nanomaterials,” *Biosens Bioelectron,* vol. 76, pp. 195-212, Feb 15, 2016.

[35] S. Wu, Q. He, C. Tan *et al.*, “Graphene-based electrochemical sensors,” *Small,* vol. 9, no. 8, pp. 1160-72, Apr 22, 2013.

[36] H. Y. Mao, S. Laurent, W. Chen *et al.*, “Graphene: promises, facts, opportunities, and challenges in nanomedicine,” *Chem Rev,* vol. 113, no. 5, pp. 3407-24, May 8, 2013.

[37] X. Huang, Z. Zeng, Z. Fan *et al.*, “Graphene-based electrodes,” *Adv Mater,* vol. 24, no. 45, pp. 5979-6004, Nov 27, 2012.

[38] M. Pumera, “Graphene in biosensing,” *Materials Today,* vol. 14, no. 7-8, pp. 308-315, Jul-Aug, 2011.

[39] T. Kuila, S. Bose, P. Khanra *et al.*, “Recent advances in graphene-based biosensors,” *Biosens Bioelectron,* vol. 26, no. 12, pp. 4637-48, Aug 15, 2011.

[40] R. Monošík, M. Streďanský, and E. Šturdík, "Biosensors - classification, characterization and new trends," *Acta Chimica Slovaca*, 1, 2012, p. 109.

[41] S. P. Mohanty, and E. Kougianos, “Biosensors: a tutorial review,” *IEEE Potentials,* vol. 25, no. 2, pp. 35-40, 2006.

[42] K. R. Sopka, "The Discovery of the Hall Effect: Edwin Hall’s Hitherto Unpublished Account," *The Hall Effect and Its Applications*, C. L. Chien and C. R. Westgate, eds., pp. 523-545, Boston, MA: Springer US, 1980.

[43] R. S. Popović, *Hall effect devices*, 2nd ed.: Philadelphia : Institute of Physics Pub., 2004.

[44] E. Ramsden, *Hall-Effect Sensors - Theory and Application*, 2nd ed.: Elsevier, 2006.

[45] J. B. Zheng, and A. Liu, “The application of new magnetic sensors for traffic surveillance,” *Proceedings of the 3rd International Conference of Electronic Engineering and Information Science, ICEEIS 2016*, pp. 375-378, 2017.

[46] M. Le, J. Kim, J. Kim *et al.*, “Nondestructive testing of moisture separator reheater tubing system using Hall sensor array,” *Nondestructive Testing and Evaluation,* vol. 33, no. 1, pp. 35-44, 2017.

[47] D. P. Renella, S. Spasic, S. Dimitrijevic *et al.*, “An overview of commercially available teslameters for applications in modern science and industry,” *Acta IMEKO,* vol. 6, no. 1, pp. 43-49, 2017.

[48] M. Diaz-Michelena, “Small magnetic sensors for space applications,” *Sensors (Basel),* vol. 9, no. 4, pp. 2271-88, 2009.

[49] J. Lenz, and A. S. Edelstein, “Magnetic sensors and their applications,” *IEEE Sensors Journal,* vol. 6, no. 3, pp. 631-649, Jun, 2006.

[50] T. Suresh, B. M. S. Sivesha, S. Arun *et al.*, “Automatic railway gate control using magnetic sensors,” *Journal of Advanced Research in Dynamical and Control Systems,* vol. 9, no. Special Issue 17, pp. 1016-1025, 2017.

[51] M. Urbański, M. Nowicki, R. Szewczyk *et al.*, "Flowmeter Converter Based on Hall Effect Sensor," *Advances in Intelligent Systems and Computing*, 2015, pp. 265-276.

[52] M. Bodnicki, P. Pakuła, and M. Zowade, "Miniature displacement sensor," *Advanced Mechatronics Solutions*, Advances in Intelligent Systems and Computing R. Jabłoński and T. Brezina, eds., pp. 313-318: Springer International Publishing, 2016.

[53] R. S. Popovic, “High resolution Hall magnetic sensors,” *Proceedings of the International Conference on Microelectronics, ICM*, pp. 69-74, 2014.

[54] O. Petruk, R. Szewczyk, J. Salach *et al.*, "Digitally controlled current transformer with hall sensor," *Advances in Intelligent Systems and Computing*, 2014, pp. 641-647.

[55] A. Manzin, and V. Nabaei, “Modelling of micro-Hall sensors for magnetization imaging,” *Journal of Applied Physics,* vol. 115, no. 17, May 7, 2014.

[56] S. Kurisu, D. Tadokoro, T. Matsuda *et al.*, “Detection of 2D and 3D distributions of magnetic field by moving a poly-Si micro Hall device,” *Proceedings of the 20th International Workshop on Active-Matrix Flatpanel Displays and Devices: TFT Technologies and FPD Materials, AM-FPD 2013*, pp. 145-146, 2013.

[57] G. Mihajlovic, A. Hoffmann, and S. von Molnar, “Micro-Hall position sensing of magnetic nanowires,” *Journal of Applied Physics,* vol. 106, no. 7, Oct 1, 2009.

[58] S. Reis, N. Castro, M. P. Silva *et al.*, “Fabrication and Characterization of High-Performance Polymer-Based Magnetoelectric DC Magnetic Field Sensors Devices,” *Ieee Transactions on Industrial Electronics,* vol. 64, no. 6, pp. 4928-4934, Jun, 2017.

[59] I. Duran, S. Entler, M. Kocan *et al.*, “Development of Bismuth Hall sensors for ITER steady state magnetic diagnostics,” *Fusion Engineering and Design,* vol. 123, pp. 690-694, Nov, 2017.

[60] B. I. Avdochenko, G. F. Karlova, and V. I. Yurchenko, “Weak magnetic field detectors based on Hall-effect sensors,” *13th International Scientific-Technical Conference on Actual Problems of Electronic Instrument Engineering, APEIE 2016,* vol. 1, pp. 91-93, 2016.

[61] V. N. Matveev, V. I. Levashov, O. V. Kononenko *et al.*, “Hall effect sensors on the basis of carbon material,” *Materials Letters,* vol. 158, pp. 384-387, Nov 1, 2015.

[62] R. S. Popovic, P. M. Drljaca, and C. Schott, “Bridging the gap between AMR, GMR, and Hall magnetic sensors,” *23rd International Conference on Microelectronics, MIEL 2002,* vol. 1, pp. 55-58, 2002.

[63] H. Xu, Z. Zhang, R. Shi *et al.*, “Batch-fabricated high-performance graphene Hall elements,” *Sci Rep,* vol. 3, pp. 1207, 2013.

[64] G. Research, *Magnetic Sensors Market Analysis By Technology (Hall Effect Sensing, AMR, GMR), By Application (Automotive, Consumer Electronics, Industrial) And Segment Forecasts To 2022,* 978-1-68038-161-0, 2016.

[65] O. Kazakova, V. Panchal, J. Gallop *et al.*, “Ultrasmall particle detection using a submicron Hall sensor,” *Journal of Applied Physics,* vol. 107, no. 9, May 1, 2010.

[66] E. Kojima, K. Kano, H. Wado *et al.*, “Magnetic Field Sensor of Graphene for Automotive Applications,” in SAE Technical Paper Series, 2017.

[67] M. Kachniarz, O. Petruk, J. Salach *et al.*, “Functional Properties of Monolayer and Bilayer Graphene Hall-Effect Sensors,” *Acta Physica Polonica A,* vol. 131, no. 5, pp. 1250-1253, May, 2017.

[68] Z. Wang, M. Shaygan, M. Otto *et al.*, “Flexible Hall sensors based on graphene,” *Nanoscale,* vol. 8, no. 14, pp. 7683-7, Apr 14, 2016.

[69] L. Huang, Z. Zhang, B. Chen *et al.*, “Flexible graphene hall sensors with high sensitivity,” *IEEE International Electron Devices Meeting (IEDM)*, 2015.

[70] J. Dauber, A. A. Sagade, M. Oellers *et al.*, “Ultra-sensitive Hall sensors based on graphene encapsulated in hexagonal boron nitride,” *Applied Physics Letters,* vol. 106, no. 19, May 11, 2015.

[71] L. Huang, Z. Y. Zhang, B. Y. Chen *et al.*, “Ultra-sensitive graphene Hall elements,” *Applied Physics Letters,* vol. 104, no. 18, May 5, 2014.

[72] V. Panchal, K. Cedergren, R. Yakimova *et al.*, “Small epitaxial graphene devices for magnetosensing applications,” *Journal of Applied Physics,* vol. 111, no. 7, Apr 1, 2012.

[73] D. Issadore, Y. I. Park, H. Shao *et al.*, “Magnetic sensing technology for molecular analyses,” *Lab Chip,* vol. 14, no. 14, pp. 2385-97, Jul 21, 2014.

[74] K. Skucha, P. Liu, M. Megens *et al.*, “A compact Hall-effect sensor array for the detection and imaging of single magnetic beads in biomedical assays,” *16th International Solid-State Sensors, Actuators and Microsystems Conference, TRANSDUCERS'11*, pp. 1833-1836, 2011.

[75] B. Wang, U. Akiba, and J. I. Anzai, “Recent Progress in Nanomaterial-Based Electrochemical Biosensors for Cancer Biomarkers: A Review,” *Molecules,* vol. 22, no. 7, pp. 1048, Jun 24, 2017.

[76] A. Touhami, *Biosensors and Nanobiosensors: Design and Applications*, 2014.

[77] M. L. Sin, K. E. Mach, P. K. Wong *et al.*, “Advances and challenges in biosensor-based diagnosis of infectious diseases,” *Expert Rev Mol Diagn,* vol. 14, no. 2, pp. 225-44, Mar, 2014.

[78] M. Gonzalez-Gonzalez, R. Jara-Acevedo, S. Matarraz *et al.*, “Nanotechniques in proteomics: protein microarrays and novel detection platforms,” *Eur J Pharm Sci,* vol. 45, no. 4, pp. 499-506, Mar 12, 2012.

[79] C. B. Jacobs, M. J. Peairs, and B. J. Venton, “Review: Carbon nanotube based electrochemical sensors for biomolecules,” *Anal Chim Acta,* vol. 662, no. 2, pp. 105-27, Mar 10, 2010.

[80] V. Nabaei, R. Chandrawati, and H. Heidari, “Magnetic biosensors: Modelling and simulation,” *Biosens Bioelectron,* vol. 103, pp. 69-86, Apr 30, 2018.

[81] T. Takamura, P. J. Ko, J. Sharma *et al.*, “Magnetic-particle-sensing based diagnostic protocols and applications,” *Sensors (Basel),* vol. 15, no. 6, pp. 12983-98, Jun 4, 2015.

[82] J. Llandro, J. J. Palfreyman, A. Ionescu *et al.*, “Magnetic biosensor technologies for medical applications: a review,” *Med Biol Eng Comput,* vol. 48, no. 10, pp. 977-98, Oct, 2010.

[83] T. Wang, Z. Yang, C. Lei *et al.*, “A giant magnetoimpedance sensor for sensitive detection of streptavidin-coupled Dynabeads,” *Physica Status Solidi a-Applications and Materials Science,* vol. 211, no. 6, pp. 1389-1394, Jun, 2014.

[84] M. F. Hansen, and G. Rizzi, “Exchange-Biased AMR Bridges for Magnetic Field Sensing and Biosensing,” *IEEE Transactions on Magnetics,* vol. 53, no. 4, pp. 1-11, Apr, 2017.

[85] G. Rizzi, F. W. Osterberg, A. D. Henriksen *et al.*, “On-chip magnetic bead-based DNA melting curve analysis using a magnetoresistive sensor,” *Journal of Magnetism and Magnetic Materials,* vol. 380, pp. 215-220, Apr 15, 2015.

[86] B. T. Dalslet, C. D. Damsgaard, M. Donolato *et al.*, “Bead magnetorelaxometry with an on-chip magnetoresistive sensor,” *Lab Chip,* vol. 11, no. 2, pp. 296-302, Jan 21, 2011.

[87] A. D. Henriksen, G. Rizzi, and M. F. Hansen, “Planar Hall effect bridge sensors with NiFe/Cu/IrMn stack optimized for self-field magnetic bead detection,” *Journal of Applied Physics,* vol. 119, no. 9, Mar 7, 2016.

[88] M. Volmer, M. Avram, and A. M. Avram, “Simulation and experimental results on manipulation and detection of magnetic nanoparticles using planar hall effect sensors,” *Proceedings of the International Semiconductor Conference*, pp. 117-120, 2015.

[89] M. Volmer, and M. Avram, “Using permalloy based planar hall effect sensors to capture and detect superparamagnetic beads for lab on a chip applications,” *Journal of Magnetism and Magnetic Materials,* vol. 381, pp. 481-487, May 1, 2015.

[90] H. Kim, V. Reddy, K. W. Kim *et al.*, “Single Magnetic Bead Detection in a Microfluidic Chip Using Planar Hall Effect Sensor,” *Journal of Magnetics,* vol. 19, no. 1, pp. 10-14, Mar, 2014.

[91] M. Volmer, and M. Avram, “On magnetic nanoparticles detection using planar Hall effect sensors,” *Proceedings of the International Semiconductor Conference, CAS,* vol. 2, pp. 313-316, 2012.

[92] M. Volmer, M. Avram, and A. M. Avram, “Using a planar hall effect sensor for single bead detection,” *Proceedings of the International Semiconductor Conference, CAS,* vol. 1, pp. 221-224, 2010.

[93] N. T. Thanh, B. P. Rao, N. H. Duc *et al.*, “Planar Hall resistance sensor for biochip application,” *Physica Status Solidi a-Applications and Materials Science,* vol. 204, no. 12, pp. 4053-4057, Dec, 2007.

[94] B. Bajaj, N. T. Thanh, and C. G. Kim, “Planar hall effect in spin valve structure for DNA detection immobilized with single magnetic bead,” *7th IEEE International Conference on Nanotechnology - IEEE-NANO 2007, Proceedings*, pp. 1033-1036, 2007.

[95] T. Q. Hung, S. Oh, J. R. Jeong *et al.*, “Spin-valve planar Hall sensor for single bead detection,” *Sensors and Actuators a-Physical,* vol. 157, no. 1, pp. 42-46, Jan, 2010.

[96] M. Volmer, and M. Avram, “Microbeads Detection Using Spin-Valve Planar Hall Effect Sensors,” *Journal of Nanoscience and Nanotechnology,* vol. 12, no. 9, pp. 7456-7459, Sep, 2012.

[97] N. T. Thanh, K. W. Kim, O. Kim *et al.*, “Microbeads detection using Planar Hall effect in spin-valve structure,” *Journal of Magnetism and Magnetic Materials,* vol. 316, no. 2, pp. E238-E241, Sep, 2007.

[98] J. Pelegri, D. Ramirez, and P. P. Freitas, “Spin-valve current sensor for industrial applications,” *Sensors and Actuators a-Physical,* vol. 105, no. 2, pp. 132-136, Jul 15, 2003.

[99] D. Drung, C. Assmann, J. Beyer *et al.*, “Highly sensitive and easy-to-use SQUID sensors,” *Ieee Transactions on Applied Superconductivity,* vol. 17, no. 2, pp. 699-704, Jun, 2007.

[100] T. Sun, T. Tsukamoto, T. Ishikawa *et al.*, “System Development of Biosensing Module Using CMOS Hall Sensor Array for Disposable Wireless Diagnosis Device,” *2017 Ieee 12th International Conference on Nano/Micro Engineered and Molecular Systems (Nems)*, pp. 160-163, 2017.

[101] K. Singal, R. Rajamani, M. Ahmadi *et al.*, “Magnetic sensor for configurable measurement of tension or elasticity with validation in animal soft tissues,” *IEEE Trans Biomed Eng,* vol. 62, no. 2, pp. 426-37, Feb, 2015.

[102] P. H. Kuo, J. C. Kuo, H. T. Hsueh *et al.*, “A Smart CMOS Assay SoC for Rapid Blood Screening Test of Risk Prediction,” *IEEE Trans Biomed Circuits Syst,* vol. 9, no. 6, pp. 790-800, Dec, 2015.

[103] T. Ishikawa, “Immunoassay on silicon chip,” *29th Symposium on Microelectronics Technology and Devices*, 2014.

[104] K. Aledealat, G. Mihajlovic, K. Chen *et al.*, “Dynamic micro-Hall detection of superparamagnetic beads in a microfluidic channel,” *J Magn Magn Mater,* vol. 322, no. 24, pp. L69-L72, Dec 1, 2010.

[105] P. Manandhar, K. S. Chen, K. Aledealat *et al.*, “The detection of specific biomolecular interactions with micro-Hall magnetic sensors,” *Nanotechnology,* vol. 20, no. 35, pp. 355501, Sep 2, 2009.

[106] W. Lee, S. Joo, S. U. Kim *et al.*, “Magnetic bead counter using a micro-Hall sensor for biological applications,” *Applied Physics Letters,* vol. 94, no. 15, Apr 13, 2009.

[107] L. Di Michele, C. Shelly, P. de Marco *et al.*, “Detection and susceptibility measurements of a single Dynal bead,” *Journal of Applied Physics,* vol. 110, no. 6, pp. 063916, 2011.

[108] L. Di Michele, C. Shelly, J. Gallop *et al.*, “Single particle detection: Phase control in submicron Hall sensors,” *Journal of Applied Physics,* vol. 108, no. 10, pp. 103918, 2010.

[109] A. Sandhu, and F. Handa, “Practical hall sensors for biomedical instrumentation,” *Ieee Transactions on Magnetics,* vol. 41, no. 10, pp. 4123-4127, Oct, 2005.

[110] A. Sandhu, Y. Kumagai, A. Lapicki *et al.*, “High efficiency Hall effect micro-biosensor platform for detection of magnetically labeled biomolecules,” *Biosens Bioelectron,* vol. 22, no. 9-10, pp. 2115-20, Apr 15, 2007.

[111] K. Togawa, H. Sanbonsugi, A. Sandhu *et al.*, “Detection of magnetically labeled DNA using pseudomorphic AlGaAs/InGaAs/GaAs heterostructure micro-Hall biosensors,” *Journal of Applied Physics,* vol. 99, no. 8, Apr 15, 2006.

[112] K. Togawa, H. Sanbonsugi, A. Sandhu *et al.*, “High sensitivity InSb Hall effect biosensor platform for DNA detection and biomolecular recognition using functionalized magnetic nanobeads,” *Japanese Journal of Applied Physics Part 2-Letters & Express Letters,* vol. 44, no. 46-49, pp. L1494-L1497, 2005.

[113] K. Togawa, H. Sanbonsugi, A. Lapicki *et al.*, “High-sensitivity InSb thin-film micro-Hall sensor arrays for simultaneous multiple detection of magnetic beads for biomedical applications,” *Ieee Transactions on Magnetics,* vol. 41, no. 10, pp. 3661-3663, Oct, 2005.

[114] G. Mihajlovic, P. Xiong, S. von Molnar *et al.*, “Detection of single magnetic bead for biological applications using an InAs quantum-well micro-Hall sensor,” *Applied Physics Letters,* vol. 87, no. 11, Sep 12, 2005.

[115] S. Adarsh, S. Hideaki, S. Ichiro *et al.*, “High Sensitivity InSb Ultra-Thin Film Micro-Hall Sensors for Bioscreening Applications,” *Japanese Journal of Applied Physics,* vol. 43, no. 7A, pp. L868, 2004.

[116] L. W. Ejsing, “Planar Hall sensor for influenza immunoassay,” *MIC-Department of Micro and Nanotechnology, Technical University of Denmark*, 2006.

[117] S. Sonusen, O. Karci, M. Dede *et al.*, “Single layer graphene Hall sensors for scanning Hall probe microscopy (SHPM) in 3-300 K temperature range,” *Applied Surface Science,* vol. 308, pp. 414-418, Jul 30, 2014.

[118] J. Heremans, “Solid-State Magnetic-Field Sensors and Applications,” *Journal of Physics D-Applied Physics,* vol. 26, no. 8, pp. 1149-1168, Aug 14, 1993.

[119] G. Boero, M. Demierre, P. A. Besse *et al.*, “Micro-Hall devices: performance, technologies and applications,” *Sensors and Actuators a-Physical,* vol. 106, no. 1-3, pp. 314-320, Sep 15, 2003.

[120] T. White, V. P. Kunets, Y. Hirono *et al.*, “High performance quantum well micro-hall device for current sensing in inverters,” *4th IEEE International Symposium on Power Electronics for Distributed Generation Systems*, 2013.

[121] A. Segovia, B. Chenaud, N. Feltin *et al.*, “Highly sensitive nanohall sensors on GaAlAs/GaAs heterojunctions,” *22nd International Conference on Noise and Fluctuations*, 2013.

[122] A. Abderrahmane, S. Koide, H. Okada *et al.*, “Effect of proton irradiation on AlGaN/GaN micro-Hall sensors,” *Applied Physics Letters,* vol. 102, no. 19, May 13, 2013.

[123] M. Bando, T. Ohashi, M. Dede *et al.*, “High sensitivity and multifunctional micro-Hall sensors fabricated using InAlSb/InAsSb/InAlSb heterostructures,” *Journal of Applied Physics,* vol. 105, no. 7, pp. 07E909, Apr 1, 2009.

[124] T. Berus, M. Oszwaldowski, and J. Grabowski, “High quality Hall sensors made of heavily doped n-InSb epitaxial films,” *Sensors and Actuators a-Physical,* vol. 116, no. 1, pp. 75-78, Oct 4, 2004.

[125] I. Shibasaki, “Mass production of InAs Hall elements by MBE,” *Journal of Crystal Growth,* vol. 175, pp. 13-21, May, 1997.

[126] O. Kazakova, J. C. Gallop, P. See *et al.*, “Detection of a Micron-Sized Magnetic Particle Using InSb Hall Sensor,” *IEEE Transactions on Magnetics,* vol. 45, no. 10, pp. 4499-4502, Oct, 2009.

[127] D. Petit, D. Atkinson, S. Johnston *et al.*, “Room temperature performance of submicron bismuth Hall probes,” *Iee Proceedings-Science Measurement and Technology,* vol. 151, no. 2, pp. 127-130, Mar, 2004.

[128] B. Y. Chen, L. Huang, X. M. Ma *et al.*, “Exploration of sensitivity limit for graphene magnetic sensors,” *Carbon,* vol. 94, pp. 585-589, Nov, 2015.

[129] X. Du, I. Skachko, A. Barker *et al.*, “Approaching ballistic transport in suspended graphene,” *Nat Nanotechnol,* vol. 3, no. 8, pp. 491-5, Aug, 2008.

[130] H. L. Xu, L. Huang, Z. Y. Zhang *et al.*, “Flicker noise and magnetic resolution of graphene hall sensors at low frequency,” *Applied Physics Letters,* vol. 103, no. 11, Sep 9, 2013.

[131] A. Gutes, B. Hsia, A. Sussman *et al.*, “Graphene decoration with metal nanoparticles: towards easy integration for sensing applications,” *Nanoscale,* vol. 4, no. 2, pp. 438-40, Jan 21, 2012.

[132] R. Pearce, T. Iakimov, M. Andersson *et al.*, “Epitaxially grown graphene based gas sensors for ultra sensitive NO2 detection,” *Sensors and Actuators B-Chemical,* vol. 155, no. 2, pp. 451-455, Jul 20, 2011.

[133] H. J. Yoon, D. H. Jun, J. H. Yang *et al.*, “Carbon dioxide gas sensor using a graphene sheet,” *Sensors and Actuators B-Chemical,* vol. 157, no. 1, pp. 310-313, Sep 20, 2011.

[134] R. S. Dey, and C. R. Raj, “Development of an Amperometric Cholesterol Biosensor Based on Graphene−Pt Nanoparticle Hybrid Material,” *The Journal of Physical Chemistry C,* vol. 114, no. 49, pp. 21427-21433, 2010/12/16, 2010.

[135] J. H. An, S. J. Park, O. S. Kwon *et al.*, “High-performance flexible graphene aptasensor for mercury detection in mussels,” *ACS Nano,* vol. 7, no. 12, pp. 10563-71, Dec 23, 2013.

[136] Y. Wen, F. Y. Li, X. Dong *et al.*, “The electrical detection of lead ions using gold-nanoparticle- and DNAzyme-functionalized graphene device,” *Adv Healthc Mater,* vol. 2, no. 2, pp. 271-4, Feb, 2013.

[137] S. H. Bae, Y. Lee, B. K. Sharma *et al.*, “Graphene-based transparent strain sensor,” *Carbon,* vol. 51, pp. 236-242, Jan, 2013.

[138] X. W. Fu, Z. M. Liao, J. X. Zhou *et al.*, “Strain dependent resistance in chemical vapor deposition grown graphene,” *Applied Physics Letters,* vol. 99, no. 21, pp. 213107, Nov 21, 2011.

[139] M. Muti, S. Sharma, A. Erdem *et al.*, “Electrochemical Monitoring of Nucleic Acid Hybridization by Single-Use Graphene Oxide-Based Sensor,” *Electroanalysis,* vol. 23, no. 1, pp. 272-279, 2011.

[140] Y. Ohno, K. Maehashi, Y. Yamashiro *et al.*, “Electrolyte-gated graphene field-effect transistors for detecting pH and protein adsorption,” *Nano Lett,* vol. 9, no. 9, pp. 3318-22, Sep, 2009.

[141] Y. R. Kim, S. Bong, Y. J. Kang *et al.*, “Electrochemical detection of dopamine in the presence of ascorbic acid using graphene modified electrodes,” *Biosens Bioelectron,* vol. 25, no. 10, pp. 2366-9, Jun 15, 2010.

[142] Y. Wang, Y. M. Li, L. H. Tang *et al.*, “Application of graphene-modified electrode for selective detection of dopamine,” *Electrochemistry Communications,* vol. 11, no. 4, pp. 889-892, Apr, 2009.

[143] Y. Liu, D. Yu, C. Zeng *et al.*, “Biocompatible graphene oxide-based glucose biosensors,” *Langmuir,* vol. 26, no. 9, pp. 6158-60, May 4, 2010.

[144] Z. J. Wang, X. Z. Zhou, J. Zhang *et al.*, “Direct Electrochemical Reduction of Single-Layer Graphene Oxide and Subsequent Functionalization with Glucose Oxidase,” *Journal of Physical Chemistry C,* vol. 113, no. 32, pp. 14071-14075, Aug 13, 2009.

[145] T. Ciuk, O. Petruk, A. Kowalik *et al.*, “Low-noise epitaxial graphene on SiC Hall effect element for commercial applications,” *Applied Physics Letters,* vol. 108, no. 22, pp. 223504, May 30, 2016.

[146] C. Dong Soo, H. Seung Ho, K. Hyeongkeun *et al.*, “Flexible electrochromic films based on CVD-graphene electrodes,” *Nanotechnology,* vol. 25, no. 39, pp. 395702, 2014.

[147] T. H. Han, Y. Lee, M. R. Choi *et al.*, “Extremely efficient flexible organic light-emitting diodes with modified graphene anode,” *Nature Photonics,* vol. 6, no. 2, pp. 105-110, Feb, 2012.

[148] J. S. Bunch, S. S. Verbridge, J. S. Alden *et al.*, “Impermeable atomic membranes from graphene sheets,” *Nano Lett,* vol. 8, no. 8, pp. 2458-62, Aug, 2008.

[149] R. K. Rajkumar, A. Asenjo, V. Panchal *et al.*, “Magnetic scanning gate microscopy of graphene Hall devices (invited),” *Journal of Applied Physics,* vol. 115, no. 17, May 7, 2014.

[150] Y. Grachova, S. Vollebregt, A. L. Lacaita *et al.*, "High quality wafer-scale CVD graphene on molybdenum thin film for sensing application." pp. 1501-1504.

[151] R. K. Rajkumar, A. Manzin, D. C. Cox *et al.*, “3-D Mapping of Sensitivity of Graphene Hall Devices to Local Magnetic and Electrical Fields,” *Ieee Transactions on Magnetics,* vol. 49, no. 7, pp. 3445-3448, Jul, 2013.

[152] V. Panchal, O. Iglesias-Freire, A. Lartsev *et al.*, “Magnetic Scanning Probe Calibration Using Graphene Hall Sensor,” *IEEE Transactions on Magnetics,* vol. 49, no. 7, pp. 3520-3523, Jul, 2013.

[153] T. A. P. Rocha-Santos, “Sensors and biosensors based on magnetic nanoparticles,” *Trac-Trends in Analytical Chemistry,* vol. 62, pp. 28-36, Nov, 2014.

[154] K. Enpuku, Y. Tamai, T. Mitake *et al.*, “ac susceptibility measurement of magnetic markers in suspension for liquid phase immunoassay,” *Journal of Applied Physics,* vol. 108, no. 3, pp. 034701, Aug 1, 2010.

[155] C. T. Lin, P. T. K. Loan, T. Y. Chen *et al.*, “Label-Free Electrical Detection of DNA Hybridization on Graphene using Hall Effect Measurements: Revisiting the Sensing Mechanism,” *Advanced Functional Materials,* vol. 23, no. 18, pp. 2301-2307, May 13, 2013.

[156] P. T. K. Loan, D. Wu, C. Ye *et al.*, “Hall effect biosensors with ultraclean graphene film for improved sensitivity of label-free DNA detection,” *Biosens Bioelectron,* vol. 99, pp. 85-91, Jan 15, 2018.

[157] X. Liu, C. Ye, X. Li *et al.*, “Highly Sensitive and Selective Potassium Ion Detection Based on Graphene Hall Effect Biosensors,” *Materials (Basel),* vol. 11, no. 3, Mar 7, 2018.

[158] S. P. Sanfilippo, Villigen), "Hall Probes: Physics and application to magnetometry." pp. 423-462, 08 March 2011.

[159] S. Pisana, P. M. Braganca, E. E. Marinero *et al.*, “Graphene Magnetic Field Sensors,” *IEEE Transactions on Magnetics,* vol. 46, no. 6, pp. 1910-1913, Jun, 2010.

[160] C. Bosch-Navarro, Z. P. L. Laker, A. J. Marsden *et al.*, “Non-covalent functionalization of graphene with a hydrophilic self-limiting monolayer for macro-molecule immobilization,” *FlatChem,* vol. 1, pp. 52-56, 2017/01/01/, 2017.

[161] R. R. Nair, P. Blake, A. N. Grigorenko *et al.*, “Fine structure constant defines visual transparency of graphene,” *Science,* vol. 320, no. 5881, pp. 1308, Jun 6, 2008.

[162] H. Chen, M. B. Muller, K. J. Gilmore *et al.*, “Mechanically strong, electrically conductive, and biocompatible graphene paper,” *Advanced Materials,* vol. 20, no. 18, pp. 3557-+, Sep 17, 2008.

[163] I. N. Kholmanov, S. H. Domingues, H. Chou *et al.*, “Reduced graphene oxide/copper nanowire hybrid films as high-performance transparent electrodes,” *ACS Nano,* vol. 7, no. 2, pp. 1811-6, Feb 26, 2013.

[164] L. Liang, W. Hu, Z. Xue *et al.*, “Theoretical study on the interaction of nucleotides on two-dimensional atomically thin graphene and molybdenum disulfide,” *FlatChem,* vol. 2, pp. 8-14, 2017/04/01/, 2017.

[165] C. C. Tang, M. Y. Li, L. J. Li *et al.*, “Characteristics of a sensitive micro-Hall probe fabricated on chemical vapor deposited graphene over the temperature range from liquid-helium to room temperature,” *Applied Physics Letters,* vol. 99, no. 11, Sep 12, 2011.

[166] A. K. Geim, and K. S. Novoselov, “The rise of graphene,” *Nat Mater,* vol. 6, no. 3, pp. 183-91, Mar, 2007.

[167] *Synthesis, Characterization, and Selected Properties of Graphene*, 2012 p. 1-47.

[168] P. Avouris, and F. N. Xia, “Graphene applications in electronics and photonics,” *Mrs Bulletin,* vol. 37, no. 12, pp. 1225-1234, Dec, 2012.

[169] V. Singh, G. Subramaniam, B. Irfan *et al.*, "Suspended graphene devices for electromechanics and quantum Hall effect (QHE) studies." pp. 15-18.

[170] M. S. Fuhrer, C. N. Lau, and A. H. MacDonald, “Graphene: Materially Better Carbon,” *Mrs Bulletin,* vol. 35, no. 4, pp. 289-295, Apr, 2010.

[171] W. A. de Heer, C. Berger, X. Wu *et al.*, “Epitaxial graphene electronic structure and transport,” *Journal of Physics D: Applied Physics,* vol. 43, no. 37, pp. 374007, 2010.

[172] P. Avouris, “Graphene: electronic and photonic properties and devices,” *Nano Lett,* vol. 10, no. 11, pp. 4285-94, Nov 10, 2010.

[173] Y. Zhang, T. T. Tang, C. Girit *et al.*, “Direct observation of a widely tunable bandgap in bilayer graphene,” *Nature,* vol. 459, no. 7248, pp. 820-3, Jun 11, 2009.

[174] A. K. Geim, “Graphene: status and prospects,” *Science,* vol. 324, no. 5934, pp. 1530-4, Jun 19, 2009.

[175] J. C. Meyer, A. K. Geim, M. I. Katsnelson *et al.*, “The structure of suspended graphene sheets,” *Nature,* vol. 446, no. 7131, pp. 60-3, Mar 1, 2007.

[176] A. K. Geim, and A. H. MacDonald, “Graphene: Exploring carbon flatland,” *Physics Today,* vol. 60, no. 8, pp. 35-41, Aug, 2007.

[177] I. W. Frank, D. M. Tanenbaum, A. M. Van der Zande *et al.*, “Mechanical properties of suspended graphene sheets,” *Journal of Vacuum Science & Technology B,* vol. 25, no. 6, pp. 2558-2561, Nov, 2007.

[178] K. S. Novoselov, V. I. Fal'ko, L. Colombo *et al.*, “A roadmap for graphene,” *Nature,* vol. 490, no. 7419, pp. 192-200, Oct 11, 2012.

[179] P. R. Wallace, “The Band Theory of Graphite,” *Physical Review,* vol. 71, no. 9, pp. 622-634, 05/01/, 1947.

[180] F. D. Haldane, “Model for a quantum Hall effect without Landau levels: Condensed-matter realization of the "parity anomaly",” *Phys Rev Lett,* vol. 61, no. 18, pp. 2015-2018, Oct 31, 1988.

[181] D. R. Dreyer, R. S. Ruoff, and C. W. Bielawski, “From conception to realization: an historial account of graphene and some perspectives for its future,” *Angew Chem Int Ed Engl,* vol. 49, no. 49, pp. 9336-44, Dec 3, 2010.

[182] K. S. Novoselov, A. K. Geim, S. V. Morozov *et al.*, “Two-dimensional gas of massless Dirac fermions in graphene,” *Nature,* vol. 438, no. 7065, pp. 197-200, Nov 10, 2005.

[183] AZoM. "Boron Nitride (BN) - Properties and Information on Boron Nitride," https://www.azom.com/article.aspx?ArticleID=78.

[184] Y. Zhang, Y. W. Tan, H. L. Stormer *et al.*, “Experimental observation of the quantum Hall effect and Berry's phase in graphene,” *Nature,* vol. 438, no. 7065, pp. 201-4, Nov 10, 2005.

[185] "The Nobel Prize in Physics 2010," http://www.nobelprize.org/nobel_prizes/physics/laureates/2010/.

[186] Dale A. C. Brownson, and C. E. Banks, "The Handbook of Graphene Electrochemistry," Springer, London, 2014.

[187] D. A. Brownson, D. K. Kampouris, and C. E. Banks, “Graphene electrochemistry: fundamental concepts through to prominent applications,” *Chem Soc Rev,* vol. 41, no. 21, pp. 6944-76, Nov 7, 2012.

[188] Z. Papic, M. O. Goerbig, and N. Regnault, “Theoretical expectations for a fractional quantum Hall effect in graphene,” *Solid State Communications,* vol. 149, no. 27-28, pp. 1056-1060, Jul, 2009.

[189] S. Mao, H. H. Pu, and J. H. Chen, “Graphene oxide and its reduction: modeling and experimental progress,” *RSC Advances,* vol. 2, no. 7, pp. 2643-2662, 2012.

[190] C. Lee, X. Wei, J. W. Kysar *et al.*, “Measurement of the elastic properties and intrinsic strength of monolayer graphene,” *Science,* vol. 321, no. 5887, pp. 385-8, Jul 18, 2008.

[191] T. Dürkop, S. A. Getty, E. Cobas *et al.*, “Extraordinary Mobility in Semiconducting Carbon Nanotubes,” *Nano Letters,* vol. 4, no. 1, pp. 35-39, 2004/01/01, 2004.

[192] D. L. Rode, “Electron Transport in InSb, InAs, and InP,” *Physical Review B,* vol. 3, no. 10, pp. 3287-3299, 05/15/, 1971.

[193] "Bismuth (Bi) carrier concentrations and mobilities," *Non-Tetrahedrally Bonded Elements and Binary Compounds I*, Landolt-Börnstein - Group III Condensed Matter O. Madelung, U. Rössler and M. Schulz, eds., pp. 1-11, Berlin, Heidelberg: Springer Berlin Heidelberg, 1998.

[194] C. Jacoboni, C. Canali, G. Ottaviani *et al.*, “A review of some charge transport properties of silicon,” *Solid-State Electronics,* vol. 20, no. 2, pp. 77-89, 1977/02/01/, 1977.

[195] R. S. Edwards, and K. S. Coleman, “Graphene synthesis: relationship to applications,” *Nanoscale,* vol. 5, no. 1, pp. 38-51, Jan 7, 2013.

[196] C. Soldano, A. Mahmood, and E. Dujardin, “Production, properties and potential of graphene,” *Carbon,* vol. 48, no. 8, pp. 2127-2150, Jul, 2010.

[197] P. Avouris, and C. Dimitrakopoulos, “Graphene: synthesis and applications,” *Materials Today,* vol. 15, no. 3, pp. 86-97, Mar, 2012.

[198] S. Park, and R. S. Ruoff, “Chemical methods for the production of graphenes,” *Nat Nanotechnol,* vol. 4, no. 4, pp. 217-24, Apr, 2009.

[199] I. V. Zolotukhin, I. M. Golev, A. V. Nefedov *et al.*, “Graphenes: Methods of production and application,” *Inorganic Materials: Applied Research,* vol. 2, no. 2, pp. 91-96, 2011.

[200] K. E. Whitener, and P. E. Sheehan, “Graphene synthesis,” *Diamond and Related Materials,* vol. 46, pp. 25-34, Jun, 2014.

[201] W. Choi, I. Lahiri, R. Seelaboyina *et al.*, “Synthesis of Graphene and Its Applications: A Review,” *Critical Reviews in Solid State and Materials Sciences,* vol. 35, no. 1, pp. 52-71, 2010/02/11, 2010.

[202] M. Lotya, Y. Hernandez, P. J. King *et al.*, “Liquid phase production of graphene by exfoliation of graphite in surfactant/water solutions,” *J Am Chem Soc,* vol. 131, no. 10, pp. 3611-20, Mar 18, 2009.

[203] W. B. Lu, S. Liu, X. Y. Qin *et al.*, “High-yield, large-scale production of few-layer graphene flakes within seconds: using chlorosulfonic acid and H2O2 as exfoliating agents,” *Journal of Materials Chemistry,* vol. 22, no. 18, pp. 8775-8777, 2012.

[204] D. Nuvoli, V. Alzari, R. Sanna *et al.*, “The production of concentrated dispersions of few-layer graphene by the direct exfoliation of graphite in organosilanes,” *Nanoscale Res Lett,* vol. 7, no. 1, pp. 674, Dec 13, 2012.

[205] J. N. Coleman, “Liquid exfoliation of defect-free graphene,” *Acc Chem Res,* vol. 46, no. 1, pp. 14-22, Jan 15, 2013.

[206] H. Yang, Y. Hernandez, A. Schlierf *et al.*, “A simple method for graphene production based on exfoliation of graphite in water using 1-pyrenesulfonic acid sodium salt,” *Carbon,* vol. 53, pp. 357-365, Mar, 2013.

[207] C. Mattevi, H. Kim, and M. Chhowalla, “A review of chemical vapour deposition of graphene on copper,” *Journal of Materials Chemistry,* vol. 21, no. 10, pp. 3324-3334, 2011.

[208] L. Tao, J. Lee, M. Holt *et al.*, “Uniform Wafer-Scale Chemical Vapor Deposition of Graphene on Evaporated Cu (111) Film with Quality Comparable to Exfoliated Monolayer,” *Journal of Physical Chemistry C,* vol. 116, no. 45, pp. 24068-24074, Nov 15, 2012.

[209] N. I. Zaaba, K. L. Foo, U. Hashim *et al.*, “Synthesis of Graphene Oxide using Modified Hummers Method: Solvent Influence,” *Advances in Material & Processing Technologies Conference,* vol. 184, pp. 469-477, 2017/01/01/, 2017.

[210] V. Strong, S. Dubin, M. F. El-Kady *et al.*, “Patterning and electronic tuning of laser scribed graphene for flexible all-carbon devices,” *ACS Nano,* vol. 6, no. 2, pp. 1395-403, Feb 28, 2012.

[211] S. Shivaraman, R. A. Barton, X. Yu *et al.*, “Free-standing epitaxial graphene,” *Nano Lett,* vol. 9, no. 9, pp. 3100-5, Sep, 2009.

[212] P. Sutter, “Epitaxial graphene: How silicon leaves the scene,” *Nat Mater,* vol. 8, no. 3, pp. 171-2, Mar, 2009.

[213] H. Tetlow, J. P. de Boer, I. J. Ford *et al.*, “Growth of epitaxial graphene: Theory and experiment,” *Physics Reports-Review Section of Physics Letters,* vol. 542, no. 3, pp. 195-295, Sep 20, 2014.

[214] W. A. de Heer, C. Berger, M. Ruan *et al.*, “Large area and structured epitaxial graphene produced by confinement controlled sublimation of silicon carbide,” *Proc Natl Acad Sci U S A,* vol. 108, no. 41, pp. 16900-5, Oct 11, 2011.

[215] C. Riedl, C. Coletti, and U. Starke, “Structural and electronic properties of epitaxial graphene on SiC(0 0 0 1): a review of growth, characterization, transfer doping

and hydrogen intercalation," *Journal of Physics D: Applied Physics,* vol. 43, no. 37, pp. 374009, 2010.

[216] E. Pallecchi, F. Lafont, V. Cavaliere *et al.*, "High Electron Mobility in Epitaxial Graphene on 4H-SiC(0001) via post-growth annealing under hydrogen," *Sci Rep,* vol. 4, pp. 4558, Apr 2, 2014.

[217] H. Hibino, S. Tanabe, S. Mizuno *et al.*, "Growth and electronic transport properties of epitaxial graphene on SiC," *Journal of Physics D-Applied Physics,* vol. 45, no. 15, Apr 18, 2012.

[218] W. Norimatsu, and M. Kusunoki, "Epitaxial graphene on SiC{0001}: advances and perspectives," *Phys Chem Chem Phys,* vol. 16, no. 8, pp. 3501-11, Feb 28, 2014.

[219] M. Ruan, Y. K. Hu, Z. L. Guo *et al.*, "Epitaxial graphene on silicon carbide: Introduction to structured graphene," *Mrs Bulletin,* vol. 37, no. 12, pp. 1138-1147, Dec, 2012.

[220] D. W. Johnson, B. P. Dobson, and K. S. Coleman, "A manufacturing perspective on graphene dispersions," *Current Opinion in Colloid & Interface Science,* vol. 20, no. 5-6, pp. 367-382, Oct-Dec, 2015.

[221] Z. U. Khan, A. Kausar, H. Ullah *et al.*, "A review of graphene oxide, graphene buckypaper, and polymer/graphene composites: Properties and fabrication techniques," *Journal of Plastic Film & Sheeting,* vol. 32, no. 4, pp. 336-379, Oct, 2016.

[222] M. Konig, G. Ruhl, J. M. Batke *et al.*, "Self-organized growth of graphene nanomesh with increased gas sensitivity," *Nanoscale,* vol. 8, no. 34, pp. 15490-6, Aug 25, 2016.

[223] R. B. Shi, H. L. Xu, B. Y. Chen *et al.*, "Scalable fabrication of graphene devices through photolithography," *Applied Physics Letters,* vol. 102, no. 11, Mar 18, 2013.

[224] D. Shin, S. Bae, C. Yan *et al.*, "Synthesis and applications of graphene electrodes," *Carbon Letters,* vol. 13, no. 1, pp. 1-16, Jan, 2012.

[225] L. Gao, W. Ren, H. Xu *et al.*, "Repeated growth and bubbling transfer of graphene with millimetre-size single-crystal grains using platinum," *Nat Commun,* vol. 3, pp. 699, Feb 28, 2012.

[226] V. E. Aleksandr, M. I. Inna, A. K. Andrei *et al.*, "Graphene: fabrication methods and thermophysical properties," *Physics-Uspekhi,* vol. 54, no. 3, pp. 227, 2011.

[227] M. I. Kairi, M. Khavarian, S. Abu Bakar *et al.*, "Recent trends in graphene materials synthesized by CVD with various carbon precursors," *Journal of Materials Science,* vol. 53, no. 2, pp. 851-879, Jan, 2018.

[228] A. Turchanin, "Graphene Growth by Conversion of Aromatic Self-Assembled Monolayers," *Annalen Der Physik,* vol. 529, no. 11, Nov, 2017.

[229] J. Phiri, P. Gane, and T. C. Maloney, "General overview of graphene: Production, properties and application in polymer composites," *Materials Science and Engineering B-Advanced Functional Solid-State Materials,* vol. 215, pp. 9-28, Jan, 2017.

[230] I. Levchenko, K. K. Ostrikov, J. Zheng *et al.*, “Scalable graphene production: perspectives and challenges of plasma applications,” *Nanoscale,* vol. 8, no. 20, pp. 10511-27, May 19, 2016.

[231] A. Ciesielski, and P. Samori, “Supramolecular Approaches to Graphene: From Self-Assembly to Molecule-Assisted Liquid-Phase Exfoliation,” *Adv Mater,* vol. 28, no. 29, pp. 6030-51, Aug, 2016.

[232] Y. L. Zhong, Z. M. Tian, G. P. Simon *et al.*, “Scalable production of graphene via wet chemistry: progress and challenges,” *Materials Today,* vol. 18, no. 2, pp. 73-78, Mar, 2015.

[233] M. Yi, and Z. G. Shen, “A review on mechanical exfoliation for the scalable production of graphene,” *Journal of Materials Chemistry A,* vol. 3, no. 22, pp. 11700-11715, 2015.

[234] S. Y. Toh, K. S. Loh, S. K. Kamarudin *et al.*, “Graphene production via electrochemical reduction of graphene oxide: Synthesis and characterisation,” *Chemical Engineering Journal,* vol. 251, pp. 422-434, Sep 1, 2014.

[235] P. Blake, E. W. Hill, A. H. Castro Neto *et al.*, “Making graphene visible,” *Applied Physics Letters,* vol. 91, no. 6, pp. 063124, Aug 6, 2007.

[236] L. M. Malard, M. A. Pimenta, G. Dresselhaus *et al.*, “Raman spectroscopy in graphene,” *Physics Reports-Review Section of Physics Letters,* vol. 473, no. 5-6, pp. 51-87, Apr, 2009.

[237] A. C. Ferrari, and D. M. Basko, “Raman spectroscopy as a versatile tool for studying the properties of graphene,” *Nat Nanotechnol,* vol. 8, no. 4, pp. 235-46, Apr, 2013.

[238] A. C. Ferrari, “Raman spectroscopy of graphene and graphite: Disorder, electron–phonon coupling, doping and nonadiabatic effects,” *Solid State Communications,* vol. 143, no. 1-2, pp. 47-57, 2007/07/01/, 2007.

[239] B. Ryan, C. Luiz Gustavo, and N. Lukas, “Raman characterization of defects and dopants in graphene,” *Journal of Physics: Condensed Matter,* vol. 27, no. 8, pp. 083002, 2015.

[240] A. C. Ferrari, J. C. Meyer, V. Scardaci *et al.*, “Raman spectrum of graphene and graphene layers,” *Phys Rev Lett,* vol. 97, no. 18, pp. 187401, Nov 3, 2006.

[241] D. R. Cooper, B. D’Anjou, N. Ghattamaneni *et al.*, “Experimental Review of Graphene,” *ISRN Condensed Matter Physics,* vol. 2012, pp. 56, 2012.

[242] X. Wang, C. Li, Y. Chi *et al.*, “Effect of Graphene Nanowall Size on the Interfacial Strength of Carbon Fiber Reinforced Composites,” *Nanomaterials,* vol. 8, no. 6, pp. 414, 2018.

[243] Y. Y. Wang, Z. H. Ni, T. Yu *et al.*, “Raman studies of monolayer graphene: The substrate effect,” *Journal of Physical Chemistry C,* vol. 112, no. 29, pp. 10637-10640, Jul 24, 2008.

[244] M. L. Bolen, T. Shen, J. J. Gu *et al.*, "Empirical study of hall bars on few-layer graphene on C-face 4H-SiC," *Journal of Electronic Materials.* pp. 2696-2701.

[245] S. Sahoo, G. Khurana, S. K. Barik *et al.*, "In Situ Raman Studies of Electrically Reduced Graphene Oxide and Its Field-Emission Properties," *The Journal of Physical Chemistry C,* vol. 117, no. 10, pp. 5485-5491, 2013/03/14, 2013.

[246] S. Ryu, J. Maultzsch, M. Y. Han *et al.*, "Raman Spectroscopy of Lithographically Patterned Graphene Nanoribbons," *ACS Nano,* vol. 5, no. 5, pp. 4123-4130, 2011/05/24, 2011.

[247] N. Van Tu, L. Huu Doan, N. Van Chuc *et al.*, "Synthesis of multi-layer graphene films on copper tape by atmospheric pressure chemical vapor deposition method," *Advances in Natural Sciences: Nanoscience and Nanotechnology,* vol. 4, no. 3, pp. 035012, 2013.

[248] D. Ferrah, J. Penuelas, C. Bottela *et al.*, "X-ray photoelectron spectroscopy (XPS) and diffraction (XPD) study of a few layers of graphene on 6H-SiC(0001)," *Surface Science,* vol. 615, pp. 47-56, Sep, 2013.

[249] G. Gao, D. Liu, S. Tang *et al.*, "Heat-Initiated Chemical Functionalization of Graphene," *Sci Rep,* vol. 6, pp. 20034, Jan 28, 2016.

[250] D. Yang, A. Velamakanni, G. Bozoklu *et al.*, "Chemical analysis of graphene oxide films after heat and chemical treatments by X-ray photoelectron and Micro-Raman spectroscopy," *Carbon,* vol. 47, no. 1, pp. 145-152, Jan, 2009.

[251] M. Koinuma, H. Tateishi, K. Hatakeyama *et al.*, "Analysis of Reduced Graphene Oxides by X-ray Photoelectron Spectroscopy and Electrochemical Capacitance," *Chemistry Letters,* vol. 42, no. 8, pp. 924-926, Aug 5, 2013.

[252] X. Z. Gong, G. Z. Liu, Y. S. Li *et al.*, "Functionalized-Graphene Composites: Fabrication and Applications in Sustainable Energy and Environment," *Chemistry of Materials,* vol. 28, no. 22, pp. 8082-8118, Nov 22, 2016.

[253] T. Kuila, S. Bose, A. K. Mishra *et al.*, "Chemical functionalization of graphene and its applications," *Progress in Materials Science,* vol. 57, no. 7, pp. 1061-1105, Sep, 2012.

[254] NIST. "XPS database," 01-Aug, 2018; http://srdata.nist.gov/xps/EnergyTypeValSrch.aspx.

[255] H. C. Schniepp, J. L. Li, M. J. McAllister *et al.*, "Functionalized single graphene sheets derived from splitting graphite oxide," *J Phys Chem B,* vol. 110, no. 17, pp. 8535-9, May 4, 2006.

[256] L. B. Biedermann, M. L. Bolen, M. A. Capano *et al.*, "Insights into few-layer epitaxial graphene growth on 4H-SiC (000¯1) substrates from STM studies," *Physical Review B,* vol. 79, no. 12, pp. 125411, 2009.

[257] A. Tiwari, and M. Syväjärvi, *Graphene Materials*: Scrivener Publishing LLC, 2015.

[258] P. Kumar, "Laser flash synthesis of graphene and its inorganic analogues: An innovative breakthrough with immense promise," *RSC Advances,* vol. 3, no. 30, pp. 11987-12002, 2013.

[259] S. Berciaud, S. Ryu, L. E. Brus *et al.*, "Probing the intrinsic properties of exfoliated graphene: Raman spectroscopy of free-standing monolayers," *Nano Lett,* vol. 9, no. 1, pp. 346-52, Jan, 2009.

[260] Y. Liu, X. Dong, and P. Chen, “Biological and chemical sensors based on graphene materials,” *Chem Soc Rev,* vol. 41, no. 6, pp. 2283-307, Mar 21, 2012.

[261] N. Li, G. Yang, Y. Sun *et al.*, “Free-Standing and Transparent Graphene Membrane of Polyhedron Box-Shaped Basic Building Units Directly Grown Using a NaCl Template for Flexible Transparent and Stretchable Solid-State Supercapacitors,” *Nano Lett,* vol. 15, no. 5, pp. 3195-203, May 13, 2015.

[262] K. Ghaffarzadeh, *Graphene, 2D Materials and Carbon Nanotubes: Markets, Technologies and Opportunities 2017-2027*, 2017.

[263] Y. Y. Shao, J. Wang, H. Wu *et al.*, “Graphene Based Electrochemical Sensors and Biosensors: A Review,” *Electroanalysis,* vol. 22, no. 10, pp. 1027-1036, May, 2010.

[264] M. A. Paun, J. M. Sallese, and M. Kayal, “Geometry Influence on the Hall Effect Devices Performance,” *University Politehnica of Bucharest Scientific Bulletin-Series a-Applied Mathematics and Physics,* vol. 72, no. 4, pp. 257-271, 2010.

[265] F. Lyu, Z. Zhang, E. H. Toh *et al.*, “Performance comparison of cross-like Hall plates with different covering layers,” *Sensors (Basel),* vol. 15, no. 1, pp. 672-86, Dec 31, 2014.

[266] D. P. Renella, S. Spasic, S. Dimitrijevic *et al.*, “An overview of commercially available teslameters,” *XXI IMEKO World Congress "Measurement in Research and Industry"*, 2015.

[267] M.-A. Paun, J.-M. Sallese, and M. Kayal, “Hall Effect Sensors Design, Integration and Behavior Analysis,” *Journal of Sensor and Actuator Networks,* vol. 2, no. 1, pp. 85-97, 2013.

[268] J. Jankowski, S. El-Ahmar, and M. Oszwaldowski, “Hall sensors for extreme temperatures,” *Sensors (Basel),* vol. 11, no. 1, pp. 876-85, 2011.

[269] Y. Kumagai, K. Togawa, S. Sakamoto *et al.*, “Hall biosensor with integrated current microstrips for control of magnetic beads,” *IEEE Transactions on Magnetics,* vol. 42, no. 12, pp. 3893-3895, Dec, 2006.

[270] A. Sandhu, “Thin-Film Semiconductor Hall Effect Biosensors for Medical Applications,” *IEEJ Transactions on Sensors and Micromachines,* vol. 125, no. 11, pp. 444-447, 2005.

[271] A. Lapicki, H. Sanbonsugi, T. Yamamura *et al.*, “Functionalization of micro-Hall effect sensors for biomedical applications utilizing superparamagnetic beads,” *Ieee Transactions on Magnetics,* vol. 41, no. 10, pp. 4134-4136, Oct, 2005.

[272] T. Kiyoshi, S. Hideaki, S. Adarsh *et al.*, “High Sensitivity InSb Hall Effect Biosensor Platform for DNA Detection and Biomolecular Recognition Using Functionalized Magnetic Nanobeads,” *Japanese Journal of Applied Physics,* vol. 44, no. 11L, pp. L1494, 2005.

[273] A. Sandhu, H. Sanbonsugi, I. Shibasaki *et al.*, “High sensitivity InSb ultra-thin film micro-hall sensors for bioscreening applications,” *Japanese Journal of Applied Physics Part 2-Letters & Express Letters,* vol. 43, no. 7a, pp. L868-L870, Jul 1, 2004.

[274] S. M. Hira, K. Aledealat, K. S. Chen *et al.*, “Detection of target ssDNA using a microfabricated Hall magnetometer with correlated optical readout,” *J Biomed Biotechnol,* vol. 2012, pp. 492730, 2012.

[275] O. Kazakova, J. C. Gallop, D. C. Cox *et al.*, “Optimization of 2DEG InAs/GaSb Hall Sensors for Single Particle Detection,” *IEEE Transactions on Magnetics,* vol. 44, no. 11, pp. 4480-4483, Nov, 2008.

[276] D. Issadore, H. J. Chung, J. Chung *et al.*, “muHall chip for sensitive detection of bacteria,” *Adv Healthc Mater,* vol. 2, no. 9, pp. 1224-8, Sep, 2013.

[277] S. Gambini, K. Skucha, P. P. Liu *et al.*, “A 10 kPixel CMOS Hall Sensor Array With Baseline Suppression and Parallel Readout for Immunoassays,” *IEEE Journal of Solid-State Circuits,* vol. 48, no. 1, pp. 302-317, Jan, 2013.

[278] Y. Kitamoto, T. Masaki, S. B. Trisnanto *et al.*, “Magnetic sensor for sentinel lymph node biopsy using superparamagnetic beads,” *Proceedings of IEEE Sensors*, 2012.

[279] P. Liu, K. Skucha, M. Megens *et al.*, “A CMOS Hall-Effect Sensor for the Characterization and Detection of Magnetic Nanoparticles for Biomedical Applications,” *IEEE Trans Magn,* vol. 47, no. 10, pp. 3449-3451, Oct, 2011.

[280] W. Y. Chung, H. W. Li, K. J. S. Uy *et al.*, “Hall sensor based system for detection of adiponectin protein,” *5th International Conference on Bioinformatics and Biomedical Engineering*, 2011.

[281] F. T. Abu-Nimeh, and F. M. Salem, “CMOS magnetic actuators for bio-material manipulation,” *2011 IEEE GCC Conference and Exhibition (GCC)*, pp. 335-338, 2011.

[282] P. A. Besse, G. Boero, M. Demierre *et al.*, “Detection of a single magnetic microbead using a miniaturized silicon Hall sensor,” *Applied Physics Letters,* vol. 80, no. 22, pp. 4199-4201, Jun 3, 2002.

[283] Z. Zhen, and H. Zhu, "Structure and Properties of Graphene," *Graphene*, pp. 1-12: Academic Press, 2018.

[284] T. Terse-Thakoor, S. Badhulika, and A. Mulchandani, “Graphene based biosensors for healthcare,” *Journal of Materials Research,* vol. 32, no. 15, pp. 2905-2929, Aug, 2017.

[285] B. Zhan, C. Li, J. Yang *et al.*, “Graphene field-effect transistor and its application for electronic sensing,” *Small,* vol. 10, no. 20, pp. 4042-65, Oct 29, 2014.

[286] M. Holzinger, A. Le Goff, and S. Cosnier, “Nanomaterials for biosensing applications: a review,” *Front Chem,* vol. 2, no. AUG, pp. 63, 2014.

[287] H. Shen, L. Zhang, M. Liu *et al.*, “Biomedical applications of graphene,” *Theranostics,* vol. 2, no. 3, pp. 283-94, 2012.

[288] T. Dumitrică, “Synthesis, electromechanical characterization, and applications of graphene nanostructures,” *Journal of Nanophotonics,* vol. 6, no. 1, pp. 064501, 2012.

[289] A. A. Balandin, “Low-frequency 1/f noise in graphene devices,” *Nature Nanotechnology,* vol. 8, pp. 549, 08/05/online, 2013.

[290] Y. H. Zheng, L. Huang, Z. Y. Zhang *et al.*, “Sensitivity enhancement of graphene Hall sensors modified by single-molecule magnets at room temperature,” *Rsc Advances,* vol. 7, no. 4, pp. 1776-1781, 2017.

[291] L. Huang, H. Xu, Z. Zhang *et al.*, “Graphene/Si CMOS hybrid hall integrated circuits,” *Sci Rep,* vol. 4, pp. 5548, Jul 7, 2014.

[292] F. Akbar, M. Kolahdouz, S. Larimian *et al.*, “Graphene synthesis, characterization and its applications in nanophotonics, nanoelectronics, and nanosensing,” *Journal of Materials Science-Materials in Electronics,* vol. 26, no. 7, pp. 4347-4379, Jul, 2015.

[293] V. Panchal, D. Cox, R. Yakimova *et al.*, “Epitaxial Graphene Sensors for Detection of Small Magnetic Moments,” *IEEE Transactions on Magnetics,* vol. 49, no. 1, pp. 97-100, Jan, 2013.

[294] M. Kachniarz, O. Petruk, M. Oszwałdowski *et al.*, "Temperature Dependence of Functional Properties of Graphene Hall-Effect Sensors Grown on Si Face and C Face of 4H-SiC Substrate," *Progress in Automation, Robotics and Measuring Techniques*, Advances in Intelligent Systems and Computing R. Szewczyk, C. Zieliński and M. Kaliczyńska, eds., pp. 111-120, Cham: Springer International Publishing, 2015.

[295] R. F. Neumann, M. Engel, and M. Steiner, “Two dimensional, electronic particle tracking in liquids with a graphene-based magnetic sensor array,” *Nanoscale,* vol. 8, no. 28, pp. 13652-8, Jul 14, 2016.

[296] L. Huang, Z. Zhang, Z. Li *et al.*, “Multifunctional graphene sensors for magnetic and hydrogen detection,” *ACS Appl Mater Interfaces,* vol. 7, no. 18, pp. 9581-8, May 13, 2015.

[297] O. Petruk, R. Szewczyk, T. Ciuk *et al.*, “Sensitivity and Offset Voltage Testing in the Hall-Effect Sensors Made of Graphene,” *Recent Advances in Automation, Robotics and Measuring Techniques,* vol. 267, pp. 631-640, 2014.

[298] S. Pisana, P. M. Braganca, E. E. Marinero *et al.*, “Tunable nanoscale graphene magnetometers,” *Nano Lett,* vol. 10, no. 1, pp. 341-6, Jan, 2010.

[299] J. Lu, H. Zhang, W. Shi *et al.*, “Graphene magnetoresistance device in van der Pauw geometry,” *Nano Lett,* vol. 11, no. 7, pp. 2973-7, Jul 13, 2011.

[300] X. S. Wu, Y. K. Hu, M. Ruan *et al.*, “Half integer quantum Hall effect in high mobility single layer epitaxial graphene,” *Applied Physics Letters,* vol. 95, no. 22, Nov 30, 2009.

[301] K. S. Novoselov, Z. Jiang, Y. Zhang *et al.*, “Room-temperature quantum Hall effect in graphene,” *Science,* vol. 315, no. 5817, pp. 1379, Mar 9, 2007.

[302] Z. Jiang, Y. Zhang, Y. W. Tan *et al.*, “Quantum Hall effect in graphene,” *Solid State Communications,* vol. 143, no. 1-2, pp. 14-19, 2007.

[303] T. Shen, J. J. Gu, M. Xu *et al.*, “Observation of quantum-Hall effect in gated epitaxial graphene grown on SiC (0001),” *Applied Physics Letters,* vol. 95, no. 17, Oct 26, 2009.

[304] *Indian Journal of Pure and Applied Physics,* Title 49, *Quantum Hall effect in graphene: Status and prospects*, 2011, pp. 367-371.

[305] J. Jobst, D. Waldmann, F. Speck *et al.*, “Quantum oscillations and quantum Hall effect in epitaxial graphene,” *Physical Review B,* vol. 81, no. 19, May 15, 2010.

[306] Y. Barlas, K. Yang, and A. H. MacDonald, “Quantum Hall effects in graphene-based two-dimensional electron systems,” *Nanotechnology,* vol. 23, no. 5, pp. 052001, Feb 10, 2012.

[307] Y. Zhang, Z. Jiang, J. P. Small *et al.*, “Landau-level splitting in graphene in high magnetic fields,” *Phys Rev Lett,* vol. 96, no. 13, pp. 136806, Apr 7, 2006.

[308] J. E. Lenz, “A Review of Magnetic Sensors,” *Proceedings of the IEEE,* vol. 78, no. 6, pp. 973-989, Jun, 1990.

[309] R. S. Popovic, J. A. Flanagan, and P. A. Besse, “The future of magnetic sensors,” *Sensors and Actuators a-Physical,* vol. 56, no. 1-2, pp. 39-55, Aug, 1996.

[310] T. H. Hewett, and F. V. Kusmartsev, “Extraordinary magnetoresistance: sensing the future,” *Central European Journal of Physics,* vol. 10, no. 3, pp. 602-608, Jun, 2012.

[311] D. T. Bui, M. D. Tran, H. D. Nguyen *et al.*, “High-sensitivity planar Hall sensor based on simple gaint magneto resistance NiFe/Cu/NiFe structure for biochip application,” *Advances in Natural Sciences-Nanoscience and Nanotechnology,* vol. 4, no. 1, Mar, 2013.

[312] M. Costa, J. Gaspar, R. Ferreira *et al.*, “Integration of magnetoresistive sensors with atomic force microscopy cantilevers for scanning magnetoresistance microscopy applications,” *IEEE International Magnetics Conference*, 2015.

[313] L. V. Panina, and K. Mohri, “Magneto-impedance in multilayer films,” *Sensors and Actuators a-Physical,* vol. 81, no. 1-3, pp. 71-77, Apr 1, 2000.

[314] N. A. Porter, and C. H. Marrows, “Linear magnetoresistance in n-type silicon due to doping density fluctuations,” *Sci Rep,* vol. 2, pp. 565, 2012.

[315] M. Volmer, and M. Avram, “Improving the detection sensitivity of magnetic microbeads by spin valve sensors,” *AIP Conference Proceedings,* vol. 1311, pp. 261-266, 2010.

[316] J. Heremans, D. L. Partin, C. M. Thrush *et al.*, “Narrow-Gap Semiconductor Magnetic-Field Sensors and Applications,” *Semiconductor Science and Technology,* vol. 8, no. 1, pp. S424-S430, Jan, 1993.

[317] M. Kaneo, U. Tsuyoshi, and L. V. Panina, “Recent advances of micro magnetic sensors and sensing application,” *Sensors and Actuators A: Physical,* vol. 59, no. 1-3, pp. 1-8, 4//, 1997.

[318] P. Ripka, and M. Janosek, “Advances in Magnetic Field Sensors,” *IEEE Sensors Journal,* vol. 10, no. 6, pp. 1108-1116, Jun, 2010.

[319] C. Panait, V. Sârbu, and G. Căruntua, “The noise main characteristic for magnetic microsensors structures,” *Proceedings of SPIE - The International Society for Optical Engineering,* vol. 7297, 2009.

[320] D. Chen, B. Q. Zhao, and X. Zhang, “High Signal-to-Noise Ratio Hall Devices with a 2D Structure of Dual delta-Doped GaAs/AlGaAs for Low Field Magnetometry,” *Chinese Physics Letters,* vol. 32, no. 12, pp. 128502, Dec, 2015.

[321] Y. Sugiyama, and S. Kataoka, “S/N Study of Micro-Hall Sensors Made of Single-Crystal Insb and Gaas,” *Sensors and Actuators,* vol. 8, no. 1, pp. 29-38, Sep, 1985.

[322] J. Moritz, B. Rodmacq, S. Auffret *et al.*, “Extraordinary Hall effect in thin magnetic films and its potential for sensors, memories and magnetic logic applications,” *Journal of Physics D-Applied Physics,* vol. 41, no. 13, pp. 135001, Jul 7, 2008.

[323] A. D. McNaught, A. Wilkinson, A. Jenkins *et al.*, "Compendium of Chemical Terminology (Gold Book)," I. U. o. P. a. A. Chemistry, ed., Blackwell Science, 2014.

[324] S. Song, H. Xu, and C. Fan, “Potential diagnostic applications of biosensors: current and future directions,” *Int J Nanomedicine,* vol. 1, no. 4, pp. 433-40, 12/, 2006.

[325] G. A. Rechnitz, R. K. Kobos, S. J. Riechel *et al.*, “A bio-selective membrane electrode prepared with living bacterial cells,” *Anal Chim Acta,* vol. 94, no. 2, pp. 357-65, Dec 1, 1977.

[326] A. Kumar M., S. Jung, and T. Ji, “Protein Biosensors Based on Polymer Nanowires, Carbon Nanotubes and Zinc Oxide Nanorods,” *Sensors,* vol. 11, no. 5, pp. 5087, 2011.

[327] H. Ma, J. Zeng, J. Song *et al.*, “A facile ultra sound - Assisted fabrication of graphene nanosheets-silver nanowires hybrid nanomaterial and their application to electrically conductive adhesives,” *China Semiconductor Technology International Conference*, 2016.

[328] A. Ali, M. S. AlSalhi, M. Atif *et al.*, “Potentiometric urea biosensor utilizing nanobiocomposite of chitosan-iron oxide magnetic nanoparticles,” *21st International Laser Physics Workshop,* vol. 414, no. 1, pp. 012024, 2013.

[329] B. Kaur, T. Pandiyan, B. Satpati *et al.*, “Simultaneous and sensitive determination of ascorbic acid, dopamine, uric acid, and tryptophan with silver nanoparticles-decorated reduced graphene oxide modified electrode,” *Colloids Surf B Biointerfaces,* vol. 111, pp. 97-106, Nov 1, 2013.

[330] L. Wang, D. Lu, S. Yu *et al.*, “Voltammetric determination of alkannin using an Au nanoparticles–poly(diallyldimethylammonium chloride)-functionalized graphene nanocomposite film,” *Journal of Applied Electrochemistry,* vol. 43, no. 8, pp. 855-863, 2013.

[331] S. J. Rowley-Neale, E. P. Randviir, A. S. A. Dena *et al.*, “An overview of recent applications of reduced graphene oxide as a basis of electroanalytical sensing platforms,” *Applied Materials Today,* vol. 10, pp. 218-226, Mar, 2018.

[332] Z. Z. Zhu, “An Overview of Carbon Nanotubes and Graphene for Biosensing Applications,” *Nano-Micro Letters,* vol. 9, no. 3, Jul, 2017.

[333] L. Wang, Y. Zhang, A. Wu *et al.*, “Designed graphene-peptide nanocomposites for biosensor applications: A review,” *Anal Chim Acta,* vol. 985, pp. 24-40, Sep 8, 2017.

[334] GrandViewResearch, *Biosensors Market Analysis By Application (Medical applications, Food Toxicity Detection, Industrial Process Control, Agriculture, Environment) By Technology (Thermal Biosensors, Electrochemical Biosensors, Piezoelectric Biosensors, Optical Biosensors) By End-use (Home Healthcare Diagnostics, Point of Care Testing, Food Industry, Research Laboratories) And Segment Forecasts To 2020,* 978-1-68038-321-8, 2015.

[335] P. D'Orazio, “Biosensors in clinical chemistry - 2011 update,” *Clin Chim Acta,* vol. 412, no. 19-20, pp. 1749-61, Sep 18, 2011.

[336] H. L. Lee, Y. C. Yang, and W. J. Chang, “Mass Detection Using a Graphene-Based Nanomechanical Resonator,” *Japanese Journal of Applied Physics,* vol. 52, no. 2, Feb, 2013.

[337] C. Chen, S. Rosenblatt, K. I. Bolotin *et al.*, "NEMS applications of graphene." pp. 10.6.1-10.6.4.

[338] S. Kochmann, T. Hirsch, and O. S. Wolfbeis, “Graphenes in chemical sensors and biosensors,” *Trac-Trends in Analytical Chemistry,* vol. 39, pp. 87-113, Oct, 2012.

[339] S. Johnstone, “Is there potential for use of the Hall effect in analytical science?,” *Analyst,* vol. 133, no. 3, pp. 293-6, Mar, 2008.

[340] G. Mihajlovic, P. Xiong, S. von Molnar *et al.*, “InAs quantum well Hall devices for room-temperature detection of single magnetic biomolecular labels,” *Journal of Applied Physics,* vol. 102, no. 3, Aug 1, 2007.

[341] B. T. Dalslet, C. D. Damsgaard, S. C. Freitas *et al.*, “Bead capture and release on a magnetic sensor in a microfluidic system,” *Proceedings of IEEE Sensors*, pp. 242-245, 2008.

[342] Y. Kim, W. Lee, J. Hong *et al.*, “Detection of a countable number of magnetic particles for biological applications using a Hall device,” *Journal of the Korean Physical Society,* vol. 52, no. 2, pp. 513-516, Feb, 2008.

[343] Y. Kumagai, Y. Imai, M. Abe *et al.*, “Sensitivity dependence of Hall biosensor arrays with the position of superparamagnetic beads on their active regions,” *Journal of Applied Physics,* vol. 103, no. 7, Apr 1, 2008.

[344] C. R. Tamanaha, S. P. Mulvaney, J. C. Rife *et al.*, “Magnetic labeling, detection, and system integration,” *Biosens Bioelectron,* vol. 24, no. 1, pp. 1-13, Sep 15, 2008.

[345] G. Mihajlovic, and S. von Molnar, “Solid-State Magnetic Sensors for Bioapplications,” *Nanoscale Magnetic Materials and Applications*, pp. 685-710, 2009.

[346] F. W. Osterberg, B. T. Dalslet, C. D. Damsgaard *et al.*, “Bead Capture on Magnetic Sensors in a Microfluidic System,” *Ieee Sensors Journal,* vol. 9, no. 5-6, pp. 682-688, May-Jun, 2009.

[347] M. S. Gabureac, L. Bernau, G. Boero *et al.*, “Single paramagnetic bead detection and direct measurement of the spatial magnetic resolution using novel nanocomposite Hall sensors,” *Proceedings of the IEEE Conference on Nanotechnology*, 2012.

[348] K. Skucha, S. Gambini, P. Liu *et al.*, “Design Considerations for CMOS-Integrated Hall-Effect Magnetic Bead Detectors for Biosensor Applications,” *J Microelectromech Syst,* vol. 22, no. 6, pp. 1327-1338, Jun 5, 2013.

[349] M. S. Gabureac, L. Bernau, G. Boero *et al.*, “Single Superparamagnetic Bead Detection and Direct Tracing of Bead Position Using Novel Nanocomposite Nano-Hall Sensors,” *Ieee Transactions on Nanotechnology,* vol. 12, no. 5, pp. 668-673, Sep, 2013.

[350] J. Wang, A. N. Kawde, A. Erdem *et al.*, “Magnetic bead-based label-free electrochemical detection of DNA hybridization,” *Analyst,* vol. 126, no. 11, pp. 2020-4, Nov, 2001.

[351] H. Fukumoto, K. Takeguchi, M. Nomura *et al.*, "Rapid and high sensitive bio-sensing system utilizing magnetic beads." pp. 1780-1783.

[352] J. B. Haun, N. K. Devaraj, S. A. Hilderbrand *et al.*, “Bioorthogonal chemistry amplifies nanoparticle binding and enhances the sensitivity of cell detection,” *Nat Nanotechnol,* vol. 5, no. 9, pp. 660-5, Sep, 2010.

[353] O. Kazakova, J. Gallop, G. Perkins *et al.*, “Scanned micro-Hall microscope for detection of biofunctionalized magnetic beads,” *Applied Physics Letters,* vol. 90, no. 16, pp. 162502, 2007.

[354] G. Landry, M. M. Miller, B. R. Bennett *et al.*, “Characterization of single magnetic particles with InAs quantum-well Hall devices,” *Applied Physics Letters,* vol. 85, no. 20, pp. 4693-4695, Nov 15, 2004.

[355] G. Mihajlovic, K. Aledealat, P. Xiong *et al.*, “Magnetic characterization of a single superparamagnetic bead by phase-sensitive micro-Hall magnetometry,” *Applied Physics Letters,* vol. 91, no. 17, Oct 22, 2007.

[356] M. A. M. Gijs, “Magnetic bead handling on-chip: new opportunities for analytical applications,” *Microfluidics and Nanofluidics,* vol. 1, no. 1, pp. 22-40, Nov, 2004.

[357] Q. A. Pankhurst, J. Connolly, S. K. Jones *et al.*, “Applications of magnetic nanoparticles in biomedicine,” *Journal of Physics D-Applied Physics,* vol. 36, no. 13, pp. R167-R181, Jul 7, 2003.

[358] O. Florescu, M. Mattmann, and B. Boser, “Fully integrated detection of single magnetic beads in complementary metal-oxide-semiconductor,” *Journal of Applied Physics,* vol. 103, no. 4, Feb 15, 2008.

[359] T. S. Aytur, T. Ishikawa, and B. E. Boser, “A 2.2-mm(2) CMOS bioassay chip and wireless interface,” *2004 Symposium on VLSI Circuits*, pp. 314-317, 2004.

[360] F. T. Abu-Nimeh, and F. M. Salem, “Integrated magnetic array for bio-object sensing and manipulation,” *IEEE Biomedical Circuits and Systems Conference*, pp. 62-65, 2010.

[361] Y. Kumagai, Y. Imai, M. Abe *et al.*, “Sensitivity dependence of Hall biosensor arrays with the position of superparamagnetic beads on their active regions,” *Journal of Applied Physics,* vol. 103, no. 7, pp. 07A309, Apr 1, 2008.

[362] A. Manzin, E. Simonetto, G. Amato *et al.*, “Modeling of graphene Hall effect sensors for microbead detection,” *Journal of Applied Physics,* vol. 117, no. 17, May 7, 2015.

[363] Y. Huang, X. Dong, Y. Shi *et al.*, “Nanoelectronic biosensors based on CVD grown graphene,” *Nanoscale,* vol. 2, no. 8, pp. 1485-8, Aug, 2010.

[364] Y. M. Lin, and P. Avouris, “Strong suppression of electrical noise in bilayer graphene nanodevices,” *Nano Lett,* vol. 8, no. 8, pp. 2119-25, Aug, 2008.

[365] A. Ambrosi, C. K. Chua, A. Bonanni *et al.*, “Electrochemistry of graphene and related materials,” *Chem Rev,* vol. 114, no. 14, pp. 7150-88, Jul 23, 2014.

[366] V. Georgakilas, J. N. Tiwari, K. C. Kemp *et al.*, “Noncovalent Functionalization of Graphene and Graphene Oxide for Energy Materials, Biosensing, Catalytic, and Biomedical Applications,” *Chem Rev,* vol. 116, no. 9, pp. 5464-519, May 11, 2016.

[367] M. Pumera, “Electrochemistry of graphene, graphene oxide and other graphenoids: Review,” *Electrochemistry Communications,* vol. 36, pp. 14-18, Nov, 2013.

[368] M. Pumera, A. Ambrosi, A. Bonanni *et al.*, “Graphene for electrochemical sensing and biosensing,” *TrAC Trends in Analytical Chemistry,* vol. 29, no. 9, pp. 954-965, 2010.

[369] D. A. Brownson, and C. E. Banks, “Graphene electrochemistry: an overview of potential applications,” *Analyst,* vol. 135, no. 11, pp. 2768-78, Nov, 2010.

[370] A. Ambrosi, C. K. Chua, N. M. Latiff *et al.*, “Graphene and its electrochemistry - an update,” *Chem Soc Rev,* vol. 45, no. 9, pp. 2458-93, May 7, 2016.

[371] R. Zhang, and W. Chen, “Recent advances in graphene-based nanomaterials for fabricating electrochemical hydrogen peroxide sensors,” *Biosens Bioelectron,* vol. 89, no. Pt 1, pp. 249-268, Mar 15, 2017.

[372] J. Kim, M. Ishihara, Y. Koga *et al.*, “Low-temperature synthesis of large-area graphene-based transparent conductive films using surface wave plasma chemical vapor deposition,” *Applied Physics Letters,* vol. 98, no. 9, pp. 091502, Feb 28, 2011.

[373] D. Li, W. Zhang, X. Yu *et al.*, “When biomolecules meet graphene: from molecular level interactions to material design and applications,” *Nanoscale,* vol. 8, no. 47, pp. 19491-19509, Dec 1, 2016.

[374] C. K. Chua, and M. Pumera, “Chemical reduction of graphene oxide: a synthetic chemistry viewpoint,” *Chem Soc Rev,* vol. 43, no. 1, pp. 291-312, Jan 7, 2014.

[375] Z. Z. Sun, S. Kohama, Z. X. Zhang *et al.*, “Soluble graphene through edge-selective functionalization,” *Nano Research,* vol. 3, no. 2, pp. 117-125, Feb, 2010.

[376] D. Parviz, S. Das, H. S. Ahmed *et al.*, “Dispersions of non-covalently functionalized graphene with minimal stabilizer,” *ACS Nano,* vol. 6, no. 10, pp. 8857-67, Oct 23, 2012.

[377] H. Grigg, “The principles and practice of the Xylophone Bar Magnetometer,” Thesis (Ph. D.)--University of Newcastle upon Tyne, 2014., Newcastle upon Tyne, 2014.

[378] R. Steiner, C. Maier, A. Haberli *et al.*, “Offset reduction in Hall devices by continuous spinning current method,” *Sensors and Actuators a-Physical,* vol. 66, no. 1-3, pp. 167-172, Apr 1, 1998.

[379] C. Xiaoqing, X. Yue, X. Xiaopeng *et al.*, “A novel Hall dynamic offset cancellation circuit based on four-phase spinning current technique,” *Semiconductor Technology International Conference*, pp. 1-3, 2015.

[380] Y. Xu, H. B. Pan, S. Z. He *et al.*, “A highly sensitive CMOS digital Hall sensor for low magnetic field applications,” *Sensors (Basel),* vol. 12, no. 2, pp. 2162-74, 2012.

[381] N. Khlebtsov, and L. Dykman, “Biodistribution and toxicity of engineered gold nanoparticles: a review of in vitro and in vivo studies,” *Chem Soc Rev,* vol. 40, no. 3, pp. 1647-71, Mar, 2011.

[382] N. Nath, and A. Chilkoti, “A colorimetric gold nanoparticle sensor to interrogate biomolecular interactions in real time on a surface,” *Anal Chem,* vol. 74, no. 3, pp. 504-9, Feb 1, 2002.

[383] J. M. Pingarron, P. Yanez-Sedeno, and A. Gonzalez-Cortes, “Gold nanoparticle-based electrochemical biosensors,” *Electrochimica Acta,* vol. 53, no. 19, pp. 5848-5866, Aug 1, 2008.

[384] K. Saha, S. S. Agasti, C. Kim *et al.*, “Gold nanoparticles in chemical and biological sensing,” *Chem Rev,* vol. 112, no. 5, pp. 2739-79, May 9, 2012.

[385] W. Zhao, M. A. Brook, and Y. Li, “Design of gold nanoparticle-based colorimetric biosensing assays,” *Chembiochem,* vol. 9, no. 15, pp. 2363-71, Oct 13, 2008.

[386] M.-A. Paun, J.-M. Sallese, and M. Kayal, "Offset Drift Dependence of Hall Cells with their Designed Geometry," *International Journal of Electronics and Telecommunications*, 2, 2013, p. 169.

[387] M. A. Paun, J. M. Sallese, and M. Kayal, “Comparative study on the performance of five different Hall effect devices,” *Sensors (Basel),* vol. 13, no. 2, pp. 2093-112, Feb 5, 2013.

[388] M. A. Paun, “Effect of structure scaling on the offset levels for CMOS Hall Effect sensors,” *International Conference on Computer as a Tool*, pp. 1-6, 8-11 Sept. 2015, 2015.

[389] V. P. Kunets, S. Easwaran, W. T. Black *et al.*, “InSb Quantum-Well-Based Micro-Hall Devices: Potential for pT Detectivity,” *Ieee Transactions on Electron Devices,* vol. 56, no. 4, pp. 683-687, Apr, 2009.

[390] M. S. Gabureac, L. S. Alvarez, and C. H. Marrows, “Co/Pt Hall sensors for low field detection,” *Proceedings of the Eurosensors Xxiii Conference,* vol. 1, no. 1, pp. 851-+, 2009.

[391] C. Ravi Kumar, T. S. Abhilash, B. P. C. Rao *et al.*, "GaAs/AlGaAs heterostructure based micro-hall sensors and response to A.C. excitation," *Studies in Applied Electromagnetics and Mechanics*, 2012, pp. 241-246.

[392] V. P. Kunets, W. T. Black, Y. I. Mazur *et al.*, “Highly sensitive micro-Hall devices based on Al0.12In0.88Sb / InSb heterostructures,” *Journal of Applied Physics,* vol. 98, no. 1, pp. 014506, 2005.

[393] S. Del Medico, T. Benyattou, G. Guillot *et al.*, “Micro-Hall magnetic sensors with high magnetic sensitivity based on III-V heterostructures,” *Proceedings of SPIE - The International Society for Optical Engineering,* vol. 2779, pp. 289-293, 1996.

[394] N. Haned, and M. Missous, “Nano-tesla magnetic field magnetometry using an InGaAs-AlGaAs-GaAs 2DEG Hall sensor,” *Sensors and Actuators a-Physical,* vol. 102, no. 3, pp. 216-222, Jan 1, 2003.

[395] A. Lanzara. "Viewpoint: Graphene Gets a Good Gap," 2018; https://physics.aps.org/articles/v8/91.

[396] R. B. Wu, K. Zhou, C. Y. Yue *et al.*, “Recent progress in synthesis, properties and potential applications of SiC nanomaterials,” *Progress in Materials Science,* vol. 72, pp. 1-60, Jul, 2015.

[397] A. Das, B. Chakraborty, and A. K. Sood, “Raman spectroscopy of graphene on different substrates and influence of defects,” *Bulletin of Materials Science,* vol. 31, no. 3, pp. 579-584, Jun, 2008.

[398] S. N. Yannopoulos, A. Siokou, N. K. Nasikas *et al.*, “CO2-Laser-Induced Growth of Epitaxial Graphene on 6H-SiC(0001),” *Advanced Functional Materials,* vol. 22, no. 1, pp. 113-120, Jan 11, 2012.

[399] D. P. Wei, and X. F. Xu, “Laser direct growth of graphene on silicon substrate,” *Applied Physics Letters,* vol. 100, no. 2, Jan 9, 2012.

[400] J. B. Park, W. Xiong, Y. Gao *et al.*, “Fast growth of graphene patterns by laser direct writing,” *Applied Physics Letters,* vol. 98, no. 12, Mar 21, 2011.

[401] S. Lee, M. F. Toney, W. Ko *et al.*, “Laser-synthesized epitaxial graphene,” *ACS Nano,* vol. 4, no. 12, pp. 7524-30, Dec 28, 2010.

[402] M. Kato, M. Ichimura, E. Arai *et al.*, “Electrochemical etching of 6H-SiC using aqueous KOH solutions with low surface roughness,” *Japanese Journal of Applied Physics Part 1-Regular Papers Short Notes & Review Papers,* vol. 42, no. 7a, pp. 4233-4236, Jul, 2003.

[403] R. E. J. Watkins, P. Rockett, S. Thoms *et al.*, “Focused Ion-Beam Milling,” *Vacuum,* vol. 36, no. 11-12, pp. 961-967, Nov-Dec, 1986.

[404] Z. Moktadir, "Graphene nanoelectromechanics (NEMS)," *Graphene*, V. Skákalová and A. B. Kaiser, eds., pp. 341-362: Woodhead Publishing, 2014.

[405] H. Wang, Y. Wang, X. Cao *et al.*, “Vibrational properties of graphene and graphene layers,” *Journal of Raman Spectroscopy,* vol. 40, no. 12, pp. 1791-1796, 2009.

[406] F. T. Johra, J.-W. Lee, and W.-G. Jung, “Facile and safe graphene preparation on solution based platform,” *Journal of Industrial and Engineering Chemistry,* vol. 20, no. 5, pp. 2883-2887, 2014/09/25/, 2014.

[407] M. Boutchich, A. Jaffré, D. Alamarguy *et al.*, “Characterization of graphene oxide reduced through chemical and biological processes,” *Journal of Physics: Conference Series,* vol. 433, no. 1, pp. 012001, 2013.

[408] D. S. Mellet, and M. du Plessis, “A novel CMOS Hall effect sensor,” *Sensors and Actuators a-Physical,* vol. 211, pp. 60-66, May 1, 2014.

[409] O. O. Ekiz, M. Urel, H. Guner *et al.*, “Reversible electrical reduction and oxidation of graphene oxide,” *ACS Nano,* vol. 5, no. 4, pp. 2475-82, Apr 26, 2011.

[410] L. Feng, A. Zhao, J. Ren *et al.*, “Lighting up left-handed Z-DNA: photoluminescent carbon dots induce DNA B to Z transition and perform DNA logic operations,” *Nucleic Acids Res,* vol. 41, no. 16, pp. 7987-96, Sep, 2013.

[411] W. Wang, L. Cheng, and W. G. Liu, “Biological applications of carbon dots,” *Science China-Chemistry,* vol. 57, no. 4, pp. 522-539, Apr, 2014.

[412] P. Vilela, A. El-Sagheer, T. M. Millar *et al.*, "Graphene Oxide-Upconversion Nanoparticle Based Optical Sensors for Targeted Detection of mRNA Biomarkers Present in Alzheimer's Disease and Prostate Cancer," *ACS Sens,* vol. 2, no. 1, pp. 52-56, Jan 27, 2017.

[413] L. Chen, G. Yang, P. Wu *et al.*, "Real-time fluorescence assay of alkaline phosphatase in living cells using boron-doped graphene quantum dots as fluorophores," *Biosens Bioelectron,* vol. 96, pp. 294-299, Oct 15, 2017.

[414] Y. Li, L. Sun, J. Qian *et al.*, "Fluorescent "on-off-on" switching sensor based on CdTe quantum dots coupled with multiwalled carbon nanotubes@graphene oxide nanoribbons for simultaneous monitoring of dual foreign DNAs in transgenic soybean," *Biosens Bioelectron,* vol. 92, pp. 26-32, Jun 15, 2017.

[415] J. Shi, J. Lyu, F. Tian *et al.*, "A fluorescence turn-on biosensor based on graphene quantum dots (GQDs) and molybdenum disulfide (MoS2) nanosheets for epithelial cell adhesion molecule (EpCAM) detection," *Biosens Bioelectron,* vol. 93, pp. 182-188, Jul 15, 2017.

[416] P. Suvarnaphaet, C. S. Tiwary, J. Wetcharungsri *et al.*, "Blue photoluminescent carbon nanodots from limeade," *Mater Sci Eng C Mater Biol Appl,* vol. 69, pp. 914-21, Dec 1, 2016.

[417] R. J. Chen, Y. Zhang, D. Wang *et al.*, "Noncovalent sidewall functionalization of single-walled carbon nanotubes for protein immobilization," *J Am Chem Soc,* vol. 123, no. 16, pp. 3838-9, Apr 25, 2001.

[418] V. Georgakilas, M. Otyepka, A. B. Bourlinos *et al.*, "Functionalization of graphene: covalent and non-covalent approaches, derivatives and applications," *Chem Rev,* vol. 112, no. 11, pp. 6156-214, Nov 14, 2012.

[419] V. K. Kodali, J. Scrimgeour, S. Kim *et al.*, "Nonperturbative chemical modification of graphene for protein micropatterning," *Langmuir,* vol. 27, no. 3, pp. 863-5, Feb 1, 2011.

[420] D. Izci, C. Dale, N. Keegan *et al.*, "Design and construction of a high sensitive graphene magnetosensing system," *2017 IEEE Sensors Conerence*, pp. 1-3, 2017.

[421] D. Izci, C. Dale, N. Keegan *et al.*, "The Construction of a Graphene Hall Effect Magnetometer," *IEEE Sensors Journal*, pp. 1-8, 2018.

[422] P. V. Kumar, N. M. Bardhan, G. Y. Chen *et al.*, "New insights into the thermal reduction of graphene oxide: Impact of oxygen clustering," *Carbon,* vol. 100, pp. 90-98, Apr, 2016.

[423] N. Galvao, G. Vasconcelos, R. Pessoa *et al.*, "A Novel Method of Synthesizing Graphene for Electronic Device Applications," *Materials (Basel),* vol. 11, no. 7, pp. 1120, Jun 30, 2018.